THÈSE

En vue de l'obtention du

DOCTORAT DE L'UNIVERSITÉ DE TOULOUSE

Délivré par : *l'Université Toulouse 3 Paul Sabatier (UT3 Paul Sabatier)*

Présentée et soutenue le *12/02/2015* **par :**

ADÈLE POUBEAU

Simulation des émissions d'un moteur à propergol solide : vers une modélisation multi-échelle de l'impact atmosphérique des lanceurs

---

JURY

J.-L. ATTIE	Prof. - Université Toulouse 3	Président du Jury
D. VEYNANTE	Directeur de recherche - CNRS	Rapporteur
S. BEKKI	Directeur de recherche - CNRS	Rapporteur
F. GRASSO	Professeur - CNAM	Examinateur
S. PETITOT	Ingénieur - CNES	Examinateur
N. MURRAY	Ingénieur - ESA	Examinateur
R. PAOLI	Chercheur Senior - CERFACS	Directeur de thèse
J.-C. CHASTENET	Ingénieur - Herakles	Invité

École doctorale et spécialité :
SDU2E : Océan, Atmosphère et Surfaces Continentales
Unité de Recherche :
Equipe Aviation et Environnement (URA 1875), CERFACS
Directeur de Thèse :
Roberto PAOLI
Rapporteurs :
Denis VEYNANTE et *Slimane BEKKI*

A ma famille

στον Δημήτρη

Remerciements

Tournesol *: Ouf !... Le danger est passé !... Je respire !... Je puis vous avouer maintenant que j'ai bien eu peur...*
Haddock *: Nous aurions été vraiment réduits en miettes ?...*
Tournesol *: Si ce n'est que ça !... Mais c'est beaucoup plus grave !... Oui, je puis vous le dire à présent : si mes prévisions ne s'étaient pas réalisées, j'aurais dû recommencer tous mes calculs !...*

On a marché sur la Lune, Hergé, éd. Casterman, coll. Tintin, 1954, t. 17, p. 15

Mes premiers remerciements vont à Roberto Paoli. Ce fut un vrai plaisir de t'avoir comme directeur de thèse. Tu as été un excellent guide, me laissant une grande liberté tout en étant toujours disponible dès que je débarquais dans ton bureau avec mes questions. Tu as même trouvé le temps de gérer à la fois une thésarde en pleine rédaction et un p'tit loup, le tout sur des continents différents, alors tu as toute mon admiration. J'ai beaucoup appris en travaillant avec toi, et je t'en remercie.

Je suis également très reconnaissante à Daniel Cariolle de m'avoir accueilli si chaleureusement dans son équipe et de m'avoir donné toute sa confiance et ses conseils pour cette thèse.

Je remercie naturellement mes deux rapporteurs, Denis Veynante et Slimane Bekki, qui m'ont fait l'honneur de lire mon manuscrit et d'y apporter des commentaires essentiels et très pertinents. Un grand merci également aux autres membres de mon jury, Francesco Grasso, Stéphane Petitot, Neil Murray, Jean-Luc Attié et Jean-Claude Chastenet, pour toute l'attention qu'ils ont portée à mes travaux.

Ce travail est le fruit d'une collaboration entre le CNES et le CERFACS. A ce titre, je remercie Stéphane Petitot, Michel Pons, Sandrine Richard, Estelle Champesting et Nathalie Fuentes, qui se sont tous penchés avec patience sur mon travail et m'ont apporté les données nécessaires à mes calculs. Mes remerciements vont également à Jean-Claude Chastenet, Christophe Linck et Laurence Guenot de Safran-Herakles pour leurs bons conseils. Au sein du CERFACS, j'ai eu la chance de recevoir l'aide de plusieurs équipes pour progresser sur mon sujet quelque peu exotique. Je salue d'abord l'équipe CFD au grand complet et en particulier Antoine Dauptain, Eléonore Riber, Gabriel Staffelbach, Bénédicte Cuenot, Olivier Vermorel et Thierry Poinsot. Tous m'ont permis de résoudre un problème, de mettre en place des simulations complexes ou de m'éclairer par des interprétations fines. Je souhaite mentionner également Florent Duchaine de l'équipe GlobC et Gaofeng Wang pour toute l'aide qu'ils m'ont apportée dans l'utilisation de TurboAVBP.

Je remercie l'équipe CSG (dont Fabrice, Gérard, Isabelle, Patrick, Maurice...) pour leur grande compétence, leur réactivité et leur dévotion. Et enfin le CERFACS ne serait pas aussi plaisant sans la bonne humeur des génies de l'administratif, en particulier Chantal, Michèle et Nathalie.

J'ai passé trois belles années (et un peu plus d'ailleurs) parmi l'équipe Aviation et Environnement, petite mais costaude. Je salue tous ceux que j'ai côtoyés, en particulier Odile Thouron, Emanuele Emili, Hannah Clark, Elodie Jaumouillé (j'attends toujours ta recette de canelés !), Bojan Sic, Frank Auguste... Et comment pourrais-je ne pas citer Joris Picot et Alexis Praga, mes deux collègues thésards, qui sont devenus bien vite des amis chers. De soirées sushis en soirées crêpes en passant par les soirées Wii (et Minecraft aussi), de pauses thé (Kukicha) en pauses café (surtout vers la fin...), leur compagnie m'a été précieuse. Je remercie aussi Hélène, qui a illuminé mes derniers mois dans l'équipe : je te souhaite bon courage pour ta thèse qui, je n'en ai aucun doute, sera une belle réussite ! Je n'oublie pas tous mes collègues et amis, du CERFACS ou d'ailleurs, en particulier Audrey, Marie D. & Marie P., Lisa, Thomas, Sophie, Yunic... avec une mention spéciale pour Marie-No, la reine de la supply chain !

Enfin, je remercie mes parents, qui m'ont toujours supportée avec une patience folle et ce quelque soit ma lubie (même celle de faire une thèse). J'en profite pour saluer toute ma famille et rappeler à mon grand-père Dédé que j'ai maintenant le droit d'investir son salon et de changer la chaîne comme bon me semble.

Et Dimitris, bien sûr :) Pour ton soutien indéfectible, les voyages, les soupes de lentilles et le rakomelo. Il fallait bien tout ça pour réussir cette thèse !

Abstract

Rockets have an impact on the chemical composition of the atmosphere, and particularly on stratospheric ozone. Among all types of propulsion, Solid-Rocket Motors (SRMs) have given rise to concerns since their emissions are responsible for a severe decrease in ozone concentration in the rocket plume during the first hours after a launch. The main source of ozone depletion is due to the conversion of hydrogen chloride, a chemical compound emitted in large quantities by ammonium perchlorate based propellants, into active chlorine compounds, which then react with ozone in a destructive catalytic cycle, similar to those responsible for the Antartic "Ozone hole". This conversion occurs in the hot, supersonic exhaust plume, as part of a strong second combustion between chemical species of the plume and air. The objective of this study is to evaluate the active chlorine concentration in the far-field plume of a SRM using large-eddy simulations (LES). The gas is injected through the entire nozzle of the SRM and a local time-stepping method based on coupling multi-instances of the fluid solver is used to extend the computational domain up to 400 nozzle exit diameters downstream of the nozzle exit. The methodology is validated for a non-reactive case by analyzing the flow characteristics of the resulting supersonic co-flowing under-expanded jet. Then the chemistry of chlorine is studied off-line using a complex chemistry solver applied on trajectories extracted from the LES time-averaged flow-field. Finally, the online chemistry is analyzed by means of the multi-species version of the LES solver using a reduced chemical scheme. To the best of our knowledge, this represents one of the first LES of a reactive supersonic jet, including nozzle geometry, performed over such a long computational domain. By capturing the effect of mixing of the exhaust plume with ambient air and the interactions between turbulence and combustion, LES offers an evaluation of chemical species distribution in the SRM plume with an unprecedented accuracy. These results can be used to initialize atmospheric simulations on larger domains, in order to model the chemical reactions between active chlorine and ozone and to quantify the ozone loss in SRM plumes.

Résumé

Les lanceurs ont un impact sur la composition de l'atmosphère, et en particulier sur l'ozone stratospherique. Parmi tous les types de propulsion, les moteurs à propergol solide ont fait l'objet d'une attention particulière car leurs émissions sont responsables d'un appauvrissement significatif d'ozone dans le panache lors des premières heures suivant le lancement. Ce phénomène est principalement dû à la conversion de l'acide chlorhydrique, un composé chimique présent en grandes quantités dans les émissions de ce type de moteur, en chlore actif qui réagit par la suite avec l'ozone dans un cycle catalytique similaire à celui responsable du "trou de la couche d'ozone", cette diminution périodique de l'ozone en Antarctique. Cette conversion se produit dans le panache supersonique, où les hautes températures favorisent une seconde combustion entre certaines espèces chimiques du panache et l'air ambiant. L'objectif de cette étude est d'évaluer la concentration de chlore actif dans le panache d'un moteur à propergol solide en utilisant la technique des Simulations aux Grandes Echelles (SGE). Le gaz est injecté à travers la tuyère d'un moteur et une méthode de couplage entre deux instances du solveur de mécanique des fluides est utilisée pour étendre autant que possible le domaine de calcul derrière la tuyère (jusqu'à l'équivalent de 400 diamètres de sortie de la tuyère). Cette méthodologie est validée par une première SGE sans chimie, en analysant les caractéristiques de l'écoulement supersonique avec co-écoulement obtenu par ce calcul. Ensuite, le chimie mettant en jeu la conversion des espèces chlorées est étudiée au moyen d'un modèle "hors-ligne" permettant de résoudre une chimie complexe le long de lignes de courant extraites d'un écoulement moyenné dans le temps résultant du calcul précédent (non réactif). Enfin, une SGE multi-espèces est réalisée, incluant un schéma chimique auparavant réduit afin de limiter le coût de calcul. Cette simulation représente une des toutes premières SGE d'un jet supersonique réactif, incluant la tuyère, effectuée sur un domaine de calcul aussi long. En capturant avec précision le mélange du panache avec l'air ambiant ainsi que les interactions entre turbulence et combustion, la technique des simulations aux grandes échelles offre une évaluation des concentrations des espèces chimiques dans le jet d'une précision inédite. Ces résultats peuvent être utilisés pour initialiser des calculs atmosphériques sur de plus larges domaines, afin de modéliser les réactions entre chlore actif et ozone et de quantifier l'appauvrissement en ozone dans le panache.

Contents

Preamble

Combustion emissions from rocket launchers have an impact on the composition of the atmosphere, and particularly on the concentration of stratospheric ozone. This impact was first considered in the years 1970's (Cicerone and Stedman, 1974), while concerns about the ozone depletion effects of chlorofluorocarbons (CFCs) were raised (Molina and Rowland, 1974; Rowland and Molina, 1975). Since then, a large number of modelling studies has been performed to assess the impact of American launchers on ozone, mainly by the Aerospace Corporation (Denison et al., 1994; Zittel, 1994; Beiting, 1997; Brady et al., 1997; Ross et al., 1997b). This effort led to two *in-situ* measurements campaigns, the Rocket Impacts on Stratospheric Ozone (RISO) campaign (1996-1998) and the Atmospheric Chemistry of Combustion Emissions Near the Tropopause (ACCENT) campaign (1999-2000), both of them investigating the local ozone loss due to Solid-Rocket Motors (SRM) stratospheric plumes (Ross et al., 1997a; Danilin et al., 2003). All these studies concluded that the ozone loss caused by rocket emissions (mainly SRMs) was small and largely negligible compared to those of CFCs and other halogen gas (World Meteorological Organization, 2006). As a consequence, rocket emissions were never a part of the regulatory framework that protects the ozone layer, known as the Montreal Protocol on Substances That Deplete the Ozone Layer (1987).

These early conclusions are to be addressed with caution. The Montreal Protocol phased out 97% of ozone-depleting chemicals, allowing the ozone layer to recover by mid-century (Andersen et al., 2007). This could bring a change in the current policy regarding rocket emissions. Their impact on ozone, considered small today, might be scrutinized in the near future, particularly because it is the only source of ozone depleting chemicals which is injected directly in the ozone layer. Furthermore, a large increase in launch demand (factors of ten or more) is considered as a plausible scenario by many specialists (Sanderson, 2010). Anticipating these future problematics by new, more accurate modelling studies is all the more important that previous studies left important questions unanswered. In particular, they present large uncertainties regarding the small-scale plume effect on local and global ozone loss. Local plume effects may also have an important significance for the assessment of the potential hazards for the population living in the vicinity of launch pads as ozone acts as protecting shield from U.V. radiation.

These aspects motivated European space operators to conduct new studies, using the latest computational tools available, as a part of a general assessment of the impact of space launch operations on the environment. In the framework of the ESA Clean Space Initiative [1], the AtILa (Atmospheric Impact of Launchers) project was initiated in 2012, gathering research teams from all Europe (DLR from Germany, ONERA and CERFACS from France, Imperial College London from England and SAFRAN-HERAKLES, manufacturer of SRMs) with the objective to model the multi-scale atmospheric impact of

1. http://www.esa.int/Our_Activities/Space_Engineering/Clean_Space/What_is_Clean_Space

the rockets launched from Kourou (French Guiana). A few results are available as this manuscript is being prepared (Koch et al., 2013; Grenard et al., 2013; Bauer et al., 2013). In parallel with this study, a similar project was initiated by CNES. As a space operator subject to the French Space Law on Space Operations (FSOA), the French space agency is contractually required to assess the environmental impact of the space launches operated from Kourou. The present work has been conducted as a part of this study.

Assessing the impact of rockets on ozone involves to take into account several time and space scales, from the local effect of a rocket plume to the global, cumulative effect of worldwide launches on the ozone layer. The present study focuses on the smallest scales by aiming to model the supersonic hot jet exhaust of a SRM (whose impact on ozone largely prevails over liquid propulsion), at 20 km of altitude, and particularly the activation of chlorine species resulting from a strong second combustion between the exhaust products and the ambient air. Large uncertainties remain in modelling this small scale phenomenon, which is a key mechanism in the evaluation of local ozone depletion during the hours following the launch, as active chlorine reacts with ozone in a destructive catalytic cycle. Therefore the objective of this study is to use a high-order compressible flow solver, based on the Large Eddy Simulation (LES) technique, to entirely model the reactive jet over very long distances behind the rocket, and in particular the coupling between turbulence and chemical reactions. This technique should result in an unprecedented accurate source term for the evaluation of SRMs impact on ozone using atmospheric simulations.

Préambule

Les produits de combustion émis par les lanceurs spatiaux ont un impact sur la composition de l'atmosphère, et en particulier sur la concentration de l'ozone stratosphérique. Cette problématique est apparue dans les années 1970 (Cicerone and Stedman, 1974), alors que les premières études montrant l'effet destructeur des chlorofluorocarbures (CFC) sur l'ozone étaient publiées (Molina and Rowland, 1974; Rowland and Molina, 1975). Dès lors, de nombreuses modélisations ont été réalisées dans le but d'évaluer l'impact des lanceurs américains sur l'ozone, principalement par l'Aerospace Corporation (Denison et al., 1994; Zittel, 1994; Beiting, 1997; Brady et al., 1997; Ross et al., 1997b). Cet effort a mené à la réalisation de deux campagnes de mesures *in-situ* ayant pour objectif d'étudier l'appauvrissement en ozone dans le panache des moteurs à propergol solide : la campagne RISO (Rocket Impacts on Stratospheric Ozone) en 1996-1998 et la campagne ACCENT (Atmospheric Chemistry of Combustion Emissions Near the Tropopause), en 1999-2000 (Ross et al., 1997a; Danilin et al., 2003). Toutes ces études ont conclu que l'appauvrissement en ozone entraîné par les émissions des lanceurs (principalement les moteurs à propergol solide) était mineur et largement négligeable comparé à l'impact des CFC et des gaz halogènes (World Meteorological Organization, 2006). En conséquence, les émissions des lanceurs spatiaux n'ont jamais fait l'objet d'une régulation dans le cadre du Protocole de Montréal, signé en 1987 et visant à protéger la couche d'ozone en interdisant les CFC et autres substances nocives.

Ces premières conclusions sont à considérer avec précaution. Le Protocole de Montréal a permis d'éliminer 97% des espèces chimiques destructrices d'ozone, permettant à la couche d'ozone de retrouver sa concentration initiale dès les années 2050 (Andersen et al., 2007). Cela pourrait amener à reconsidérer la politique actuelle concernant les émissions des lanceurs. Leur impact sur l'ozone, considéré comme étant négligeable aujourd'hui, pourrait faire l'objet d'une attention particulière dans un futur proche, tout particulièrement car il s'agit de la seule source de gaz appauvrissant l'ozone injectée directement dans la couche d'ozone. De plus, une large augmentation de la demande (d'un facteur 10 ou plus) est considérée comme étant un scénario plausible par de nombreux spécialistes (Sanderson, 2010). Anticiper ces futures problématiques par de nouvelles études de modélisation, plus précises, est d'autant plus important que les précédentes études ont laissé d'importantes questions sans réponse. Par exemple, elles présentent de larges incertitudes concernant l'effet des petites échelles du panache sur l'appauvrissement local et global d'ozone. De plus, la couche d'ozone agissant comme barrière contre les rayons U.V, l'impact local d'un panache de lanceur pourrait avoir un impact significatif pour les populations vivant à proximité des sites de lancements.

Ces aspects ont motivé les agences spatiales européennes à lancer de nouvelles études, utilisant les moyens de calculs les plus récents. Ces travaux s'inscrivent dans un effort d'évaluation de l'impact global des opérations de lancements spatiaux sur l'environnement.

Dans le cadre de l'initiative Clean Space [2] menée par l'ESA (Agence Spatiale Européenne), le projet AtILa (Atmospheric Impact of Launchers), lancé en 2012, a rassemblé des équipes de recherches de toute l'Europe (DLR en Allemagne, Onera et Cerfacs en France, Imperial College London en Angleterre et Safran-Herakles, fabriquant de moteurs à propergol solide) avec l'objectif de modéliser l'impact atmosphérique multi-échelle des fusées lancées depuis Kourou (Guyane). Quelques résultats ont été publiés alors que ce manuscrit était en cours de préparation (Koch et al., 2013; Grenard et al., 2013; Bauer et al., 2013). Parallèlement à cette étude, un projet similaire a été initié par le CNES (Centre National d'Etudes Spatiales). En tant qu'opérateur soumis à la loi relative aux opérations spatiales (adoptée en 2008), le CNES a l'obligation contractuelle d'évaluer l'impact environnemental des lancements spatiaux effectués depuis Kourou. Les présents travaux ont été réalisés dans le cadre de cette étude.

L'évaluation de l'impact des fusées sur l'ozone implique de prendre en compte plusieurs échelles temporelles et spatiales, depuis les effets locaux d'un panache de lanceur jusqu'aux effets cumulés, à l'échelle du globe, de tous les lancements opérés dans le monde. La présente étude se concentre sur les plus petites échelles avec l'objectif de modéliser le panache supersonique d'un moteur à propergol solide à 20 km d'altitude, et en particulier l'activation des espèces chlorées résultant d'une seconde combustion entre les émissions du moteur et l'air ambiant. Ce phénomène est un mécanisme-clé dans l'évaluation de l'appauvrissement local d'ozone car le chlore actif réagit avec l'ozone dans un cycle catalytique très destructeur. L'objectif de cette étude est donc d'utiliser un code de mécanique des fluides compressible, basé sur la technique des Simulations aux Grandes Echelles, afin de modéliser entièrement le jet sur de très longues distances derrière la fusée et en particulier le couplage entre turbulence et réactions chimiques. Ce travail devrait fournir un terme source d'une précision inédite pour l'évaluation de l'impact des moteurs à propergol solide par des simulations atmosphériques.

2. `http://www.esa.int/Our_Activities/Space_Engineering/Clean_Space/What_is_Clean_Space`

CHAPTER 1

Introduction

1.1 Impact of launchers on stratospheric ozone

1.1.1 Ozone chemistry

Ozone exists through all levels of the atmosphere, from 0 to 100 kilometers (km) altitude. A peak in ozone concentration lies around 20-30 km altitude, absorbing harmful ultraviolet (UV) radiation: it is the ozone layer. The distribution of ozone is maintained by a balance between natural production, destruction and transport (from regions of net productions to regions of net loss, driven by stratospheric fields). Ozone is naturally produced and destroyed by UV radiations, through the Chapman mechanism (Chapman, 1930).

$$O_2 + h\nu \rightarrow 2\,O \tag{1.1a}$$
$$O + O_2 + M \rightarrow O_3 + M \tag{1.1b}$$
$$O_3 + h\nu \rightarrow O_2 + O \tag{1.1c}$$
$$O_3 + O + M \rightarrow 2\,O_2 + M \tag{1.1d}$$

where $h\nu$ is the energy of a photon, indicating photodissociation reactions. Ozone destruction also occur through reactions with highly reactive radicals: oxides of nitrogen, hydrogen, bromine and chlorine, referred to as NOx, HOx, BrOx and ClOx. These radicals react with ozone in *catalytic cycles*. A single radical molecule can destroy up to 10^5 ozone molecules before being deactivated and transported out of the stratosphere. Radicals NOx, HOx, BrOx and ClOx are produced from source and reservoir gas. Their mean, steady state concentrations are determined by a balance between fluxes across the tropopause, production from radical-radical reactions, loss from photolysis and radical-reservoir reactions.

Heterogeneous chemistry on particles also has a key role in the production of active radicals from reservoir species. It is the phenomenon at stake in the creation of the "Ozone Hole" in the Antarctic stratosphere (Molina et al., 1987; Molina, 1991). During Antarctic winter, strong stratospheric winds spin around Antarctica: it is the polar vortex. The air in the center of this gigantic ring is isolated and gets cold enough for Polar Stratospheric Coulds (PSCs) to form. At the surface of ice particles in the PSCs, the two reservoir species HCl and $ClONO_2$ react to produce molecular chlorine Cl_2 and nitric acid HNO_3:

$$ClONO_2 + HCl \rightarrow Cl_2 + HNO_3 \tag{1.2}$$

This reaction would be negligibly slow without the presence of solid particles. Resulting Cl_2 is rapidly photo-dissociated into highly reactive atomic chlorine Cl, precipitating the chlorine catalytic cycle destroying ozone. The activation of reservoir species by heterogeneous chemistry is also known to occur on the surface of alumina (Molina et al., 1997) and, possibly, on soot particles (Bekki, 1997; Disselkamp et al., 2000).

1.1.2 Species in rocket exhaust

Currently, four main types or rocket engines are used : a solid rocket motor (SRM) (aluminium/ammonium perchlorate), and three liquid rocket motors (LRM) (kerosene/oxygen, hydrogen/oxygen and unsymmetrical dimethyl hydrazine (UDMH)/dinitrogen tetroxide). Launchers frequently use a combination of two types of propulsions (usually SRMs for initial thrust, combined to LRMs for other stages of the rocket). The main components present in the exhaust of these launchers are given by Ross (2004) and reproduced in Table 1.1.

Propellants	Rockets	Main emission components
SRM	Ariane 5 (2 boosters), Delta II (3 to 9 boosters) Vega (1st, 2nd & 3rd stages)	Al_2O_3, H_2O, CO_2, HCl, Cl_2, NO, H_2, N_2
UDMH/N_2O_4	Proton, Long March 2, Delta II (2nd stage)	H_2O, N_2, CO_2, NO, soot
H_2/O_2	Ariane 5 (1st & 2nd stages)	H_2O, H_2, OH, NO
Kerosene/O_2	Soyuz, Delta II (1st stage), Falcon 1 & 9	CO_2, H_2O, CO, soot, OH, NO

Table 1.1 – Main rocket exhaust species for four types of rocket engines.

Emissions from all types of engine affect ozone with a various intensity. Species with the most depleting effect on ozone are the chlorine-containing species (HCl, Clx, ClOx). As mentioned in Sec. 1.1.1, the chlorine radicals react with ozone in a destructive catalytic cycle. Heterogeneous chemistry on alumina particles also has a potential important depleting impact on ozone, although further research is required in this field. Indeed, if the heterogeneous chemistry is relatively well understood, the particle size distribution, critical for the evaluation of long-term effects, is still uncertain for most rockets. Chlorine containing species and alumina particles are exclusively found in SRM exhaust.

Oxides of nitrogen, NOx, are present in the emissions of all types of rocket. They react with stratospheric ozone in a catalytic cycle, similar to the chlorine cycle. For SRMs, the depleting effect of chlorine prevails largely over the effect of nitrogen oxides. For LRMs, NOx are the main cause of ozone loss. However their depleting effect is far less important than for chlorine oxides. Simulations of the impact of NOx emitted by a Proton rocket by Ross (2004) showed that chlorine emissions from SRMs cause 66-90 times more ozone loss compared to UDMH rockets. This difference is explained by Ross et al. (2000) by the fact that chlorine reactions are faster and that chlorine emissions are more abundant.

Finally, all rockets emit large amounts of water H_2O, the most important stratospheric source of radicals HOx. The effect of H_2O emissions on ozone loss seems negligible. Simulations by Ross (2004) showed that NOx emissions alone are responsible for 99.6% of the global ozone loss caused by a Proton rocket. The long-term impact of H_2O from Ariane 5 emissions was also found negligible, with an ozone loss reaching only 0.0001% (Jones et al., 1995).

Several other species are mentioned in the literature: hydroxyl radical (OH), sulphur, ice particles, nitrogen (N_2)... Their role was not studied in detail as their impact is thought to be small compared to the previously mentioned species, either because their concentration is too small, or because the chemical kinetics affecting ozone is negligible.

Overall, the impact of SRMs on ozone (determined essentially by chlorine chemistry and alumina particles) is largely predominant. It was estimated that LRM emissions represent only 2% of the ozone loss by SRM emissions (Ross et al., 2009). It was therefore chosen to focus this study on SRMs, even though the upcoming increase in launch of rockets using LRM (as expected for Space X's Falcon 9) makes new simulations necessary to assess precisely their impact.

Assessing the impact of rocket emissions on ozone is a complex and multidisciplinary task, which has to be conducted on several space scales:

— *local scale*: from the supersonic hot jet immediately formed by rocket exhausts to the cold plume wake, slowly mixing with ambient air for a few minutes to a few hours after the launch;

— *regional scale* (or mesoscale): during weeks and months after launch, plumes are transported and mixed into the global stratosphere;

— *global scale*: over the years, particles and source and reservoir species accumulates in the stratosphere and participate to global ozone loss (and for instance to the "Ozone Hole").

Each of these scales involves very different physics and chemistry. A large range of studies (numerical, experimental and direct measurements) contributed to identify the phenomena at stake and to estimate the loss of ozone. The following sections describe the local, regional and global mechanisms involved in ozone depletion by rocket emissions as it is currently understood, and give evaluations of ozone depletion obtained in the literature.

1.1.3 Local impact of rocket emissions

1.1.3.1 Hot plume: afterburning chemistry

To understand the mechanisms involved in ozone depletion, it is important to distinguish the hot plume from the cold plume (Hoshizaki et al., 1975). The hot plume represents the SRM jet from the combustion chamber up to the downstream position where temperature, pressure and velocity are in equilibrium with the ambient atmosphere. Beyond a few kilometers of altitude, the hot plume is supersonic and its dynamics is determined by thermodynamic properties of species in the combustion chamber (supposed at chemical equilibrium) and of ambient air. Generally, rocket combustion is optimized at an oxidizer-fuel ratio considerably less than stoichiometric. Consequently, exhaust species (mainly H_2) burn when mixing with ambient air (Simmons, 2000). This strong second combustion is commonly called *afterburning* and results in the production of ozone destroying radicals Clx (Cl and Cl_2) and NOx (Denison et al., 1994). Depending on the altitude, previous simulations observed that 21-65% of HCl is converted to Cl or Cl_2 (Denison et al., 1994; Zittel, 1994; Brady et al., 1997). This process is essential in assessing the local impact of rockets. As its modelling represents the main objective of this study, it is analyzed in detail in Sec. 1.2.

1.1.3.2 Cold plume: ozone destroying cycles

After the passage of the rocket, deposing chemical compounds at hot temperature and confined to a small volume, the plume cools down as it mixes with the surrounding air

by molecular and turbulent diffusion, and by the effects of wind shear and atmospheric turbulence. Once temperature in the plume reaches ambient temperature, afterburning chemistry does not occur anymore. Instead, the radicals Clx and NOx, resulting from the hot plume chemistry, react with atmospheric ozone in destructive catalytic cycles that can last for several hours (Martin, 1994), until radicals are converted back to non destructive reservoir species $ClONO_2$, HNO_3 and HCl. These reactions last from a few minutes to a few hours, resulting in local ozone loss.

Chlorine chemistry Two cycles were proposed to describe the destruction of ozone by active chlorine. The first one occurs naturally at mid-altitudes (Martin, 1994), but is faster at high altitudes (e.g. 30 km), in the presence of oxygen atoms (Brady et al., 1997). It is given by the reactions

$$\mathrm{Cl} + \mathrm{O_3} \rightarrow \mathrm{ClO} + \mathrm{O_2} \tag{1.3a}$$
$$\mathrm{ClO} + \mathrm{O} \rightarrow \mathrm{Cl} + \mathrm{O_2} \tag{1.3b}$$
$$\text{Net} : \mathrm{O_3} + \mathrm{O} \rightarrow 2\,\mathrm{O_2} \tag{1.3c}$$

At lower altitudes (typically around 20 km), a more complex cycle involving chlorine oxide dimer Cl_2O_2 prevails, which is similar to the reaction chain causing the Ozone Hole (Molina et al., 1987; Martin, 1994). The formation of Cl_2O_2 requires either low temperature or high concentrations of chlorine. In the case of the Ozone Hole above Antarctic, the low temperatures in the PSCs promote the formation of Cl_2O_2, while in rocket plumes, it is the high concentrations of Cl (produced by afterburning) which is the key factor. This cycle is given by the following reactions (Martin, 1994; Ross et al., 1997b; Brady et al., 1997):

$$\mathrm{Cl_2} + h\nu \rightarrow 2\,\mathrm{Cl} \tag{1.4a}$$
$$2\,(\mathrm{Cl} + \mathrm{O_3} \rightarrow \mathrm{ClO} + \mathrm{O_2}) \tag{1.4b}$$
$$2\,\mathrm{ClO} \rightarrow \mathrm{Cl_2O_2} \tag{1.4c}$$
$$\mathrm{Cl} + \mathrm{Cl_2O_2} \rightarrow \mathrm{Cl_2} + \mathrm{ClO_2} \tag{1.4d}$$
$$\mathrm{ClO_2} + \mathrm{M} \rightarrow \mathrm{Cl} + \mathrm{O_2} + \mathrm{M} \tag{1.4e}$$
$$\text{Net} : 2\,\mathrm{O_3} \rightarrow 3\,\mathrm{O_2} \tag{1.4f}$$

Photolysis of Cl_2 is represented by reaction (1.4a). This step is essential in releasing active chlorine, particularly since a large fraction of HCl is converted to Cl_2 in the hot plume. It was pointed out as the reaction controlling the rate of ozone destruction when Clx are in excess of ozone (Ross et al., 2000). This reaction also implies that local ozone depletion by SRMs can only occur during daytime. Direct measurements taken at night in the plume of a Titan IV rocket revealed that no significant ozone loss occurred (Ross et al., 1997a). However, recent simulations [1] showed that for a night launch, the chlorine cycle is activated when sun rises, causing a similar ozone loss as for a daytime launch.

The destructive cycles continue until active chlorine Cl and ClO are converted to reservoir species HCl (Brady et al., 1997):

$$\mathrm{Cl} + \mathrm{H} \rightarrow \mathrm{HCl} \tag{1.5a}$$
$$\mathrm{Cl} + \mathrm{CH_4} \rightarrow \mathrm{HCl} + \mathrm{CH_3} \tag{1.5b}$$

1. conducted in the framework of the AtILa project by D. Cariolle (private communication).

In standard stratosphere, reactions (1.5) are able to convert Cl and ClO to HCl within a few minutes. However, in a SRM plume, the concentrations of these two radicals are so high that they rapidly consume ambient methane and hydrogen, allowing a significant ozone depletion to take place locally (Brady et al., 1997).

Nitrogen chemistry On short time scales, the nitric oxide NO formed in the hot plume reacts with ozone in a catalytic cycle similar to this of chlorine (1.3) (Brady et al., 1997):

$$NO + O_3 \rightarrow NO_2 + O_2 \tag{1.6a}$$
$$NO_2 + O \rightarrow NO + O_2 \tag{1.6b}$$

$$\text{Net} : O_3 + O \rightarrow 2O_2 \tag{1.6c}$$

As for chlorine species, this cycle ends when NOx are turned into reservoir species $ClONO_2$ and HNO_3 (Brady et al., 1997).

Heterogeneous chemistry on alumina particles Measurements of nitrogen species in the plume of an Athena II, conducted in the framework of the ACCENT campaign, revealed the production of HNO_3 on alumina particles via reaction (1.2) (Popp et al., 2002). This reaction, similar to heterogeneous chemistry occurring on ice particles in Antarctic PSCs, directly releases active chlorine, which may have an immediate depleting effect on ozone (Molina et al., 1997; Danilin et al., 2003). Other heterogeneous reactions might occur, but have not been studied in detail (Gates, 2002):

$$ClONO_2 + H_2O \rightarrow HOCl + HNO_3 \tag{1.7a}$$
$$HCl + HOCl \rightarrow Cl_2 + H_2O \tag{1.7b}$$

In addition, direct destruction of ozone can take place on particle surface (Bekki, 1997).

The local impact of this chemistry is still debated. So far, models have detected no significant effect (Denison et al., 1994; Brady and Martin, 1995; Lohn et al., 1999). Brady and Martin (1995) argued that $ClONO_2$, required for the surface reactions, is present in too low concentrations in the ambient atmosphere. However, heterogeneous reactions on alumina were proposed as a possible effect to explain the impossibility to reproduce entirely the ozone loss measured in the plume of a Delta II rocket with homogeneous chemistry only (Ross et al., 2000). As a results, further research seems necessary to conclude on the role of alumina particles on local ozone loss. In particular, the mechanisms, kinetics and rate constants of the heterogeneous reactions on alumina surfaces still present very large uncertainties (Sander et al., 2011). The effect of coating also needs to be taken into account. A variety of species are likely to stick to the particles, affecting the reaction rates of chlorine activation (Danilin et al., 2003; Cziczo, 2002) and the cloud nucleating properties of the particles (Murray et al., 2013).

A summary of the chemical mechanisms occurring in the hot and cold plume of a SRM is presented in Fig. 1.1.

1.1.3.3 Estimation of ozone depletion by measurements and simulations

Direct measurements during the RISO (Ross et al., 1997a) and ACCENT (Ross et al., 2000) campaigns proved that ozone is almost entirely depleted in the plumes of SRMs.

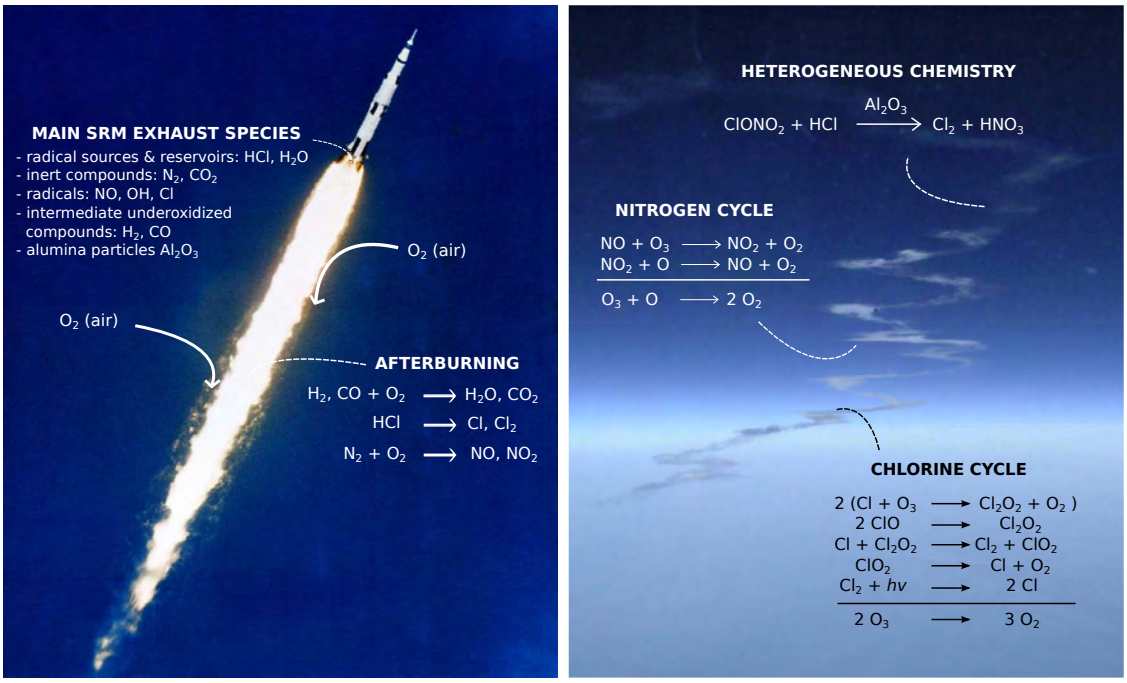

(a) Chemistry in a SRM hot plume. (b) Chemistry in a SRM cold plume.

Figure 1.1 – Chemical mechanisms leading to ozone depletion in SRM plumes.

Figure 1.2 depicts variations of chemical species concentrations in the plume of a Delta II rocket between 18 and 18.6 km altitude, measured during the ACCENT campaign. The plane, a WB-57F, encountered the plume six times in 46 minutes (Fig. 1.2a). At each plume encounter, high amounts of reactive chlorine under the form of chlorine monoxide ClO were measured,[2] as well as very low concentrations of ozone. Two of the ozone measurements even observed a complete ozone depletion in a small portion of the plume center of about 0.4 km long, 39 min after the launch (fifth plume encounter, Fig. 1.2b).

Simulations were able to reproduce afterburning and subsequent ozone depletion in the plumes of American launchers using SRMs (Denison et al., 1994; Zittel, 1994; Brady et al., 1997; Lohn et al., 1999), even if no model managed to obtain the same quantitative results as those obtained by direct measurements. Chlorine chemistry was clearly identified as the main mechanism involved in ozone depletion. It was also found that the resulting ozone hole lifetime and size are controlled by the plume diffusion rate (Brady et al., 1997), which may be influenced by stratospheric winds, the direction of launch (Ross, 1996) or atmospheric turbulence. At higher altitude, the decrease in pressure entails a larger initial wake diameter, which results in a larger local ozone hole that lasts longer: from 1500s at 15 km to 5000s at 40 km according to simulations ran by Lohn et al. (1999).

Measurements also revealed that ozone loss in SRM plume does not scale linearly with the size of the rocket. Local ozone loss observed in the plume of a Delta II rocket (Ross et al., 2000) is comparable to the loss caused by a Titan IV rocket, whose SRM emissions are about eleven times more important (Ross et al., 1997b).

Large uncertainties remain in the assessment of local ozone depletion. Recent techniques, like Large Eddy Simulations, need to be used to model the complex interactions between nonlinear mixing processes, chemistry and small scale plume effects. The super-

2. This does not mean that ClO is the main form of active chlorine. Ross et al. (2000) determined that 90% of the active chlorine is under the form Cl_2 during the steady state.

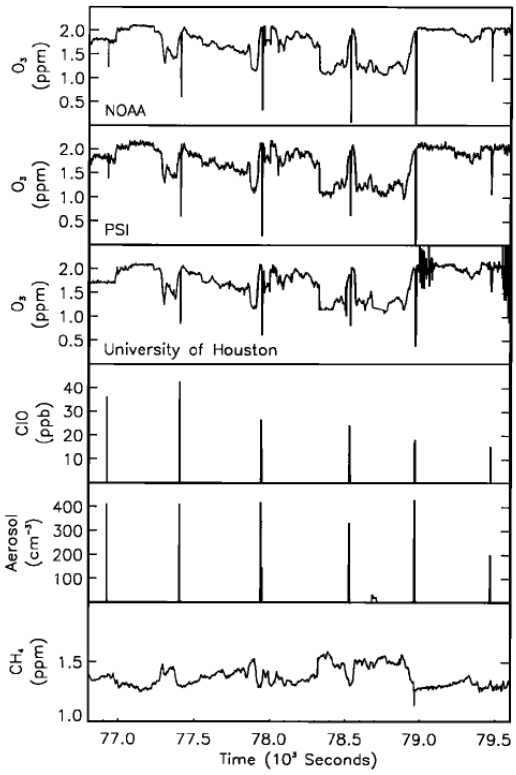

(a) Time series of measurements during the 46 minute period that included the six plume encounters.

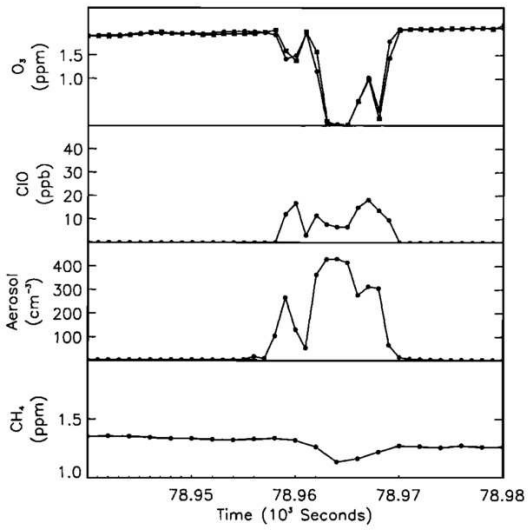

(b) Expanded time series for the fifth plume encounter (39 min after the launch). In the topmost panel, data from NOAA and PSI instruments are given by circles and squares, respectively.

Figure 1.2 – Variations of species concentrations taken in the plume of a Delta II. Ozone concentrations are taken by three independent instruments. Units are mixing ratio in parts per million by volume (ppmv), parts per billion by volume (ppbv), and total (volatile and nonvolatile) aerosol number density in the size range 0.3 to 4 grn. The bottom axis is Universal Time on 17 May 1998. WB-57F airspeed is about 190 ms^{-1}. Reproduced from Ross et al. (2000)

sonic hot plume, where chlorine is activated, also deserves a more precise modelling, which has to be integrated to cold plume simulations.

1.1.4 Regional and global impact of rocket emissions

1.1.4.1 Chemical mechanisms

Homogeneous chemistry The regional and global impact of rockets is thought to be very small (and has been estimated so by many models), though it is still not clearly understood. The day following the launch of a SRM, all chlorine emissions are converted back to the reservoir species HCl through reactions (1.5). In the stratosphere, HCl has a limited lifetime (1 year or less). It is slowly converted back to active chlorine through the reactions (Brady and Martin, 1997):

$$\mathrm{HCl} + \mathrm{OH} \rightarrow \mathrm{Cl} + \mathrm{H_2O} \tag{1.8a}$$

$$2\,\mathrm{Cl} + \mathrm{M} \rightarrow \mathrm{Cl_2} + \mathrm{M} \tag{1.8b}$$

These reactions also occur during afterburning in the hot plume, but much faster. The resulting chlorine reacts with ozone in cycles previously described (reactions (1.3) and (1.4)).

Heterogeneous chemistry As for gaseous phase, the global impact of alumina particles appears very limited, even if results of all studies conducted so far diverge. Reaction (1.2) is believed to have the most effect (Molina et al., 1997; Danilin et al., 2003), even if other reactions might occur, but have not been studied in detail (Gates, 2002).

The importance of heterogeneous chemistry depends on the size of alumina particles. Only the smallest, with a diameter less than $\sim 1\mu$m, remain in the stratosphere for years and can contribute to the steady-state ozone loss (Danilin et al., 2001; Schmid, 2003). Particles with diameter larger than 1μm have a short stratospheric lifetime (weeks to a few months) due to efficient removal by gravitational settling. The fraction of alumina particles emitted by SRMs with a small enough diameter is largely uncertain. Previous studies reported values between 1% and 30% (Cofer et al., 1991; Beiting, 1995; Ross et al., 1999; Cziczo, 2002; Schmid, 2003). Depending on this estimation, global impact of alumina particles was estimated to be one-third of this of chlorine (Jackman et al., 1998), half (Schmid, 2003) or equivalent (Ross et al., 2009).

Only direct measurements in the plume (in the stratosphere) can provide essential data like the size distribution of particles, as well as their microphysics and reactivity in the exhaust plume. Furthermore, these measurements have to be conducted for every type of rocket, because particle properties vary widely between SRMs.

1.1.4.2 Assessments of global impact

Using various models and launch scenarios, previous simulations agree that the change in annually averaged global total ozone due to total SRM emissions does not exceed the relatively small value of 0.03% (Jones et al., 1995; Jackman et al., 1998; Ross et al., 2009) On a regional scale, effects can be more pronounced. For instance, for a single launch of an Ariane 5 rocket, Jones et al. (1995) estimated that the maximum ozone loss during the following 30 days was 0.01%. Further studies are necessary, particularly to represent diffusion and dispersion of the plume. Satellites or direct measurements revealed that rocket plumes can form clouds which travel long distances. For instance, a cloud observed near California in 1997 was identified as the plume originating from a Soyuz rocket launched twelve days earlier from central Asia (Newman et al., 2001).

Furthermore, no study has taken into account the local plume and the regional effects to assess global ozone loss. In particular, it is not known if the cumulative effect of the local "ozone holes" is significant (Ross et al., 2009).

1.1.5 The importance of modelling SRM hot plume

Assessing the impact of SRM emissions on ozone requires complex, multi-disciplinary and multi-scales simulations. A chain of models and simulations is necessary to evaluate SRM impact at all scales (Koch et al., 2013). In this context, an accurate model of the hot plume is the essential first block of this computation chain. Ideally, this kind of simulation should be able to predict the amount of chlorine activated by afterburning in the hot plume (which is then involved in the main ozone depleting mechanism). It should also assess the importance of the characteristics of the jet dynamics (jet diameter, species distribution, mixing with air), which are critical parameters for evaluation of local ozone loss. Performing such a simulation is the objective of this study.

1.2 SRM jets: phenomenology, models and simulations

1.2.1 Overview of solid rocket engines

1.2.1.1 Applications

Solid Rocket Motors (SRMs) or Solid Rocket Boosters (SRBs) have been largely used for rocket propulsion. This technology is the simplest of all rocket designs. Their ability to remain in storage for long periods and then reliably launch on short notice has made them popular for military applications (such as missiles). They are also used at different stages of a launcher in order to jettison payloads to orbital velocities (Vega), or as strap-on boosters on larger rockets (Delta II, Ariane 5, see Fig. 1.3) to provide enough initial thrust. The largest SRMs ever produced were used for the lift-off of the Space Shuttle. The two SRMs were able to provide 23,000,000 Newtons of thrust, for a total load of propellant of 1,000 tons. [3]

1.2.1.2 Principle

The main components of a typical SRM are shown in Fig. 1.4 and detailed explanations of the principals are provided for instance by Sutton and Biblarz (2001). The solid propellant, or grain, accounts for 82 to 94% of the mass of the engine. The combustion is started by the igniter and takes place along the cylindrical cavity at the center of the engine, until all the propellant is exhausted. The shape of this cavity, often forming a star, drives the internal pressure evolution of the motor. The hot gas flow along this cavity toward the convergent-divergent nozzle, which accelerates them to provide thrust. The motor case, considered a pressure vessel, is protected from hot gases by a sacrificial thermal protection.

1.2.1.3 Nature of propellants

There are different types of solid propellants, often tailored to specific applications. Historically, rocket propellants are grouped into two classes: double-base propellant were

3. http://www.nasa.gov/returntoflight/system/system_SRB.html

Figure 1.3 – Lift-off of an Ariane 5 ECA launcher (launch no. 196) from Kourou, French Guiana. During this phase, the two boosters provide 92% of the total thrust.

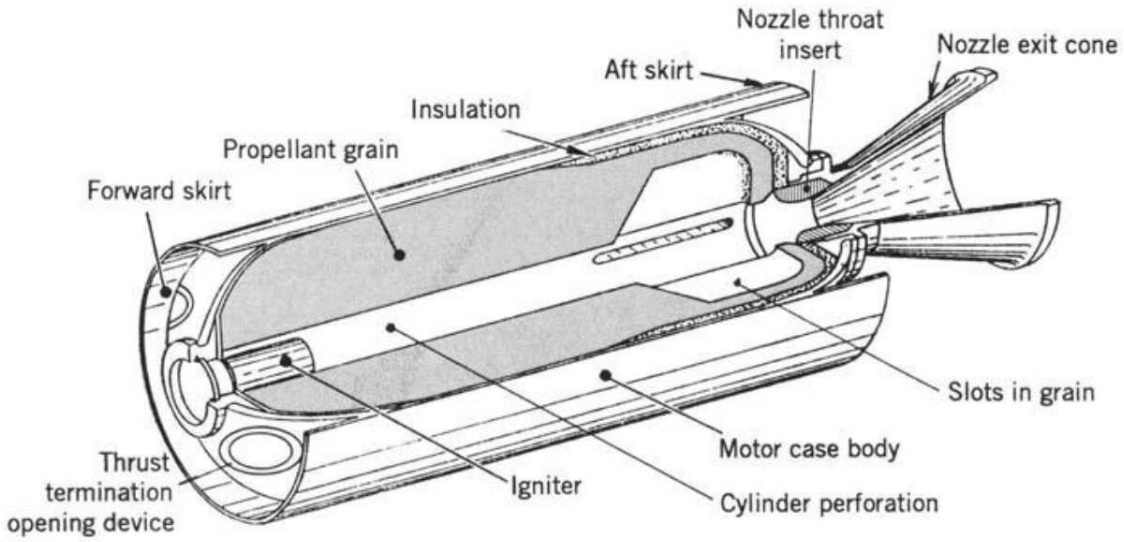

Figure 1.4 – Simplified perspective three-quarter section of a typical solid rocket motor. Reproduced from Sutton and Biblarz (2001).

first used, before the development of polymers as binders made the composite propellants feasible (Sutton and Biblarz, 2001).

Double-base propellants form a homogeneous grain, which usually consists of nitrocellulose plus some additives. They were mainly used for tactical missiles, as they do not produce traceable wakes.

Composite propellants form a heterogeneous propellant grain. The oxidizer is crystallized or finely ground mineral salt (usually ammonium perchlorate), and represents between 60 to 72% of the mass of the propellant. The fuel, up to 22% of the mass, is aluminium powder. Oxidizer and fuel are held together by a binder (8 to 16% of the mass), such as polybutadiene (HTPB). In the past three decades the composite propellants have been the most commonly used class, delivering higher densities, specific impulse, and a wider range of burning rates compared to the double-base propellants.

This study focuses on composite propellants: they are the most commonly used and their combustion exhaust products include HCl and alumina particles Al_2O_3, which are the main species involved in ozone depletion.

1.2.2 Characteristics of SRM exhaust plumes

1.2.2.1 Dynamics of SRM jets

The structure of a SRM jet is quite complex and varies with flight regime (Simmons, 2000). The atmospheric pressure and total pressure at the nozzle inlet determine whether the jet is over or underexpanded, i.e. if the pressure at the nozzle exit is smaller or larger than the atmospheric pressure. Beyond a low altitude, typically a couple of kilometers, the jet remains underexpanded. Then, as the rocket gains in altitude, the drop in atmospheric pressure causes a wider expansion of the jet (visible in Fig. 1.5 for a Vega launcher), and therefore an increase in jet diameter and a decrease in temperature.

For the range of altitudes of interest for the study of SRM impact on ozone (15-40 km), a SRM jet is a coflowing supersonic underexpanded jet. According to previous modelling work of SRM jets (Calhoon, 1998; Grenard et al., 2013) and current knowledge on supersonic jets (Pope, 2000; Yüceil and Ötügen, 2002), four characteristic zones can be identified and are represented in Fig. 1.6:

— an *adaptation pressure region* with shocks, along which the jet pressure decreases to reach atmospheric pressure;
— a *potential core* surrounded by a *mixing layer*;
— a *transition region* where different scales of turbulence develop;
— a *self-similar region*.

For a gas-phase flow, the shock pattern in the adaptation pressure region depends on the nozzle shape, the rocket velocity (which determines the air coflow velocity) and the thermodynamic conditions in the chamber and in the atmosphere. The shock pattern represented in Fig. 1.6 corresponds to a large weak oblique shock reflected at the centerline (followed by smaller shock cells, not represented), formed by a Prandtl-Meyer expansion. It is the structure observed in simulations by Calhoon (1998); Grenard et al. (2013), but a simulation of a Titan IIIC SRM plume by Lohn et al. (1999) obtained the formation of a Mach disk, followed by a subsonic region.

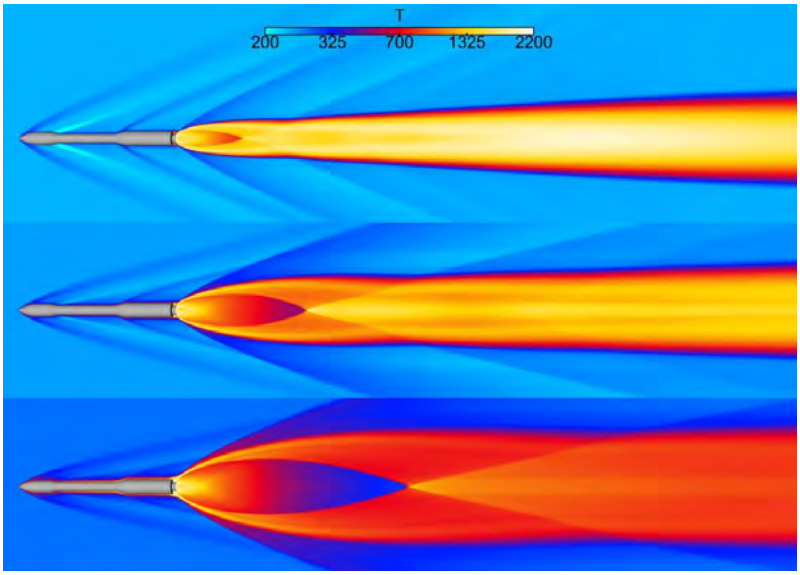

Figure 1.5 – Longitudinal cut of the exhaust plume of a Vega rocket showing temperature (K), for three altitudes: 18.7 km (up), 30 km (middle), 42 km (bottom). Reproduced from Grenard et al. (2013)

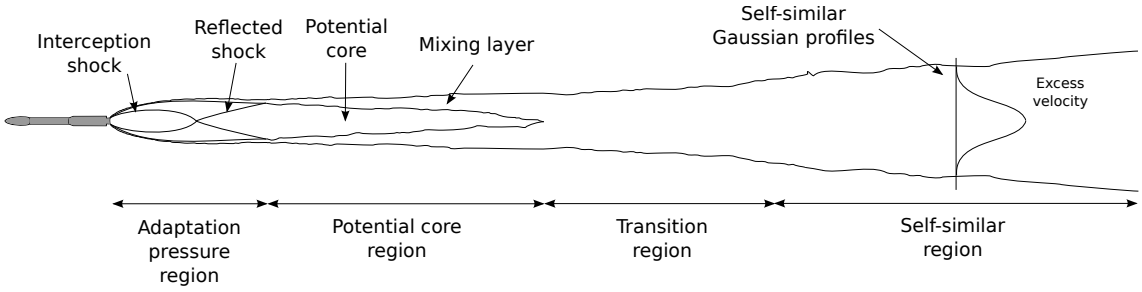

Figure 1.6 – Structure of SRM jet for an altitude within 15-40 km.

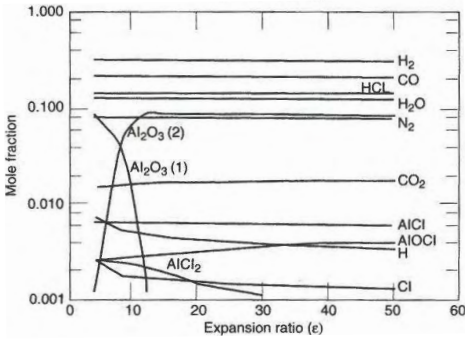

Figure 1.7 – Nozzle exit composition as a function of the expansion ratio for a typical composite solid propellant. Reproduced from Simmons (2000).

1.2.2.2 Main chemical species at the nozzle exit

Combustion products arriving from the chamber to the entrance of the nozzle are far from perfect gas. All three phases of matter are represented (solid, liquid, gas), and continue to react in the nozzle (Simmons, 2000). Nozzle flow codes are able to evaluate the SRM exhaust composition in the nozzle. For a typical SRM using composite propellant, Simmons (2000) gives the mole fractions of the main chemical species at the nozzle exit as a function of the nozzle expansion ratio. These results were obtained with the One-Dimensional Kinetic (ODK) code by JANNAF (Joint Army-Navy-NASA-Air Force) and are reproduced in Fig. 1.7. The expansion ratio ϵ is defined as the area of the exit divided by the area of the throat. Main species are: H_2, CO, HCl, H_2O, Al_2O_3, N_2 and CO_2. Small concentrations of radicals and minor species are also noted, but their evaluation can vary with the code employed and the exact composition of the propellant.

Large quantities of alumina Al_2O_3 (approximately 30% in mass) are produced by oxidation taking place at the surface of aluminium particles. Alumina is formed as liquid particles and remains so at the high temperatures of the chamber. As the liquid particles pass through the nozzle, their temperature drops with a lag dependent on their size. Then they solidify, at a size-dependent rate. The resulting size distribution of the solid particles in the plume varies with the type of propellant and the altitude. A tri-modal distribution was predicted by Beiting (1997) and later verified by direct measurements in SRM plumes (Ross et al., 2009; Schmid, 2003). However, as mentioned earlier in Sec. 1.1.4.1, the size distribution of alumina in SRM plumes is still largely unknown.

1.2.2.3 Chemistry in the hot plume

Afterburning A summary of chemistry in the hot plume is shown in Fig. 1.1a. The mechanisms were identified and confirmed by several modelling studies (Gomberg and Stewart, 1976; Denison et al., 1994; Leone and Turns, 1994; Zittel, 1994; Lohn et al., 1999) and laboratory measurements (Burke and Zittel, 1998). As the jet mixes with ambient air, the temperature in the hot plume is high enough to trigger the combustion of H_2, present in the exhaust gas, with the dioxygen of the ambient air, producing H_2O. Carbon monoxide CO also gets oxidized to form CO_2. These reactions lead to very high temperatures in the mixing layer, an effect that dominates infrared emission production over a wide range of altitudes (Simmons, 2000). Combustion takes the form of a diffusion (or non-premixed) flame, lying in the mixing layer of the near-field plume, around the potential core. An example of such flame is visible in Fig. 1.1a.

Chlorine activation The combustion H_2-CO entails the formation of radicals H, O and OH which allows the partial conversion of plume species HCl to active chlorine Cl through reactions such as:

$$HCl + OH = Cl + H_2O \tag{1.9a}$$
$$HCl + H = Cl + H_2 \tag{1.9b}$$
$$HCl + O = Cl + OH \tag{1.9c}$$
$$\tag{1.9d}$$

These reactions are relatively fast and exothermic or nearly thermoneutral. In the cooler post-afterburning region, the amount of Cl produced is limited by recombination to form Cl_2 via the reaction

$$2Cl + M = Cl_2 + M \tag{1.10a}$$

Simulations of afterburning in the plume of a Titan IV SRM were conducted by Zittel (1994). At 20 km altitude, radical Cl is completely converted in Cl_2 about 1 km downstream of the nozzle, as shown in Fig. 1.8a. Other chlorine species like ClO, HOCl or ClO_2 are formed in negligible quantities compared to Cl and Cl_2 (not more than 1% of total chlorine species). The formation of Cl_2 was also found by Denison et al. (1994) for a generic SRM jet, even if the computational domain was not long enough to reach a complete conversion of Cl to Cl_2.

All modelling studies found that the fraction of HCl activated in the form Cl or Cl_2 increases with the altitude. The variations of fractions of chlorine species with altitude obtained by Zittel (1994) is shown in Fig. 1.8b. The fraction of active chlorine ($Cl + Cl_2$) resulting from afterburning varies from 30% at 15 km, to 80% at 40 km.

These results are close to those found by Denison et al. (1994) for a smaller SRM. They have also been qualitatively confirmed by a laboratory study (Burke and Zittel, 1998). Afterburning in conditions close to those of a Titan IV SRM plume at 20 and 26 km altitude was reproduced. Measurements confirmed that chlorine liberated via HCl consumption ends up almost exclusively in the form of Cl_2. For pressure corresponding to 20 km altitude, a fraction of Cl_2 of 38% was measured, which corresponds to the 37% obtained by Zittel (1994) (see Fig. 1.8). For the smaller pressure corresponding to 26 km altitude, a fraction of 58% of Cl_2 was measured, which is 15% higher (absolute value) than interpolated value in Fig. 1.8b for the same altitude. Inaccuracies were pointed out in the experimental set-up, which could partly explain these differences: the experimental flame was premixed (fuel and oxidized premixed before burning), whereas the flame in a rocket plume is non-premixed, and the viscous effects were not reproduced.

NOx formation NOx (NO and NO_2) can be produced from nitrogen and dioxygen in the afterburning region, mainly via the Zeldovitch mechanism (Brady et al., 1997):

$$N_2 + O = NO + N \tag{1.11a}$$
$$N + O_2 = NO + O \tag{1.11b}$$
$$N + OH = NO + H \tag{1.11c}$$
$$O + N_2 + M = N_2O + M \tag{1.11d}$$
$$O + N_2O = 2\,NO \tag{1.11e}$$
$$H + N_2O = NH + NO \tag{1.11f}$$

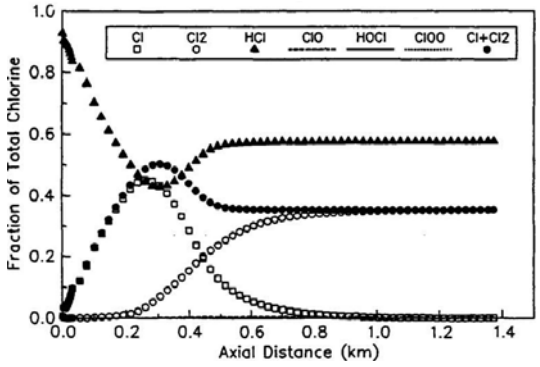

(a) Chemical identity of chlorine in the plume (20 km).

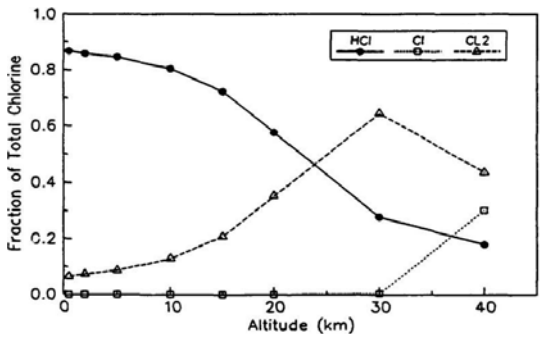

(b) Far-field chemical identity of chlorine as a function of altitude.

Figure 1.8 – Afterburning modelling in a Titan IV SRM. Reproduced from Zittel (1994).

This mechanism is activated only for high temperatures. Leone and Turns (1994) conducted simulations of afterburning in the Shuttle SRB exhaust plume at various altitudes. It was observed that nitric oxide production is divided by a factor 1000 when the altitude increases from 0.7 to 30km. Previous modelling studies (Denison et al., 1994; Zittel, 1994; Leone and Turns, 1994) found that small quantities of NOx were formed, with a negligible effect on local ozone depletion compared to chlorine.

Afterburning cessation For sufficiently high altitudes, combustion between ambient air and exhaust emissions can no longer be sustained. This phenomenon was studied for military purposes (infrared emissions due to afterburning can be used to detect and track rockets), for instance by Calhoon (1998). This study suggests that high turbulence mixing might offer an explanation for afterburning cessation. When altitude increases, pressure decreases which results in a larger expansion of the jet, therefore a lower jet temperature (see Fig. 1.5). Two phenomena could then prevent afterburning:

— turbulence mixing continuously mixes hot exhaust jet with cold air; with a jet temperature too low, turbulence mixing could cool the jet at a higher rate than chemical reactions can produce heat and a pool of radicals sufficient to initiate combustion;

— a flame blow-off mechanism: the decrease in jet temperature entails a decreasing reaction rate. The chemistry becomes too slow and the flame becomes locally extinguished due to high flow strain. This results in an ignition delay of the flame, which will appear further and further downstream of the nozzle when altitude increases, until it eventually blows-off.

1.2.2.4 Other factors of influence on SRM jets

Impact of the presence of particles in the flow As mentioned in Sec. 1.2.2.2, liquid droplets of alumina are solidified in the nozzle as temperature decreases. Alumina particles represent about 30% of the total exhaust emissions mass. Their density is two orders of magnitude higher than the gaseous species mix. Consequently, they do not expand due to the pressure gradients developed by the nozzle expansion contour (unlike the gaseous mix), but instead react to the drag force created by the relative velocity between air and the exhaust supersonic jet (Murray et al., 2013). The drag force modifies the trajectory of the particles, which then modifies the trajectory of the gaseous mix itself. The change in the

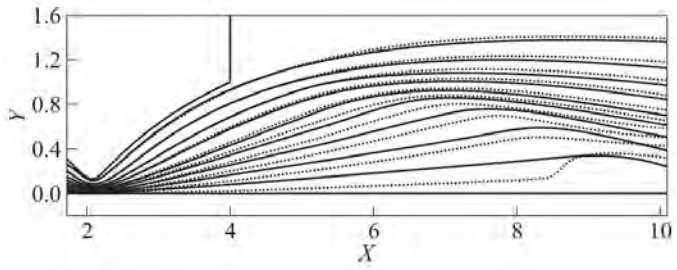

Figure 1.9 – Streamlines in a nozzle and plume without particles (solid curves) and with particles (dotted curves). Spatial coordinates are nondimensionalized by the nozzle exit radius. Reproduced from Rosario (2011).

streamlines can be relatively important, as simulated by Rosario (2011) and Grenard et al. (2013) and shown in Fig. 1.9. Particles reduce the flow velocity, resulting in an increase in temperature which may enhance afterburning and production of active chlorine and NOx. However, Grenard et al. (2013) observed that the position of the diffusion flame (due to afterburning) does not seem influenced by the particles. The flow could be affected mainly at its center, where the concentration of particles is higher.

The effect of particles on the flow also depends on their size: the heavier ones exert more force on the flow, leading to a change in the plume shape.

Launcher configuration The shape of the rocket is responsible for changes in the freestream flow surrounding the plume. Unsteady phenomena such as turbulent boundary, buffeting and vortex shedding increase the complexity of the air coflow, which might have an effect on mixing and afterburning (Murray et al., 2013).

The effect of a configuration with several engines also has to be considered. Few rockets use only one SRM at a time, like the Vega launcher. For most rockets, a combination of two or more SRMs with a LRM is commonly used. For instance, the first stage of Ariane 5 uses two SRMs ("Etage d'Accélération à Poudre", EAP) and one LRM (Vulcain 2). The multiple plumes interact in a complex flowfield. Beyond an altitude of a few kilometers, the plumes are expected to merge at a downstream location which varies with altitude (Simmons, 2000). Recirculation between the nozzles could also have an impact on afterburning ignition (Simmons, 2000). Only accurate CFD tools can model the interactions between several jets and their effect on afterburning and chlorine activation. Considering a single-equivalent nozzle seems to lead to important mispredictions of hot plume chemistry (Simmons, 2000). Lohn et al. (1999) ran RANS simulations of the twin supersonic plume of a Titan IIIC. This study predicted that the interactions of the two jets while expanding result in high temperature regions which might enhance chlorine activation by 10%. However the coarse resolution of the mesh should temper this result. Further investigations using more accurate methods are necessary

1.3 Strategies for SRM jet simulations in the stratosphere

1.3.1 Previous modelling efforts of reactive SRM jets

1.3.1.1 Standard Plume Flowfield (SPF) code

So far, chemical and dynamics processes at stake in rocket plumes have been studied mainly for military purposes. Plumes are a source of radiations (particularly infrared),

which can provide the basis for detection and tracking of rockets. A large variety of numerical models for plumes have been developed since the years 1970's (a review of these models is given by Simmons (2000)). Several of these codes were used to model radical activation by afterburning until late 1990's. The most famous of them is the Standard Plume Flowfield (SPF) code. The current version is SPF-III (Pergament, 1992), and is distributed by the Chemical Propulsion Information Analysis Center (CPIAC). [4] This code relies on modules, each one of them representing separate parts of the flow-field. The nozzle flow-field module handles the flow in the supersonic section of the nozzle, using elliptic Navier-Stokes formulation in steady state, coupled with non-equilibrium chemistry and two-phase flow. It provides input to the plume flow-field module, which solves parabolized Navier-Stokes equations. This module treats separately two components of the plume: the core, considered inviscid, and the overlaid mixing layer, for which boundary-layer approximation are applied. Extra modules can provide a fitted solution for the bow shock in case the rocket reaches supersonic velocities, or take into account a base separated region.

This code was used by Denison et al. (1994) and Zittel (1994) to model the reactive exhaust plume of an hypothetical SRM and a Titan IV SRM respectively. Even though the SPF code treats non-equilibrium chemistry and two-phase flow, it is based on crude approximations of Navier-Stokes equations. The dynamics of the flow cannot be predicted accurately and the coupling between turbulence and combustion is completely neglected.

A predecessor of the SPF code, the Low-Altitude Plume Program (LAPP) code, was used by Gomberg and Stewart (1976) to model the hot plumes of a Space Shuttle SRB and a Titan III-C SRM. One of the main disadvantages of the LAPP code is that it does not take into account the non-isentropic expansion of the jet, leading to a wrong evaluation of the temperature, which is critical to model afterburning.

1.3.1.2 Nozzle performance code

Most simulations using the SPF code (or a dedicated plume code) do not compute the nozzle flow. They rely on nozzle performance codes to compute the state of combustion products at the nozzle exit, which is then used as inlet condition by plume codes. For plume simulations including the nozzle flow, these nozzle performance codes can be used to provide flow properties at the nozzle inlet.

JANNAF codes (also distributed by the CPIAC) are the most used American nozzle flow solvers. They offer different levels of complexity and accuracy. The One-Dimensional kinetic (ODK) and the Two-dimensional kinetic (TDK) codes are both able to evaluate finite-rate chemistry in the chamber and the nozzle, assuming respectively a 1D inviscid flow and a 2D axisymmetric inviscid flow (Simmons, 2000). In Europe, the nozzle performance codes OPHELIE (1D isentropic solver, developed by HERAKLES) and COPPELIA (Calcul et Optimisation des Performances Energétiques des Systèmes Liés à l'Autopropulsion, developed by ONERA) are used to provide inlet conditions, respectively for SRM and LRM exhaust plumes (Troyes et al., 2006; Koch et al., 2013). Both codes are derived from the CEA (Chemical Equilibrium with Application) code, formulated by the NASA Lewis Laboratory (Gordon and McBride, 1971). If these codes are easy to use and do not require large computational resources, they are not designed for an accurate prediction of the flow chemical composition. Combustion and flow processes are idealized. Specifically, perfect mixing and 100% combustion efficiency in the chamber are assumed, which may lead to underestimations of product H_2, OH and CO.

4. `https://www.cpia.jhu.edu/node/20`

1.3.1.3 CFD codes

To model SRM hot plume, Computational Fluid Dynamics (CFD) codes are more precise, but also more computer-intensive, even if the latest technologies and developments in high performance computing have allowed high-resolution CFD which were hardly considered a few decades ago. The most affordable option is the Reynolds-Averaged Navier-Stokes (RANS) approach. It consists in solving the balance equations for Reynolds or Favre averaged quantities to obtain a flow solution corresponding to averages over time. The closure rules require the use of a turbulence model to describe the flow dynamics, and a turbulent combustion model to handle chemical reactions and heat release (Poinsot and Veynante, 2005).

A commercial RANS code, Fluent/RAMPANT, was used by Lohn et al. (1999) to compute the twin nozzle Titan III-C exhaust plumes. Very few details are given on the computational methodology, apart from the use of a coarse mesh which seems to limit the accuracy of the resulting shock structure. Calhoon (1998) modelled the exhaust plume of a generic SRM using the General Aerodynamic Simulation Program (GASP) code, a compressible solver based on a RANS formulation. [5] Calhoon (1998) pointed out the lack of any treatment of the effect of turbulent fluctuations on the mean reaction rate in the species conservation equations in the GASP code, which limits greatly the accuracy of the simulation. Note that these simulations focused on the evaluation of afterburning cessation: only the combustion of H_2 and CO with ambient air was modelled. Simulations using a RANS approach were also conducted by European teams. Two-dimensional reactive two-phase axisymmetric simulations of a LP11 small scale motor exhaust plume (including the nozzle and the jet up to 160 nozzle exit diameters downstream of the nozzle) were achieved using the CEDRE code by Troyes et al. (2006). More recently, in the framework of the AtILa (Atmospheric Impact of Launchers) project, this code was used to conduct 3D RANS of Ariane 5 and Soyuz exhaust plumes and 2D RANS of Vega and Athena II plumes (Koch et al., 2013; Bauer et al., 2013). The computational domains included the nozzle and rocket body flows, and the jets up to 1500 m behind the rocket (for a maximum mesh size of 5 million cells). A turbulence model $k-\omega$ SST was used, with constants adapted to axisymmetric flows. Finite-rate chemistry was computed and large alumina particles were modelled by an Eulerian dispersed phase solver. These simulations were conducted for three different altitudes: 18.7, 30 and 42 km. They probably represent the most complete study of supersonic rocket exhaust plumes achieved so far for steady simulations in the RANS context.

1.3.2 LES approach

Other CFD techniques are more accurate than RANS for combustion modelling of unsteady compressible flows. Direct Numerical Simulations (DNS) represent the most accurate approach to solve such flows. The full unsteady Navier-Stokes equations are solved without any model for turbulence, however, due to the high computational cost associated to these simulations, DNS are still limited to academic flows and cannot be currently applied for SRM exhaust plume modelling. On the other hand, Large Eddy Simulations (LES) offer an interesting compromise.

5. The inlet boundary conditions at the nozzle exit plane were specified by the TDK code.

1.3.2.1 Principles and advantages

LES consist in calculating the large turbulent scales whereas the smaller ones are modelled using subgrid closures (Poinsot and Veynante, 2005). This technique has become a standard research tool with the recent breakthrough in the field of high performance computing. It offers a better prediction of turbulence, which shall bring more accuracy to a SRM exhaust plume simulation. In particular, the mixing layer, were the diffusion flame occurs, should be better represented: turbulence is a key parameter for mixing of reactants, which is an essential mechanism in non-premixed combustion. LES would also offer a more accurate prediction of turbulent combustion, which is the two-way coupling between turbulence and combustion. The use of LES models would result in a more reliable chemical species and temperature distribution in the resulting jet, and a better representation of combustion ignition and quenching. This is the technique chosen to model a SRM exhaust jet in this study.

1.3.2.2 Challenge of a long computational domain

LES have been largely used for simulations of inert compressible jet (e.g. Bogey and Bailly (2009); de Cacqueray N. et al. (2011); Munday et al. (2011); Rana et al. (2011); Dauptain et al. (2012); Vuorinen et al. (2013)) and non-premixed jet flame (Branley and Jones, 2001; Sheikhi et al., 2005; Domingo et al., 2008; Boivin et al., 2012), but mainly for laboratory configurations and limited longitudinal domains. Considering the size of a rocket nozzle (several meters of diameter) and the high velocities involved ($2400 m/s$ for a Space Shuttle SRB (Gomberg and Stewart, 1976)), the jet has to be modelled over several hundreds meters in the downstream direction in order to capture the flame and the chlorine chemistry. Furthermore, to use the results of the LES of a supersonic SRM jet for the initialization of atmospheric simulations (that typically employ incompressible formulation of the Navier–Stokes equations), the computational domain needs to extend up to a location where the excess velocity of the jet tends to zero and the effect of compressibility can be neglected.

Converging LES of a jet over a long downstream distance is computationally expensive. Modelling the nozzle flow, which brings more accuracy to the computations, entails an extra cost, particularly if the LES solver is explicit. For such solvers, numerical stability imposes the time step Δt to be limited by the smallest cell size Δx in the grid and by the fastest acoustic propagation speed $u + c$, with u standing for velocity and c for sound speed (Courant-Friedrichs-Lewy criterion (Courant et al., 1952)):

$$\Delta t = CFL \frac{\min(\Delta x)}{\max(u + c)} \tag{1.12}$$

where CFL is the Courant number. For a SRM jet, the region of the nozzle, which necessitates a fine grid, would therefore impose a time step that can be an order of magnitude smaller than for the downstream jet. Such configuration would be extremely demanding in terms of computational resources. In previous work, this issue has been tackled in various fashions. One way consists in using an inlet to simulate the flow at the nozzle exit (Bogey and Bailly, 2009; Maidi and Lesieur, 2005) and avoid expensive computations of the nozzle flow. However, this option cannot reproduce entirely the pressure adaptation region: particularly the shock-cell structure, which influences the diameter of the jet, the potential core region, and the development of instabilities. With the objective to solve the flow in the nozzle while limiting computational cost, a recent technique, called the recorded interface boundary condition method (Clark and Loth, 2013), consists in performing a simulation of the far-field jet using a boundary condition that reproduces the

mean and turbulent velocities of the near-field jet, previously recorded from a near-field jet simulation. This way, the far-field can be simulated with a larger time step. This method looks promising but needs more investigation before it can be applied to general flow configurations.

The technique chosen for the present study uses local time stepping to simulate the jet flow on a computational domain that includes the nozzle. It has the advantage of introducing very little error in the simulation while offering a significant cut in the computational cost. The concept has already been applied in the LES context (Esnault et al., 2010), and it was adapted to the LES solver AVBP with the use of overlapping grids to provide a generic implementation (Wang et al., 2013, 2014).

1.4 Objectives and outlines of the study

1.4.1 Objectives of the study

The objective of this study is to conduct and analyse fully three-dimensional LES of a generic SRM exhaust jet, including the internal geometry of the nozzle and the hot-plume chemistry related to ozone depletion. These simulations are performed at nominal flight conditions at 20 km of altitude, in the rocket frame of reference, which involves a supersonic coflow of air. The domain extends up to 400 nozzle exit diameters. To the best of our knowledge, this should be the first LES of a reactive supersonic jet, including nozzle geometry, performed over such a long computational domain. To achieve this objective, four main steps were followed.

As mentioned previously, a particular attention was paid to the reduction of the computational cost of these simulations. This led to the application of an overset grid method to prevent the limitation of the simulation time step by the small cells of the nozzle grid. To test and validate this method, the SRM exhaust jet was first computed without chemistry, using a thermodynamically equivalent gas to model the exhaust gas of the engine. The purpose of this single-species simulation of the SRM jet is to validate the technique by a thorough analysis of the jet dynamics and comparison of the results with current knowledge. This analysis also has to ensure that no significant error is introduced by the coupling method.

Before conducting complex and computationally expensive reactive LES, it was chosen to obtain a first prediction of the hot-plume chemistry by applying a simple model based on constant-pressure reactors. This model is able to evaluate the temperature and chemical species distributions resulting from the afterburning chemistry along streamlines of an existing frozen flow. By applying this model to a time-averaged flow-field obtained from LES of a single-species SRM jet, the objectives are to:

- validate the choice of the chemical mechanism by ensuring the results are coherent with previous work (Denison et al., 1994; Zittel, 1994);
- identify the regions of interest in the flow-field, in order to anticipate locations of probes in the jet and the potential changes to be done to the LES grid;
- obtain a first evaluation of the amount of chlorine activated due to afterburning. The accuracy of the results is limited by the fact that this model is applied to a time averaged flow-field and that the coupling turbulence/combustion is not taken into account. By comparing these results to the reactive LES, it is possible to evaluate the impact of turbulent combustion on the species distribution and particularly on

the active chlorine Cl and Cl_2.

Following the validation of the chemical mechanism, a step of reduction of this mechanism was necessary before its implementation for LES, in order to meet with the objectives of CPU cost while preserving the accuracy of the results.

Finally, LES of a reactive SRM exhaust jet were conducted, using the overset grid method and the chemical scheme previously reduced. To limit the computational cost, the alumina particles are represented as an inert gas. Analyses of the results focus on:

— the phenomenology of the diffusion flame: auto-ignition, flame location, quenching, mixing of species;
— the comparison of the results to those obtained using the streamline model and to previous studies;
— evidencing the need for a combustion model dedicated to the diffusion flame.

1.4.2 Outline of the dissertation

The manuscript is organized as follows:

Chapter 2 details the governing equations and the computational techniques used for LES.

Chapter 3 describes the case parameters and numerical domain.

Chapter 4 focuses on LES of a single-species SRM jet applying the overset grid method. The dynamics of the jet are studied in detail and compared to previous knowledge to ensure the reliability of the coupling technique.

Chapter 5 provides definitions and properties concerning laminar diffusion flames, which are essential for the analysis of the SRM reactive jet.

Chapter 6 applies a model based on constant-pressure reactors to give a first prediction of hot-plume chemistry, using only the single-species LES results of Chapter 3.

Chapter 7 describes the derivation of a reduced chemical scheme, suitable for LES, from the reference mechanism. Test cases are performed to ensure the accuracy of the reduced scheme for afterburning modelling at 20 km of altitude.

Chapter 8 presents the results of LES of the reactive SRM jet using the reduced scheme described in Chapter 7.

CHAPTER 2

Equations of fluid motion

2.1 Governing equations

2.1.1 Conservation equations for compressible reactive flows

Multi-species and reactive flows are characterized by a set of partial differential equations, the Navier-Stokes equations, which describe the conservation of total mass, mass of each species k, momentum and energy in a compressible fluid. Using Einstein's notation, they read

$$\frac{\partial \rho}{\partial t} + \frac{\partial \rho u_i}{\partial x_j} = 0 \tag{2.1a}$$

$$\frac{\partial \rho Y_k}{\partial t} + \frac{\partial}{\partial x_j}(\rho Y_k u_j) = -\frac{\partial J_{j,k}}{\partial x_j} + \dot{\omega}_k \tag{2.1b}$$

$$\frac{\partial \rho u_i}{\partial t} + \frac{\partial}{\partial x_j}(\rho u_i u_j) = -\frac{\partial}{\partial x_j}(P\delta_{ij} - \tau_{ij}) \tag{2.1c}$$

$$\frac{\partial \rho E}{\partial t} + \frac{\partial}{\partial x_j}(\rho E u_j) = -\frac{\partial}{\partial x_j}\left[u_i(P\delta_{ij} - \tau_{ij}) + q_j\right] + \dot{\omega}_T \tag{2.1d}$$

In Eqs. (2.1), $E = e_s + \frac{1}{2}u_i u_i$ is the total energy per unit mass of the fluid, with e_s the sensible energy, $\mathbf{u}$ is the velocity vector, ρ the fluid density, P the pressure. The viscous stresses tensor τ_{ij} for Newtonian fluids (such as air) can be computed as:

$$\tau_{ij} = \mu\left(\frac{\partial u_i}{\partial x_j} + \frac{\partial u_j}{\partial x_i}\right) - \frac{2}{3}\mu\frac{\partial u_l}{\partial x_l}\delta_{ij} \tag{2.2}$$

where μ is the dynamic viscosity of the fluid, explicited in Sec. 2.1.4. $J_{j,k}$ is the diffusive flux of species k, presented in Sec. 2.1.3, q_j is the heat flux vector, defined in Sec. 2.1.5, $\dot{\omega}_k$ and $\dot{\omega}_T$ are respectively the reaction rate of species k and the heat release, both detailed in Sec. 2.1.6.

In this study, the species diffusion due to temperature gradients (the Soret effect), the molecular transport due to pressure gradients and the enthalpy diffusion due to mass fraction gradients (i.e., the Dufour effect) are neglected.

2.1.2 Thermodynamical variables

For a mixture of N perfect gases, the total pressure P is:

$$P = \rho \frac{R}{W} T \quad \text{where} \quad \rho = \sum_{k=1}^{N} \rho_k = \sum_{k=1}^{N} \rho Y_k \tag{2.3}$$

In Eq. (2.3), T is the temperature, $R = 8.314 J/mol.K$ is the perfect gas constant and W is the mean molecular weight of the mixture given by:

$$\frac{1}{W} = \sum_{k=1}^{N} \frac{Y_k}{W_k} \tag{2.4}$$

For a mixture of perfect gases, the mass heat capacity at constant pressure c_{pk} and the mass heat capacity at constant volume c_{vk} read:

$$c_{pk} = \frac{dh_k}{dT} \tag{2.5a}$$

$$c_{vk} = \frac{de_k}{dT} \tag{2.5b}$$

where h_k and e_k are respectively the enthalpy and the energy per unit mass of species k. Equation (2.5a) gives:

$$h_k(T) = \underbrace{\int_{T_0}^{T} c_{pk} \mathrm{d}T}_{h_{sk}} + \Delta h^0_{f,k} \tag{2.6}$$

where the subscript $_0$ and superscript ^{0} refer to the standard reference state, at pressure $P_0 = 1$ bar and temperature $T_0 = 298.15K$. $\Delta h^0_{f,k}$ is the mass enthalpy of formation, defined such that $\Delta h^0_{f,k} = h_k(T = T_0)$: it is the enthalpy needed to form 1 kg of species k at the reference temperature T_0. The first term in the definition of h_k in Eq. (2.6) is the sensible enthalpy of species k, written h_{sk}. The energy e_k can be written using the c_{vk}, but can be also deduced from the enthalpy h_k with the relation $e_k = h_k - P_k/\rho_k$:

$$e_k(T) = \underbrace{\int_{T_0}^{T} c_{vk} \mathrm{d}T - \frac{RT_0}{W_k}}_{e_{sk}} + \Delta h^0_{f,k} \tag{2.7a}$$

$$= h_k(T) - \frac{RT}{W_k} \tag{2.7b}$$

where e_{sk} is the sensible energy of species k.

The heat capacities c_{pk} and c_{vk} are taken constant between T_i and $T_{i+1} = T_i + 100$. Therefore the sensible enthalpy h_{sk} of a species k is tabulated every $100K$, from 0 to $5000K$. The tables provided by JANAF [1] are a classic reference. The sensible energy at temperature T_i can be deduced from Eq. (2.7b), and the values of sensible enthalpy and energy at any temperature T can be easily computed via a linear interpolation. The values of c_{pk} and c_{vk} are obtained from Eq. (2.5), and the heat capacities of the mixture are given by:

$$c_p = \sum_{k=1}^{N} c_{pk} Y_k \tag{2.8a}$$

$$c_v = \sum_{k=1}^{N} c_{vk} Y_k \tag{2.8b}$$

1. `http://kinetics.nist.gov/janaf/`

The specific heat ratio is written $\gamma = c_p/c_v$. Finally, the enthalpy h and the energy e of the mixture are defined by:

$$h = \sum_{k=1}^{N} h_k Y_k \tag{2.9a}$$

$$e = \sum_{k=1}^{N} e_k Y_k \tag{2.9b}$$

2.1.3 Conservation of mass and correction diffusion velocity

The mass conservation equation for species k is written:

$$\frac{\partial \rho Y_k}{\partial t} + \frac{\partial}{\partial x_j}(\rho(u_j + V_j^k)Y_k) = \dot{\omega}_k \tag{2.10}$$

where V_j^k is the j-component of the diffusion velocity V^k of species k. For a multi-species flow, mass conservation leads to the necessary condition:

$$\sum_{k=1}^{N} Y_k V_j^k = 0 \tag{2.11}$$

To express the diffusion velocity, the Hirschfelder and Curtiss approximation (Hirshfelder et al., 1969) is used:

$$X_k V_j^k = -D_k \frac{\partial X_k}{\partial x_j} \tag{2.12a}$$

$$\text{or} \quad Y_k V_j^k = -D_k \frac{W_k}{W} \frac{\partial X_k}{\partial x_j} \tag{2.12b}$$

where D_k is an equivalent diffusion coefficient of species k into the rest of the mixture. When summing Eq. (2.12b) for $k = 1..N$, the global conservation of mass, defined by Eq. (2.11), is not verified. A solution is to introduce a correction velocity V_j^c to the diffusion velocity:

$$V_j^k = -D_k \frac{1}{Y_k} \frac{W_k}{W} \frac{\partial X_k}{\partial x_i} + V_j^c \tag{2.13}$$

To recover global mass conservation, V_j^c must read:

$$V_j^c = \sum_{k=1}^{N} D_k \frac{W_k}{W} \frac{\partial X_k}{\partial x_j} \tag{2.14}$$

Finally, the diffusive flux of species k introduced in Eq. (2.1b) is written:

$$J_{j,k} = -\rho \left(D_k \frac{W_k}{W} \frac{\partial X_k}{\partial x_j} - Y_k V_j^c \right) \tag{2.15}$$

2.1.4 Transport coefficients

In most fluid dynamics solvers dealing with multi-species flows, the dynamic viscosity μ is assumed independent of the mixture composition and close to those of air. The power law is used to determine μ:

$$\mu = \mu_0 \left(\frac{T}{T_{ref}} \right)^b \tag{2.16}$$

where b is typically within 0.5-1.0 (air: $b = 0.76$). The heat diffusion coefficient λ is defined assuming the Prandlt number, Pr, is constant (in time and space):

$$\lambda = \frac{\mu c_p}{Pr} \tag{2.17}$$

The diffusion coefficients D_k are written using the binary diffusion coefficients D_{jk}, obtained from Bird et al. (1960):

$$D_k = \frac{1 - Y_k}{\sum_{j \neq k}^{N} X_j / D_{jk}} \tag{2.18}$$

Binary diffusion coefficients are complex functions of collision integrals and thermodynamic variables. This formulation is well adapted in the case of complex chemistry. However, in most fluid dynamics solvers, reduced chemical mechanisms are used and the definition for diffusion coefficients does not require such level of accuracy. A simpler approach is adopted. Considering that the Schmidt number Sc_k of each species is constant in space and time, diffusion coefficients D_k can be defined as:

$$D_k = \frac{\mu}{\rho Sc_k} \tag{2.19}$$

2.1.5 Heat flux vector

For multi-species flows, the heat flux vector q_j is composed of two terms: the heat flux due to conduction and the heat flux due to heat transport by species diffusion:

$$q_j = \underbrace{-\lambda \frac{\partial T}{\partial x_j}}_{\text{conduction}} + \underbrace{\sum_{k=1}^{N} J_{j,k} h_{sk}}_{\text{species diffusion}} \tag{2.20}$$

where λ is the heat diffusion coefficient, defined in Sec. 2.1.4.

2.1.6 Chemical kinetics

Chemistry is modeled using an Arrhenius law written for N reactants $\mathcal{M}_k$ and M reactions as:

$$\sum_{k=1}^{N} \nu'_{kj} \mathcal{M}_{kj} \rightleftharpoons \sum_{k=1}^{N} \nu''_{kj} \mathcal{M}_{kj}, \quad j = 1..M \tag{2.21}$$

where ν'_{kj} and ν''_{kj} are the molar stoichiometric coefficients of the reactants and products, respectively, in reaction j. The mass reaction rate $\dot{\omega}_k$ of species k is the sum of rates $\dot{\omega}_{kj}$ produced by all M reactions:

$$\dot{\omega}_k = \sum_{k=1}^{M} \dot{\omega}_{kj} = W_k \sum_{k=1}^{M} \nu_{kj} Q_j \tag{2.22}$$

with $\nu_{kj} = \nu''_{kj} - \nu'_{kj}$. Q_j is the rate of progress of reaction j, defined as:

$$Q_j = K_{fj} \prod_{k=1}^{N} \left(\frac{\rho Y_k}{W_k} \right)^{\nu'_{kj}} - K_{rj} \prod_{k=1}^{N} \left(\frac{\rho Y_k}{W_k} \right)^{\nu''_{kj}} \tag{2.23}$$

where K_{fj} and K_{rj} are the forward and reverse rates of reaction j. The forward rates are expressed using the empirical Arrhenius law:

$$K_{fj} = A_{fj} T^{n_j} \exp\left(-\frac{E_{aj}}{RT} \right) \tag{2.24}$$

where A_{fj}, n_j and E_{aj} are respectively the pre-exponential constant, the temperature exponent and the activation energy of reaction j. The reverse rate K_{rj} are computed from the forward rates through the equilibrium constants:

$$K_{rj} = \frac{K_{fj}}{K_{eq,j}} \tag{2.25a}$$

$$\text{with} \qquad K_{eq,j} = \left(\frac{P_a}{RT}\right)^{\sum_{k=1}^{N}\nu_{kj}} \exp\left(\frac{\Delta S_j^0}{R} - \frac{\Delta H_j^0}{RT}\right) \tag{2.25b}$$

where $P_a = 1$ bar and ΔH_j^0 and ΔS_j^0 are respectively enthalpy and entropy changes for reaction j, defined by:

$$\Delta H_j^0 = h_j(T) - h_j(0) = \sum_{k=1}^{N} \nu_{kj} W_k h_k(T) \tag{2.26a}$$

$$\Delta S_j^0 = \sum_{k=1}^{N} \nu_{kj} W_k s_k(T) \tag{2.26b}$$

The entropy s_k of species k is considered constant between T_i and $T_{i+1} = T_i + 100K$. Like the sensible enthalpy, the entropy is tabulated every $100K$, from 0 to $5000K$. Finally, the heat release $\dot{\omega}_T$ in Eq. (2.1d) is written

$$\dot{\omega}_T = -\sum_{k=1}^{N} \Delta h_{f,k}^0 \dot{\omega}_k \tag{2.27}$$

2.1.7 Governing equations for LES

2.1.7.1 Large Eddy Simulations

Turbulence is a three dimensional unsteady phenomenon, involving various time and space scales. A first approach is Direct Numerical Simulations (DNS). It consists in solving the full Navier-Stokes equations without any model for turbulence, thus explicitly determining all turbulence scales. Due to the high CPU costs it involves, this method is still limited to simple academic flows, although current progress in the field of High Performance Computing shows that DNS should soon be applicable to industrial application (Moureau et al., 2011).

Reynolds Averaged Navier-Stokes (RANS) is the traditional approach developed to solve turbulent flows. An operator is applied to the system of equations, which consists of a temporal or ensemble average over a set of realizations of the studied flow. These averaged equations require a turbulence model for closure of the system. This method is robust but implies modelling the entire turbulence spectrum.

Large Eddy Simulations (LES) represent a compromise between the last two methods. A spatial filtering of the Navier-Stokes equations is performed so that the turbulent large scales are explicitly calculated whereas the smaller ones are modelled using subgrid closure rules. Figure 2.1 shows on a typical turbulent spectrum the differences between DNS, RANS and LES. Due to the filtering approach, LES allows a dynamic representation of the large scale motions whose contributions are critical in complex geometries. The LES predictions of complex turbulent flows are therefore closer to the physics since large scale phenomena such as large vortex shedding and acoustic waves are embedded in the set of governing equations. For these reasons, LES appears as the best suited approach to solve the highly supersonic reactive jet of a SRM. However, the accuracy of the results is restricted by the hypothesis introduced in the construction of LES models.

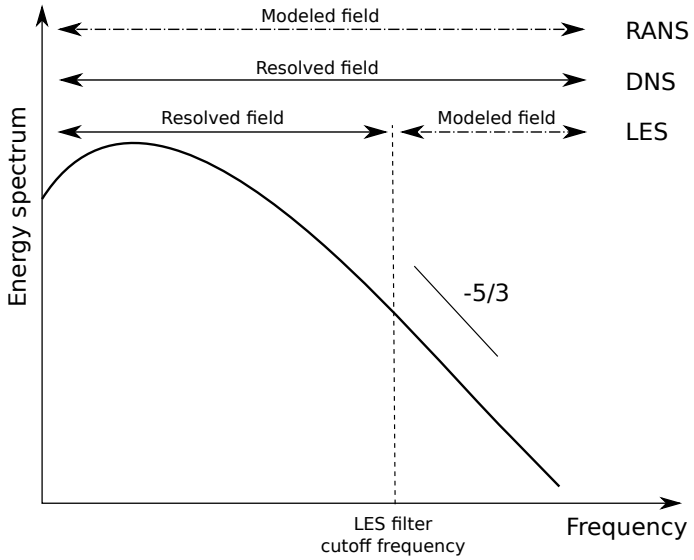

Figure 2.1 – Conceptual differences between RANS, DNS and LES when applied to a homogeneous isotropic turbulent flow.

2.1.7.2 Filtering of the governing equations

In LES, the Navier–Stokes equations are spatially filtered using the operator

$$\overline{f(\mathbf{x},t)} = \int f(\mathbf{x}',t)F(\mathbf{x}-\mathbf{x}')\mathrm{d}\mathbf{x}' \tag{2.28}$$

where F is the filtering kernel. The size Δ of this filter is fixed and does not depend on time. The simulation solves the filtered quantity $\overline{f}$. In compressible flows, the mass-weighted Favre filtering operator is also used,

$$\widetilde{f} = \frac{\overline{\rho f}}{\overline{\rho}} \tag{2.29}$$

where ρ is the density. The governing equations for LES are obtained by application of the last filtering to the instantaneous transport equations for reacting flows (Eqs. (2.1)):

$$\frac{\partial \bar{\rho}}{\partial t} + \frac{\partial}{\partial x_j}\left(\bar{\rho}\widetilde{u_i}\right) = 0 \tag{2.30a}$$

$$\frac{\partial \bar{\rho}\widetilde{Y_k}}{\partial t} + \frac{\partial}{\partial x_j}\left(\bar{\rho}\widetilde{Y_k}\widetilde{u_j}\right) = -\frac{\partial}{\partial x_j}\left(\overline{J_{j,k}} + \overline{J_{j,k}}^t\right) + \overline{\dot{\omega}_k} \tag{2.30b}$$

$$\frac{\partial \bar{\rho}\widetilde{u_i}}{\partial t} + \frac{\partial}{\partial x_j}\left(\bar{\rho}\widetilde{u_i}\widetilde{u_j}\right) = -\frac{\partial}{\partial x_j}\left(\overline{P}\delta_{ij} - \overline{\tau_{ij}} - \overline{\tau_{ij}}^t\right) \tag{2.30c}$$

$$\frac{\partial \bar{\rho}\widetilde{E}}{\partial t} + \frac{\partial}{\partial x_j}\left(\bar{\rho}\widetilde{E}\widetilde{u_j}\right) = -\frac{\partial}{\partial x_j}\left[\overline{u_i(P\delta_{ij} - \tau_{ij})} + \overline{q_j} + \overline{q_j}^t\right] + \overline{\dot{\omega}_T} \tag{2.30d}$$

The filtered viscous terms $\overline{\tau_{ij}}, \overline{J_{j,k}}$ and $\overline{q_j}$ are computed following approximations detailed in Sec. 2.1.7.3. In order to get a closed set of equations, the turbulent terms $\overline{\tau_{ij}}^t, \overline{J_{j,k}}^t$ and $\overline{q_j}^t$ are expressed using a subgrid scale (SGS) model, as explained in Sec. 2.1.7.4.

2.1.7.3 Filtered viscous terms

The filtered stress tensor $\overline{\tau_{ij}}$ is respectively written and computed as:

$$\overline{\tau_{ij}} = \overline{\mu\left(\frac{\partial u_i}{\partial x_j} + \frac{\partial u_j}{\partial x_i}\right) - \frac{2}{3}\mu\frac{\partial u_l}{\partial x_l}\delta_{ij}} \tag{2.31a}$$

$$\text{approximation}: \quad \overline{\tau_{ij}} \approx \overline{\mu}\left(\frac{\partial \widetilde{u_i}}{\partial x_j} + \frac{\partial \widetilde{u_j}}{\partial x_i}\right) - \frac{2}{3}\overline{\mu}\frac{\partial \widetilde{u_l}}{\partial x_l}\delta_{ij} = 2\overline{\mu}(\widetilde{S}_{ij} - \frac{1}{3}\delta_{ij}\widetilde{S}_{ll}) \tag{2.31b}$$

$$\text{with}: \quad \widetilde{S}_{ij} = \frac{1}{2}\left(\frac{\partial \widetilde{u_j}}{\partial x_i} + \frac{\partial \widetilde{u_i}}{\partial x_j}\right) \tag{2.31c}$$

The filtered diffusive flux vector $\overline{J_{j,k}}$ is given by:

$$\overline{J_{j,k}} = -\overline{\rho\left(D_k\frac{W_k}{W}\frac{\partial X_k}{\partial x_j} - Y_k V_j^c\right)} \tag{2.32a}$$

$$\text{approximation}: \quad \overline{J_{j,k}} \approx -\overline{\rho}\left(\overline{D}_k\frac{W_k}{W}\frac{\partial \widetilde{X_k}}{\partial x_j} - \widetilde{Y}_k\widetilde{V}_j{}^c\right) \tag{2.32b}$$

Finally, the filtered heat flux vector $\overline{q_j}$ is:

$$\overline{q_j} = -\overline{\lambda\frac{\partial T}{\partial x_j}} + \sum_{k=1}^{N}\overline{J_{j,k}h_{sk}} \tag{2.33a}$$

$$\text{approximation}: \quad \overline{q_j} \approx -\overline{\lambda}\frac{\partial \widetilde{T}}{\partial x_j} + \sum_{k=1}^{N}\widetilde{J_{j,k}h}_{sk} \tag{2.33b}$$

2.1.7.4 Subgrid scale turbulent terms

The subgrid scale turbulent terms of the system hold a small portion of the kinetic energy but are responsible for the dissipation of energy in the turbulent cascade. As a result, they need to be modelled using a SGS model. The SGS stress tensor $\overline{\tau_{ij}}^t$, defined in Eq. (2.34a), is modelled using the Boussinesq assumption in Eq. (2.34b):

$$\overline{\tau_{ij}}^t = -\overline{\rho}(\widetilde{u_i u_j} - \widetilde{u_i}\widetilde{u_j}) \tag{2.34a}$$

$$\text{SGS model}: \quad \overline{\tau_{ij}}^t = 2\overline{\rho}\nu_t(\widetilde{S}_{ij} - \frac{1}{3}\delta_{ij}\widetilde{S}_{ll}) \tag{2.34b}$$

where ν_t is a subgrid scale turbulent viscosity, defined in Sec. 2.1.7.5. This approach assumes that the effect of subgrid scales is only dissipative. The SGS diffusive flux vector $\overline{J_{j,k}}^t$, defined in Eq. (2.35a), is modelled in Eq. (2.35b) following the same approach.

$$\overline{J_{jk}}^t = \overline{\rho}(\widetilde{u_j Y_k} - \widetilde{u_j}\widetilde{Y_k}) \tag{2.35a}$$

$$\text{SGS model}: \quad \overline{J_{j,k}}^t = -\overline{\rho}\left(D_k^t\frac{W_k}{W}\frac{\partial \widetilde{X_k}}{\partial x_j} - \widetilde{Y}_k\widetilde{V}_j{}^{c,t}\right) \tag{2.35b}$$

$$\text{with}: \quad D_k^t = \frac{\nu_t}{Sc_k^t} \tag{2.35c}$$

This model introduces a turbulent Schmidt number Sc_k^t. Studies showed that this parameter is not constant, and complex models have been developed. However, in most

studies and LES solver, Sc_k^t is assumed constant for all species. In this study, we consider $Sc_k^t = 0.6$. Finally, the SGS heat flux vector $\overline{q_j}^t$ is defined and modelled as follows:

$$\overline{q_j}^t = \overline{\rho}(\widetilde{u_j E} - \widetilde{u_j}\widetilde{E}) \tag{2.36a}$$

$$\text{SGS model}: \quad \overline{q_j}^t = -\lambda_t \frac{\partial \widetilde{T}}{\partial x_j} + \sum_{k=1}^{N} \overline{J_{j,k}}^t \widetilde{h}_{sk} \tag{2.36b}$$

$$\text{with}: \quad \lambda_t = \frac{\mu_t c_p}{Pr^t} \tag{2.36c}$$

with a turbulent Prandtl number Pr^t fixed at 0.6. Finally, the correction diffusion velocities are obtained from Eqs. (2.19) and (2.35c):

$$\widetilde{V}_i^c + \widetilde{V}_i^{c,t} = \sum_{k=1}^{N} \left(\frac{\overline{\mu}}{\overline{\rho} Sc_k} + \frac{\mu_t}{\overline{\rho} Sc_k^t} \right) \frac{W_k}{W} \frac{\partial \widetilde{X}_k}{\partial x_i} \tag{2.37}$$

2.1.7.5 SGS models

Several models for the turbulent viscosity ν_t have been developed. They all rely on the spatially and temporally invariance of the LES filter. Change in cell topology is only accounted for through the use of a scale representative of the local cell volume, $\Delta = V_{\text{cell}}^{1/3}$. Only the two models used for the simulations presented in this study are detailed in this section.

The Smagorinsky model (Smagorinsky, 1963), developed in the 1960s, is the most popular because of its simple formulation. The turbulent viscosity is modelled from dimensional arguments as:

$$\nu_t = (C_S \Delta)^2 |\overline{S}| = (C_S \Delta)^2 (2 \overline{S}_{ij} \overline{S}_{ij})^{1/2} \tag{2.38}$$

where C_S is the model constant, which can vary between 0.1 and 0.18 depending on the flow configuration. To improve this model, the Dynamic Smagorinsky approach, proposed by Germano et al. (1991), determines the model constant C_{S_D} within the simulation. The expression of C_{S_D} results from the Germano inequality and follows the procedure by Lilly (1992):

$$C_{S_D}^2 = \frac{1}{2} \frac{M_{ij} M_{ij}}{L_{ij} L_{ij}} \tag{2.39a}$$

$$\text{with}: \quad M_{ij} = \hat{\Delta}^2 (2 < \widetilde{S}_{ij} >< \widetilde{S}_{ij} >)^{1/2} < \widetilde{S}_{ij} > \tag{2.39b}$$

$$L_{ij} =< \widetilde{u}_i >< \widetilde{u}_i > - < \widetilde{u}_i \widetilde{u}_i > \tag{2.39c}$$

This expression introduces the notion of "test" filter of characteristic length $\hat{\Delta}$, equal to the cubic root of the volume defined by all the cells surrounding the cell of interest.

2.2 Numerics

2.2.1 The LES solver AVBP

The numerical solver used for these simulations is AVBP [2] (Schönfeld and Rudgyard, 1999). It is a massively parallel code that solves the three-dimensional reactive compressible Navier-Stokes equations on unstructured grids. It follows an LES approach to

2. http://www.cerfacs.fr/4-26334-The-AVBP-code.php

calculate unsteady flows. The discretization of the governing equations uses a cell-vertex formulation and implements finite volume schemes like Lax-Wendroff (second order in time and space) of finite element schemes like Taylor-Galerkin "TTG4A" (fourth order in time and third order in space). These schemes are spatially centered and explicitly time-advanced (which makes them accurate for LES) with artificial viscosity to filter high frequency oscillations and reduce strong gradients.

2.2.2 Numerical schemes for the solution of Navier-Stokes

In AVBP, all numerical schemes implemented are expressed in the cell-vertex numerical discretization approach, for its compactness and effectiveness on parallel HPC. First, the filtered flow equations are rewritten in a more compact conservative form:

$$\frac{\partial \mathbf{w}}{\partial t} + \nabla \cdot \vec{\mathcal{F}} = 0, \tag{2.40}$$

where $\mathbf{w}$ is the vector of conserved variables and $\vec{\mathcal{F}}$ the corresponding flux tensor. For convenience, this flux is usually divided into two components, the convective flux $\vec{\mathcal{F}}^C$ and the viscous flux $\vec{\mathcal{F}}^V$:

$$\vec{\mathcal{F}} = \vec{\mathcal{F}}^C(\mathbf{w}) + \vec{\mathcal{F}}^V(\mathbf{w}, \vec{\nabla}\mathbf{w}), \tag{2.41}$$

The cell-based residuals, *i.e.* the spatially dependent terms of the equations on each control volume Ω_j, are then calculated by integrating the fluxes over the cell as:

$$\mathbf{R}_{\Omega_j} = \frac{1}{V_{\Omega_j}} \int_{\partial\Omega_j} \vec{\mathcal{F}} \cdot \vec{n}\, dS, \tag{2.42}$$

where V_{Ω_j} is the cell volume and $\partial\Omega_j$ its boundary with normal vector $\vec{n}$. Since the integration is obtained around a vertex, a distributed version of these cell-based residuals $\mathbf{R}_k$ is constructed via distribution matrices. One can hence express Eq. (2.40) into the semi-discrete scheme

$$\frac{d\mathbf{w}_k}{dt} = \mathbf{R}_k = -\frac{1}{V_k} \sum_{j|k\in\Omega_j} D^k_{\Omega_j} V_{\Omega_j} \mathbf{R}_{\Omega_j}, \tag{2.43}$$

where V_k is the control volume associated with the node k and $D^k_{\Omega_j}$ is the distribution matrix that weights the cell residual from the cell center Ω_j to node k (Donea, 1984; Lamarque, 2007), given by:

$$D^k_{\Omega_j} = \frac{1}{n_v(\Omega_j)} \left(I - \frac{\Delta t_{\Omega_j}}{2n_d} \frac{n_v^2(\Omega_j)}{V_{\Omega_j}} \mathcal{A}_{\Omega_j} S^k_{\Omega_j} \right) \tag{2.44}$$

where n_d is the number of dimensions, n_v is the number of nodes of the cell Ω_j and S_{Ω_j} is the area weighted normals of the cell faces.

Several numerical schemes are available. Only two of those are presently considered. First, the Lax-Wendroff scheme (LW) is a 2^{nd}-order finite volume scheme in time and space, which corresponds to the accuracy of most commercial codes as well as most of the turbomachinery CFD tools available today (Lax and Wendroff, 1964). Secondly, the two-step Taylor-Galerkin finite element scheme TTG4A (4^{th}-order in time and 3^{rd}-order in space) provides improved LES quality on unstructured grids (Selmin, 1987).

2.2.2.1 Lax-Wendroff scheme

The Lax-Wendroff (Lax and Wendroff, 1964) scheme is a second order accurate in space and time, finite volume scheme. It is based on a Taylor expansion in time of the solution $\mathbf{w}$:

$$\mathbf{w}^{n+1} = \mathbf{w}^n + \Delta t \left(\frac{\partial \mathbf{w}}{\partial t}\right)^n + \frac{1}{2}\Delta t^2 \left(\frac{\partial^2 \mathbf{w}}{\partial t^2}\right)^n + O(\Delta t^3) \tag{2.45}$$

The first temporal derivative can be straightforwardly replaced using Eq. (2.40):

$$\frac{\partial \mathbf{w}}{\partial t} = -\nabla \cdot \vec{\mathcal{F}} \tag{2.46}$$

The second temporal derivative is recast in a similar fashion:

$$\frac{\partial^2 \mathbf{w}}{\partial t^2} = \frac{\partial}{\partial t}(-\nabla \cdot \vec{\mathcal{F}}) = -\nabla \cdot \frac{\partial \vec{\mathcal{F}}}{\partial t} = -\nabla \left[\mathcal{A}\left(\frac{\partial \mathbf{w}}{\partial t}\right)\right] = \nabla \cdot [\mathcal{A}(\nabla \cdot \vec{\mathcal{F}})] \tag{2.47}$$

In Eq. (2.47), $\mathcal{A}$ is the Jacobian of the flux tensor.

2.2.2.2 Two step Taylor-Galerkin schemes

Taylor-Galerkin (TG) schemes were first derived by Donea (1984), the key idea of the method being the coupling between a Taylor expansion in time and a Galerkin discretization in space. Selmin (1987) extended this approach, and proposed the family of Two-step Taylor Galerkin (TTG) schemes, where an additional intermediate step $\tilde{\mathbf{w}}$ is computed between $\mathbf{w}^n$ and $\mathbf{w}^{n+1}$. The TTG4A scheme reaches third order accuracy in space and fourth-order in time. The general form of the TTG schemes is the following:

$$\tilde{\mathbf{w}}^n = \mathbf{w}^n + \alpha \Delta t \left(\frac{\partial \mathbf{w}}{\partial t}\right)^n + \beta \Delta t^2 \left(\frac{\partial^2 \mathbf{w}}{\partial t^2}\right)^n \tag{2.48a}$$

$$\mathbf{w}^{n+1} = \mathbf{w}^n + \Delta t \left[\theta_1 \left(\frac{\partial \mathbf{w}}{\partial t}\right)^n + \theta_2 \left(\frac{\partial \tilde{\mathbf{w}}}{\partial t}\right)^n\right] + \Delta t^2 \left[\epsilon_1 \left(\frac{\partial^2 \mathbf{w}}{\partial t^2}\right)^n + \epsilon_2 \left(\frac{\partial^2 \tilde{\mathbf{w}}}{\partial t^2}\right)^n\right] \tag{2.48b}$$

where $\alpha = 1/3$, $\beta = 1/12$, $\theta_1 = 1$, $\theta_2 = 0$, $\epsilon_1 = 0$ and $\epsilon_2 = 1/2$ for the TTG4A scheme. The first and second order temporal derivatives are replaced by spatial derivatives as in the Lax-Wendroff scheme. The distribution matrix is also similar. The Galerkin method is then applied on the resulting equations which makes a mass-matrix appear in the left-hand-side. More details about the derivation of these schemes in the cell-vertex discretization framework can be found in Lamarque (2007).

2.2.3 Artificial viscosity

The numerical discretization methods implemented in AVBP are spatially centered. As such, they are naturally subject to small-scale oscillations in the vicinity of steep solution variations. It is therefore common to add a term of artificial viscosity to the discrete equations to filter high-frequency oscillations and reduce strong gradients. The artificial viscosity models implemented in AVBP are characterized by a linear preserving property which leaves unmodified a linear solution on any type of element. The models are based on a combination of a shock capturing term (called 2^{nd} order artificial viscosity) and a background dissipation term (called 4^{th} order artificial viscosity). The addition of artificial viscosity is performed in two steps:

— based on the flow characteristics, a sensor detects if any artificial viscosity is necessary,
— then a certain amount of 2nd and 4th artificial viscosity is applied, depending on the sensor value and on user-defined parameters.

2.2.3.1 The Jameson sensor

In the present simulations, the application of artificial viscosity is determined by a Jameson sensor (Jameson et al., 1981). This sensor consists in comparing different evaluations (on different stencils) of the gradient of a given scalar (pressure, total energy, mass fractions...). If these gradients are identical, then the solution is locally linear and the sensor is zero. On the contrary, if these two estimations are different, local non-linearities are present and the sensor is activated.

For every cell Ω_j, the Jameson cell-sensor $\zeta^J_{\Omega_j}$ is the maximum over all cell vertices of the Jameson vertex-sensor ζ^J_k:

$$\zeta^J_{\Omega_j} = \max_{k\in\Omega_j} \zeta^J_k \tag{2.49}$$

Denoting S the scalar quantity the sensor is based on (usually S is the pressure), the Jameson vertex-sensor is:

$$\zeta^J_k = \frac{|\Delta^k_1 - \Delta^k_2|}{|\Delta^k_1| + |\Delta^k_2| + |S_k|} \tag{2.50}$$

where the Δ^k_1 and Δ^k_2 functions are defined as:

$$\Delta^k_1 = S_{\Omega_j} - S_k \tag{2.51a}$$

$$\Delta^k_2 = (\vec{\nabla} S)_k . (\vec{x}_{\Omega_j} - \vec{x}_k) \tag{2.51b}$$

where a k subscript denotes cell-vertex values while Ω_j is the subscript for cell-averaged values. $(\vec{\nabla} S)_k$ is the gradient of S at node k as computed in AVBP. Δ^k_1 measures the variation of S inside the cell Ω_j (using only quantities defined on this cell). Δ^k_2 is an estimation of the same variation but on a wider stencil (using all the neighbouring cell of the node k). This sensor is smooth: it is roughly proportional to the amplitude of the deviation from linearity.

2.2.3.2 Operators of artificial viscosity

A cell contribution of the 2$^{\text{nd}}$ order artificial viscosity is first computed on each vertex of the cell Ω_j:

$$R^2_{k\in\Omega_j} = -\frac{1}{n_v} \frac{V_{\Omega_j}}{\Delta t_{\Omega_j}} \mathsf{smu2}\ \zeta_{\Omega_j} (w_{\Omega_j} - w_k) \tag{2.52}$$

For the 4$^{\text{th}}$ order artificial viscosity, the contribution is written

$$R^4_{k\in\Omega_j} = \frac{1}{n_v} \frac{V_{\Omega_j}}{\Delta t_{\Omega_j}} \mathsf{smu4}\ \left[\left(\vec{\nabla} w\right)_{\Omega_j} \cdot (\vec{x}_{\Omega_j} - \vec{x}_k) - (w_{\Omega_j} - w_k) \right] \tag{2.53}$$

Parameters smu2 and smu4 are dimensionless and are provided by the user. The nodal value is then found by adding every surrounding cells contributions:

$$dw_k = \sum_j R^2_{k\in\Omega_j} + \sum_j R^4_{k\in\Omega_j} \tag{2.54}$$

2.2.4 The MISCOG method

To reduce the computational costs, the simulations used the Multi Instances Solvers Coupled via Overlapping Grids (MISCOG) method, which has been recently implemented in the code TurboAVBP (Wang et al., 2013, 2014; Papadogiannis et al., 2014). It consists in coupling two (or more) instances of AVBP via the coupling tool OpenPALM (Duchaine et al., 2013; Piacentini et al., 2011), using the Schwarz method (Lions, 1988).

Figure 2.2 shows a sketch of the application of the MISCOG method on two subdomains, AVBP 1 and AVBP 2, each one having its own grid and its own time step, for instance Δt_1 and Δt_2 for AVBP 1 and AVBP 2 respectively, with $\Delta t_2 = n\Delta t_1$ (n being an integer). The subdomains share an overlapping zone, where asynchronous data interpolation (or exchange if both subdomains have the same overlapping grid) between the two simulations occur every time step Δt_2 (or every n time steps Δt_1) in order to solve the problem on each subdomain in a consistent way. The additive overlapping domain method to decouple local time steps has been principally investigated by Yu (1999) and numerically validated by two test cases of acoustic wave propagation and two-dimensional jet (Esnault et al., 2010).

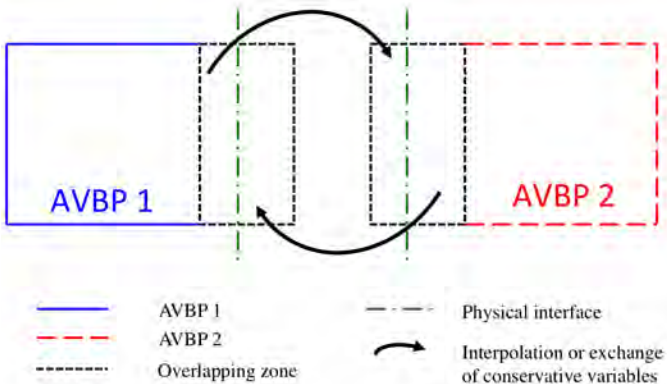

Figure 2.2 – Principle of the MISCOG method applied on two subdomains.

CHAPTER 3

Simulation setup

This chapter describes the simulation setup of a typical SRM exhaust jet at 20 km altitude. The first part describes the computational domain, the initial and boundary conditions and the application of the overset grid method. The second part focuses on the chemical composition of the exhaust gas and the chemical mechanisms characterizing the hot plume chemistry.

3.1 Computational domain

3.1.1 Thermodynamics properties

A sketch of the numerical domain is presented in Fig. 3.1. The domain is composed of a high-pressure tank connected to a low-pressure tank, representing ambient air, by means of the convergent-divergent nozzle of a SRM. The high-pressure tank is initially filled with the combustion products of the SRM chamber at pressure P_0, temperature T_0 and density ρ_0. These parameters take values which are those in a typical combustion chamber upstream of the nozzle, as the rocket reaches 20 km altitude. The low-pressure tank contains air at pressure P_∞ = 5619 Pa and temperature T_∞ = 203 K. These values are climate averages of data from ECMWF (European Centre for Medium-Range Weather Forecasts [1]) between 2000 and 2010 at 20 km above the launch pad in French Guiana. During the simulation, the pressure gradient drives the gas through the nozzle to the low-pressure tank. As the study takes place in the reference frame of the rocket, a supersonic coflow of air is added in the low-pressure tank as an initial condition and maintained during the simulation with an inlet condition. The coflow velocity, u_∞, corresponds to the supersonic velocity of the rocket at that altitude. The nozzle exit is located at x = 0 and the jet propagates along the x-axis. The nozzle exit diameter is noted D_e.

3.1.2 Domain size and boundary conditions

The sizes of the tank are chosen large enough to avoid uncontrolled effects of boundary conditions in the regions of interest for the study. Consequently, all boundaries (except the coflow inlet and the low-pressure tank outlet) are treated as adiabatic slip walls. In particular, an adiabatic slip condition is applied to the nozzle in order to avoid the formation of an artificial boundary layer due to coarse resolution of the wall (Vuorinen et al., 2013). The large size of the high-pressure tank makes it possible to maintain a

1. http://www.ecmwf.int/

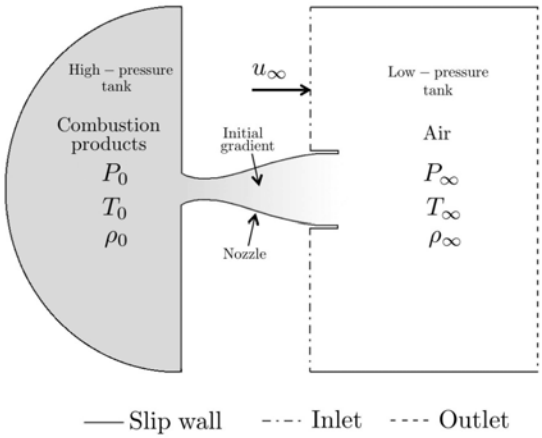

Figure 3.1 – Cut of the numerical domain (not scaled): initial and boundary conditions.

constant mass flow rate during the simulation. At the extremity of the low-pressure tank, a constant static pressure outlet is imposed following the NSCBC formulation (Poinsot and Lele, 1992).

The computational grids are unstructured tetrahedra grids. They are refined at the location of the jet, up to $400D_e$ downstream of the nozzle. Details about the grids are given in Sec. 4.1.2.

3.1.3 Turbulent coflow of air

The coflow of air is injected through a supersonic inlet (see Figs. 3.1 and 3.2). Because of the computational cost, the mesh cannot be designed fine enough in the vicinity of the mixing layer to make the turbulence of the flow appear by itself. A solution consists in adding a perturbation to the coflow in order to destabilize the flow. The code implements the Kraichnan/Celik method (Kraichnan, 1970) that generates artificial inhomogeneous anisotropic turbulence with a Passot-Pouquet energy spectrum. In this simulation, the velocity fluctuations are generated by the coflow supersonic inlet, up to a radial distance $r = 13.4r_e$ from the x-axis ($r_e = D_e/2$ and $r = \sqrt{y^2 + z^2}$). Their most energetic length scale is equal to the nozzle exit diameter D_e. The amplitude of the fluctuations does not exceed 5.5% of the coflow velocity. It is the minimum value required in order to trigger flow turbulence. This technique mimics the air coflow closer to reality. Indeed, the air flow around the rocket body causes perturbations which certainly have an effect on the plume, even though their amplitude is not well-known.

3.1.4 Domain decomposition - application of MISCOG method

A nozzle lip of $0.0134r_e$ thickness is added between the nozzle exit and the supersonic inlet (see Fig. 3.2). This lip imposes the smallest cell size Δx_{min} to be an order of magnitude smaller than in the immediate surrounding flow. Since the solver is explicit and these cells are the smallest of the whole computational domain, they limit the time step, making the simulation extremely expensive in computational time. A solution to reduce the computational cost is to employ TurboAVBP, which uses the MISCOG method described in Sec. 2.2, to separate the high pressure tank, the nozzle and the small cells of the lip (AVBP 1) from the rest of the atmospheric domain (AVBP 2), as shown in Fig. 3.3. The simulations AVBP 1 and AVBP 2 run with their own time steps, respectively Δt_1

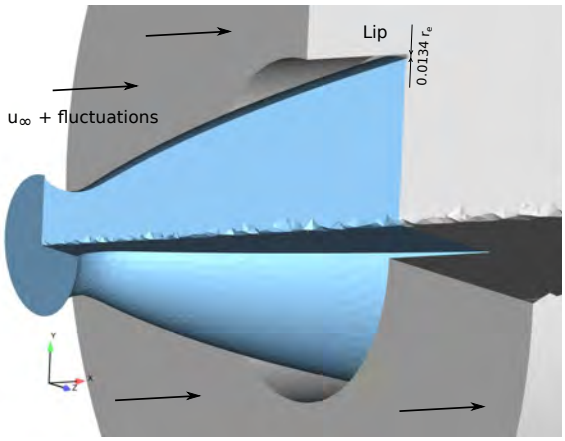

Figure 3.2 – Three-quarter section view of the nozzle (in blue) and of a portion of the inlet boundary and jet domain.

and Δt_2, with $\Delta t_2 = n\Delta t_1$ (where n is an integer larger than 1).

3.2 Chemical aspects

3.2.1 Chemistry in the nozzle

The chemical composition and the thermodynamics conditions of the flow in the combustion chamber and along the nozzle were evaluated by HERAKLES, using the OPHELIE code. [2] As mentioned in Sec. 1.3.1, OPHELIE performs thermochemical equilibrium computations from the chamber to the nozzle exit, with the hypotheses of isentropic one-dimensional flow. The evolution of the emission composition in the nozzle reveals a complex chemical activity, involving at least 24 species and phase changes. Modelling this chemistry in the LES of the SRM jet would be computationally expensive, for a limited modelling interest. Therefore, it was chosen to consider a frozen flow in the nozzle, while adopting the following strategy to account for the effects of chemistry in the nozzle:

— no chemical reaction is activated in the nozzle so the composition of the gas in the high-pressure tank and at the nozzle exit are the same;

— the pressure P_0 and temperature T_0 in the high-pressure tank (which correspond to the stagnation conditions) are determined such that the temperature at the nozzle exit T_e and the mass flow rate $\dot{m}$ correspond to the results given by the nozzle flow code, assuming that the flow is one-dimensional and isentropic. Details about the computation of P_0 and T_0 are provided in Appendix A.

3.2.2 Alumina particles modelling

As mentioned in Sec 1.2.2.2, liquid droplets of alumina solidify in the nozzle, due to the expansion and the consequent drop in temperature. At the nozzle exit, solid alumina particles should be added to the jet simulation in order to model both their effect on jet dynamics (deformation of streamlines, increase in temperature) and activation of chlorine (heterogeneous reactions at their surface). Two-phase flow modelling can be achieved using an Eulerian or a Lagrangian approach. However, these methods entail an additional computational cost which could not be supported for the present study. Moreover, the lack

2. C. Linck, private communication.

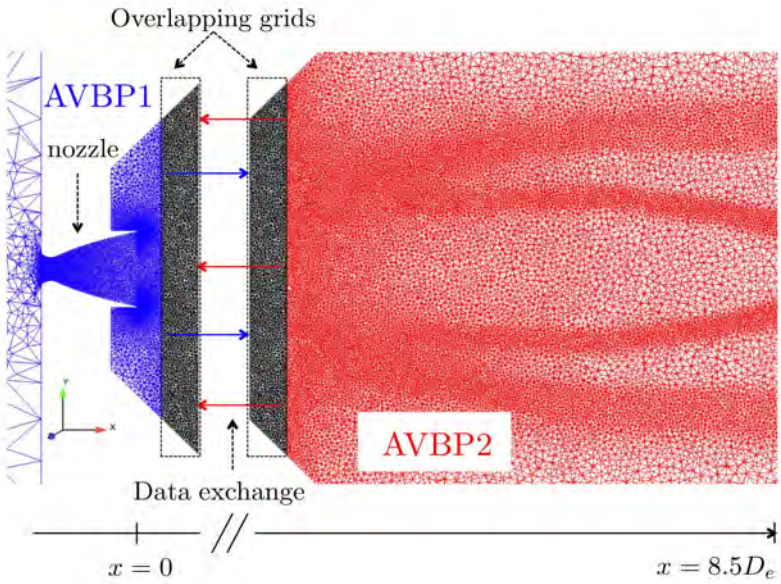

Figure 3.3 – Setup of the MISCOG method: the two meshes for simulations AVBP 1 and AVBP 2 both have the same portion mesh, a conical frustum, represented in black.

of knowledge concerning particle size distribution and their surface density in the plume is critical for heterogeneous chemistry. At the present time, this would make inaccurate any attempt of LES taking into account chlorine activation on alumina surface. It was therefore chosen to consider a single-phase flow, as a first approximation.

Previous studies showed that alumina particles are in thermal equilibrium with gas (Grenard et al., 2013), which partially justifies a representation of alumina as an inert perfect gas. This gaseous species would contribute to the sensible enthalpy of the system (and therefore to the temperature) via the heat capacity $c_p(T)$ of the alumina Al_2O_3(a). The potential change in plume shape and increase in temperature due to particles will not be captured by the LES due to this approximation. However, Grenard et al. (2013) noticed that particles affect the plume dynamics mainly at its center. As chemical reaction with air occur in the mixing layer, the effect of a temperature rise due to particles on afterburning chemistry may be limited. As for chlorine activation by heterogeneous chemistry on alumina surface, its importance for local ozone depletion is still highly debated, as discussed in Sec. 1.1.3.2.

3.2.3 Chemical composition at the nozzle exit

In order to limit the computational cost, aluminium containing species (other than Al_2O_3) are neglected. They represent 9 species, with a maximum mass fraction of 4.5×10^{-5}, and do not have an impact on hot plume chemistry. Their total mass fraction is 3.2×10^{-4}. This value was added to the mass fraction of species N_2, which is inert in these simulations, in order to ensure that the mass fraction of the system is equal to one. The final composition of the exhaust gas at the SRM nozzle exit was given by HERAKLES (private communication) and consists of 13 species, including alumina Al_2O_3 treated as a chemically (yet not thermodynamically) inert gas. Main reactive chemical species are HCl, H_2, CO, CO_2 and H_2O. The exhaust emissions also include minor fractions of radicals H, OH and H, and chlorine species Cl and Cl_2. The mole fraction of these species at the nozzle exit correspond to typical values for modern composite propellants, as illustrated

in Table 3.1 for a Titan IIIC SRM at 20 km of altitude.

Species	Mole fractions	Molecular weights W_i (g/mol)
CO	2.452×10^{-1}	28.0
CO_2	1.81×10^{-2}	44.0
Cl	1.2×10^{-3}	35.45
H	3.2×10^{-3}	1.0
OH	1.0653×10^{-4}	17.0
H_2O	1.051×10^{-1}	18.0
N_2	8.05×10^{-2}	28.0
H_2	3.136×10^{-1}	2.0
HCl	1.5×10^{-1}	36.5
Al_2O_3(a)	7.17×10^{-2}	102.0

Table 3.1 – Mole fractions and molecular weights of species at the nozzle exit of a Titan IIIC SRM, at 20 km of altitude (Stewart and Gomberg, 1976).

3.2.4 Chemical mechanism

As previously described in Sec. 1.2.2.3, the afterburning process in a SRM jet consists in the oxidation of hydrogen molecules and carbon monoxide emitted by the booster, forming free radicals O, OH, H, water H_2O and carbon dioxide CO_2. The detailed chemical-kinetic scheme used in the following development to model the H_2-CO combustion is based on the GRI-Mech 3.0 mechanism (Smith et al., 1999). It consists of 11 species and 30 reactions listed in Table 3.2: reactions 1 to 20 describe the oxidation of H_2 and reactions 21 to 30 the oxidation of CO. This scheme, and in particular the submechanism for H_2-O_2 combustion, are commonly used as a simplified mechanism of the original chemistry (which can involve several hundred equations), as they proved to give excellent predictions in a large range of conditions (Saxena and Williams, 2006).

The free radicals produced during hydrogen combustion are involved into a partial conversion of HCl, present in the exhaust gas, into active chlorine Cl and Cl_2. In previous SRM hot plume simulations (Denison et al., 1994; Brady and Martin, 1995), this process was mainly modelled by 6 reactions involving the chlorine species HCl, Cl and Cl_2. They were chosen for the present study, with the addition of the reaction of dissociation of HCl, recommended by Jensen and Jones (1978). These reactions are numbered from 31 to 37 in Table 3.2. Their rate parameters are those advised by Jensen and Jones (1978) and Baulch et al. (1981) for ranges of high temperatures. To the best of our knowledge, there is no recent evaluation of the rate parameters of the dissociation reactions of HCl and Cl_2 (reac. 36 and 37). The choice was made to use the coefficients given by Jensen and Jones (1978), but the sensitivity of the fraction of active chlorine to uncertainties on these coefficients has to be evaluated. Other species like ClO, ClOO or HOCl also participate to the chemical mechanism, however, it was shown in previous studies that their concentrations remained very low and that they had no noticeable impact on the fraction of active chlorine (Zittel, 1994). Therefore they were not included in the chemistry description of the present work.

Finally, considering the negligible effect of NOx formation on local ozone loss found in

previous studies (Denison et al., 1994; Zittel, 1994; Leone and Turns, 1994), it was chosen not to model this mechanism again to save computational time.

3.3 Conclusion

The computational setup of the simulation of a typical SRM exhaust jet at 20 km was described. A few approximations were adopted to simplify the simulation and match objectives in terms of computational time:

— particles of alumina are treated like a perfect gas; this may affect the shape of the plume and its temperature (at the center of the potential core mainly); as heterogeneous chemistry will not be modelled, this might lead to a slight underestimation of the active chlorine in the jet;

— the chemistry in the nozzle is not modelled; the total pressure and temperature in the chamber were adapted so that the nozzle exit parameters obtained with the nozzle flow code OPHELIE are verified;

— the formation of NOx is not taken into account, as it is considered negligible in many studies.

Overall, the resulting chemistry involves 16 species and 37 reactions. As discussed in Chapter 7 of this manuscript, chemistry still needs to be reduced for reactive LES to keep affordable CPU resources.

No.	Reactions	Rate parameters			Ref.
		A	n	E	
1	$H + O_2 = O + OH$	2.65(16)	-0.671	17041	(Smith et al., 1999)
2	$O + H_2 = H + OH$	3.87(04)	2.7	6260	(Smith et al., 1999)
3	$OH + H_2 = H + H_2O$	2.16(08)	1.51	3430	(Smith et al., 1999)
4	$2\,OH = O + H_2O$	3.57(04)	2.4	-2110	(Smith et al., 1999)
5	$2\,H + M = H_2 + M$	1.0(18)	-1	0	(Smith et al., 1999)
6	$H + OH + M = H_2O + M$	2.2(22)	-2	0	(Smith et al., 1999)
7	$O + H + M = OH + M$	5.0(17)	-1	0	(Smith et al., 1999)
8	$2\,O + M = O_2 + M$	1.2(17)	-1	0	(Smith et al., 1999)
9	$H + O_2 + M = HO_2 + M$	2.8(18)	-0.86	0	(Smith et al., 1999)
10	$H + HO_2 = O_2 + H_2$	4.48(13)	0	1068	(Smith et al., 1999)
11	$2\,OH + M = H_2O_2 + M$	(k_f) 7.4(13)	-0.37	0	(Smith et al., 1999)
		(k_{f0}) 2.3(18)	-0.9	-1700	(Smith et al., 1999)
12	$HO_2 + H = O + H_2O$	3.97(12)	0	671	(Smith et al., 1999)
13	$HO_2 + H = 2\,OH$	8.4(13)	0	635	(Smith et al., 1999)
14	$HO_2 + O = OH + O_2$	2.0(13)	0	0	(Smith et al., 1999)
15 (a)	$HO_2 + OH = O_2 + H_2O$	1.45(13)	0	-500	(Smith et al., 1999)
15 (b)		5.0(15)	0	17330	(Smith et al., 1999)
16 (a)	$2\,HO_2 = O_2 + H_2O_2$	1.3(11)	0	-1630	(Smith et al., 1999)
16 (b)		4.2(14)	0	12000	(Smith et al., 1999)
17	$H_2O_2 + H = HO_2 + H_2$	1.21(07)	2	5200	(Smith et al., 1999)
18	$H_2O_2 + H = OH + H_2O$	1.0(13)	0	3600	(Smith et al., 1999)
19	$H_2O_2 + O = OH + HO_2$	9.63(06)	2	4000	(Smith et al., 1999)
20(a)	$H_2O_2 + OH = HO_2 + H_2O$	2.0(12)	0	427	(Smith et al., 1999)
20(b)		1.7(18)	0	29410	(Smith et al., 1999)
21	$CO + O + M = CO_2 + M$	(k_f) 1.8(10)	0	2385	(Smith et al., 1999)
		(k_{f0}) 6.02(14)	0	3000	(Smith et al., 1999)
22	$CO + OH = CO_2 + H$	4.76(07)	1.228	70	(Smith et al., 1999)
23	$CO + O_2 = CO_2 + O$	2.5(12)	0	47800	(Smith et al., 1999)
24	$CO + HO_2 = CO_2 + OH$	1.5(14)	0	23600	(Smith et al., 1999)
25	$HCO + H = CO + H_2$	7.34(13)	0	0	(Smith et al., 1999)
26	$HCO + O = CO + OH$	3.0(13)	0	0	(Smith et al., 1999)
27	$HCO + O = CO_2 + H$	3.0(13)	0	0	(Smith et al., 1999)
28	$HCO + OH = CO + H_2O$	5.0(13)	0	0	(Smith et al., 1999)
29	$HCO + M = CO + H + M$	1.87(17)	-1	17000	(Smith et al., 1999)
30	$HCO + O_2 = CO + HO_2$	1.345(13)	0	400	(Smith et al., 1999)
31	$Cl + HO_2 = HCl + O_2$	3.0(13)	0	0	(Baulch et al., 1981)
32	$H + Cl_2 = HCl + Cl$	8.6(13)	0	1172	(Baulch et al., 1981)
33	$Cl + H_2 = HCl + H$	1.45(13)	0	4372	(Baulch et al., 1981)
34	$H_2O + Cl = HCl + OH$	1.68(13)	0	17227	(Baulch et al., 1981)
35	$OH + Cl = HCl + O$	5.9(12)	0	5683	(Baulch et al., 1981)
36	$H + Cl + M = HCl + M$	1.4(22)	-2	0	(Jensen and Jones, 1978)
37	$2\,Cl + M = Cl_2 + M$	7.26(14)	0	-1788	(Jensen and Jones, 1978)

Table 3.2 – Reference mechanism for H_2–CO combustion and conversion of HCl to active chlorine Cl and Cl_2. The rate parameters are expressed as $k = AT^n \exp(-E/RT)$. Units are cm, s, mol and cal. In the column for A, the number in parenthesis is the exponent of 10 (for instance, $2.65(16) = 2.65 \times 10^{16}$).

CHAPTER 4

Large Eddy Simulations of a single-species SRM jet

Large Eddy Simulations of a multi-species, reactive SRM jet following the numerical setup described in Chapter 3 is particularly complex and computationally expensive to achieve. In particular, the implementation of an overset grid method (described in Sec. 3.1.4) adds complexity to the numerical setup, as well as a potential source of uncertainty. It is particularly important to assess the accuracy of the results without engaging all the computational resources needed for a multi-species, reactive simulation. This objective can be achieved by conducting LES of a single-species SRM jet (i.e. for which the SRM exhaust gas is represented by a single equivalent species), and ensuring the reliability of the results by comparing the dynamical properties of the jet to previous knowledge.

Beyond the validation of the setup of the overset grid method, this simulation represents, to the best of our knowledge, one of the first LES of supersonic jet attempted on such a long computational domain (400 nozzle exit diameters downstream of the nozzle). This offers the possibility to study in detail the dynamics of an underexpanded jet, and particularly the far-field region, usually available only through experiments.

In the following developments, a first section describes elements in the simulation setup which are specific to this configuration and not covered in Chapter 3. Details about the convergence of the simulation are given, followed by a comparative study showing the accuracy of the MISCOG method. Then, each region of the flow is identified and characterized by mean centerline and radial parameters, and turbulence length scales. When possible, the results are compared to previous simulations and experiments of compressible jets.

4.1 Simulation setup and convergence of computations

The computational domain used for this simulation, including the initial and boundary conditions and the domain decomposition, corresponds to description in Sec. 3.1.

4.1.1 Equivalent gas

4.1.1.1 Thermodynamic variables

As this simulation only focuses on jet thermodynamics to validate the coupling configuration, the multi-species air and SRM exhaust gas were replaced by thermodynamically equivalent single-species gas. No chemistry is modelled, therefore for each equivalent gas,

the required thermochemical parameters are the mean molecular weights and the tabulated sensible enthalpies.

The high pressure tank is filled with a gas thermodynamically equivalent to the multi-species gas at the nozzle exit. The mean molecular weight W_g of this equivalent exhaust gas is given by:

$$W_g = \sum_{k=1}^{13} X_k^0 W_k = 26.3 \text{ g/mol}. \tag{4.1}$$

where X_k^0 is the mole fraction of species k at the nozzle exit and W_k the molecular weight. The tabulated molar sensible enthalpies for this equivalent gas are noted $\tilde{h}_{s,g}^m(T_i)$, where the symbol ~ denotes tabulated values, and $T_i = 100i\,K$, for $i = 0..50$. They are given by:

$$\tilde{h}_{s,g}^m(T_i) = \sum_{k=1}^{13} X_k^0 \int_{T_0}^{T_i} C_{p,k}^m dT = \sum_{k=1}^{13} X_k^0 \tilde{h}_{s,k}^m(T_i) \tag{4.2}$$

where $C_{p,k}^m$ is the molar heat capacity of species k and $\tilde{h}_{s,k}^m$ the sensible molar enthalpie of species k. The reference temperature is $T_0 = 298.15K$.

In the low pressure tank, air is represented by an equivalent species thermodynamically equivalent to a mixing of O_2 and N_2 such that:

$$W_\infty = X_{O_2}^\infty W_{O_2} + X_{N_2}^\infty W_{N_2} = 28.85 \text{ g/mol} \tag{4.3a}$$

$$\tilde{h}_{s,\infty}^m(T_i) = X_{O_2}^\infty \tilde{h}_{s,O_2}^m(T_i) + X_{N_2}^\infty \tilde{h}_{s,N_2}^m(T_i) \tag{4.3b}$$

where $X_{N_2}^\infty$ and $X_{O_2}^\infty$ are respectively the mole fraction of species N_2 and O_2 in the air.

Finally, the values of pressure P_0 and temperature T_0 in the high pressure tank were chosen so that the temperature at the nozzle exit T_e and the mass flow rate correspond to the results given by the nozzle flow code OPHELIE (as precised in Sec. 3.2.1 and detailed in Appendix A.

Nota Bene: the following simulation was conducted with an equivalent exhaust gas which was provided by HERAKLES to model the combustion chamber. Therefore this gas does not verify Eqs. (4.1) and (4.2). Later on, the composition of the SRM exhaust gas at 20 km of altitude was made available to us. A second equivalent exhaust gas, verifying Eqs. (4.1) and (4.2), was used in a second simulation, similar to the simulation presented in this chapter. The results being close to these previously obtained with the first equivalent gas, it was decided not to perform again all the analyses (which, for some of them, require a considerable computational time). However, these latest results were used to provide streamlines in Chapter 6 and an initial condition for the reactive LES described in Chapter 8.

4.1.1.2 Transport parameters

The dynamic viscosity is given by the power law:

$$\mu = \mu_0 \left(\frac{T}{T_{ref}} \right)^b \tag{4.4}$$

with $\mu_0 = 1.788 \cdot 10^{-5} kg.m^{-1}s^{-1}$, $b = 0.686$ and $T_{ref} = 300K$. These values were found to fit quite well the real viscosity of the mixture. A constant Prandtl number $Pr = 0.75$ is imposed (a classic value for non reactive flows), as well as constant Schmidt numbers $Sc_g = Sc_a = 0.75$ (which is the value usually taken for air).

Case	Simulation duration	c_1: cells AVBP 1	c_2: cells AVBP 2	c_o: cells overlap	Δt_1	Δt_2	$\Delta x_{min}/D_e$
A	$2t_c$	2,905,302	74,291,783	928,190	$0.938\mu s$	$7.504\mu s$	1/300
B	$2.5t_c$	2,909,615	78,538,175	928,148	$1.24\mu s$	$7.44\mu s$	1/300

Table 4.1 – Mesh parameters for Cases A & B.

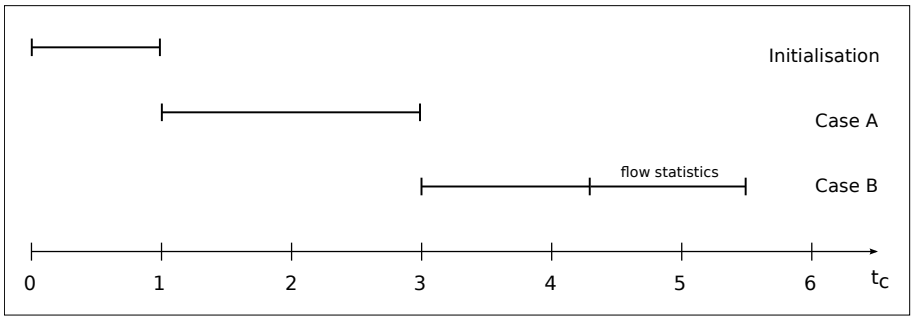

Figure 4.1 – Diagram showing the successive steps to converge the LES of a single-species SRM jet.

4.1.1.3 Subgrid scale model

The subgrid scale model used for this simulation is the Smagorinsky model (see Sec. 2.1.7.5).

4.1.2 Convergence of the simulation

The simulation was initialized using a coarse mesh and the low-order Lax-Wendroff scheme for one convective time t_c (a convective time is the physical time required for a fluid particle to reach the outlet of the domain; at $400D_e$ downstream the nozzle exit, it is estimated at 1.1s). The results were interpolated on a finer mesh (case A in table 4.1) and the simulation was run with the high-order scheme TTG4A for $2t_c$. The averaged results obtained from case A made it possible to design (by hands) a second, adapted mesh (case B, Fig. 4.2) that is finer at the locations of high velocity and temperature gradients (particularly in the mixing layer between equivalent gas and air), and coarser inside the potential core, where fluctuations are weak. Adding finer cells in the mixing layer makes the computation and the evaluation of turbulent statistics more accurate. The grid for case B, shown in Fig. 4.2, contains a minimum of 60 cells per jet diameter. In the pressure adaptation region, the mixing layer and the zones of high gradients are computed with a spatial resolution of the order of $D_e/30$. In the potential core, the mesh is also refined at the location of the mixing layer, with a resolution of $D_e/15$. If these resolutions are slightly lower than those used in recent works on smaller jets (Dauptain et al., 2012; Vuorinen et al., 2013), they still offer realistic and accurate results, as it is shown in Sec. 4.2. The last instantaneous solution of case A was interpolated on the new grid to provide an initial solution for case B, which is then run for $1.3t_c$ in order to reach statistical convergence of the flow. The simulation was continued for $1.2t_c$ to obtain mean and turbulence results (presented in the next section). As a whole, the SRM jet was run on cases A and B for a physical time of $4.5t_c = 4.95s$. A summary of the successive steps for converging the simulation is presented in Fig. 4.1.

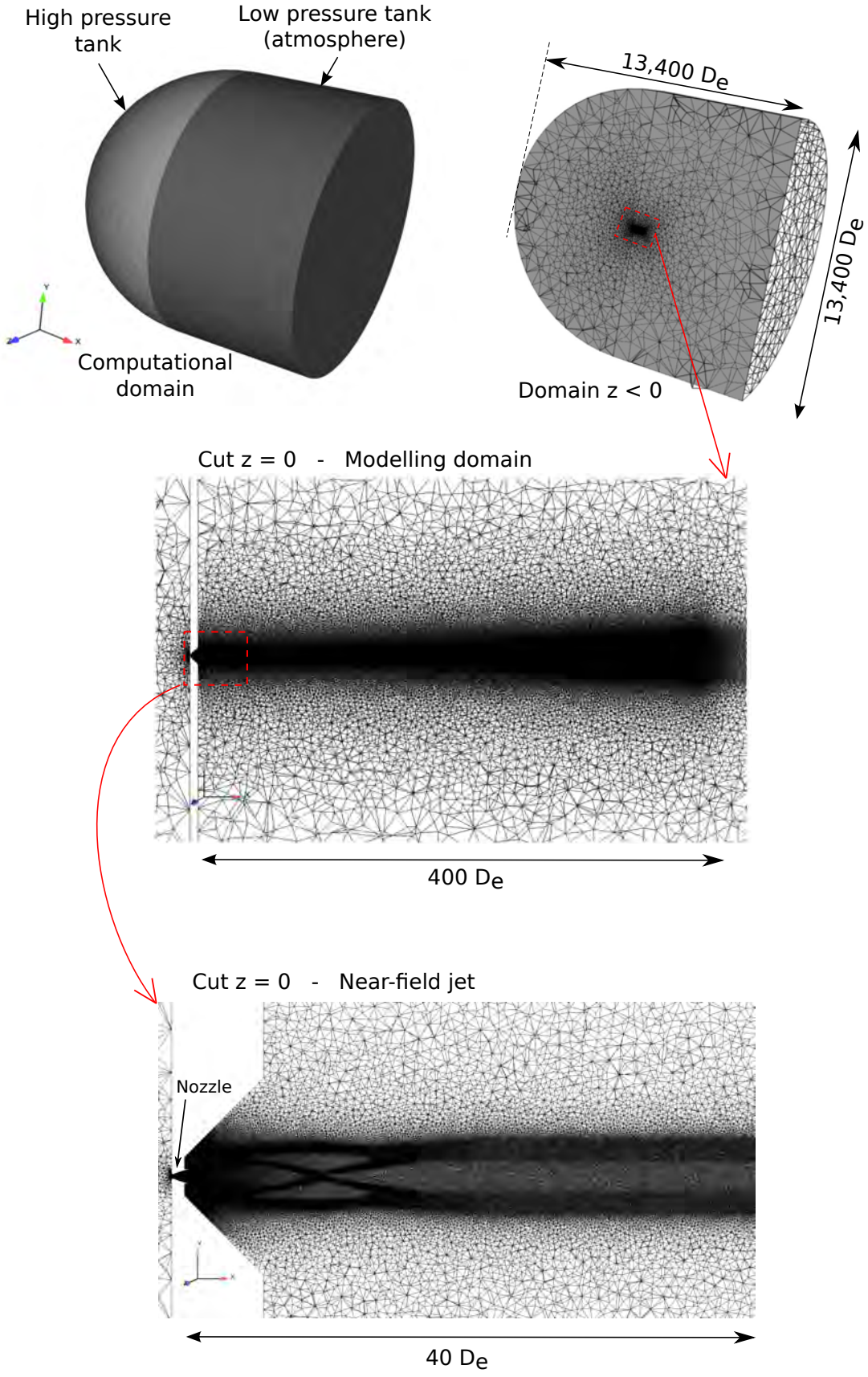

Figure 4.2 – Views of the computational domain (top), cuts of the mesh (case B) showing the jet zone (middle) and near-field jet (bottom). The last cut shows the mesh is refined in the mixing layer and in the oblique shocks zone.

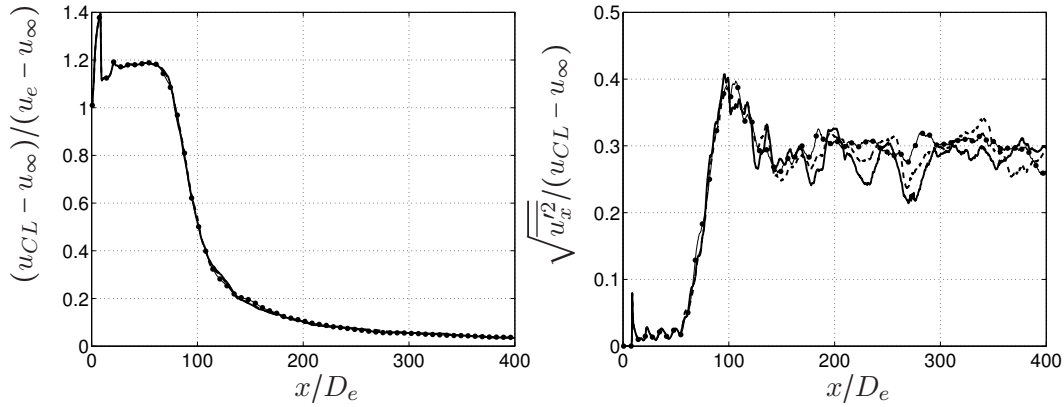

(a) (b)

Figure 4.3 – Centerline profiles: (a) axial velocity excess $(u_{CL}-u_\infty)/(u_e-u_\infty)$ and (b) rms axial velocity $\sqrt{\overline{u_x'^2}}/(u_{CL}-u_\infty)$, averaged between t_0 and $t_0+\Delta T$ (—), t_0 and $t_0+2\Delta T$(- - -), t_0 and $t_0+3\Delta T$(-•-) (the rms axial velocity is nondimensionalized by the centerline axial velocity excess $u_{CL}-u_\infty$ averaged on the interval $[t_0, t_0+3\Delta T]$).

4.1.3 Analysis of statistical convergence

The statistical convergence of the simulation is proven by Fig. 4.3, which shows the longitudinal evolution of centerline axial velocity excess $u_{CL}-u_\infty$ (nondimensionalized by the nozzle exit velocity excess u_e-u_∞), and of root-mean-squared axial velocity (nondimensionalized by the averaged centerline axial velocity excess). These parameters are averaged over three time intervals $[t_0, t_0+\Delta T]$, $[t_0, t_0+2\Delta T]$ and $[t_0, t_0+3\Delta T]$, with $t_0 = 3.3t_c$ and $\Delta T = 0.28t_c$. The three plots depicting axial velocity excess differ very little from each other. The plots of axial fluctuations show oscillations around the value 0.3 for $x > 150D_e$, but still converge toward the plot averaged on the longest interval. These differences can be attributed to the fact that a longer averaged period is needed in order to get fully satisfactory fluctuations profiles.

4.1.4 CPU time

A simple computation shows the cut in computational time for a simulation using MISCOG compared to a simulation AVBP on a single domain, for the same physical simulation time. For N_1 iterations of the standalone simulation, AVBP 1 and AVBP 2 in the coupled simulation respectively run for N_1 and $N_2 = N_1/n$ iterations (where $n = \Delta t_2/\Delta t_1$). The ratio of CPU times of the two cases gives:

$$\frac{t_{CPU,\,\text{AVBP standalone}}}{t_{CPU,\,\text{MISCOG}}} = \frac{N_1 \Delta t_{CPU} \cdot (c_1 + c_2 - c_o)}{N_1 \Delta t_{CPU} c_1 + \frac{N_1}{n} \Delta t_{CPU} c_2} \tag{4.5a}$$

$$= \frac{c_1 + c_2 - c_o}{c_1 + c_2/n} \tag{4.5b}$$

where Δt_{CPU} is the computational time step per iteration per cell. Applying Eq. 4.5b with the parameters for Case B (Table 4.1) gives a ratio of 5. In total, this simulation required 150, 000 CPU hours and was performed using HPC resources from GENCI-TGCC/CINES (grant 2013–fac6131). Without MISCOG, the same simulation would have needed about 750,000 CPU hours.

Typical runs used 1024 cores. These cores were attributed to each sub-domain so that the physical time steps to compute n iterations of sub-domain AVBP 1 and one iteration of sub-domain AVBP 2 are as close as possible, to avoid one simulation to wait for the other when exchanging data. This requirement is expressed in the following relations:

$$p_1 + p_2 = p_{\text{tot}} \tag{4.6a}$$

$$np_1c_1\Delta t_{CPU} = p_2c_2\Delta t_{CPU} \tag{4.6b}$$

where p_{tot} is the total number of cores used for the simulation, p_1 and p_2 are the number of cores attributed to AVBP 1 and AVBP 2 respectively. Equations (4.6) give:

$$p_1 = \frac{p_{\text{tot}}c_2}{nc_1 + c_2} \tag{4.7a}$$

$$p_2 = \frac{np_{\text{tot}}c_1}{nc_1 + c_2} \tag{4.7b}$$

A typical run for case B, with $p_{\text{tot}} = 1023$ (one core is attributed to data exchange between both domains), would have the following core distribution:

$$p_1 = 186 \tag{4.8a}$$

$$p_2 = 837 \tag{4.8b}$$

4.2 Results and discussion

4.2.1 Accuracy of the MISCOG method

In the validation study of MISCOG method (Wang et al., 2013, 2014), it was shown that if the grids of the overlapping zone are the same for both domains (as in the present simulations), the data between the domains are simply exchanged, therefore there is no degradation of the spatial order of the numerical scheme due to the interpolation step. In order to ensure the accuracy of the MISCOG method for the present application, a comparative study has been carried out. The objective is to compare a simulation "MISCOG" which applies the coupling method (case 1 in Table 4.2) with a simulation "AVBP" on a single domain (case 2), in order to determine wether the MISCOG method introduces some errors and their extent. The comparison is performed in the vicinity of the overlapping zone, as it would be computationally too expensive to run a simulation without the local time-stepping method on the entire domain described in Chapter 3. The grid is identical for both simulations and refined up to $3D_e$ behind the nozzle. A converged instantaneous solution from case B was interpolated on each grid to provide the same initial condition for the two cases. No turbulence is added to the coflow in order to avoid any statistic bias. Both simulations were run for a physical time of 37.8 ms, which is enough to obtain a converged solution at $x = 3D_e$. Then, three axial cuts were performed on the two series of averaged results: upstream, inside and downstream the overlapping zone, as shown in Fig. 4.4 (or at the corresponding locations for case 2). Figures 4.5a, 4.5c and 4.5e show the distribution of the absolute differences on the grid points of both simulations for three variables: density, temperature and axial velocity. Table 4.3 gives the integral values of these plots for easier comparison. The distributions have similar profiles between the cuts and tend rapidly to zero. For the three cuts, nearly 99% of grid points of the cut show differences less than 1%. Table 4.3 confirms this analysis by showing that the integral

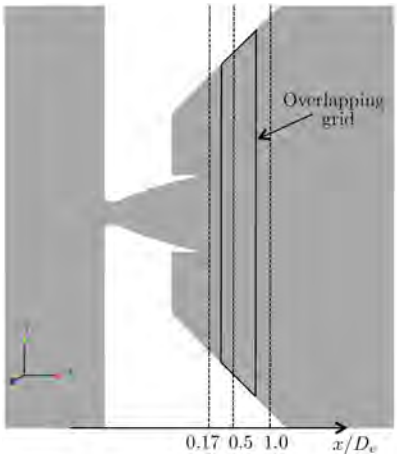

Figure 4.4 – Cut of the numerical domain showing the positions of the three axial cuts (dashed lines) performed on the results of cases 1, 2 and 3 : at $x = 0.17D_e$ (upstream the overlapping zone), $x = 0.5D_e$ (inside the overlapping zone) and $x = 1.0D_e$ (downstream the overlapping zone).

CASE 1	CASE 2	CASE 3
MISCOG method	single domain	single domain
ParMETIS partitionning	ParMETIS partitionning	RIB partitionning
$\Delta t_2 = 6.3\mu s$, $\Delta t_1 = 1.26\mu s$	$\Delta t = \Delta t_1 = 1.26\mu s$	$\Delta t = \Delta t_1 = 1.26\mu s$

Table 4.2 – Description of the three cases simulated in order to conclude on the accuracy of the MISCOG method.

values of these plots remain within a small interval, between 0.0679 and 0.0972.
The minor differences between cases 1 and 2 that have been highlighted by these statistics can be explained by a mesh partitioning which differs between simulations. Despite the fact that ParMETIS (Parallel Graph Partitioning and Fill-reducing Matrix ordering (Karypis and Kumar, 1998)) algorithm is used in both cases, the partitioning cannot be exactly the same on the single mesh of case 2 and on the two meshes of case 1. These differences in partitioning are known for introducing differences in the results (Senoner et al., 2008). In order to corroborate this hypothesis for the present simulations, a third AVBP simulation was run (case 3), with the same conditions as case 2, but using the RIB partitioning algorithm (Recursive Inertial Bisection (Williams, 1991)). The results of case 3 are compared to case 2 using the same procedure described previously. The distributions are shown in Figs. 4.5b, 4.5d, and 4.5f, and the integrated values of the plots are given in Table 4.3. The distributions show the same trend and their integral values are of the same order as for cases 1 and 2. Therefore, the differences noticed between cases 1 and 2 can be reasonably attributed to the application of the partitioning algorithm rather than the overlapping technique. Based on this observation, it is possible to conclude that the MISCOG method does not introduce significant error in this simulation of a SRM jet.

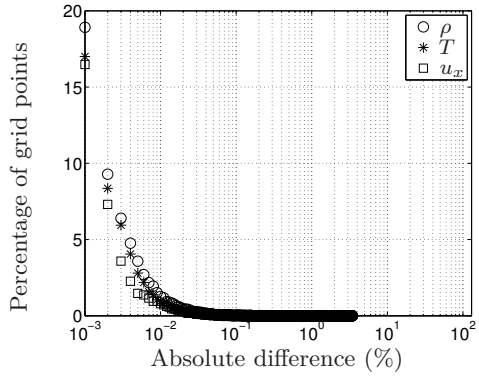

(a) $x = 0.17D_e$, comparison of cases 1 and 2.

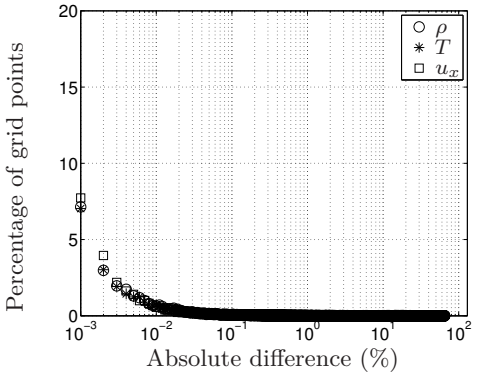

(b) $x = 0.17D_e$, comparison of cases 2 and 3.

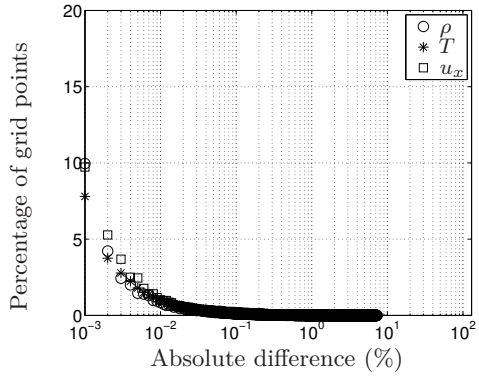

(c) $x = 0.5D_e$, comparison of cases 1 and 2.

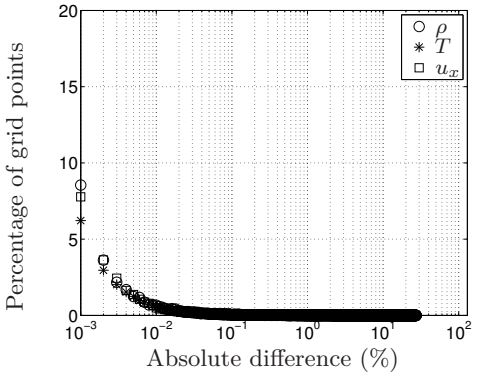

(d) $x = 0.5D_e$, comparison of cases 2 and 3.

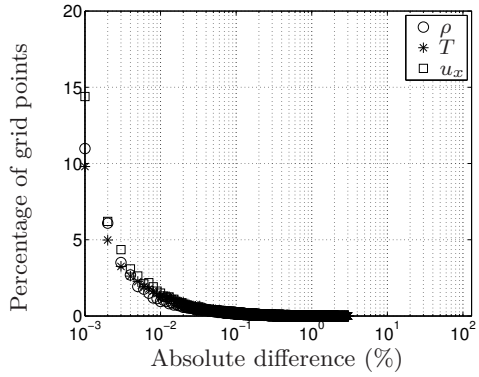

(e) $x = 1.0D_e$, comparison of cases 1 and 2.

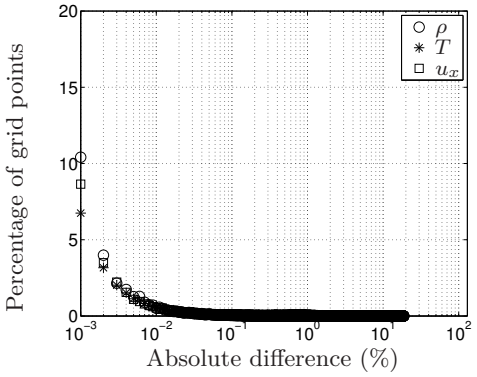

(f) $x = 1.0D_e$, comparison of cases 2 and 3.

Figure 4.5 – Comparison of absolute differences between cases 1 and 2 (left column) and between cases 2 and 3 (right column). The comparison is done on the points of three axial cuts whose positions are described on Figure 4.4.

	Comparison cases 1 & 2			Comparison cases 2 & 3		
	$x = 0.17D_e$ (a)	$x = 0.5D_e$ (c)	$x = 1.0D_e$ (e)	$x = 0.17D_e$ (b)	$x = 0.5D_e$ (d)	$x = 1.0D_e$ (f)
ρ	$8.4 \cdot 10^{-2}$	$8.4 \cdot 10^{-2}$	$9.6 \cdot 10^{-2}$	$9.4 \cdot 10^{-2}$	$8.6 \cdot 10^{-2}$	$9.3 \cdot 10^{-2}$
T	$7.5 \cdot 10^{-2}$	$7.9 \cdot 10^{-2}$	$9.1 \cdot 10^{-2}$	$9.1 \cdot 10^{-2}$	$8.2 \cdot 10^{-2}$	$8.9 \cdot 10^{-2}$
u_x	$6.9 \cdot 10^{-2}$	$7.7 \cdot 10^{-2}$	$9.1 \cdot 10^{-2}$	$8.8 \cdot 10^{-2}$	$8.0 \cdot 10^{-2}$	$8.7 \cdot 10^{-2}$

Table 4.3 – Integrated values of the plots of absolute differences in Figure 4.5.

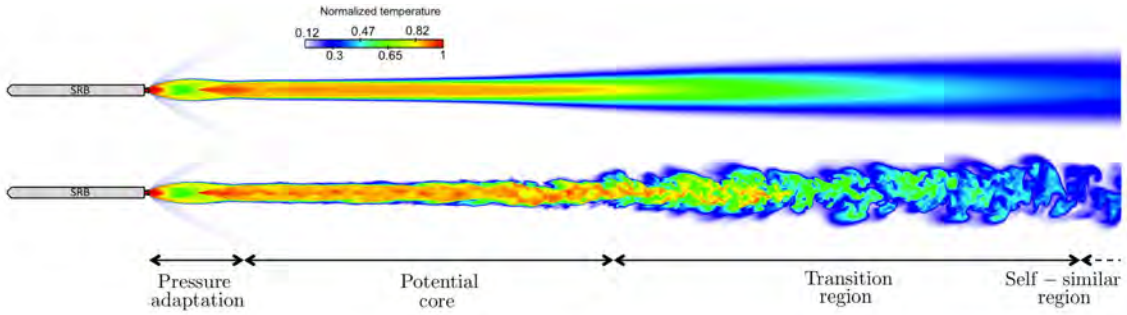

Figure 4.6 – Cut of the jet up to $180D_e$ behind the nozzle showing instantaneous (bottom) and mean (top) normalized temperature.

4.2.2 Flow visualization

Two cuts of the jet depicting the instantaneous and average normalized temperature are presented in Fig. 4.6. The instantaneous cut shows that after the pressure adaptation region, the jet is destabilized due to the injection of turbulence in the coflow, enabling a progressive transition to turbulence and a mixing with the ambient air. In the averaged cut, four distinctive regions of the jet can be identified: a pressure adaptation region ($0 < x < 25D_e$), a potential core ($25D_e < x < 84D_e$), a transition region ($84D_e < x < 180D_e$) and a self-similar region ($x > 180D_e$). These characteristics have been identified not only on rocket jets (Simmons, 2000) but also on any supersonic under-expanded jet (Vuorinen et al., 2013; Murakami and Papamoschou, 2002; Pope, 2000).

The transition to turbulence can be observed from a visualization of the second invariant of the velocity gradient tensor $Q = 1/2(\Omega_{ij}\Omega_{ij} - S_{ij}S_{ij})$, where S_{ij} the symmetric part of velocity gradient tensor, and Ω_{ij} its asymmetric part (Dubief and Delcayre, 2000). Figure 4.7 shows an isosurface of positive Q, from the middle of the potential core to the transition region. In the potential core region, elongated, streamwise oriented vortices are visible, which are typical of high Mach number flows (Freund et al., 2000b; Maidi and Lesieur, 2005). Downstream of the potential core, the jet appears chaotic, with a complex interaction of large and smaller vortices.

The centerline evolution of mean velocity, temperature and mass fraction of equivalent gas is shown in Fig. 4.8. After the oscillations due the pressure adaptation, they present a plateau in the region of the potential core, and then start decreasing to reach atmospheric values. The mean centerline velocity in the potential core u_{PC} can be considered as approximately constant and is defined as $u_{PC} - u_\infty = 1.18(u_e - u_\infty)$. In this region, the jet reaches a Reynolds number of $Re = 6.9 \times 10^7$.

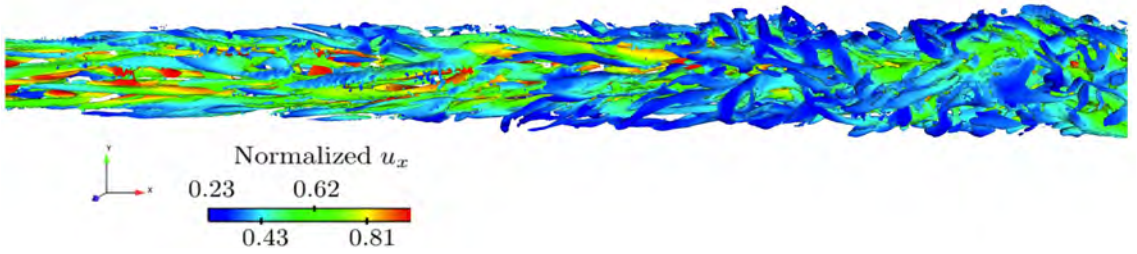

Figure 4.7 – Isosurface of $Q = 0.0326(u_e/D_e)^2$ (or $Q = 0.31(u_{PC}/D_{PC})^2$, with D_{PC} the diameter of the jet in the potential core region), colored in axial velocity, for $45D_e < x < 100D_e$.

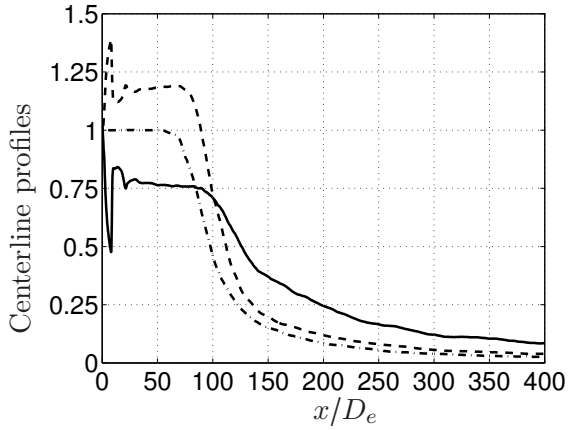

Figure 4.8 – Mean normalized centerline temperature excess $(T_{CL} - T_\infty)/(T_e - T_\infty)$ (—) , axial velocity excess $(u_{CL} - u_\infty)/(u_e - u_\infty)$ (- - -) and mass fraction of equivalent gas Y_g $(\cdot - \cdot)$.

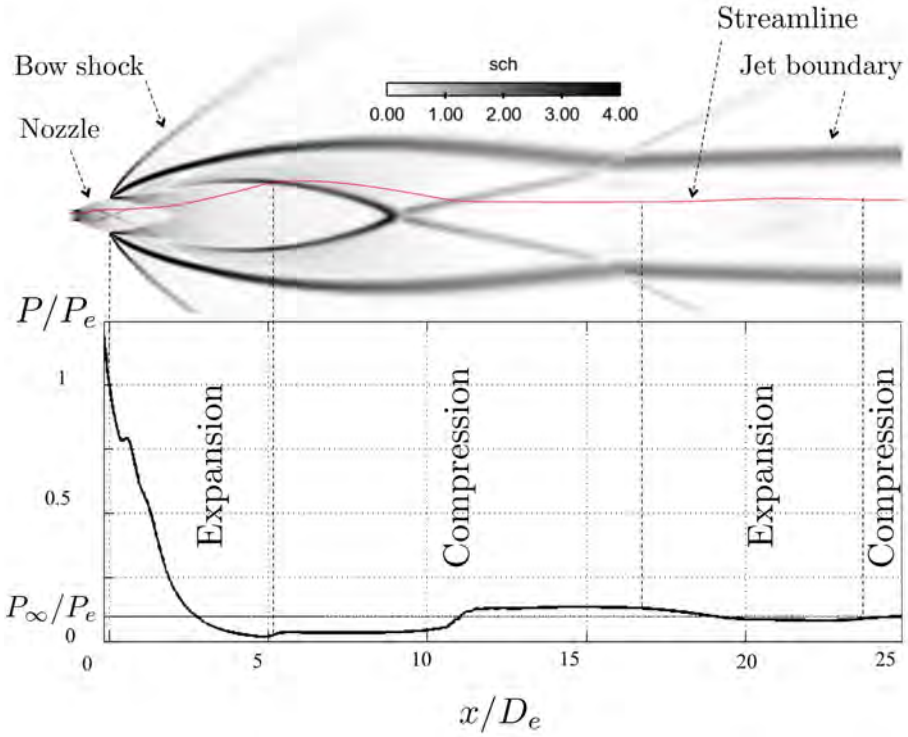

Figure 4.9 – Top: Cut of the jet from the inlet of the nozzle up to $x = 25D_e$ downstream, showing $\left\|\vec{\nabla}\rho\right\|/\rho$ and a streamline; Bottom: mean pressure along the streamline, normalized by P_e.

4.2.3 Nozzle and pressure adaptation region

As the flow at the nozzle exit is supersonic with a pressure P_e much larger than the atmospheric pressure P_∞, the jet is highly under-expanded. The flow expands so that the pressure reaches the value P_∞ through a series of Prandtl-Meyer expansion and compression waves generated from the nozzle lip. Figure 4.9 shows a numerical Schlieren cut of the quantity $\left\|\vec{\nabla}\rho\right\|/\rho$ in the nozzle and in the pressure adaptation region, where ρ is the mean density. A streamline is added to highlight the effect of the weak shock waves on the fluid trajectory. Under the cut, the mean pressure along the streamline is plotted. From the nozzle exit up to $x = 5D_e$, the fluid particle gets through an expansion region: the pressure decreases dramatically below P_∞. The expansion also makes the flow velocity increase and peak at $x = 5D_e$. In the region $5D_e < x < 16.7D_e$, the streamline crosses two compression waves: the pressure increases slightly above P_∞ and the velocity decays. Finally, P reaches P_∞ after other cycles of expansion-compression, much weaker than the first one. On the other hand, a second set of oblique shocks can be seen in the nozzle. This is first created at the throat, is reflected just past the nozzle exit and crosses the compression shocks mentioned above, having a limited influence on the expansion of the jet. Previous simulations of a SRM jet showed a similar shock pattern (Calhoon, 1998). It it important to point out that this shock pattern is influenced by the supersonic coflow, as noticed by Lovaraju and Rathakrishnan (2011).

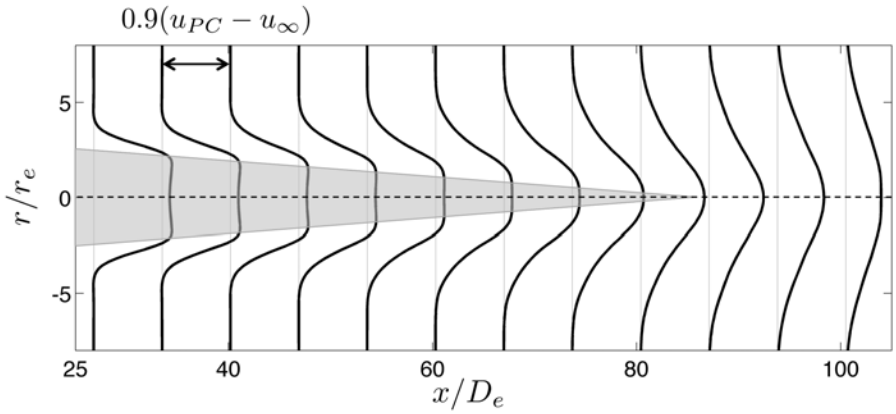

Figure 4.10 – Longitudinal variation of radial profiles of mean axial velocity excess $u_x - u_\infty$ and potential core (in grey).

4.2.4 Potential core and transition region

After the initial expansion of the jet, at $x = 25D_e$, the flow consists of two parts: a potential, inviscid core, where velocity and thermodynamic parameters are uniform, surrounded by a viscous mixing layer. As the eddies in the mixing layer are convected, their size increases which makes the potential core decay until it closes. The effect of coflow on the potential core was assessed in previous studies, mostly in the context of jet aeroacoustics (Morris, 1976; Larson et al., 1978; Sarohia, 1978; André et al., 2013). It was shown that increasing the Mach number of the coflow reduces the shear across the mixing layer, thus delaying the growth rate of the jet instability. As a result, the potential core is elongated and the spreading rate reduced. The next paragraphs analyse the potential core region by focusing on mean radial profiles, the evolution of the shear layer thickness and the radial profiles of Reynolds stresses.

4.2.4.1 Mean flow

Figure 4.10 presents mean radial profiles of axial velocity excess. They are azimuthally and time averaged, and plotted from the beginning of the potential core to a location in the transition region. They evolve from a top-hat shape to a Gaussian shape as the potential core closes (Murakami and Papamoschou, 2002). Two lines passing through the edges of the plateau of each profile highlight the position and extent of the potential core. It can be observed that it varies linearly with the axial distance and closes at about $x = 85D_e$, so its length is about $60D_e$. Other parameters like temperature, density or mass fraction of equivalent gas, follow the same trend, as shown in Figs. 4.11-4.13.

4.2.4.2 Compressibility effect on the thickness of the mixing layer

Previous results about the effect of compressibility on the thickness of the mixing layer (which is related to the potential core length) can be used for comparison with the present jet. In particular, Papamoschou and Roshko (1988) established an expression for the growth rate of a shear layer:

$$\delta' = C\frac{(1-r)(1+\sqrt{s})}{1+r\sqrt{s}}(0.23 + 0.77e^{-3.5M_c^2}) \tag{4.9}$$

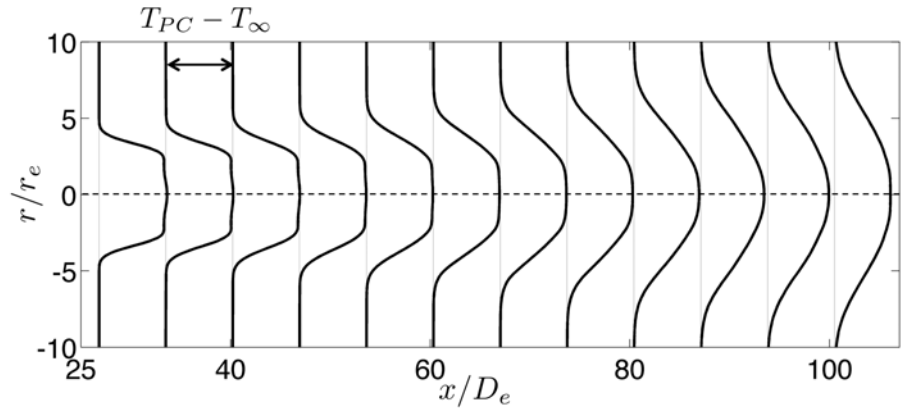

Figure 4.11 – Longitudinal variation of radial profiles of mean axial temperature excess $T - T_\infty$.

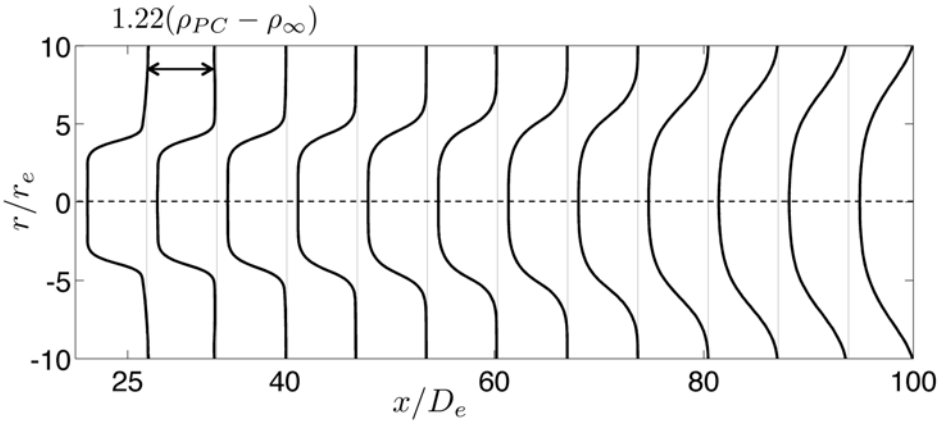

Figure 4.12 – Longitudinal variation of radial profiles of mean axial density deficit $\rho - \rho_\infty$.

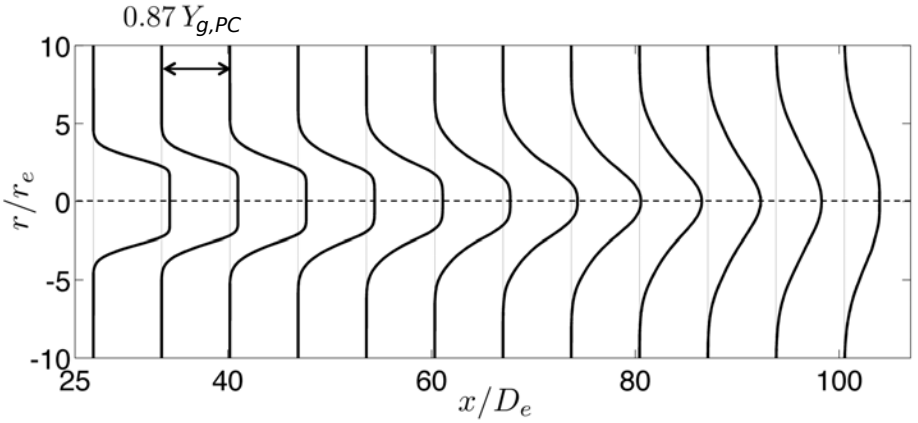

Figure 4.13 – Longitudinal variation of radial profiles of mean axial mass fraction of equivalent gas Y_g.

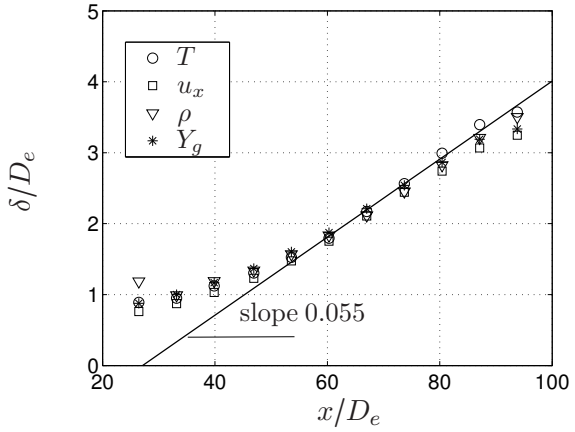

Figure 4.14 – Thickness of the mixing layer δ.

with $r = u_\infty/u_{PC}$, $s = \rho_\infty/\rho_{PC}$, while C is a constant determined by Papamoschou and Roshko (1988) to be $C = 0.14$. M_c is the convective Mach number, defined as:

$$M_c = \frac{u_{PC} - u_\infty}{a_{PC} + a_\infty} \tag{4.10}$$

with a the speed of sound. This relation corresponds to a model of planar shear layer, but it has been demonstrated that it can be applied to three-dimensional jets (Murakami and Papamoschou, 2002). The application of Eq. 4.9 with the parameters of SRM jet gives a growth rate $\delta' = 0.055$. In order to compare this value with the present simulation results, the mixing layer thickness δ was measured from the profiles of mean temperature, axial velocity, density and mass fraction of the equivalent gas. It is defined as the width of the averaged radial profile from 5% to 95% of the difference of the coflow values. Figure 4.14 depicts the evolution of δ along the x-axis, normalized by D_e. From $x = 40D_e$, the different plots of δ follow a quasi linear growth, which is a characteristic of fully turbulent mixing layers (Troutt and McLaughlin, 1982). The growth rate is $\delta' = \mathrm{d}(\delta/D_e)/\mathrm{d}(x/D_e) = 0.055$, which matches nicely the value obtained from Eq. 4.9. This agreement between the simulation results and the relation established by Papamoschou and Roshko (1988) for the growth rate, as well as the linearity of the mixing layer are encouraging for a sound validation of this region of the simulation.

4.2.4.3 Reynolds stresses

Figures 4.15a and 4.15b show the averaged radial profiles of the (resolved) Reynolds stresses (axial and normal Reynolds stress $\sqrt{\overline{u'_x u'_x}}$ and radial normal $\sqrt{\overline{u'_x u'_r}}$) at different locations in the potential core and in the transition region. It can be noticed that for every x location before the potential core closes, the profiles peak all at the same radial distance, $r \approx 3r_e$, which roughly corresponds to the middle of the mixing layer. For the axial normal stress, the peak reaches a maximum at the closure of the core, and is still visible for a short axial distance after, before the profiles become Gaussian. For the radial normal stress, the maximum peak is reached slightly after the potential core closes. Let us precise that the azimuthal normal stress follows a similar trend as the radial normal stress, with similar peak values. Similar behaviors were observed for supersonic jets in the literature (Freund et al., 2000b).

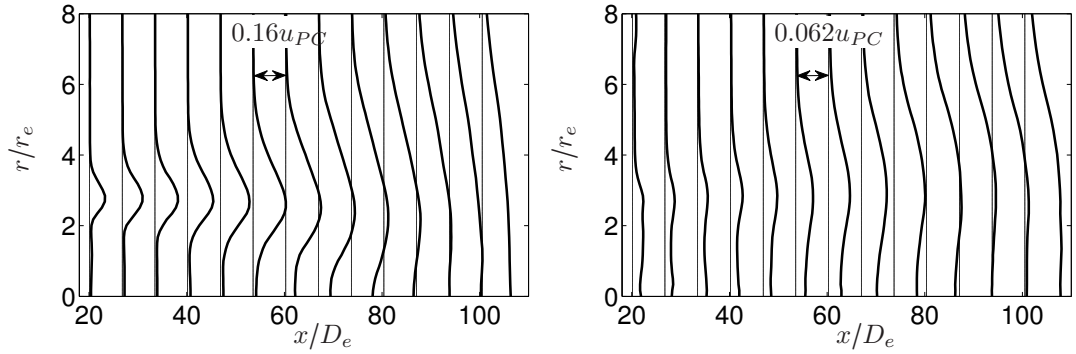

(a) $\sqrt{\overline{u'_x u'_x}}$ (b) $\sqrt{\overline{u'_r u'_r}}$

Figure 4.15 – Longitudinal variation of radial profiles of Reynolds stresses: $\sqrt{\overline{u'_x u'_x}}$ (a) and $\sqrt{\overline{u'_r u'_r}}$ (b).

4.2.5 Self-similar region

After the potential core closure and the development of turbulence scales in the transition region, the jet is expected to become self-similar, as classically known for axisymmetric turbulent free jets (Pope, 2000). Mean centerline and radial profiles are used to assess the location of self-similarity for the mean and turbulent flows. The analysis also focuses on the characterization of centerline velocity, spreading rate and amplitudes of Reynolds stresses, with the objective to compare the results with previous jets. Finally, turbulence length and time scales are studied by means of two-point correlations.

4.2.5.1 Self-similarity of mean flow

In the self-similar region of a jet, the mean flow is characterized by the centerline velocity and by the spreading rate. For an incompressible free turbulent jet without coflow, the inverse of mean axial centerline velocity increases linearly with longitudinal distance (Pope, 2000). The conservation of momentum flow rate entails that the jet spreads linearly. This scaling differs in the presence of a coflow. For incompressible coflowing jet, it was observed that the centerline velocity excess decays as $x^{-2/3}$ in the far field and the jet width scales with $x^{1/3}$ (Nickels and Perry, 1996; Saudreau et al., 2004). In the present simulation, the density is not constant, as visible in Fig. 4.17. In order to account for this variation, the longitudinal variation of $\rho(u_x - u_\infty)$ is considered rather than the excess velocity alone. Figure 4.16a shows that $\rho(u_x - u_\infty)$ scales with $x^{-0.77}$ in the far field. This is close to the scaling in $x^{-2/3}$ observed for incompressible coflowing jets (Nickels and Perry, 1996). Furthermore, the conservation of momentum flow rate dictates that the jet width has to increase as $x^{1/3}$ (see Appendix B for details of the analysis). Figure 4.16b shows the longitudinal evolution of the jet half-width $r_{1/2,\rho u_x}$, defined as

$$[\rho(u_x - u_\infty)](x, r_{1/2,\rho u_x}) = \frac{1}{2}[\rho(u_x - u_\infty)](x, r = 0). \tag{4.11}$$

It can be observed that in the far field, $r_{1/2,\rho u_x}$ does scale with $x^{1/3}$, thus verifying the theoretical prediction.

The establishment of self-similarity of the mean flow is confirmed by the observation of mean radial profiles of axial velocity and temperature excess. Figure 4.18a shows the radial profiles of axial velocity excess, azimuthally and time averaged, for different longitudinal

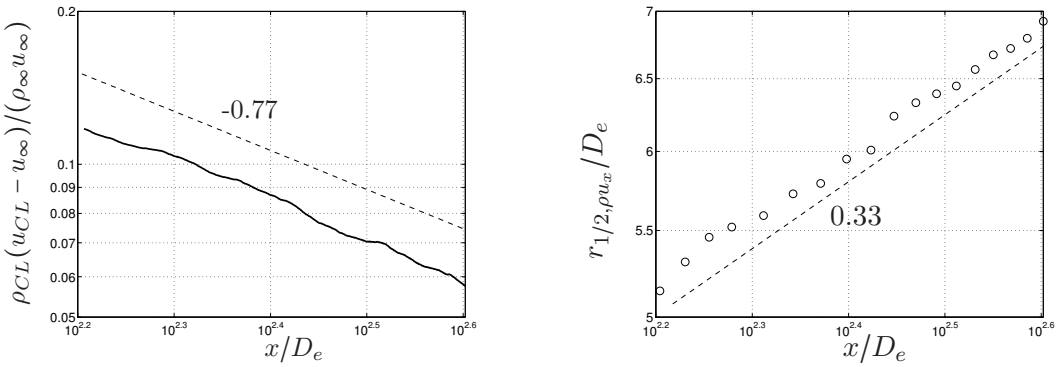

(a) (b)

Figure 4.16 – Longitudinal variation (logarithmic scale) between $160D_e < x < 400D_e$ of: $\rho_{CL}(u_{CL}-u_\infty)/(\rho_\infty u_\infty)$ (a) and $r_{1/2,\rho u_x}/D_e$, half width at half maximum of $\rho(u-u_\infty)$ (b).

locations in the self-similar region. The axial velocity excess $u_x - u_\infty$ is normalized by the centerline axial velocity excess $u_{CL} - u_\infty$. The radial distance r is normalized by the axial velocity half-width of the jet $r_{1/2,u_x}$, defined such that:

$$(u_x - u_\infty)(x, r_{1/2,u_x}) = \frac{1}{2}(u_x - u_\infty)(x, r = 0). \tag{4.12}$$

In Fig. 4.18a, it is clearly visible that the profiles normalized this way fall into a single curve from $x = 180D_e$, following approximately a Gaussian distribution defined as:

$$\frac{u_x - u_\infty}{u_{CL} - u_\infty} = e^{-\ln 2\left(r/r_{1/2,u_x}\right)^2} \tag{4.13}$$

This trend was observed by Yüceil and Ötügen (2002) for experimental supersonic underexpanded jets. The divergence from the Gaussian function for $r > 1.5r_{1/2,u_x}$ can be attributed to the presence of a coflow, as noticed by Nickels and Perry (1996). In Fig. B.1, similar results are found for the mean radial profiles of $\rho(u_x - u_\infty)$, by normalizing the radial distance r by $r_{1/2,\rho u_x}$, defined in Eq. 4.11. The curves seem to fall into a single profile slightly further downstream than for the axial velocity excess, at around $x = 220D_e$. The same approach can be adopted to normalize the radial profiles of mean temperature excess, as shown in Fig. 4.18b. The radial distance is nondimensionalized by $r_{1/2,T}$, which is the temperature half-width of the jet. The radial profiles from $x = 180D_e$ fall into a single curve. This result is similar to what has been observed for compressible jets (Yüceil and Ötügen, 2002).

4.2.5.2 Self-similarity of Reynolds stresses

In previous experiments and simulations, it was observed that self-similarity occurs in turbulent flow where the velocity fluctuations $\sqrt{\overline{f'^2}}/(u_{CL}-u_\infty)$ (where $f_1 = u_x$, $f_2 = u_r$ and $f_3 = u_\theta$) become independent of the axial distance (Bogey and Bailly, 2009). The centerline velocity fluctuations along the x-axis and the radial profiles of velocity fluctuations in the far field are presented in Figs. 4.19 and 4.20 respectively. The results for the axial normal stress (Figs. 4.19 and 4.20a) and for the shear stress (Fig. 4.20d) are quite satisfactory, as they display a roughly constant behavior from $x = 220D_e$ (particularly for $r > r_{1/2,u_x}$), which suggests that the turbulent flow becomes self-similar from this location. As for the radial and azimuthal normal stress, Figs. 4.20b) and 4.20c) show that they exhibit

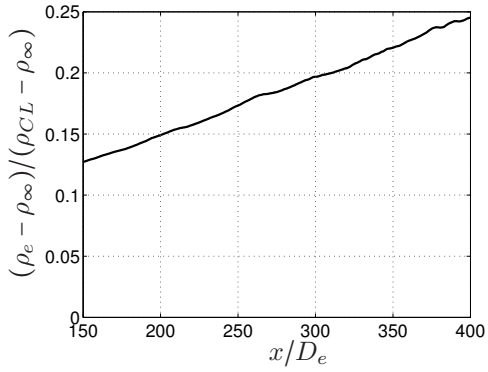

Figure 4.17 – Longitudinal variation of inverse of centerline mean density.

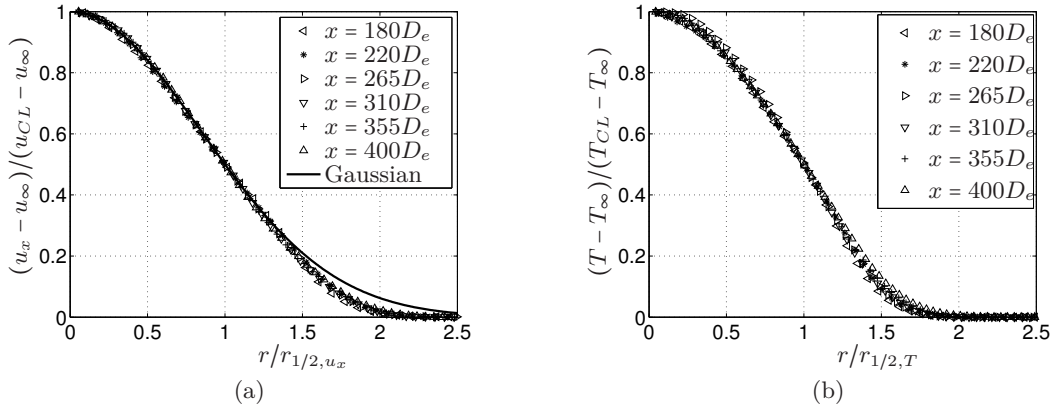

(a) (b)

Figure 4.18 – Longitudinal variation of mean normalized radial profiles of axial velocity excess (a) and temperature excess (b).

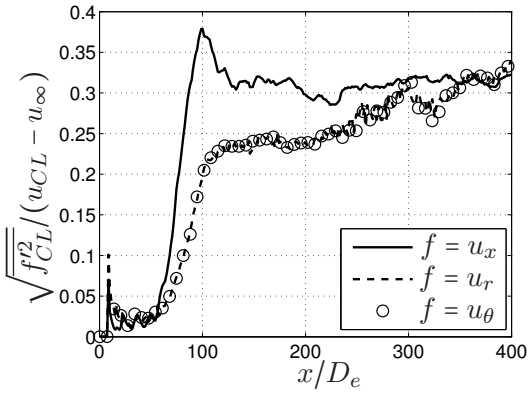

Figure 4.19 – Centerline variation of normal stresses. In order to ensure visibility of the plots, the azimuthal normal stress is plotted with a circle marker every $6.7D_e$.

a constant behavior for $r > r_{1/2,u_x}$, from $x = 220D_e$, but their centerline values keep increasing, as visible in Fig. 4.19. This could be due to insufficient averaging of the data (or the use of cartesian grids for averaging quantities in cylindrical coordinates), or resulting from a compressibility effect or difference of density between the flow and the coflow. However, the experiments of coflowing jets conducted by Antonia and Bilger (1973) also exhibited a tendency of the stresses to increase, even at a far distance where the jet is expected to be self-similar. It is of interest to compare the amplitude of stresses with results from previous results. At $x = 400D_e = 110D_{PC}$, the axial normal stress intensity at the centerline is $I_{u_x} = \sqrt{\overline{u_x'^2}}/(u_{CL} - u_\infty) \approx 0.32$; the maximum shear stress intensity is $I_{u_x u_r} = \sqrt{\overline{u_r' u_x'}}/(u_{CL} - u_\infty) \approx 0.22$, and the ratio of axial normal to radial normal stress intensity $I_{u_x/u_r} = \sqrt{\overline{u_x'^2}/\overline{u_r'^2}} \approx 0.94$. These values agree well with previous experiments of coflowing jets (Nickels and Perry, 1996; Biringen, 1986; Antonia and Bilger, 1973; Saudreau et al., 2004), where I_{u_x} was found to vary between 0.24 and 0.48, $I_{u_x u_r}$ between 0.13 and 0.25, and I_{u_x/u_r} between 1.05 and 1.54.

4.2.5.3 Turbulence length scales and two-point correlations

Two-point space correlations are used to estimate the size of turbulent structures in the longitudinal direction. These parameters will be of great importance in order to set up atmospheric model for a simulation of dissipation of the SRM plume in the atmosphere on larger time and space scales. The longitudinal two-point velocity correlations for the three velocity components are calculated for points located at (x_0, r_0, θ_0) as

$$R^1_{ii}(\delta x) = \frac{\overline{f_i'(x_0, r_0, \theta_0) f_i'(x_0 + \delta x, r_0, \theta_0)}}{\overline{f_i'^2(x_0, r_0, \theta_0)}} \tag{4.14}$$

where δx is the separation distance, and f_1, f_2 and f_3 respectively stand for u_x, u_r and u_θ. One thousand probes were located between $x = 170D_e$ and $x = 400D_e$, at a fixed radial position $r_0 = 11r_e$, where $r_0 = [r_{1/2,u_x}(x = 170D_e) + r_{1/2,u_x}(x = 400D_e)]/2$, and at ten different azimuthal angles θ_0 to get the azimuthal averages. The radial position r_0 is the closest approximation to the middle of the mixing layer (where the fluctuations are expected to be maximum) throughout the axial range of the probe locations. Figure 4.21 shows the plots of R^1_{11}, R^1_{22} and R^1_{33}, evaluated at three longitudinal locations $x_0 = 280D_e$, $334D_e$, and $381D_e$. All plots peak at $\delta x = 0$ and decay to small values around zero, which

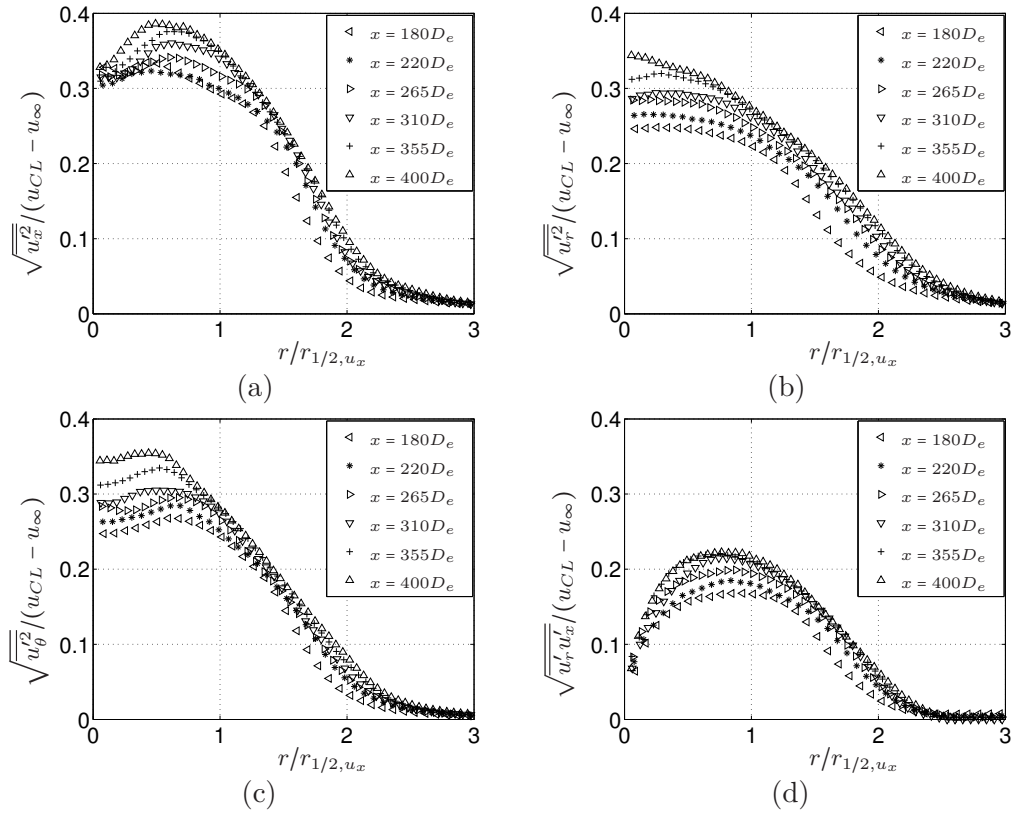

Figure 4.20 – Longitudinal evolution of radial profiles of Reynolds stresses: $\sqrt{\overline{u_x'^2}}/(u_{CL} - u_\infty)$ (a), $\sqrt{\overline{u_r'^2}}/(u_{CL} - u_\infty)$ (b), $\sqrt{\overline{u_\theta'^2}}/(u_{CL} - u_\infty)$ (c) and $\sqrt{\overline{u_r'u_x'}}/(u_{CL} - u_\infty)$ (d).

is characteristic of free-shear turbulent flows. Furthermore, all profiles of R^1_{22} and R^1_{33} are similar and narrower than R^1_{11}, which denotes that the length scales associated to u_r and u_θ in the x direction are smaller than the length scale associated to u_x.

The integral length scales of the velocity components in the x direction are defined as

$$L^1_{ii}(x_0) = \int_0^\infty R^1_{ii}(u)du \tag{4.15}$$

However, in practice, L^1_{ii} can be evaluated by the half width at half maximum of R^1_{ii} (Maidi and Lesieur, 2005; Freund et al., 2000b), in order to avoid the noise due to the low values of correlation and the coarse grid far from the jet centerline:

$$L^1_{ii}(x_0) \approx \frac{1}{2}\left(x_r + x_l\right) \tag{4.16}$$

where x_r and x_l are defined such that $R^1_{ii}(x_r) = 0.5$ and $R^1_{ii}(-x_l) = 0.5$. The longitudinal variation of the turbulence length scales measured at $r = r_0$ (non-dimensioned by D_e) is plotted in Fig. 4.22a. The length scales slightly increase with the axial distance, L^1_{11} being consistently about twice larger than L^1_{22} and L^1_{33}. These last two plots are similar to each other, a feature observed in supersonic jets (Freund et al., 2000b). On the other hand, integral length scales are expected to become self-similar in the far field. Wygnanski and Fiedler (1969) measured the radial profiles of integral length scales, normalized by the jet velocity half-width and proved they were self-similar. Figure 4.22b shows the longitudinal variations of $L^1_{ii}/r_{1/2,u_x}$. The plots are roughly constant, which is in favor of the hypothesis of establishment of self-similarity for the turbulence scales in the present simulations. The averages over the longitudinal range $280 < x/D_e < 390$ give $L^1_{11} = 0.73 r_{1/2,u_x}$ and $L^1_{22} = L^1_{33} = 0.40 r_{1/2,u_x}$. Wygnanski and Fiedler (1969) conducted measurements in the self-similar region of a non-coflowing jet ($\mathrm{Re} \approx 10^5$), which gave $L^1_{11} = 0.75 r_{1/2,u_x}$ at the radial location of maximum turbulence. This value is fairly close to the results of the present study. However, to the best of our knowledge, there is no previous analysis of this sort for compressible coflowing jet.

Finally, following the approach described by Freund et al. (2000a), it is possible to define a axial turbulence time scale of the flow as:

$$T^1_{ii} = \frac{L^1_{ii}}{\sqrt{\overline{f'^2(x)}}} \tag{4.17}$$

where f_1, f_2 and f_3 stand for u_x, u_r and u_θ respectively. Figure 4.23 shows the evolution of these three time scales with axial distance. The plots follow a linear growth, with T^1_{11} being 1.5 larger than T^1_{22} and T^1_{33}. T^1_{11} can be considered as a maximum large-eddy turn-over time. We can compare the total simulation time to T^1_{11} in order to confirm *a posteriori* the statistical convergence of the computations even at the farmost downstream location $x/D_e = 400$, where the simulation time corresponds to 10 large eddy turn-over times (including a spin-up of about one eddy turn-over time that is needed to get convergence of the mean flow).

From these observations, it is possible to conclude that the SRM jet obtained from these simulations presents a self-similar region which appears at $x = 180 D_e$ for the mean flow, and at $x = 220 D_e$ for Reynolds stresses. The decay of centerline velocity excess like $x^{-2/3}$ was found to be coherent with the scaling of the jet width with $x^{1/3}$. Finally, elements in favor of the establishment of self-similarity for the integral length scales of the velocity components in the x direction were given. Integral length scales were used to compute turbulence time scales of the flow, which validate the statistical convergence of the computations.

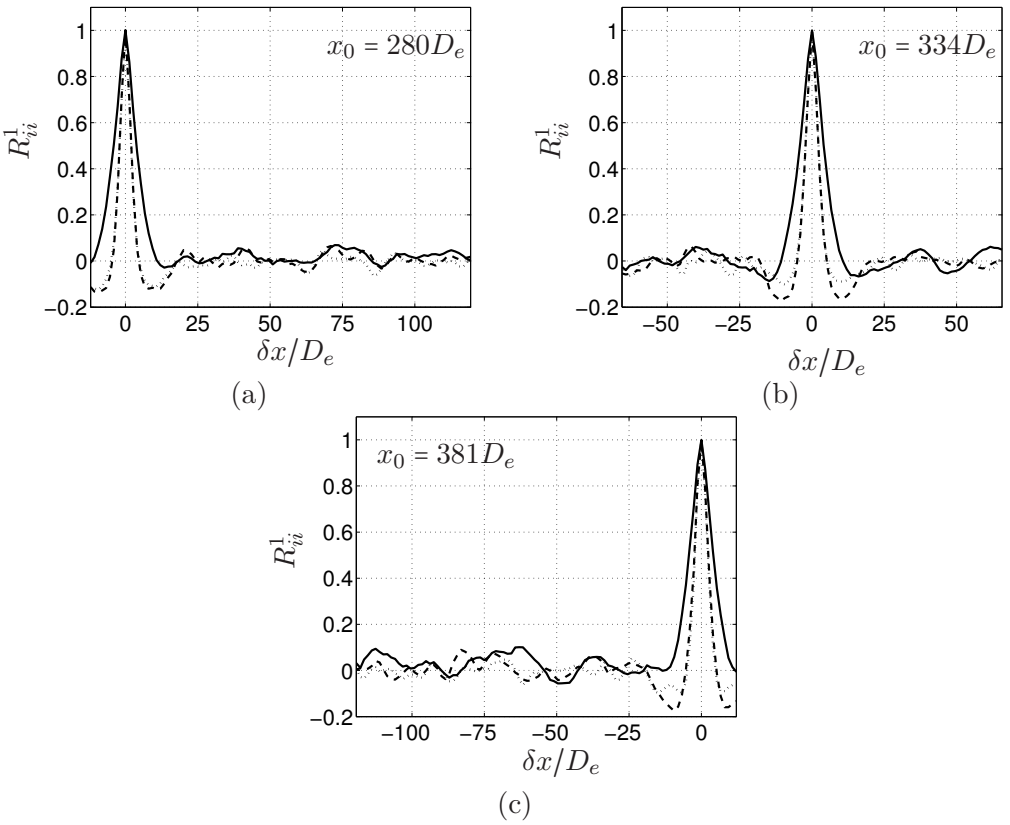

Figure 4.21 – Two-point velocity correlations at $r_0 = 11r_e$ and $x_0 = 280D_e$ (a), $334D_e$ (b) and $381D_e$ (c) ; R^1_{11} (—), R^1_{22} (- - -), R^1_{33} ($\cdots$).

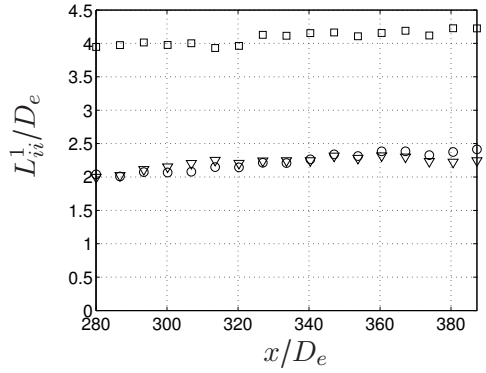

(a)

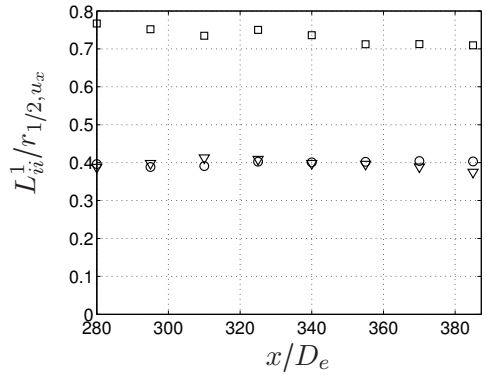

(b)

Figure 4.22 – Turbulence length scales L^1_{ii}/D_e (a) and $L^1_{ii}/r_{1/2,u_x}$ (b) at $r_0 = 11r_e$; L^1_{11} (□), L^1_{22} (∘), L^1_{33} (▽).

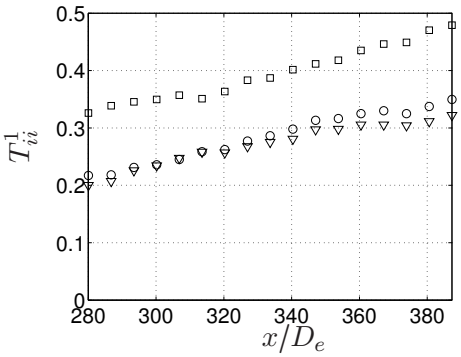

Figure 4.23 – Turbulence time scales (s) at $r_0 = 11r_e$; T^1_{11} (□), T^1_{22} (∘), T^1_{33} (▽).

4.3 Conclusion

The objective of this chapter was to apply and validate a new local-time-stepping method, the MISCOG algorithm, to LES of a SRM exhaust jet. This simulation was achieved using a thermodynamically equivalent gas to model the exhaust gas, as the aim is to validate the resulting jet by analyzing only the flow dynamics.

The application of the MISCOG method made it possible to reduce the computational cost by a factor of 5, and it has been shown that it does not introduce significant error in the vicinity of the coupling zone.

In order to confirm the accuracy of the results, turbulence statistics including mean flow and Reynolds stresses have been analyzed and compared to previous results in literature. Four typical regions of supersonic under-expanded jets were identified. The expansion of the jet occurs through a double set of weak shock waves, one of them occurring in the nozzle. A similar expansion was obtained by Calhoon (1998). This region is followed by a potential core, elongated by the supersonic coflow, where the main features of the flow are in line with experimental studies. In particular, the longitudinal variation of thickness of the mixing layer is consistent with the results of Papamoschou and Roshko (1988). Then a transition zone leads to the self-similar region. For the mean flow, radial profiles of velocity and temperature have shown that self-similarity occurs for $x > 180D_e$. Furthermore, the centerline velocity excess (multiplied by the density) was found to decay as $x^{-2/3}$, and the jet width to increase as $x^{1/3}$. These results are the equivalent to those for incompressible coflowing jets (Nickels and Perry, 1996). As for the turbulent flow, if the radial profiles of Reynolds stresses are less satisfactory (probably due to a lack of averaging), they do suggest a self-similar behavior from $x = 220D_e$. The magnitude of Reynolds stresses are also consistent with previous results for incompressible coflowing jets. Finally, two-point correlations computed in the self-similar region showed that turbulence length scales in the x direction exhibit a behavior comparable to non-coflowing jets. Results also tend to support that the longitudinal turbulence length scales reach self-similarity.

This simulation validates the use of the MISCOG algorithm for LES of SRM exhaust jet. This technique can be applied for LES of the multi-species, reactive SRM exhaust jet.

The work presented in this chapter corresponds to the article "Large-Eddy Simulations of a Single-Species Solid Rocket Booster Jet", published in AIAA Journal.

CHAPTER 5

Laminar diffusion flames

The chemistry occurring in SRM jet should follow the structure of a turbulent jet flame, as already observed by Calhoon (1998). When fuel and oxidizer are not premixed before combustion, as it is the case for SRM jets, this kind of flame enters in the category of diffusion (or non-premixed) flame. This chapter presents the fundamental concepts and definitions related to these flames, before giving the main characteristics of laminar jet diffusion flames. Then the results of a first application of the afterburning chemistry to counterflow flames are detailed, with the objective to investigate the structure of the flame and its variation with flow strain rate.

5.1 Definitions and properties

In diffusion flames, reactions occur only in zones where fuel and oxidizer are mixed adequately (the most favorable conditions being the stoichiometric proportions). As opposite to premixed flames, these flames do not propagate and their position and thickness depend on flow dynamics. In the following developments, a chemistry with a single reaction is considered:

$$\nu_{\mathrm{F}}\mathrm{F} + \nu_{\mathrm{O}}\mathrm{O} \longrightarrow \nu_{\mathrm{P}}\mathrm{P} \tag{5.1}$$

where F, O and P respectively stand for "Fuel", "Oxidizer" and "Product". The following hypotheses, denoted (H), are assumed:

— static pressure is constant
— all species share the same diffusion coefficients D
— all species share the same heat capacities C_p.

5.1.1 Mixture fraction z

The local mixing between fuel and oxidizer is characterised by the mixture fraction z. Under the hypotheses (H), the conservation equations for fuel and oxidizer can be combined (Poinsot and Veynante, 2005) to obtain a single equation without source term, verified by the passive scalar $Z = sY_F - Y_O$, where s is the mass stoichiometric ratio, defined as

$$s = \frac{\nu_O W_O}{\nu_F W_F} = \left(\frac{Y_O}{Y_F}\right)_{st} \tag{5.2}$$

where the subscript "st" stands for stoichiometric conditions. Normalizing Z gives the definition of the mixture fraction z:

$$z = \frac{Z - Z_O}{Z_F - Z_O} = \frac{sY_F - Y_O + Y_O^0}{sY_F^0 + Y_O^0} \tag{5.3}$$

In Eq. (5.3), the superscript ^{0} refers to the injection stream conditions. In the case of a chemistry involving multiple species and reactions, a definition of z based on atoms is preferred (Bilger et al., 1990). The passive scalar for the atom i is written

$$Z_i = W_i \sum_{k=1}^{N} a_{ki} \frac{Y_k}{W_k} \tag{5.4}$$

where a_{ki} is the number of atoms i in the species k. Normalizing Z_i gives the mixture fraction z_i:

$$z_i = \frac{Z_i - Z_i(Y_O^0)}{Z_i(Y_F^0) - Z_i(Y_O^0)} \tag{5.5}$$

Equation (5.3) gives the boundary conditions for z:

— $z = 1$ in the pure fuel stream,

— $z = 0$ in the pure oxidizer stream.

At the stoichiometric point, $sY_F = Y_O$ according to Eq. (5.2), which gives

$$z_{st} = \frac{Y_O^0}{sY_F^0 + Y_O^0} \tag{5.6}$$

In the flow, the flame lies along the stoichiometric line where $z = z_{st}$. For irreversible infinitely fast chemistry, Burke and Schumann (1928) derived the structure of the flame as a function of mixture fraction z, displayed in Fig. 5.1. Fuel and oxidizer cannot coexist, and at $z = z_{st}$, both mass fractions Y_F and Y_O are null. The mixing lines are also represented: they describe how fuel and oxidizer would mix without combustion.

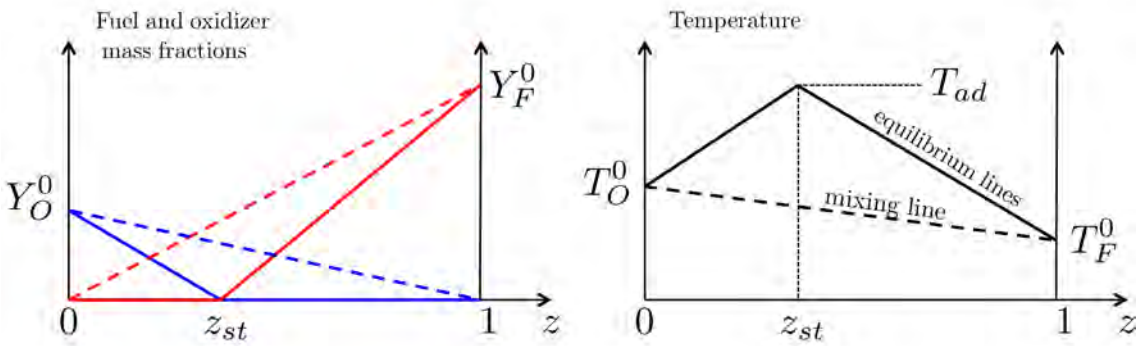

Figure 5.1 – Mass fractions of fuel and oxidizer and temperature as a function of the mixture fraction z for irreversible infinitely fast chemistry and pure mixing. Plain and dashed lines represent respectively equilibrium and mixing lines. Adapted from Poinsot and Veynante (2005).

5.1.2 Scalar dissipation rate χ

If the position of a diffusion flame is controlled by the mixture fraction z, the strength of the combustion is directly determined by the gradients of fuel and oxidizer which feed the

flame from each side of the stoichiometric line. This is evaluated by the scalar dissipation rate χ. Under the assumptions (H), χ is defined as:

$$\chi = 2D|\nabla z|^2 \tag{5.7}$$

where D is the diffusion coefficient. For species with Lewis numbers equal to unity, χ may be evaluated using the heat diffusivity coefficient D_{th}:

$$D_{th} = \frac{\lambda}{\rho C_p} \tag{5.8}$$

where λ denotes the heat diffusion coefficient and C_p the heat capacity at constant pressure. For fast chemistry, the scalar dissipation rate has non-zero values on a very narrow zone around the stoichiometric point. The stoichiometric value of scalar dissipation rate is denoted χ_{st}. Finally, the scalar dissipation rate increases with the strain rate.

5.1.3 Reversible chemistry

Most chemical mechanisms are, in fact, reversible. Even if reactions are infinitely fast, each point in the flame verifies the equilibrium conditions (Poinsot and Veynante, 2005):

$$\frac{Y_F^{\nu_F} Y_O^{\nu_O}}{Y_P^{\nu_P}} = K(T) \tag{5.9}$$

where $K(T)$ is the reaction equilibrium constant at temperature T. In this case, fuel and oxidizer can coexist in the flame, as illustrated in Fig. 5.2.

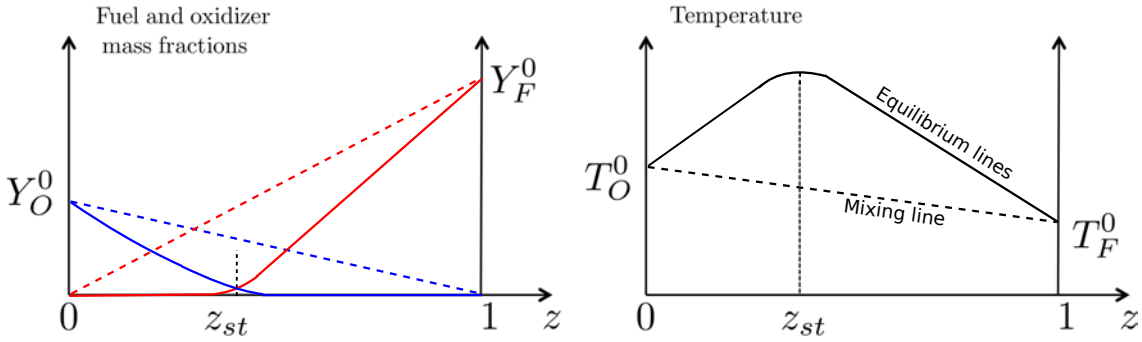

Figure 5.2 – Mass fractions of fuel and oxidizer and temperature as a function of the mixture fraction z for reversible infinitely fast chemistry.

5.1.4 Finite rate chemistry

When combustion is not infinitely fast, the flame results from a competition between flow and chemical time scales. This effect is quantified by the Damköhler number:

$$D_a^{fl} = \frac{\tau_f}{\tau_c} \tag{5.10}$$

where τ_f and τ_c are respectively the flow and chemical time scales. The analysis of the Damköhler number determines the combustion regime. If chemistry is infinitely fast, τ_c is very small and D_a^{fl} takes infinite values: this situation corresponds to Fig. 5.1. For finite

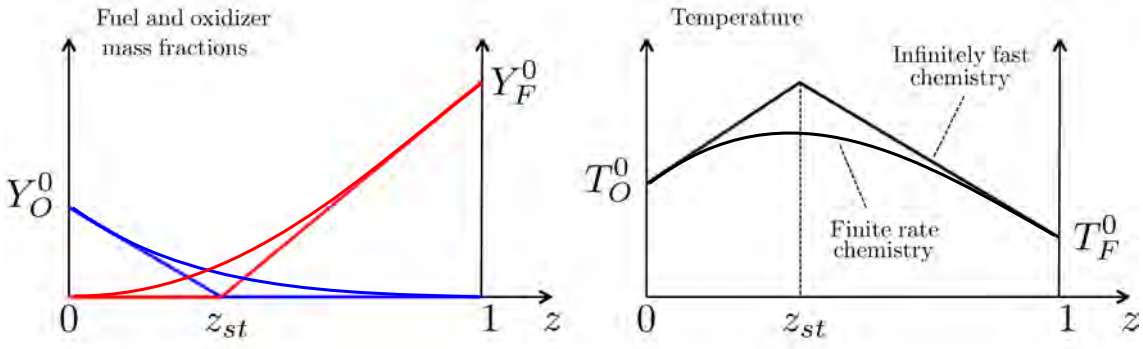

Figure 5.3 – Mass fractions of fuel and oxidizer and temperature as a function of the mixture fraction z for irreversible infinitely fast chemistry and finite rate chemistry.

rate chemistry, D_a^{fl} has finite values. In the region where reactions take place, fuel and oxidizer can coexist as shown in Fig. 5.3. Outside this region, the flame structure remains the same as for infinitely fast chemistry.

As the scalar dissipation rate measures mixture fraction gradients, it can be used to define the flow time scale:

$$\tau_f \approx \chi_{st}^{-1} \tag{5.11}$$

which gives:

$$D_a^{fl} = \frac{1}{\chi_{st}\tau_c} \tag{5.12}$$

Equation (5.12) shows that the Damköhler number is directly related to the scalar dissipation rate, and therefore to strain rate. When the strain rate (or scalar dissipation rate) of the flow increases, τ_f, thus D_a^{fl}, decrease: mixing is enhanced, combustion gets stronger. However, when τ_f gets smaller enough and come close to τ_c, chemistry does not have enough time to consume the reactants which enter the reaction zone and becomes the limiting factor: quenching occurs.

5.1.5 Diffusion flame thickness

Unlike premixed flames, diffusion flames do not have an intrinsic characteristic thickness. However, two length scales, strongly related to flow characteristics, can be defined (Poinsot and Veynante, 2005) (see Fig. 5.4). The diffusion thickness l_d is the thickness of the zone where the mixture fraction varies from 0 to 1. Equation (5.7) gives:

$$\chi_{st} \approx 2D_{st}\left(\frac{\Delta z}{l_d}\right) \tag{5.13}$$

where D_{st} is the value of molecular diffusivity at the stoichiometric surface. As l_d is defined such as $\Delta z = 1$, Eq. (5.13) yields

$$l_d \approx \sqrt{\frac{D_{st}}{\chi_{st}}} \tag{5.14}$$

In Eq. (5.14), a factor $\sqrt{2}$ is missing compared to Eq. (5.7) to ensure consistency with the classical diffusion time relation $\tau_f = l_d^2/D_{st}$, with $\tau_f = 1/\chi_{st}$.

The second length scale is the reaction thickness, which corresponds to the zone where reactions occur. This region lies around the stoichiometric line $z = z_{st}$ (see Fig. 5.4).

According to asymptotic theories (Linan, 1974), l_r can be related to l_d in the case a single reaction like Eq. (5.1):

$$\frac{l_r}{l_d} \approx \left(D_a^{fl}\right)^{-1/\alpha} \tag{5.15}$$

with $\alpha = \nu_F + \nu_O + 1$.

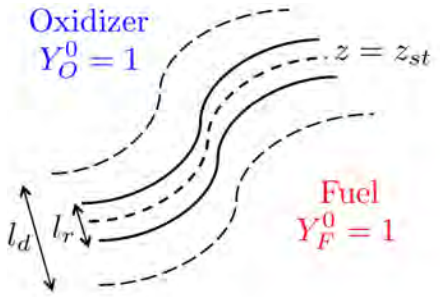

Figure 5.4 – Characteristic length scales for diffusion flames.

5.2 Structure of jet diffusion flames

A jet diffusion flame is formed when a jet of fuel discharges into oxidizer (usually ambient air). In this configuration (see Fig. 5.5), mixing between fuel and oxidizer occurs in a mixing layer which separates two zones: the fuel side (mix of fuel and products) and the oxidizer side (mix of air and products). For hydrocarbon flames, soot is also present: it is formed in the fuel side of the reaction zone, and consumed in the oxidizing region, giving the flame an orange or yellow color.

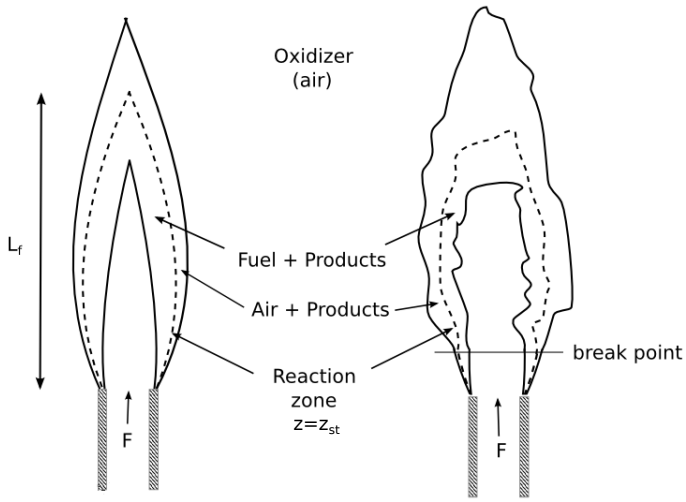

Figure 5.5 – Scheme of an attached laminar (left) and turbulent (right) jet flame.

For fuel jets at high Reynolds number R_e, the flame becomes turbulent beyond a break point, which gets closer to the injector lip when R_e increases. For sufficiently high R_e, the flame is no longer attached and becomes lifted; then it may be extinguished by "blow-off". The flame length L_f is defined as the distance between the injector lip and the intersection between the axis passing by the center of the jet and the stoichiometric line, where $z = z_{st}$

(see Fig. 5.5). It can be measured as a function of R_e, as shown in Fig. 5.6. For laminar flames, molecular diffusivity is fixed: the length flame is proportional to the fuel mass flow rate or R_e. When the flow becomes turbulent, at higher R_e, L_f decreases before reaching a constant value. The length flame is also determined by several parameters (Turns, 1996):

— dynamics properties of oxidizer and fuel streams;
— ambient pressure;
— injector geometry;
— chemistry (the value of z_{st} in particular).

Analytical solutions for L_f can be found in the literature for laminar flames (Spalding, 1979; Lin et al., 1999; Altenkirch et al., 1976; Villermaux and Durox, 1992).

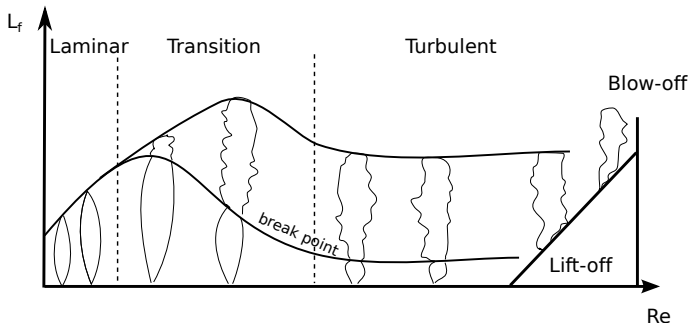

Figure 5.6 – Variation of the jet flame length L_f with the jet Reynolds number R_e (adapted from Hottel and Hawthorne (1949) by Poinsot and Veynante (2005)).

For turbulent flames, the structure of the mixing layer can be locally assimilated to a counterflow flame configuration, with a diffusion flame being formed between fuel and oxidizer streams (see Fig. 5.7). [1] As discussed in Sec. 5.1.4, the flow strain influences the burning rate. Increasing the strain rate will first promote combustion, but at highly strained locations, it may cause flame extinction, resulting in holes in the flame surface (Lyons et al., 2005).

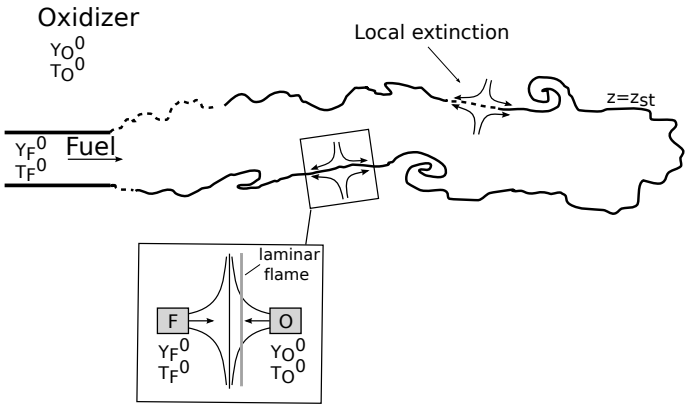

Figure 5.7 – Schematic view of a turbulent diffusion flame (adapted from Sánchez and Williams (2014)).

1. This approximation is valid only in cases of large Damköhler numbers. This idea is the base of flamelet modelling.

5.3 Counterflow flames simulations

A counterflow flame is formed when a jet of fuel (pure or diluted) is opposed to a jet of oxidizer (usually air). This configuration has been largely used in numerical simulations and experiments to investigate the impact of flow strain, pressure, fuel dilution or temperature on diffusion flames stuctures and extinction limits (Balakrishnan et al., 1995; Trees et al., 1995; Brown et al., 1997; Pellett et al., 1998; Pons et al., 2008). As a first application of the afterburning chemistry detailed in Table 3.2, axisymmetric counterflow flames were simulated with the chemical solver Cantera. These simulations give indications of the impact of flow strain rate on the flame structure.

5.3.1 Configuration of the simulations

The configuration of the simulations is showed in Fig. 5.8. A jet, whose chemical composition corresponds to this of the SRM jet at the nozzle exit plan is opposed to a jet of air. The conditions of temperature and pressure approximately reproduce those of the SRM jet mixing layer, at the longitudinal location of the potential core. The fuel temperature, in particular, is fixed at a value T_F close to T_{PC}, the temperature in the SRM jet potential core, with $(T_F - T_\infty)/(T_e - T_\infty) = 0.68$ (T_e is the temperature at the nozzle exit centerline).

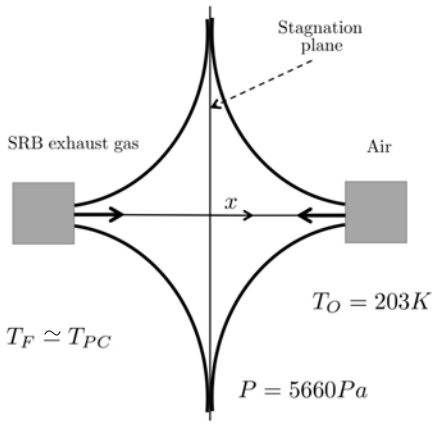

Figure 5.8 – Scheme of the counterflow flame.

5.3.2 Flame structure

Let us consider a counterflow flame with a fixed strain rate of $1.8s^{-1}$ (corresponding to the free-stream value of the strain rate on the air side of counterflow flame). This value is in the range of strain rates which can be measured in the mixing layer of LES of a single-species SRM jet. This is a relatively small value, which is mostly due to the low atmospheric pressure. Figure 5.9 depicts profiles of species mole fractions and temperature along the x-axis. The results are coherent with the structures previously observed for counterflow flames simulations, particularly for H_2-CO flames (Chung and Williams, 1990). In the reaction zone, located around $x = 0.47\ m$, the H_2-O_2 combustion is represented by a production of radicals (peak of X_H) and H_2O, and an increase in temperature. It can be noticed that reactants H_2 and O_2 coexist in the reaction zone, which illustrates a finite-rate chemistry with reversibility effects. The oxidation of CO results in a peak of CO_2 in the reaction zone, and the reactions of HCl with radicals

produce Cl and small fractions of Cl_2. It is interesting to notice that two peaks of Cl_2 are formed, the first one at about the same x location as other peaks of products, and the second on the air-side of the flame. The second peak no longer appears for higher flow strain rates. Finally, it can be noticed that reactions occurs in the fuel side. This can be explained by the presence of radicals in the SRM exhaust, which is enough to trigger reactions considering the high temperature of the fuel stream.

As seen in Sec. 5.1.1, the mixture fraction is an interesting tool to investigate the structure of a diffusion flame. However, for this application, the definition of a mixture fraction is not trivial. Considering that $Le_i \neq 1$ for species i, Eq. (5.5) is technically not a suitable mixture fraction. However, for a lack of better alternative, this definition will still be applied for the present study to draw qualitative results. Three mixture fractions can be defined to characterize the flame structure: z_H, z_C and z_Cl, respectively associated to the elements H, C and Cl. For the atom H, Eqs. (5.4) and (5.5) give

$$Z_H = W_H \left(\frac{2Y_{\mathrm{H_2}}}{W_{\mathrm{H_2}}} + \frac{Y_\mathrm{H}}{W_\mathrm{H}} + \frac{2Y_{\mathrm{H_2O}}}{W_{\mathrm{H_2O}}} + \frac{Y_\mathrm{OH}}{W_\mathrm{OH}} + \frac{2Y_{\mathrm{HO_2}}}{W_{\mathrm{HO_2}}} + \frac{2Y_{\mathrm{H_2O_2}}}{W_{\mathrm{H_2O_2}}} + \frac{Y_\mathrm{HCl}}{W_\mathrm{HCl}} + \frac{Y_\mathrm{HCO}}{W_\mathrm{HCO}} \right) \tag{5.16}$$

$$z_H = \frac{Z_H - 0}{Z_H(Y_F^0) - 0} = \frac{Z_H}{2Y^0_{\mathrm{H_2}} \frac{W_H}{W_{\mathrm{H_2}}} + Y^0_\mathrm{H} + 2Y^0_{\mathrm{H_2O}} \frac{W_H}{W_{\mathrm{H_2O}}} + Y^0_\mathrm{HCl} \frac{W_H}{W_\mathrm{HCl}} + Y^0_\mathrm{OH} \frac{W_H}{W_\mathrm{OH}}} \tag{5.17}$$

where Y_i^0 is the mass fractions of species i at the nozzle exit. Similarly, z_C and z_Cl are given by

$$z_C = \frac{Y_\mathrm{CO}/W_\mathrm{CO} + Y_{\mathrm{CO_2}}/W_{\mathrm{CO_2}} + Y_\mathrm{HCO}/W_\mathrm{HCO}}{Y^0_\mathrm{CO}/W_\mathrm{CO} + Y^0_{\mathrm{CO_2}}/W_{\mathrm{CO_2}}} \tag{5.18}$$

$$z_\mathrm{Cl} = \frac{Y_\mathrm{HCl}/W_\mathrm{HCl} + Y_\mathrm{Cl}/W_\mathrm{Cl} + 2Y_{\mathrm{Cl_2}}/W_{\mathrm{Cl_2}}}{Y^0_\mathrm{HCl}/W_\mathrm{HCl} + Y^0_\mathrm{Cl}/W_\mathrm{Cl} + 2Y^0_{\mathrm{Cl_2}}/W_{\mathrm{Cl_2}}} \tag{5.19}$$

$$\tag{5.20}$$

Because full transport is used in Cantera to solve these counterflow flames, the mixture fractions z_H, z_C and z_Cl are not equal, as illustrated by Fig. 5.10. However, z_C and z_Cl are very close, which shows that differential diffusion has a limited effect for species containing elements C and Cl.

Figures 5.11 and 5.12 present three z-diagrams depicting the variations of species mass fraction with their corresponding mixture fraction. They all show reversible finite rate chemistries. Figure 5.11 shows the z_H-diagrams for species and temperature. They illustrate the H_2-O_2 combustion, with a structure similar to this of Fig. 5.3 (for the case of finite rate chemistry). The stoichiometric mixture fraction approximately corresponds to the peaks of product H_2O and temperature, and is $z_{st,H} \approx 0.56$ (position of the peak of H_2O in Fig. 5.11). This high value means the flame lies on the fuel side. The distinctive fuel-side curvature, visible for instance for the plot of $Y_{\mathrm{H_2O}}$, is certainly introduced by differential diffusion, as already seen in Chung and Williams (1990).

The z_C-diagram (Fig. 5.12) represents the oxidation of CO. An approximative value for $z_{st,C}$ can be given, corresponding to the peak of mass fraction of CO_2: $z_{st,C} \approx 0.36$. Finally, the distribution of chlorine species is visible in the z_Cl-diagram (Fig. 5.12). A mixing line for the species HCl was added to the diagram: the mass fraction of HCl stays very close to this line, which illustrates the reversible character of this submechanism. The position of the peak of Cl gives a pseudo stoichiometric mixture fraction: $z_{st,\mathrm{Cl}} \approx 0.30$. The second

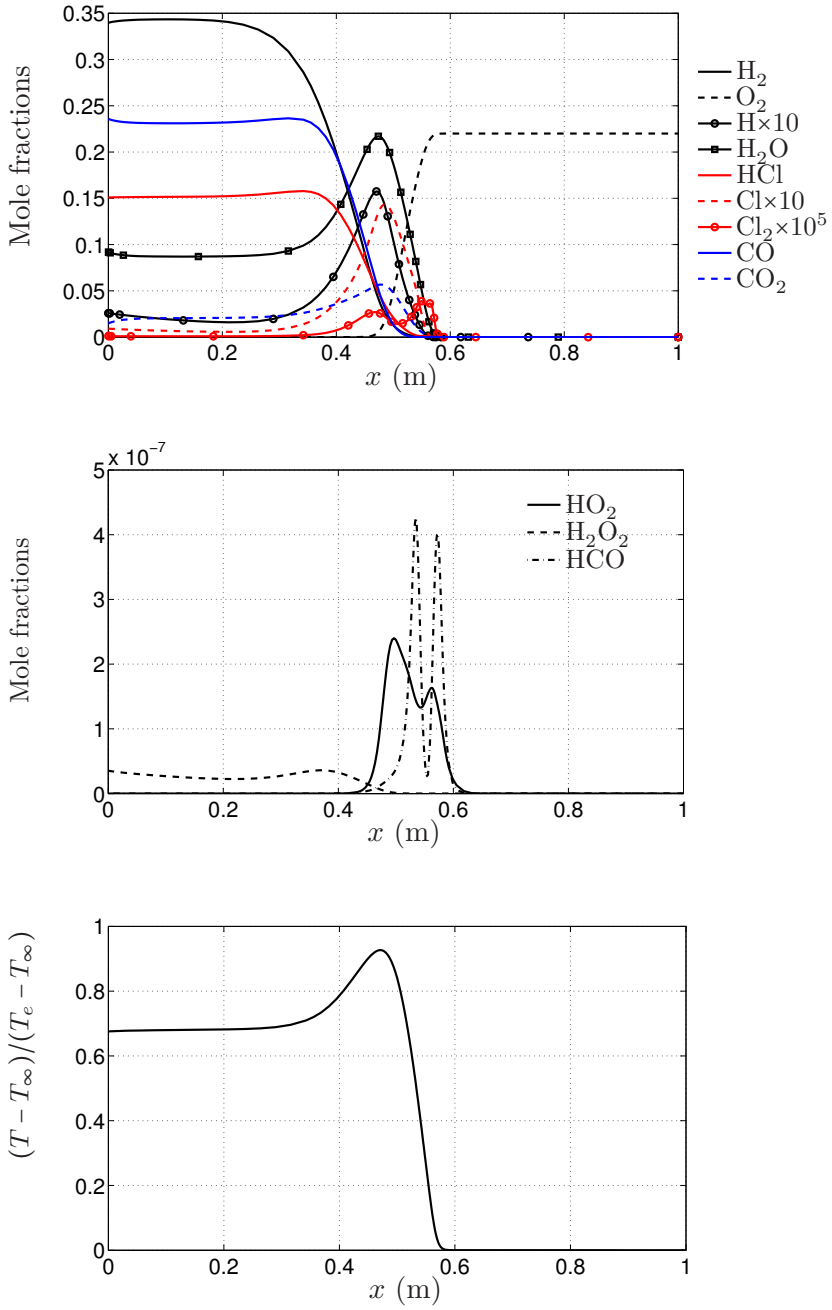

Figure 5.9 – Profile of species mole fractions and temperature across the SRM exhaust gas - air counterflow flame.

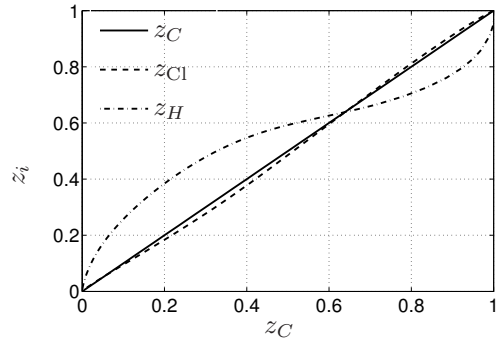

Figure 5.10 – Variation of mixture fractions z_H and z_{Cl} with z_C.

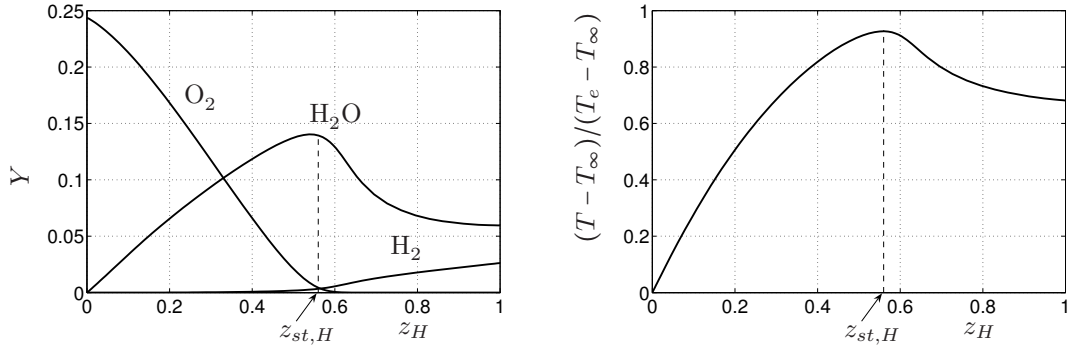

Figure 5.11 – Mass fraction of species H_2, O_2 and H_2O versus mixture fraction z_H.

peak of Cl_2 appears for a low value of z, around 0.023, which indicates it occurs on the air side of the flame. All three values $z_{st,H}$, $z_{st,C}$ and $z_{st,\mathrm{Cl}}$ correspond to three x locations very close to each other in the flame: $x_{st,H}$ = 0.47 m, $x_{st,C}$ = 0.481 m and $x_{st,\mathrm{Cl}}$ = 0.49 m. Considering the uncertainty in the evaluation of the different stoichiometric mixture fractions, $z_{st,H}$ will be used in the following sections only to provide a rough estimation of the location of the flame.

5.3.3 Effect of strain rate

The effect of strain on the flame structure is illustrated by Fig. 5.13, which shows the profiles of temperature and mole fraction of H across the flame for four values of strain rate:

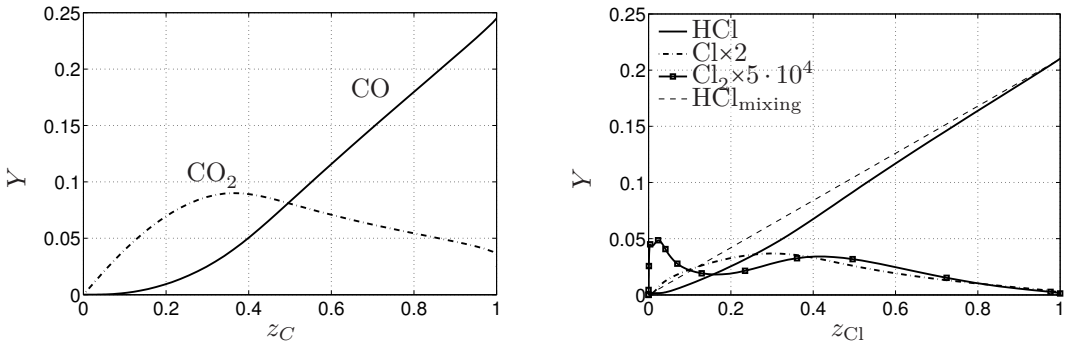

Figure 5.12 – Mass fraction of species versus mixture fraction z_C and z_{Cl}.

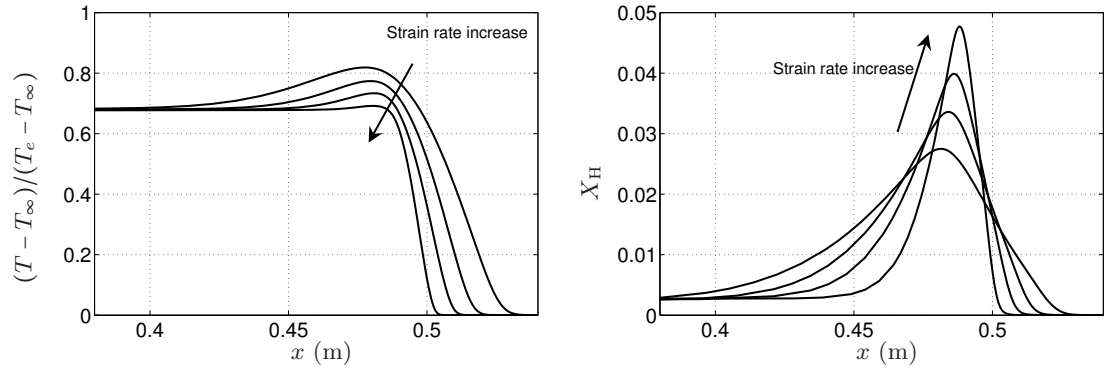

Figure 5.13 – Variations of T and mole fraction of H along x when the strain rate increases.

8.7, 17.3, 34.5 and 88.6 s^{-1}. When the strain rate increases, the reaction zone gets thinner and the maximum temperature decreases, as previously observed for H_2-O_2 chemistry, for instance in Sánchez and Williams (2014). These trends are confirmed by the plots in Fig. 5.14, showing the variation of the maximum temperature and mole fractions of H_2O, CO_2, Cl and H with the strain rate A. When the strain rate increases, the maximum value of X_{H_2O} decreases (a trend already observed for H_2-O_2 chemistry by Wehrleyer et al. (1996)), while $X_{CO_2,max}$ and $X_{Cl,max}$ increases. For values of A sufficiently high, chemistry is not enhanced anymore and quenching occurs. The maximum temperature does not exceed this of the fuel stream, and the maximum mole fraction of all products decreases with A.

Finally, the impact of strain rate on the integrated reaction rates of H_2 and CO, denoted respectively $\left|\dot{\Omega}_{H_2}\right|$ and $\left|\dot{\Omega}_{CO}\right|$, is shown in Fig. 5.15. The integrated reaction rate per unit flame area of a species k is given by

$$\dot{\Omega}_k = \int_{x_f^-}^{x_f^+} \dot{\omega}_k \mathrm{d}x \tag{5.21}$$

where $\dot{\omega}_k$ is the reaction rate of species k; x_f^- and x_f^+ are points located on each side of the flame front, infinitely close to it. The variations of $\left|\dot{\Omega}_{H_2}\right|$ and $\left|\dot{\Omega}_{CO}\right|$ are plotted against their corresponding stoichiometric scalar dissipation rate, respectively $\chi_{st,H}$ and $\chi_{st,C}$, which are written, according to Eq. (5.7), [2]

$$\chi_{st,i} = 2D_{th,st,i}|\nabla z|^2_{st,i} \tag{5.22}$$

where $D_{th,st,i}$ is the value of the diffusion coefficient defined in Eq. (5.8) for $z = z_{st,i}$. Figure 5.15 shows that both integrated reaction rate increase with $\chi_{st,i}$, following the relation

$$\left|\dot{\Omega}_i\right| \propto \sqrt{\chi_{st,i}} \tag{5.23}$$

This relation has been observed in previous simulations and can be easily derived analytically for counterflow flames verifying hypotheses (H), with constant density and flow strain (Poinsot and Veynante, 2005). However, for sufficiently high $\chi_{st,i}$, quenching occurs and Eq. (5.23) is no longer verified.

2. This definition is only valid when hypotheses (H) are verified, which is not the case for these simulations. However, it can still provide an order of magnitude for χ_{st} and can be applied to LES results to allow comparison.

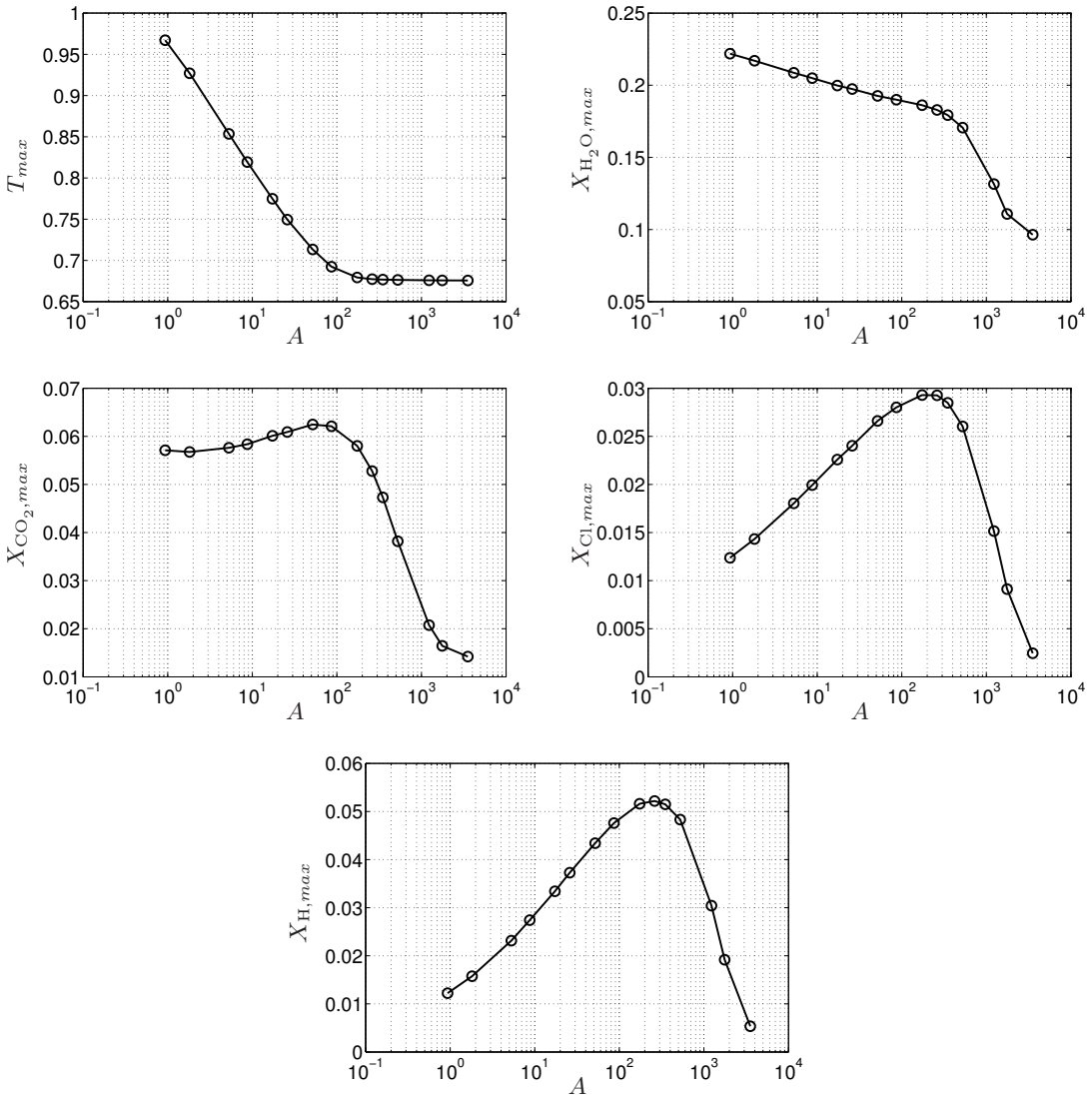

Figure 5.14 – Variations of the maximum temperature and mole fractions of H_2O, CO_2, Cl and H in the counterflow flame with flow strain rate A (1/s).

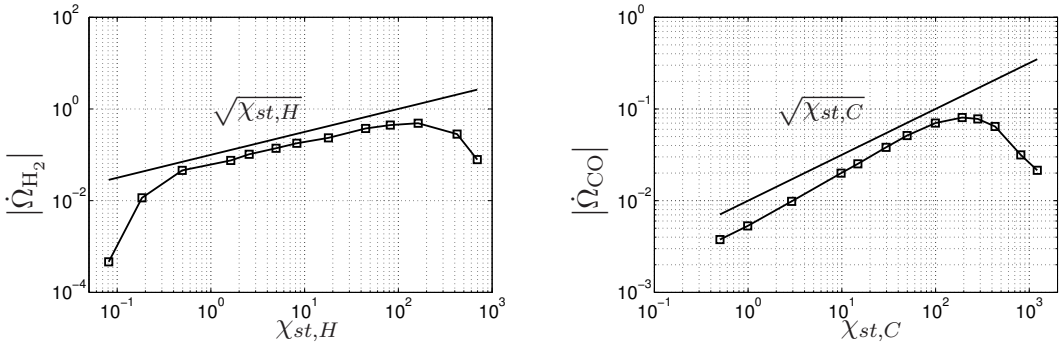

Figure 5.15 – Variations of integrated reaction rate $\left|\dot{\Omega}_{\mathrm{H}_2}\right|$ (mol/s) with $\chi_{st,H}$ (1/s) and $\left|\dot{\Omega}_{\mathrm{CO}}\right|$ (mol/s) with strain rate $\chi_{st,C}$ (1/s).

5.3.4 Effect of the SRM jet thermodynamics properties

The thermodynamics properties of the SRM jet at 20 km of altitude which are used for these counterflow flames simulations are peculiar: fuels (mainly H_2 and CO) are diluted and preheated, air is very cold, and due to the high altitude, pressure is largely under usual values considered in most previous studies (Pons et al., 2008). Previous work can give indications about the impact of these conditions on the flame structure.

— In Eq. (5.6), diluting fuel is equivalent to decreasing Y_F^0, which increases z_{st}. As a consequence, the flame lies closer to the fuel side. Fuel dilution also leads to a smaller extinction strain rate (verified by Balakrishnan et al. (1995) for H_2-O_2 chemistry).

— For H_2-O_2 diffusion flames, increasing the fuel (or the oxidizer) temperature was found to increase the extinction strain rate (Balakrishnan et al., 1995). This result was verified by counterflow flames simulations, computed at conditions described in Fig. 5.8 but with a lower fuel stream temperature $T_F = 1000K$, for various strain rates. The extinction strain rate obtained was smaller than for higher stream jet temperature.

— The effect of pressure has been studied in previous work on diffusion flames, for instance by Pons et al. (2008). It was found that flame thickness varies like $1/\sqrt{p}$, and that consumption and heat increase linearly with $\sqrt{p}$ (although the study does not cover pressure lower than 1 bar). Furthermore, the extinction strain rate is found to decrease with the pressure. It seems that this effect prevails in the present simulations: the low pressure entails a thicker flame, a lower heat release and fuel reaction rate, and also a lower extinction strain rate. These effects should get enhanced if a higher altitude (therefore lower atmospheric pressure) were considered.

5.4 Conclusion

This section presented theoretical tools for diffusion flames, which will be later used in the analysis of the LES of reactive SRM jet. The effect of strain rate on laminar diffusion flame was explained and illustrated by counterflow flames simulations of the afterburning chemistry: combustion (and production of active chlorine) is enhanced by an increase in strain rate, up to a point for which chemistry becomes too slow and extinction of the flame occurs. This phenomenon is fundamental in turbulent combustion and highlights

the necessity to model correctly the flow strain rate induced by turbulence in order to obtain accurate chemical results.

CHAPTER 6

An off-line model for afterburning chemistry along jet streamlines

Before implementing the afterburning chemistry in LES, it is useful to build a simple model using homogeneous reactors, capable of exploiting the results of the single-species LES to provide a first prediction of the effect of hot-plume chemistry at a negligible computational cost. In the following chapter, this off-line chemical model are described and implemented on a large number of streamlines extracted from LES of the single-species SRM jet, providing a first distribution of chemical species in the jet. The model is used to assess the effect of uncertainties on kinetic rate parameters on the results. Finally, the limits of the model are clearly established.

6.1 Description of the model

The principle of the model consists in applying the chemical mechanism described in Table 3.2 on streamlines obtained from the mean flow corresponding to averaged LES of the single-species SRM jet (see Fig. 6.1). Considering a fluid particle at the nozzle exit, where its chemical composition is known, it is possible to model its evolution while traveling along a streamline by a constant-pressure reactor, which would take into account the thermodynamic properties of the frozen flow (taken from the streamline) as well as the heat release and chemical composition due to afterburning reactions. To describe the

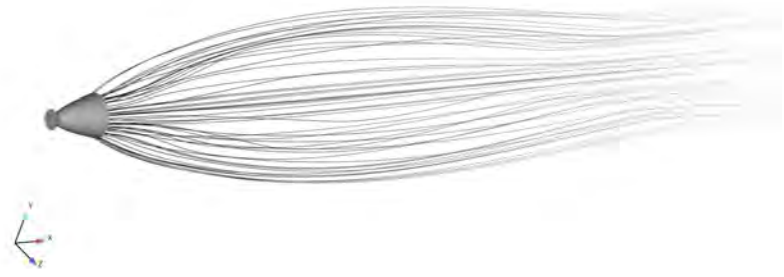

Figure 6.1 – Streamlines originating from the nozzle exit plan, extracted from averaged LES of a single-species SRM jet.

method, let us first consider one streamline, originating from the nozzle exit and crossing the jet passing by the center. This streamline is discretized into $(N+1)$ points, starting from the nozzle exit, at $x = 0$, where the composition of the gas is known, up to the

end of the computational domain, at $x = 400D_e$. The longitudinal location of point k is $x_k = (k-1)\Delta x$, where $k = 1, .., N+1$ and Δx is the distance between two consecutive points. For each point k, the pressure, temperature, velocity and mass fraction of air and equivalent gas are respectively P_k^s, T_k^s, u_k^s, $Y_{a,k}^s$ and $Y_{g,k}^s$ (where the superscript s stands for "streamline"). This discretization is illustrated in Fig. 6.2. Finally, the particle of fluid located at point k at $t = t_k$ travels to point $k+1$ during a period which can be estimated at the second order as

$$\Delta t_k = t_{k+1} - t_k = \frac{2(x_{x+1} - x_k)}{\|u_k^s\| + \|u_{k+1}^s\|} \tag{6.1}$$

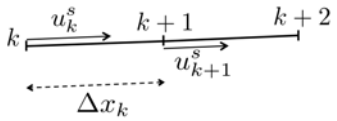

Figure 6.2 – Representation three points k, $k+1$ and $k+2$ along a discretized streamline.

Between point k and $k+1$, the fluid particle undergoes two phenomena:

— the dilution with ambient air

— the hot plume chemistry, driven by the addition of oxidizer O_2 from ambient air which mixes with exhaust species as the plume dilutes in the atmosphere.

To simplify the computations, chemistry and dilution can be decoupled and modelled independently if Δx is taken small enough. For each point k of the streamline, a constant-pressure reactor models the chemistry during Δt_k. The effect of the dilution is then applied on the reactor outputs. This loop of computations is illustrated in Fig. 6.3, and can be formalized as follows:

1. The evolution of the reactor is obtained by solving the following system between $t = t_k$ and $t = t_{k+1}$ [1]:

$$\rho \frac{dY_i}{dt} = W_i \dot{\omega}_i \tag{6.2a}$$

$$\rho C_p \frac{dT}{dt} = -\sum_i h_i W_i \dot{\omega}_i \tag{6.2b}$$

where C_p is the heat capacity at constant pressure of the mixture and h_i the mass enthalpy of species i. Density ρ is linked to the reactor volume V via the relation $\rho = m/V$, where m is the total mass of gas in the reactor (remaining constant when dilution does not occur). The value of density is deduced from the ideal gas law:

$$\rho = \frac{PW}{RT} \tag{6.3}$$

where W is the mean molecular weight of the mixture, given by

$$\frac{1}{W} = \sum_i \frac{Y_i}{W_i} \tag{6.4}$$

1. Eqs. (6.2) are derived in Appendix C.

The initial conditions of the system of equations (6.2a) and (6.2b) for step k are:

$$P[t_k] = P^s_k \tag{6.5a}$$
$$Y_i[t_k] = Y_{i,k} \tag{6.5b}$$
$$T[t_k] = T_k \tag{6.5c}$$
$$V[t_k] = V_k \tag{6.5d}$$

For the first step $k = 1$, a volume $V_1 = 1m^3$ is imposed and $Y_{i,1}$ corresponds to the mass fraction of species i at the nozzle exit. After Δt_k, the resulting temperature, mass fractions and reactor volume are written T^c_{k+1}, $Y^c_{i,k+1}$ and V^c_{k+1} (the superscript c stands for chemistry).

2. The second step consists in applying the dilution operator:

$$T_{k+1} = T^c_{k+1}\frac{T^s_{k+1}}{T^s_k} \tag{6.6a}$$
$$V_{k+1} = V^c_{k+1}\frac{Y^s_{g,k}}{Y^s_{g,k+1}} \tag{6.6b}$$
$$Y_{i,k+1} = Y^c_{i,k+1}\frac{Y^s_{g,k+1}}{Y^s_{g,k}} \quad \text{for } i \neq \mathrm{O_2}, \mathrm{N_2} \tag{6.6c}$$

Note that because the temperature is not uniform at the nozzle exit plane where $Y^s_{g,1} = 1$, the effect of dilution on temperature cannot be computed from Y^s_k. For the species O_2 and N_2, which are both in the plume and in the air, the dilution has to be applied using the following expressions:

$$Y_{i,k+1} = \underbrace{(Y^c_{i,k+1} - Y^\infty_i Y^s_{a,k})\frac{Y^s_{g,k+1}}{Y^s_{g,k}}}_{\text{Dilution of the species of the plume}} + \underbrace{Y^\infty_i Y^s_{a,k}}_{\text{Dilution of the species of the air}} \tag{6.7}$$

where $Y^s_{a,k} = 1 - Y^s_{g,k}$ is the mass fraction of air along the streamline and Y^∞_i is the mass fraction of species $i = \mathrm{O_2}, \mathrm{N_2}$ within air (considered as a constant). After rearrangement, Eq. (6.7) gives

$$Y_{i,k+1} = Y^c_{i,k+1}\frac{Y^s_{g,k+1}}{Y^s_{g,k}} + Y^\infty_i\left(1 - \frac{Y^s_{g,k+1}}{Y^s_{g,k}}\right) \tag{6.8}$$

The error introduced by decoupling chemistry and dilution tends to zero when a small enough spatial step Δx is applied. It was verified that a maximum step $\Delta x = 0.33D_e$ can be used.

6.2 Application to the centerline streamline

This model was implemented using the code Cantera (Goodwin et al., 2013). First it was applied to a centerline streamline originating at the nozzle exit and passing through the center of the jet. This streamline (as well as all streamlines used in the following sections) was extracted from an averaged solution of the LES of a single-species SRM jet described in Chapter 4. A spatial step $\Delta x = 0.33D_e$ was used in the discretization of the streamline. Figure 6.4 shows the resulting mole fractions of the species along the

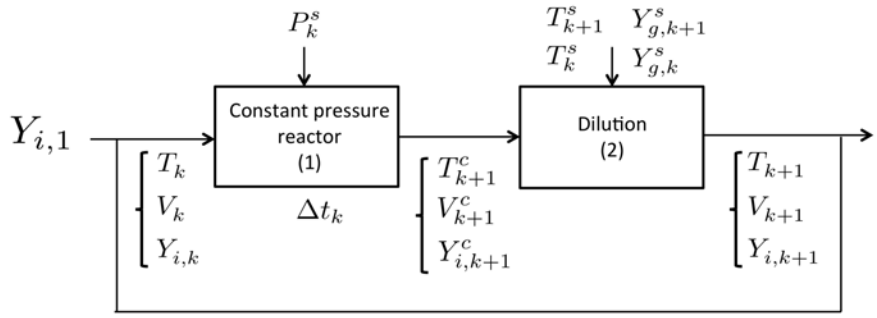

Figure 6.3 – Schematic representation of the off-line chemical model applied on a streamline.

centerline, and Fig. 6.5 the temperature and heat release. The evolution of the mole fraction of Al_2O_3(a) and N_2 is purely driven by dilution of the jet into ambient air. To illustrate this effect, the profile of mass fraction of equivalent gas Y_g^s was added to the graph and scaled to the Al_2O_3(a) profile to show their perfect superposition. This validates the computation of the dilution in the off-line model.

The combustion H_2-O_2 is clearly modelled. There is consumption of H_2 (which is complete) and O_2 and a production of H_2O. Radicals O, H and OH are also produced in the combustion area, between $x = 80D_e$ and $x = 200D_e$. It can be noticed that combustion is initiated at the potential core closure, where the jet starts mixing with air. The oxidation of CO into CO_2 is highlighted by the total consumption of CO and the production of CO_2 (a peak is clearly visible in the combustion zone). Finally, the graph depicting the evolution of mole fractions of HCl, Cl and Cl_2 evidences a partial conversion of HCl into Cl in the combustion area. Downstream of the flame, from $x = 200D_e$, Cl is progressively converted to Cl_2. The absence of Cl_2 upstream is certainly due to the fact that in the presence of radical H, the reaction $H + Cl_2 \longrightarrow HCl + Cl$ (32) prevails over the reaction producing Cl_2 (forward 37 and backward 32). The active chlorine being the species of interest in this study, Fig. 6.4 also shows the mole fractions of each chlorine species in total chlorine. They are defined as follows:

$$X'_{\mathrm{HCl}} = \frac{X_{\mathrm{HCl}}}{X_{\mathrm{HCl}} + X_{\mathrm{Cl}} + 2X_{\mathrm{Cl_2}}} \tag{6.9a}$$

$$X'_{\mathrm{Cl}} = \frac{X_{\mathrm{Cl}}}{X_{\mathrm{HCl}} + X_{\mathrm{Cl}} + 2X_{\mathrm{Cl_2}}} \tag{6.9b}$$

$$X'_{\mathrm{Cl_2}} = \frac{2X_{\mathrm{Cl_2}}}{X_{\mathrm{HCl}} + X_{\mathrm{Cl}} + 2X_{\mathrm{Cl_2}}}. \tag{6.9c}$$

Additionally, the fraction of active chlorine $X'_{\mathrm{Cl}}+X'_{\mathrm{Cl_2}}$ is a clear indication of the conversion of HCl into active chlorine species. From the plots in Fig. 6.4, it can be seen that 26% of Cl is converted back to HCl between $x = 150D_e$ and $x = 250D_e$. The rest of Cl fully is converted to Cl_2, even if the conversion is not complete at $x = 400D_e$. At the extremity of the domain, the fraction of active chlorine is 24%. It should be noticed that the centerline profiles of X'_{HCl}, X'_{Cl}, $X'_{\mathrm{Cl_2}}$ and $X'_{\mathrm{Cl}}+X'_{\mathrm{Cl_2}}$ are very similar to the results obtained by Zittel (1994) and reproduced in Fig. 1.8a. This ensures the coherence of this work with previous studies. The last plot of Fig. 6.4 depicts the evolution of species HO_2, H_2O_2 and HCO. They appear in very small quantities because they are produced and consumed quickly in the flame.

The evolution of the centerline temperature and heat release is plotted in Fig. 6.5. A peak of temperature occurs at $x = 130D_e$, corresponding to the peak of heat release due to exothermic combustion. The decrease in temperature which then occurs is due to the mixing with fresh air, and follows the profile of frozen temperature (directly obtained from the LES results).

6.3 Flow visualisation

This model is computationally cheap and can be easily applied to a large series of streamlines. First, to obtain a 2D longitudinal visualisation of the flow, the chemistry was computed along 500 streamlines originating from the nozzle exit, and all included in the plan $(0, x, y)$. Figures 6.6 and 6.7 represent the resulting temperature and mole fractions of the species H_2, O_2, H_2O, CO, CO_2, HCl, Cl and Cl_2 along the streamlines, as well as the fractions X'_{HCl}, X'_{Cl}, X'_{Cl_2} and $X'_{\mathrm{Cl}} + X'_{\mathrm{Cl}_2}$ (a Delaunay triangulation was applied to smooth the views). These views represent a jet diffusion flame, attached to the nozzle lip. The combustion region can be clearly noticed on the view showing X_{H}, since H is produced only in the combustion zone. The iso-contour $z = z_{st}$ has also been added. Previous works (Calhoon, 1998) have already pointed out such a flame.

These computations confirm the results obtained in Sec. 6.2 with the centerline streamline. In the vicinity of the flame, an increase in temperature and production of H_2O can be noticed. Figure 6.6 also shows the oxidation of CO into CO_2. The partial conversion from HCl to Cl in the flame and the production of Cl_2 downstream from the flame are visible in Fig. 6.7. There is also a slight production of Cl_2 in the mixing layer as suggested by the counterflow flames simulations, which is not visible in Fig. 6.7 due to the large values in the scale used in the legend. Figure 6.8 depicts the variation of mole fraction of Cl_2 along the y-axis at $x = 33D_e$. Dichlore appears to be produced in the mixing layer of the jet, with $X_{\mathrm{Cl}_2,max} = 1.3 \times 10^{-5}$ within the range of radial distance reached by the streamlines.

Figures 6.6, 6.7 and 6.8 reveal that the outer part of the mixing layer (on the air side) does not appear to be completely modelled. Using only streamlines originating from the nozzle exit fails to fully represent the entrainment, i.e. the particles of air which are entrained in the jet.

6.4 Radial scatter plots

To further investigate the afterburning chemistry, the off-line model was applied on 10,000 streamlines originating from the nozzle exit. Figures 6.9-6.13 present scatter plots of temperature and species mole fractions versus the radial distance at four longitudinal positions.

— $x = 33D_e$: location allowing the observation of the reactive mixing layer;
— $x = 125D_e$: location in the flame, around the peak of temperature and products mole fractions;
— $x = 300D_e$: the combustion is over, the fraction of active chlorine is expected not to vary anymore with x;
— $x = 370D_e$: extremity of the domain computed in single-species LES.

First, it can be noticed that the air side of the mixing layer is still incompletely covered by the streamlines (even if results are more satisfying than with the selection of streamlines in Sec. 6.3). Secondly, it appears that the LES results from which the streamlines are

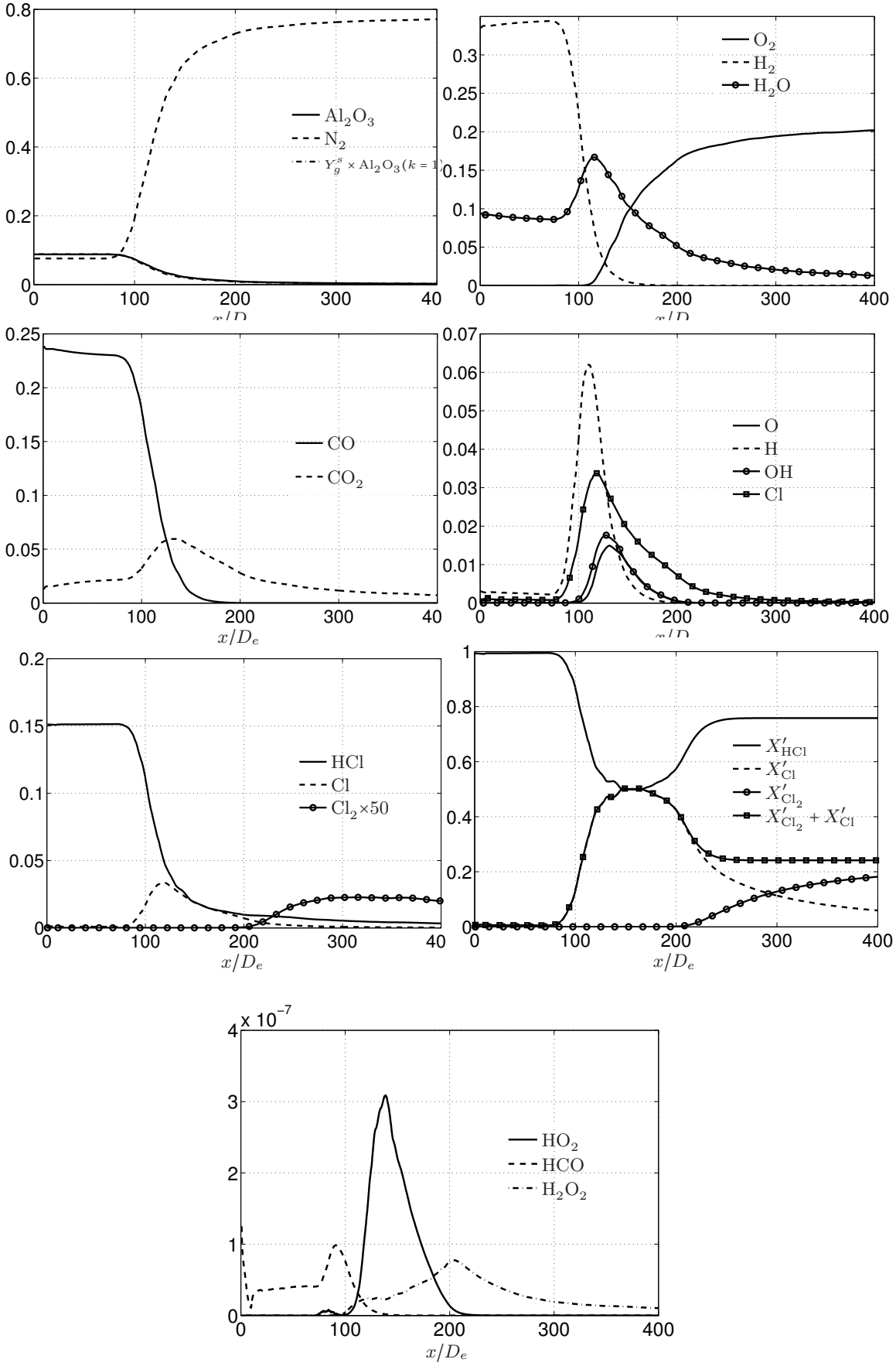

Figure 6.4 – Mole fractions of chemical species along the centerline streamline.

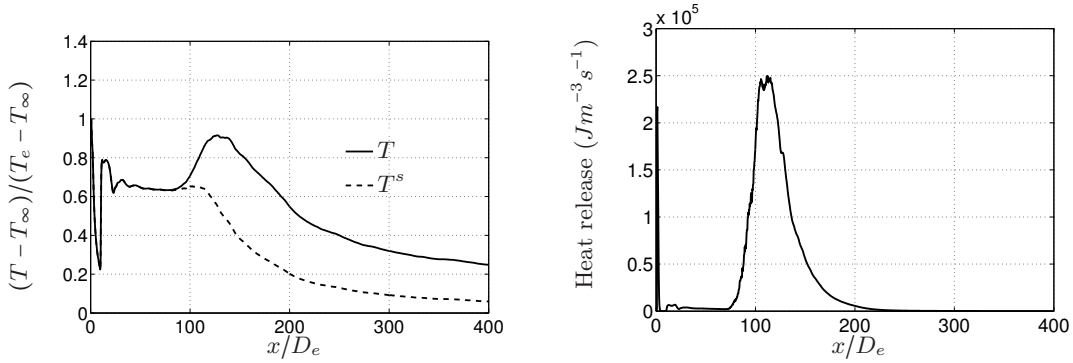

Figure 6.5 – Temperature and heat release along the centerline streamline.

extracted are not sufficiently averaged. This is particularly visible for the longitudinal locations $x = 300D_e$ and $x = 370D_e$, for which the expected Gaussian plots are distorted.

All plots seem coherent with previous simulations in Sec. 6.2 and 6.3. At $x = 33D_e$, Fig. 6.9 shows a distinctive increase in temperature and mole fraction of H_2O in the mixing layer, occurring from $r = 1.7r_e$, compared to the potential core values (at $r = 0$). This indicates the location of combustion, which seems to be limited by H_2, totally consumed from $r = 4r_e$. The oxidation of carbon monoxide CO is also clearly visible, and leads its total consumption, which reaches a quasi null fraction from $r = 4r_e$. Figures 6.11 and 6.12 show the large conversion of HCl to Cl: up to 60% in mole fraction (this maximum could reach a higher value for $r > 4r_e$, where the mixing layer is not crossed by the streamlines). A slight production of Cl_2 is visible around $r = 4r_e$, on the air side of the mixing layer. However, X_{Cl_2} does not decrease on this plot, which indicates that more Cl_2 could be produced for $r > 4r_e$. Furthermore, the maximum values of products are very close to those of the counterflow flame simulation displayed in Fig. 5.9, with a strain rate $A = 1.8s^{-1}$, appart from the presence of higher mole fraction of Cl_2 on the air side which is not modelled by counterflow simulations.

At $x = 125D_e$, the combustion is activated from the center of the jet, up to $r = 7r_e$, where H_2 has been completely consumed. The temperature is increased by 50% at $r = 0$, compared to the non-reactive case. The same observations as for the plots at $x = 33D_e$ can be done, except for a lower conversion from HCl to Cl, reaching a maximum value of 50% (Fig. 6.12). The production of Cl_2 is more visible and reaches up to 35% of the total chlorine.

At $x = 300D_e$ and $x = 370D_e$, the dihydrogen has been totally consumed, the combustion is over. The temperature and mole fractions decrease longitudinally and radially due to mixing with ambient air. The only chemistry going on involves the chlorine species. The profile of X'_{HCl} is quite similar at $x = 300D_e$ and $x = 370D_e$, which indicates that only the conversion from Cl to Cl_2 is active. This conversion is particularly visible in the plots of X'_{Cl} and X'_{Cl_2}. Between $x = 300D_e$ and $x = 370D_e$, the maximum of X'_{Cl} decreases from 12% to 7%. This illustrates that the conversion continues between these positions and even further downstream in the jet, until there is no Cl left. In reality, Cl_2 is rapidly converted back to Cl via photo-dissociation, before reacting with ozone (this phenomenon is not represented here). From $x = 300D_e$, the fraction of active chlorine $X'_{Cl} + X'_{Cl_2}$ varies between 10% and 25% (with a few points above 25%). These fluctuations do not correspond to statistic fluctuations (or root-mean square values), but result from the LES solution used to extract streamlines, which is not averaged on a period of time long enough.

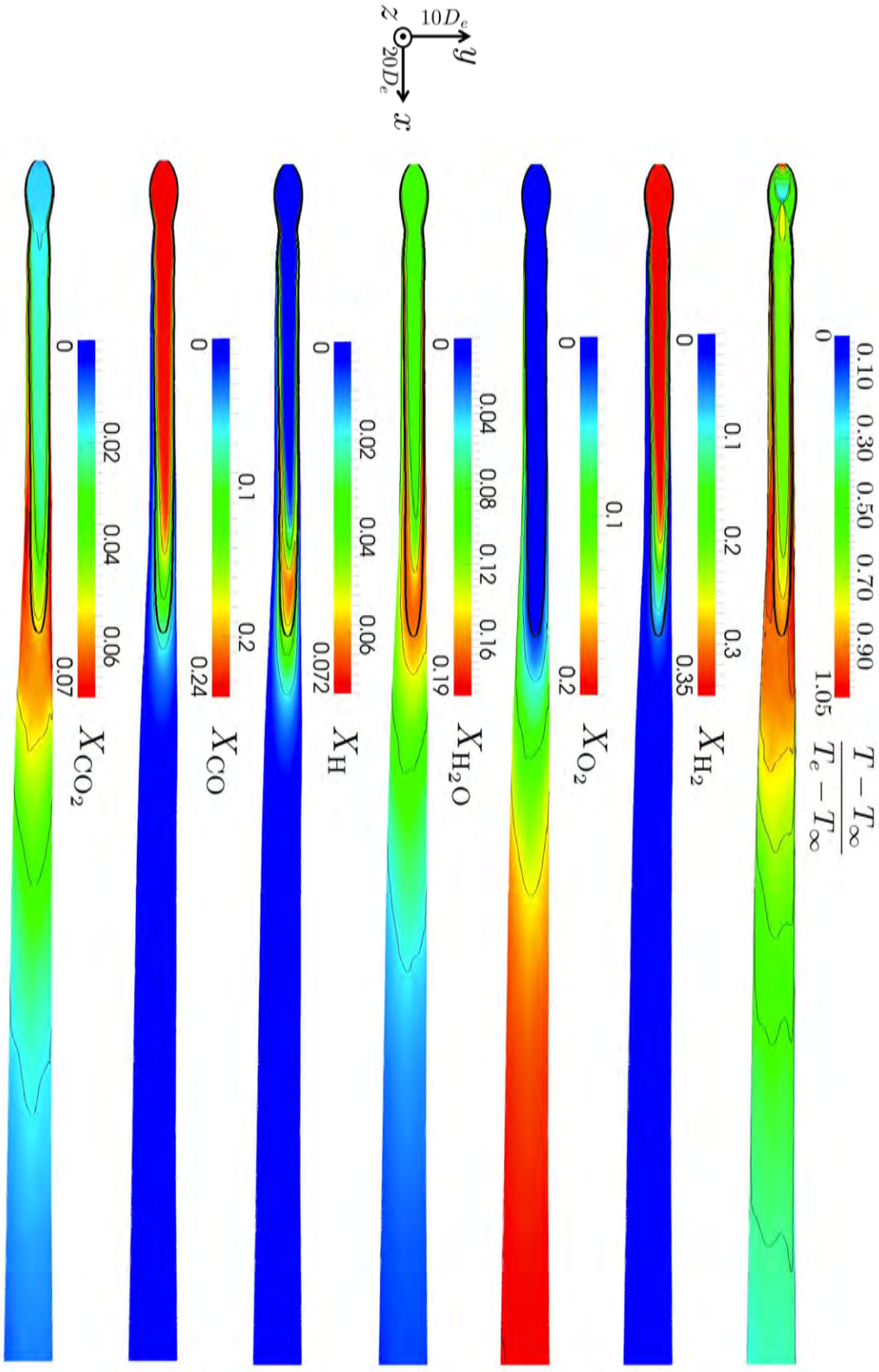

Figure 6.6 – Temperature and mole fractions of species H_2, O_2, H_2O, CO and CO_2 along 500 streamlines in the plan $(0, x, y)$. Iso-contour lines are plotted: 10 lines equally spaced in the range $[T_{min}, T_{max}]$ for the temperature, and 5 lines equally spaced in the range $[X_{i,min}, X_{i,max}]$ for each species i. The jet is represented on a $300D_e$ long domain. The iso-contour $z = z_{st,\mathrm{H}}$ is shown by a bold line.

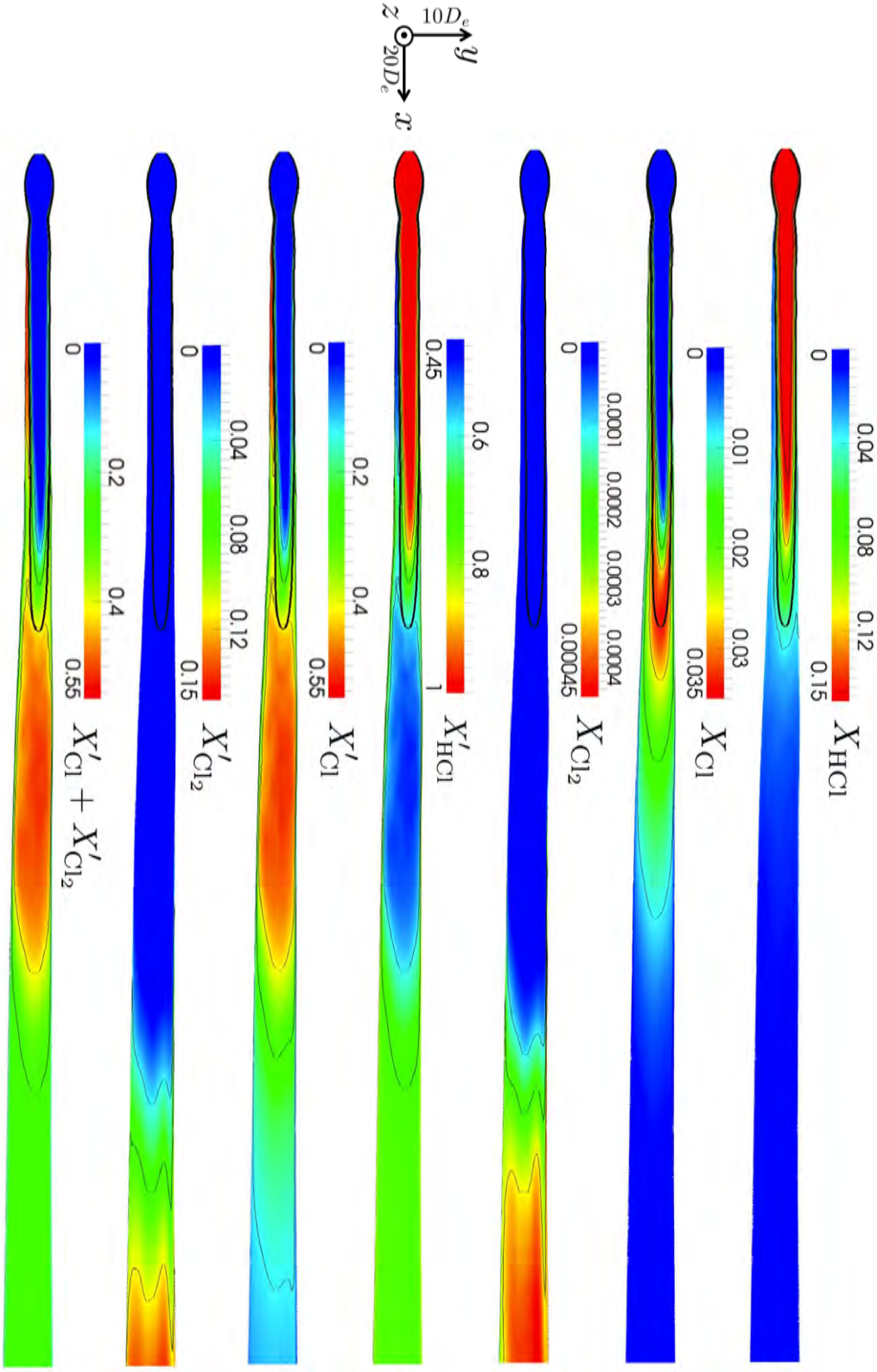

Figure 6.7 – Mole fractions of species HCl, Cl and Cl_2, mole fractions X'_{HCl}, X'_{Cl}, X'_{Cl_2} and $X'_{Cl} + X'_{Cl_2}$ along 500 streamlines in the plan $(0, x, y)$. Iso-contour lines are plotted: 5 lines equally spaced in the range $[X_{i,min}, X_{i,max}]$ for each species i. The jet is represented on a $300D_e$ long domain. The iso-contour $z = z_{st,H}$ is shown by a bold line.

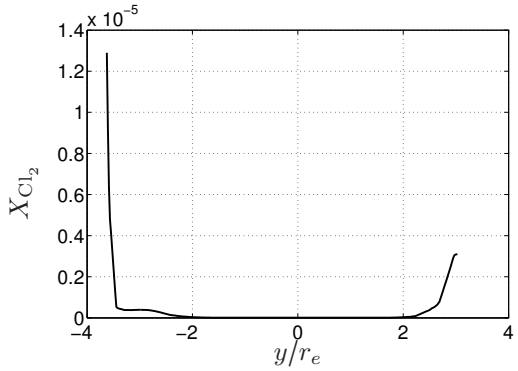

Figure 6.8 – Radial profile of mole fraction of Cl_2 at $x = 30D_e$, obtained from the application of the chemical model on 500 streamlines.

6.5 Uncertainties of this simulation

6.5.1 Uncertainty on reaction rate constants

While almost all rate constants of the reactions of combustion H_2-CO have been estimated recently and quite precisely, those of the reactions involving chlorine species, and in particular the reactions of dissociation of HCl and Cl_2 (no. 36 and 37 in Table 3.2) have uncertainties whose impact on the production of active chlorine may not be negligible (Zittel, 1994). To illustrate this effect, a sensitivity analysis was carried out to determine the consequences of a variation in the rate parameters of reactions 36 and 37 on the fraction of active chlorine. The model described in Sec. 6.1 was applied along the centerline streamline with the parameters A and E varying within the ranges of uncertainty provided by Jensen and Jones (1978). The same tests were also conducted with another set of rate constants (along with their uncertainty ranges) given by Baulch et al. (1981):

$$\begin{aligned} \text{Reac. 36}: &\quad k = 2.6 \times 10^{13} \exp(19751/RT) \quad \text{cm}^6\text{mol}^{-2}\text{s}^{-1} \\ \text{Reac. 37}: &\quad k = 2.23 \times 10^{14} \exp(1800/RT) \quad \text{cm}^6\text{mol}^{-2}\text{s}^{-1}. \end{aligned}$$

Figure 6.14 gives the evolution of the fraction of active chlorine along the streamline in the nominal case (parameters in Table 3.2) and in the cases for which the asymptotic value reaches the minimum and the maximum of all simulations. The value of $X'_{Cl} + X'_{Cl_2}$ at the end of domain ($x = 400D_e$) varies between 15% and 33%. These results are coherent with those of a previous study (Burke and Zittel, 1998). A sensibility study, quite similar to this one, showed that the fraction of active chlorine varies between 23% and 43% in a Titan IV plume at 20 km of altitude. This means that new evaluations of these constants are necessary in order to model chlorine chemistry with more accuracy.

6.5.2 Limitations of the model

Simulations presented in previous sections showed that this model of off-line chemistry along jet streamlines is able to predict all the expected chemical steps of the scheme. However, it has some critical limitations which limits the accuracy of the results.

First, Sec. 6.3 and 6.4 highlighted the difficulty to model correctly the air side of the mixing layer. To improve the results, a possible solution would be to apply the model on streamlines originating from the ambient air along the entire jet.

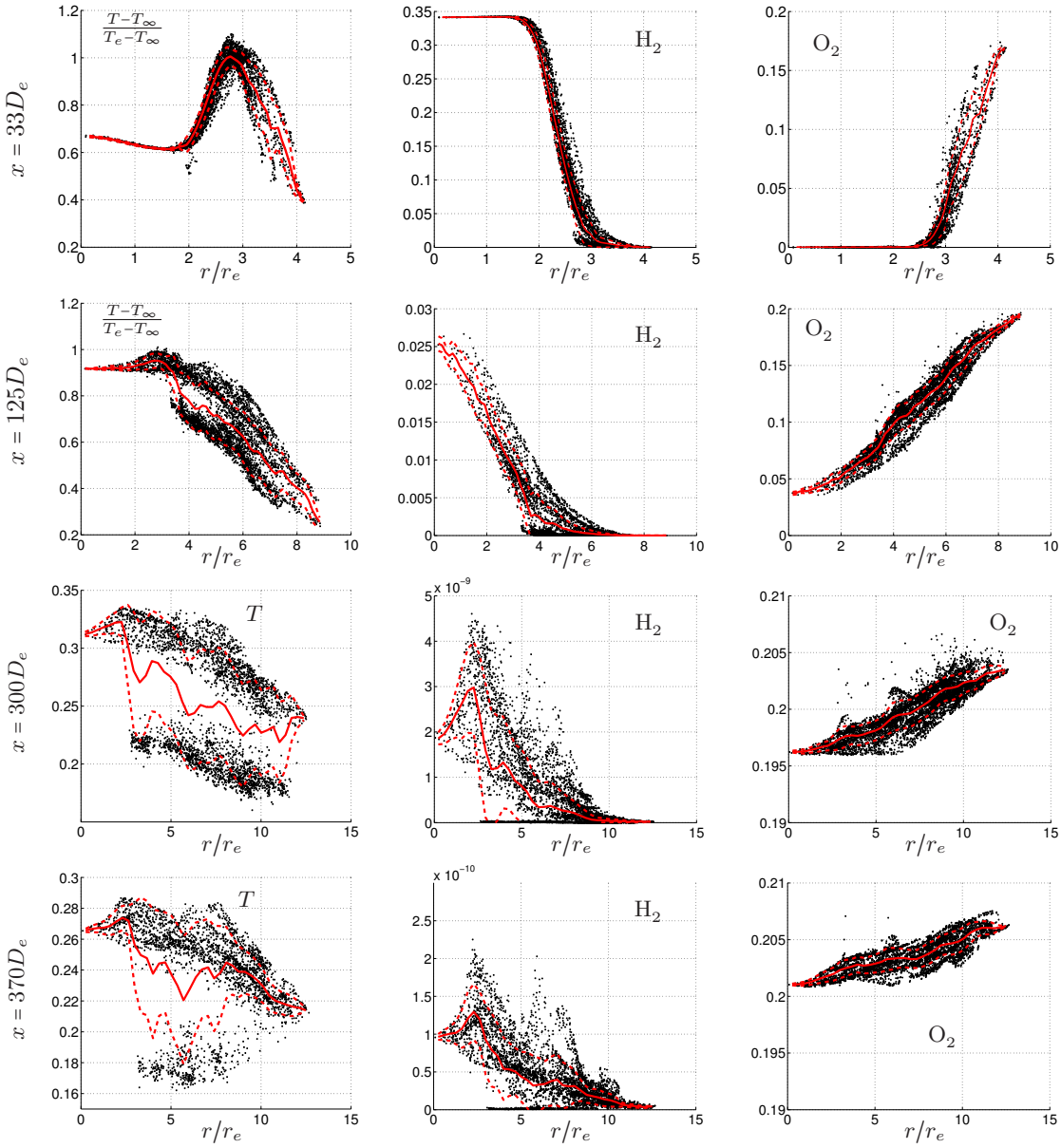

Figure 6.9 – Scatter plots of temperature and mole fractions of species H_2 and O_2 versus radial distance at $x = 33D_e$, $x = 125D_e$, $x = 300D_e$ and $x = 370D_e$. The azimuthal averages of the scatter plots (red solid curves) and the azimuthal averages plus/minus standard deviations (red dashed curve) are also included.

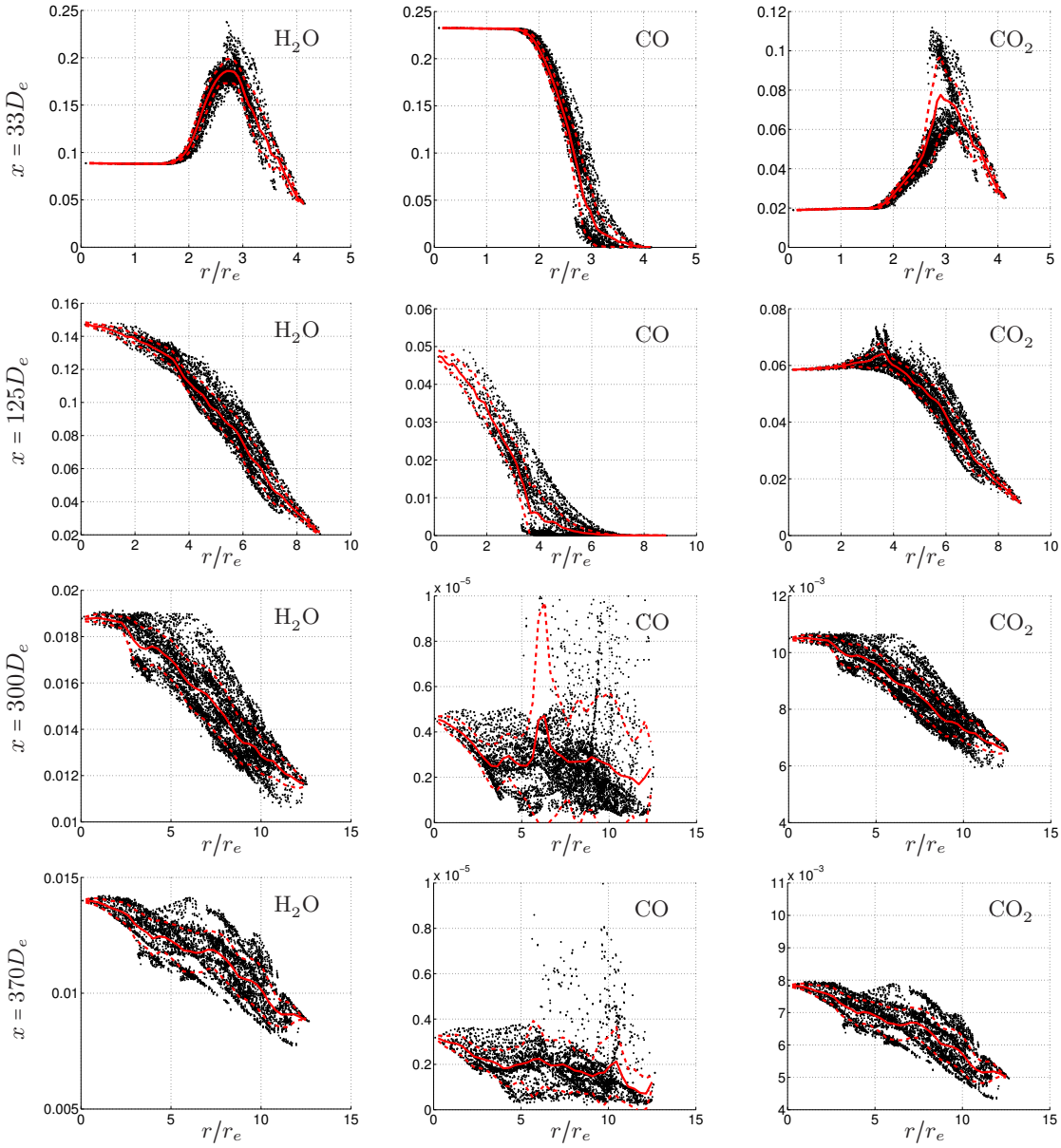

Figure 6.10 – Scatter plots of mole fractions of species H_2O, CO and CO_2 versus radial distance at $x = 33D_e$, $x = 125D_e$, $x = 300D_e$ and $x = 370D_e$. The azimuthal averages of the scatter plots (red solid curves) and the azimuthal averages plus/minus standard deviations (red dashed curve) are also included.

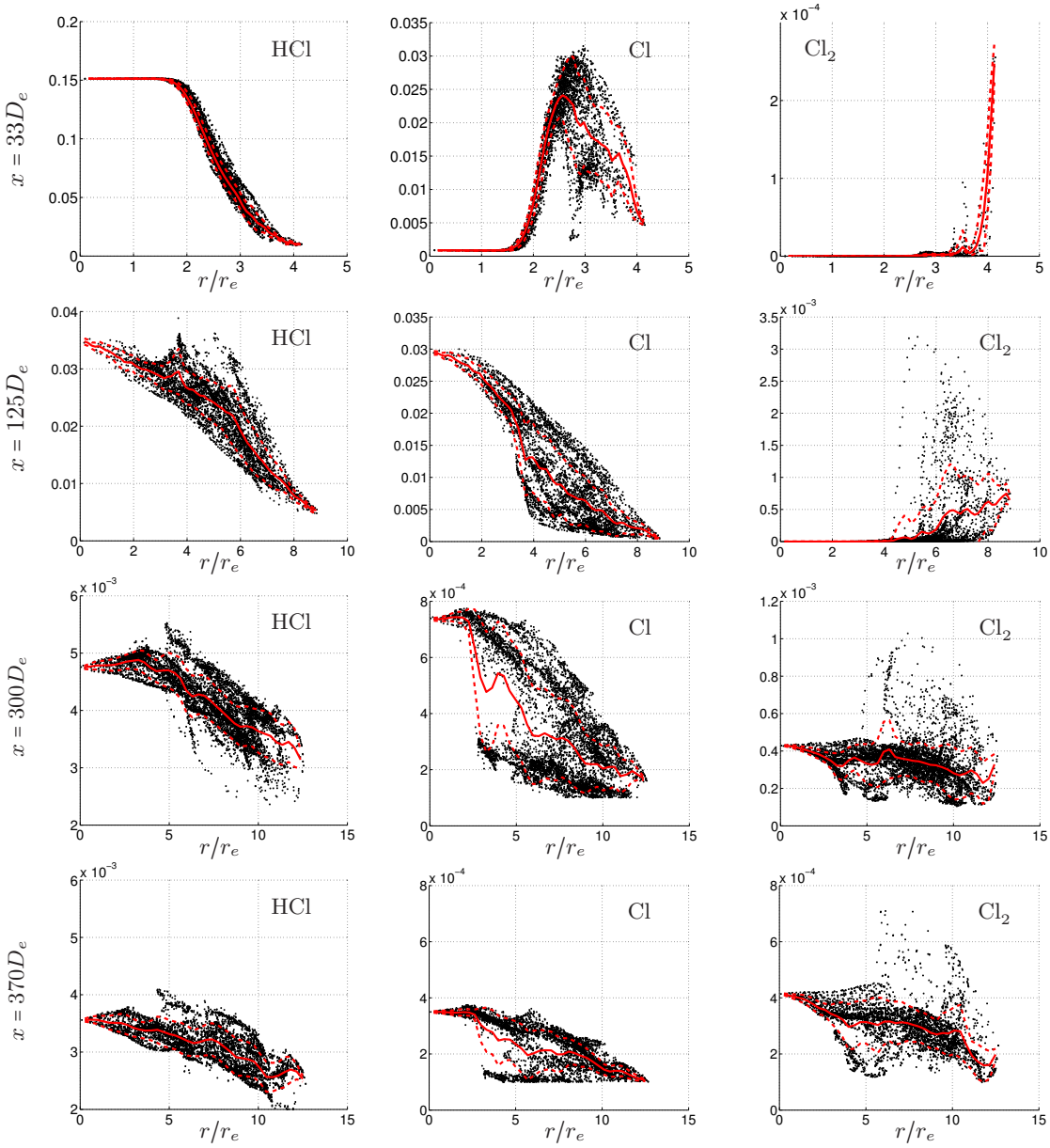

Figure 6.11 – Scatter plots of mole fractions of species HCl, Cl and Cl_2 versus radial distance at $x = 33D_e$, $x = 125D_e$, $x = 300D_e$ and $x = 370D_e$. The azimuthal averages of the scatter plots (red solid curves) and the azimuthal averages plus/minus standard deviations (red dashed curve) are also included.

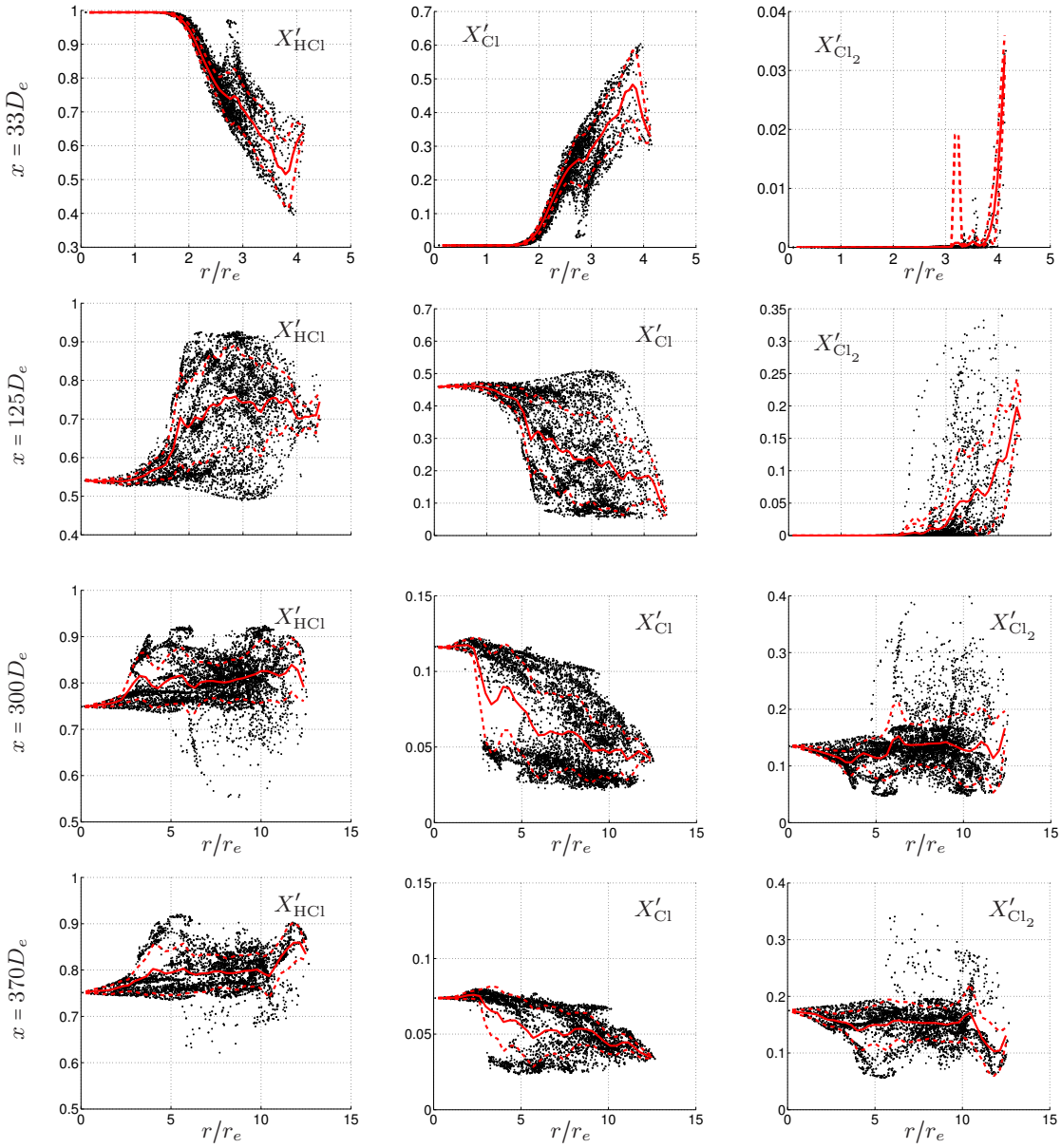

Figure 6.12 – Scatter plots of mole fractions X'_{HCl}, X'_{Cl} and X'_{Cl_2} versus radial distance at $x = 33D_e$, $x = 125D_e$, $x = 300D_e$ and $x = 370D_e$. The azimuthal averages of the scatter plots (red solid curves) and the azimuthal averages plus/minus standard deviations (red dashed curve) are also included.

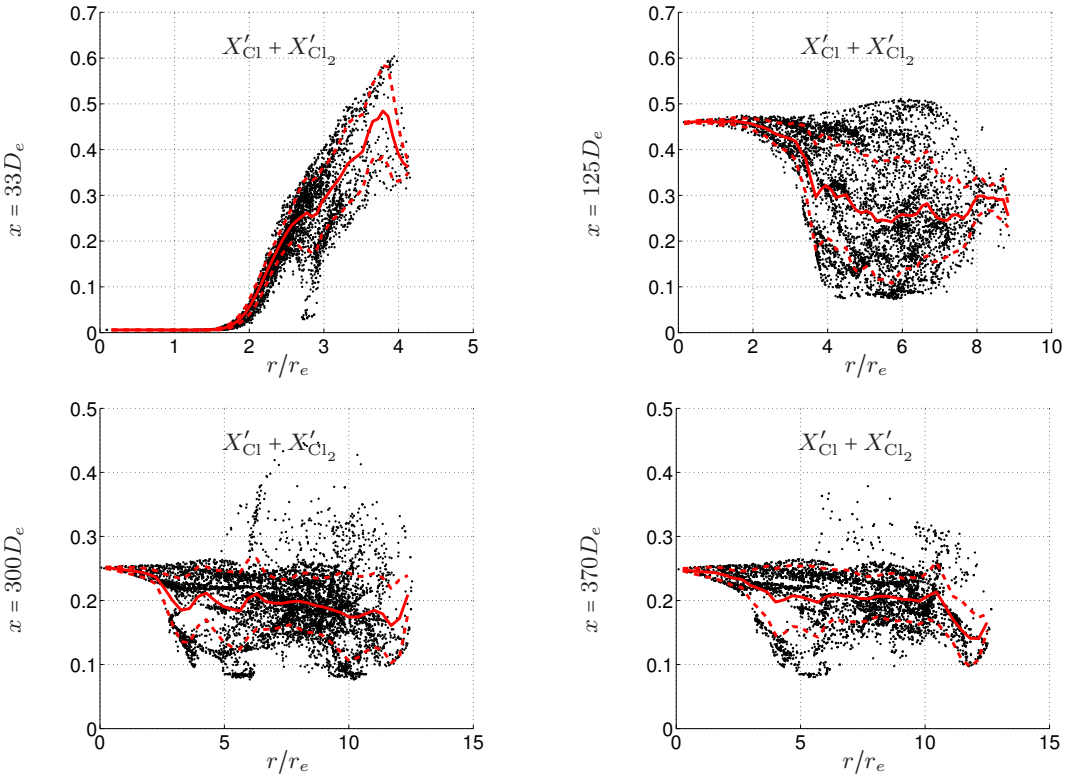

Figure 6.13 – Scatter plots of mole fraction $X'_{Cl} + X'_{Cl_2}$ versus radial distance at $x = 33D_e$, $x = 125D_e$, $x = 300D_e$ and $x = 370D_e$. The azimuthal averages of the scatter plots (red solid curves) and their standard deviations (red dashed curve) are also included.

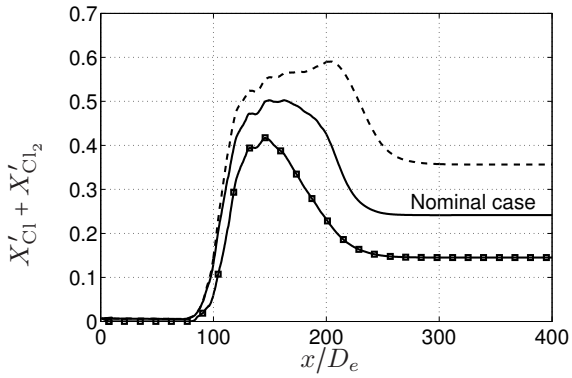

Figure 6.14 – Variation of fraction of active chlorine along the centerline streamline with uncertainty on rate parameters.

Secondly, by modelling chemistry on an averaged flow dynamically frozen (except for the temperature), this method does not take into account several critical parameters:

— the molecular transport, different for each species, which has an effect on species distribution (and therefore on chemistry);

— the complex two-way coupling between turbulence and chemistry. Strong heat release in the thin zone of the flame accelerates the flow, which can enhance (flame-generated turbulence) or damp (relaminarization) turbulence. The change of viscosity with temperature in the flame can also diminish turbulence. On the other hand, turbulence can curve and stretch a flame. This usually results in an increase in the reaction rate, but can also lead to flame quenching.

For all these reasons, it appears necessary to perform LES of the SRM jet that would also include the afterburning chemistry, to offer a better prediction of species distribution in the jet.

6.6 Conclusion

This section presented an off-line chemical model which provided a first prediction of the afterburning and chlorine chemistry occurring in the SRM jet. It relies on modelling a particle of fluid travelling along a streamline (extracted from the LES results) by a constant pressure reactor in which the chemical equations are solved. The model was applied on a large number of streamlines. The results showed that the main steps expected for this chemical scheme were captured:

— a diffusion flame is formed, illustrated by the oxidation of H_2 and CO, present in the jet, by the dioxygen of the air, producing H_2O and CO_2 and a significant heat release;

— a partial conversion of HCl to Cl and Cl_2.

Furthermore, the results given by the off-line model for the mixing layer in the early jet (before the potential core closes) are coherent with those of the counterflow flame simulation for a low strain rate presented in Sec. 5.3. Finally, a sensibility study, conducted with the off-line model, proved that the uncertainties on reaction rate constants of some reactions involving chlorine entail an important variation in the prediction of active chlorine. Therefore new evaluations of these constants are necessary.

In addition to offering a first prediction of the chlorine species distribution in the jet, this model can be used to elaborate and validate a reduced chemical mechanism, suitable for LES of a reactive SRM jet. This problematic is the object of the next chapter.

CHAPTER 7

Reduction of the chemical scheme

The chemistry occurring in SRM jets and described in Table 3.2 involves 16 species and 37 reactions, which already represents a reduced chemistry. Unfortunately, this mechanism still cannot be used directly for LES of reactive SRM jet, as it would require a tremendous amount of computational time. The main issue is related to the stiffness of the chemical system which, due to the explicit nature of the LES solver, imposes a time step several hundred time smaller than the time steps required for the single-species simulation. An extra cost is added by the large number of chemical species (one conservation equation is required for each one of them) and reactions (the reaction rates are complex functions of temperature and species concentrations).

The purpose of this section is to propose a reduction the chemical scheme of Table 3.2 in order to allow LES of the reactive SRM jet at a reasonable computational cost. The reduced scheme will be validated for the thermodynamic conditions encountered for this particular simulation.

7.1 Strategies for chemistry reduction

Various strategies have been adopted in the literature to handle numerical simulation of complex chemistry. One approach consists in implementing tabulated chemistry in order to store, for instance, chemical source terms and avoid repeating computations. The "Intrinsic Low Dimensional Manifold" (ILDM) (Maas and Pope, 1992) is an example of this technique. It aims at identifying the largest chemical time scales in order to determine the mass fractions and reaction rates as functions of a reduced set of variables (including a progress variable and a mixture fraction). These data are then stored in a table and retrieved using interpolations. This concept was used as a base for other methods, for instance the "Flame prolongation of ILDM" (FPI) (Gicquel et al., 2000), the "Flamelet Generated Manifold" (FGM) (Oijen and GOEY, 2000), or the "Rate-Controlled Constrained-Equilibrium" (RCCE) (Jones and Rigopoulos, 2005). These methods have the advantage that they do not depend on the chemical scheme. However, their implementation in CFD solvers is complex and cannot be achieved for all solver (particularly in commercial codes).

When the reference scheme is of a moderate size, analytical methods can be used to reduce it. Applying "Quasi-Steady State Approximation" (QSSA, to intermediate species or radicals at equilibrium) and partial equilibrium assumption (to fast reactions) leads to a small number of species and equations which can be relatively easily implemented in the

CFD solver. This technique has been largely employed, for instance for methane chemistry (Bilger et al., 1990), H_2/O_2 combustion (Seshadri et al., 1994; Fernández-Galisteo et al., 2009; Boivin et al., 2011b), syngas combustion (coal-derived fuel used for gas-turbines application) (Chung and Williams, 1990; Boivin et al., 2011a).

A particular attention should be given to numerical stiffness when reducing chemical mechanisms. Depending on the specific reduction developments (application of the QSSA on certain species for instance), the resulting system may be stiffer than the original one, even though it contains fewer reactions and species.

7.2 Analysis and reduction of the scheme

The reference scheme of Table 3.2 is of a moderate size and its sub-mechanisms of oxidation of H_2 and CO are well known. Therefore a reduction "by hand" was preferred to a tabulated chemistry, long and complex to implement. Analyses conducted on the reference scheme [1] did not allow the identification of species for which the application of the QSSA would improve the stiffness of the system. As a consequence, the reduction of the mechanism relies only on removing species and reactions whose impact is either found to be insignificant considering the conditions of high temperature and low pressure of the case, or balanced by a correction on the rate constant parameter A in the Arrhenius law $k = AT^n \exp(-E/RT)$. Counterflow flames simulations, off-line chemistry modelling and reactive LES were used to reduced the system while ensuring the accuracy of the results and a small impact on the LES time step, which has to be of the same order of magnitude than for the single-species.

7.2.1 The H_2/O_2 system

For high temperatures and low pressures, which are the conditions encountered in SRM jets, the radical pool is dominated by H, O and OH. Species HO_2 and H_2O_2 have a less significant role and appear in very small fractions (see Figs. 5.9 and 6.5). Therefore they were removed from the mechanism. Reactions 7 and 8 can also be neglected (Sánchez and Williams, 2014). Note that the presence of radicals in the exhaust gas is enough to ignite chemistry, as noticed for counterflow flames simulations in Sec. 5.3. Despite this reduction, reactions 2 and 3 still impose a small time step for LES. Therefore the pre-exponential constant A of these two reactions were slightly decreased to slow down chemistry.

7.2.2 Carbon monoxide oxidation

Reaction 22 is central in the description of CO oxidation (Boivin et al., 2011a) and was found to be enough to describe this mechanism at the conditions of pressure and temperature of the SRM jet. Moreover, the species HCO is negligible (see Figs. 5.9 and 6.4).

7.2.3 Chlorine chemistry

While attempting to reduce the chlorine chemistry, the use of the off-line model on the centerline streamline revealed that all reactions within this sub-mechanism have a significant role, either on the quantities of Cl and Cl_2 produced, or on the distribution of the chlorine species along the x-axis. Therefore it was not possible to reduce it further than by removing reaction 31, which has no noticeable effect on the chlorine distribution.

1. with Perrine Pepiot's Kinsolve tool

No.	Reactions
1	$H + O_2 = O + OH$
2	$O + H_2 = H + OH$
3	$OH + H_2 = H + H_2O$
4	$2\,OH = O + H_2O$
5	$2\,H + M = H_2 + M$
6	$H + OH + M = H_2O + M$
22	$CO + OH = CO_2 + H$
32	$H + Cl_2 = HCl + Cl$
33	$Cl + H_2 = HCl + H$
34	$H_2O + Cl = HCl + OH$
35	$OH + Cl = HCl + O$
36	$H + Cl + M = HCl + M$
37	$2\,Cl + M = Cl_2 + M$

Table 7.1 – Reduced mechanism for H_2–CO combustion and conversion of HCl to active chlorine.

Reaction 33 being too fast for the targeted time step, its pre-exponential constant A was decreased by a factor 10. The impact of this modification on the fractions of active chlorine was balanced by an increase in A for reaction 37.

7.2.4 Reduced scheme

The final reduced scheme is given in Table 7.1. It has 13 reactions and 13 species, and thorough tests using LES proved that a maximum time step of $1\mu s$ could be used. It is smaller than the time step imposed by mesh and flow dynamics for the second domain AVBP2, but in return the reduced mechanism shows good results when compared to the reference scheme, as it is discussed in the next section.

7.3 Validation of the reduced scheme

This section aims to validate the reduced scheme by a series of comparative test cases with the reference scheme. These tests focus on configurations which are relevant for an application of this chemistry to LES of reactive SRM jet. First, the off-line model is applied using the reduced scheme, and the results are compared with those obtained in Sec 6.2 and 6.4. Then, the equilibrium temperature, ignition time and diffusion flame structure are compared using the reference and reduced schemes in counterflow flames simulations.

7.3.1 Comparison of reference and reduced schemes using the off-line chemistry model.

7.3.1.1 Application of reduced scheme on the centerline streamline

Figures 7.1 and 7.2 show the results obtained by the application of the off-line chemical model on the centerline streamline with reference and reduced mechanisms. All profiles are matched correctly by the reduced scheme. Slight differences appear for the chlorine species, which are caused by the change in pre-exponential constants of reactions 33 and 37.

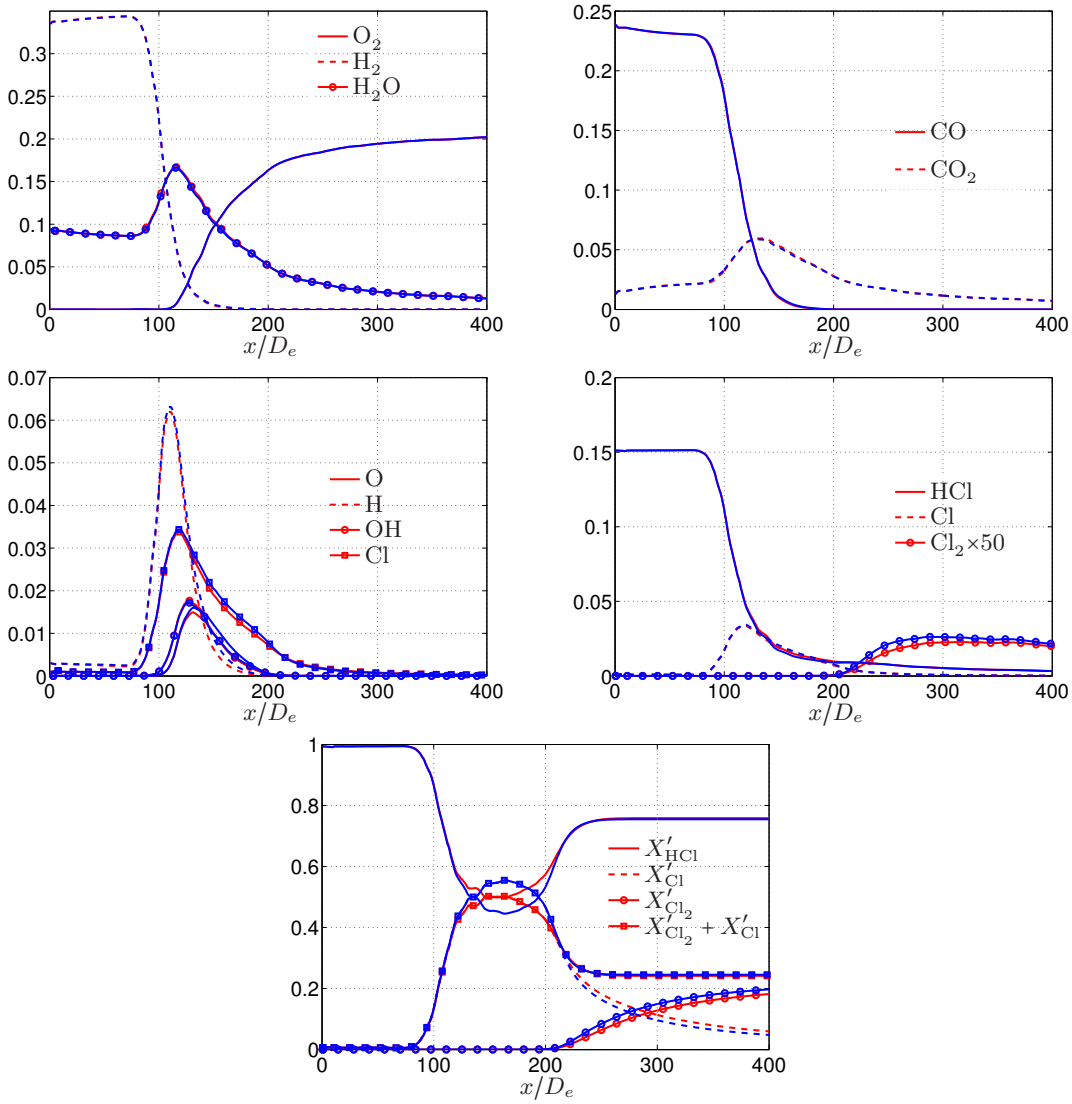

Figure 7.1 – Mole fractions of chemical species along the centerline streamline for the reference scheme (red lines) and reduced scheme (blue lines).

Downstream of the combustion zone, for $x > 250D_e$, the reduced scheme under-estimates X'_{Cl} by 0.01 (absolute error) and over-estimates X'_{Cl_2} by 0.015. Overall, the fraction of active chlorine is correctly estimated (0.245 instead of 0.241). The temperature and heat release are well predicted, with a slight under-estimation of the maximum. Overall, this test give satisfactory results.

7.3.1.2 Comparison of reference and reduced scheme on 10,000 streamlines

The same simulations as in Sec. 6.4 were achieved using the reduced scheme of Table 7.1. Results are shown in Figs. 7.3-7.7. Both schemes give very close results. The over-estimation (respectively under-estimation) of the fraction of Cl (respectively Cl_2), noted in Fig. 7.1 for the centerline streamline, is reproduced in Figs. 7.5 and 7.6 for $x > 125D_e$ (particularly visible close to the centerline, for $r < 5r_e$). The differences which can be observed between the results given by the two schemes can be largely attributed to the fact that the LES results used to extract streamlines were not averaged on a period

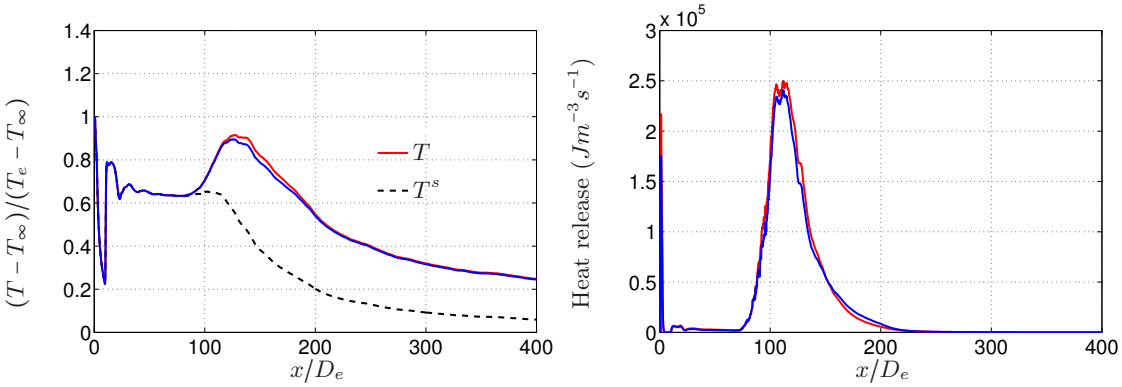

Figure 7.2 – Temperature and heat release for the reference scheme (red lines) and reduced scheme (blue lines).

of time long enough. Therefore the streamlines extracted from the flow-field (and then the azimuthal averages computed from these streamlines) cannot represent a proper axisymmetric flow. This exacerbates the divergence between the profiles, slightly visible in the mixing layer for $x = 33D_e$ (for instance the plots of temperature, H_2 or O_2 for $r > 3r_e$ in Fig. 7.3) and $x = 125D_e$ (for instance the profiles of Cl_2 for $r > 6r_e$ in Fig. 7.5), and particularly noticeable for all plots at $x = 300D_e$ and $x = 370D_e$. In particular, at the locations $x = 300D_e$ and $x = 370D_e$, the profiles of mole fraction of CO obtained with the reduced scheme (Fig. 7.4) exhibit a non-physical behavior (for $r > 5r_e$) which can be entirely attributed to numerical errors (computation of azimuthal averages), and not to the reduced scheme.

7.3.2 Validation of the reduced chemistry for laminar diffusion flames

7.3.2.1 Equilibrium temperature

Computing the equilibrium temperature is important to check if the reduced set of species gives reliable thermodynamic results. The equilibrium temperature is obtained for different initial mixtures of air (oxidizer O) and exhaust gas (fuel F), using constant pressure homogeneous reactors, solved with Cantera with the reference and reduced chemistry. Results are shown in Fig. 7.8, for initial mixture fractions Y_F^0/Y_O^0 varying from 0.02 to 50. They are similar for both schemes, proving that removing the species HO_2, H_2O_2 and HCO has no impact on equilibrium temperature.

7.3.2.2 Autoignition

The chemistry in the SRM jet is initiated in the mixing layer by autoignition, triggered by the high temperature of the exhaust gas. Then the presence of radicals in the exhaust gas is enough to initiate the shuffle reactions 1f-3f. The autoignition time t_i can be associated to the distance δ_i from the nozzle lip where combustion starts (as illustrated in Fig. 7.9), via the relation

$$\delta_i \approx u_e t_i \tag{7.1}$$

where u_e is the flow velocity at the nozzle exit.

In order to characterize the autoignition time scales associated to the reduced chemical scheme, the temporal evolution of a constant pressure reactor, initially containing a

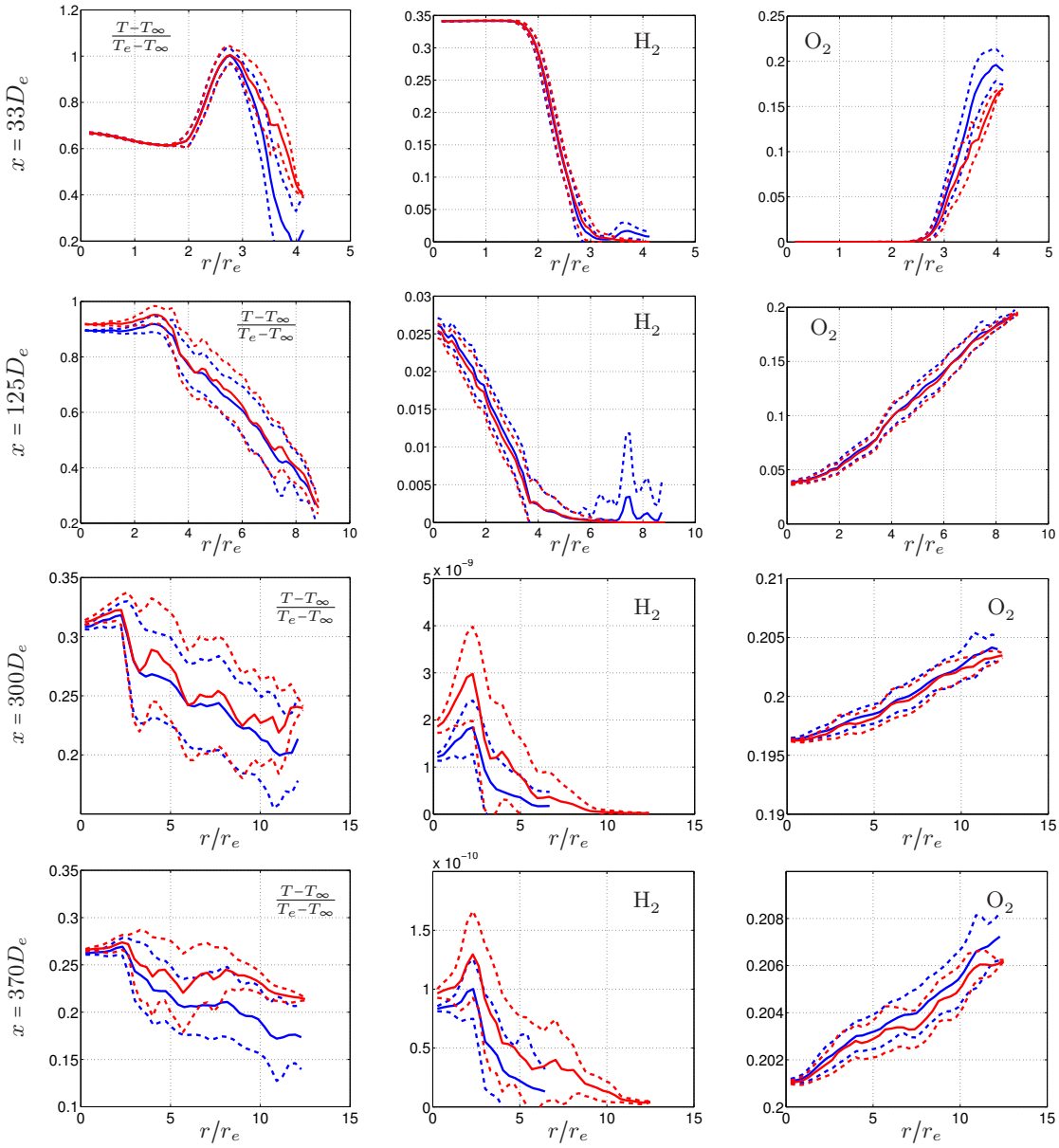

Figure 7.3 – Azimuthal averages (solid curves) and standard deviations (dashed curve) of temperature and mole fractions of species H_2 and O_2 versus radial distance at $x = 33D_e$, $x = 125D_e$, $x = 300D_e$ and $x = 370D_e$, for reference scheme (red) and reduced scheme (blue).

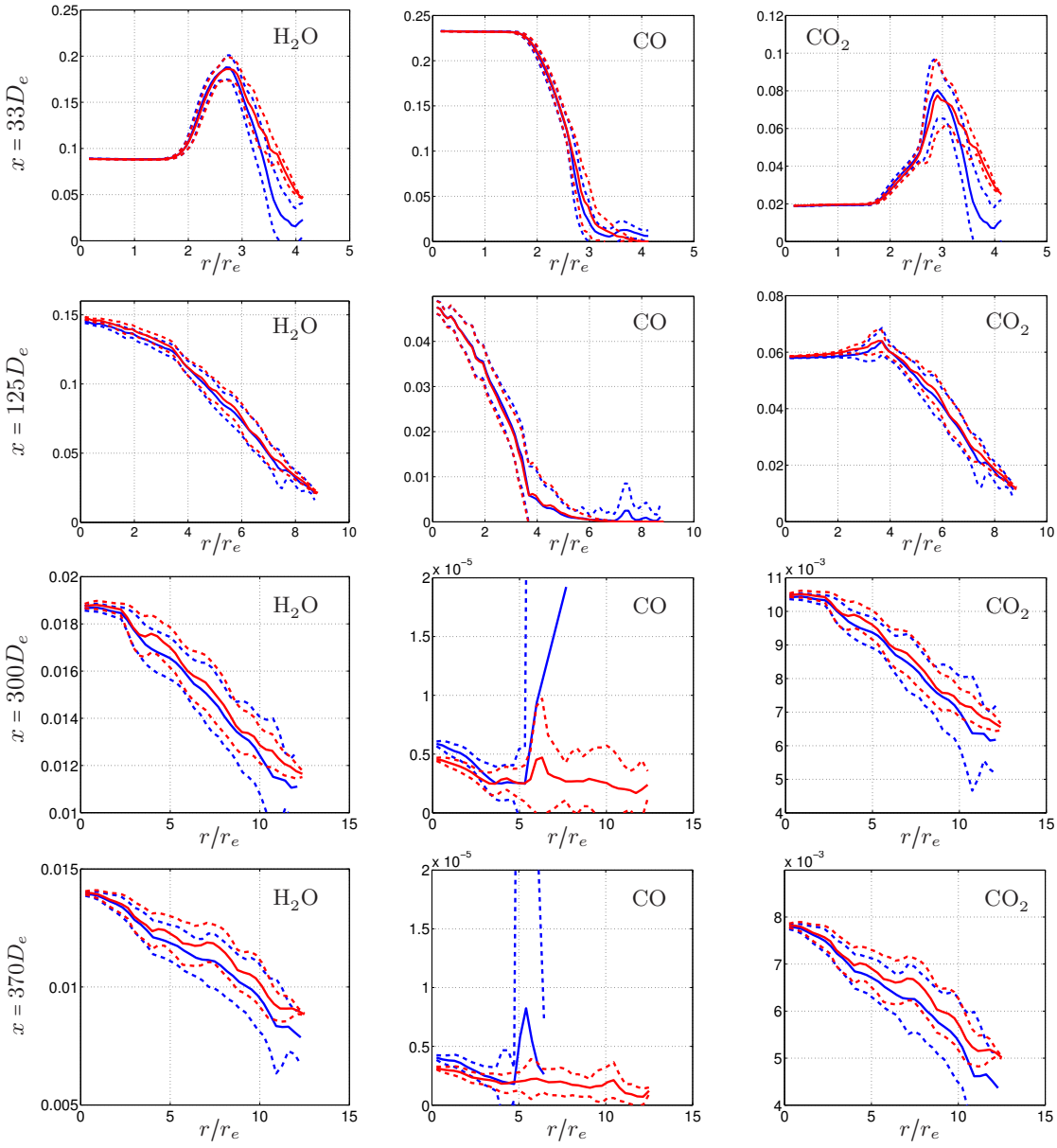

Figure 7.4 – Azimuthal averages (solid curves) and standard deviations (dashed curve) of mole fractions of species H_2O, CO and CO_2 versus radial distance at $x = 33D_e$, $x = 125D_e$, $x = 300D_e$ and $x = 370D_e$, for reference scheme (red) and reduced scheme (blue).

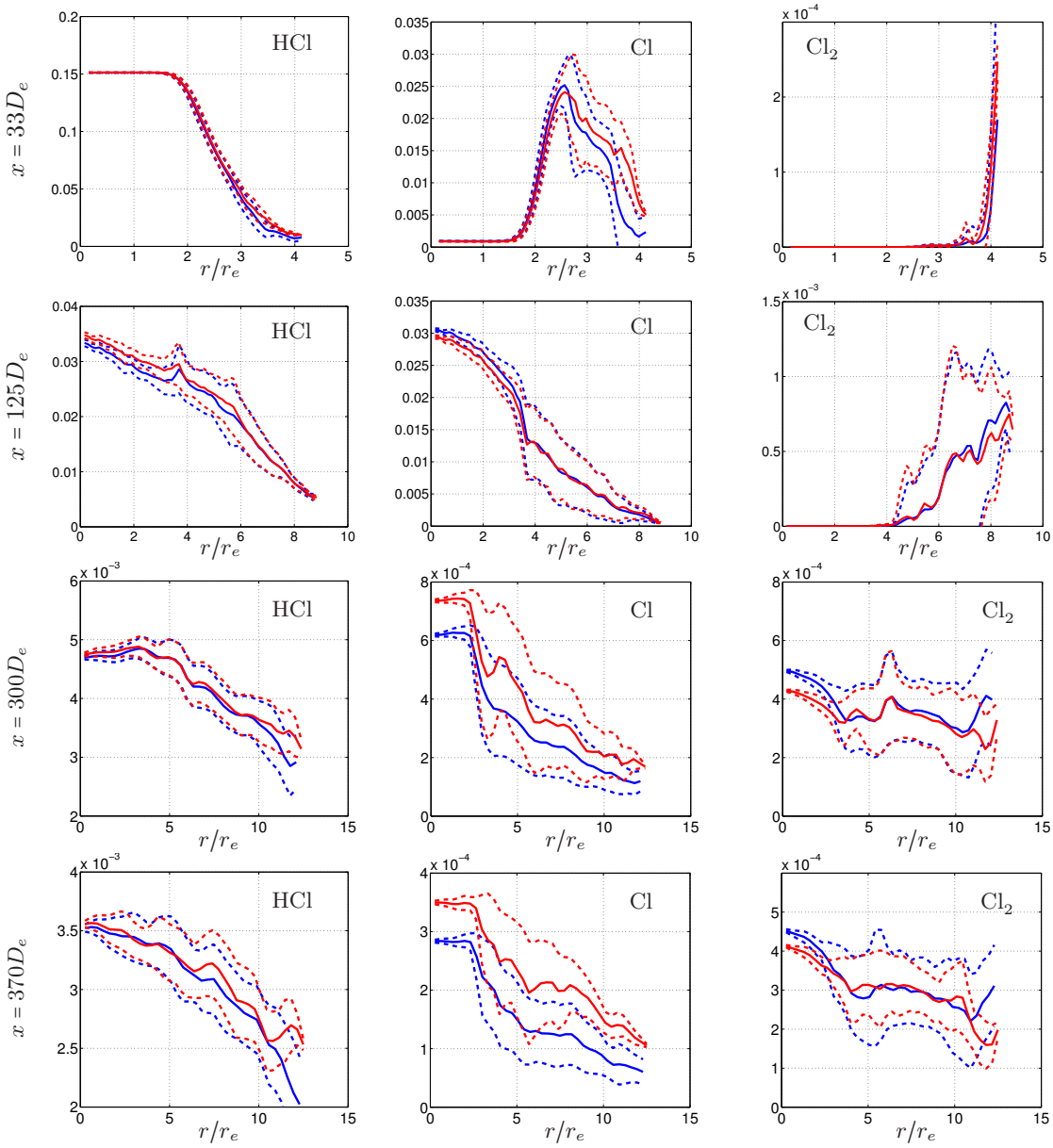

Figure 7.5 – Azimuthal averages (solid curves) and standard deviations (dashed curve) of mole fractions of species HCl, Cl and Cl_2 versus radial distance at $x = 33D_e$, $x = 125D_e$, $x = 300D_e$ and $x = 370D_e$, for reference scheme (red) and reduced scheme (blue).

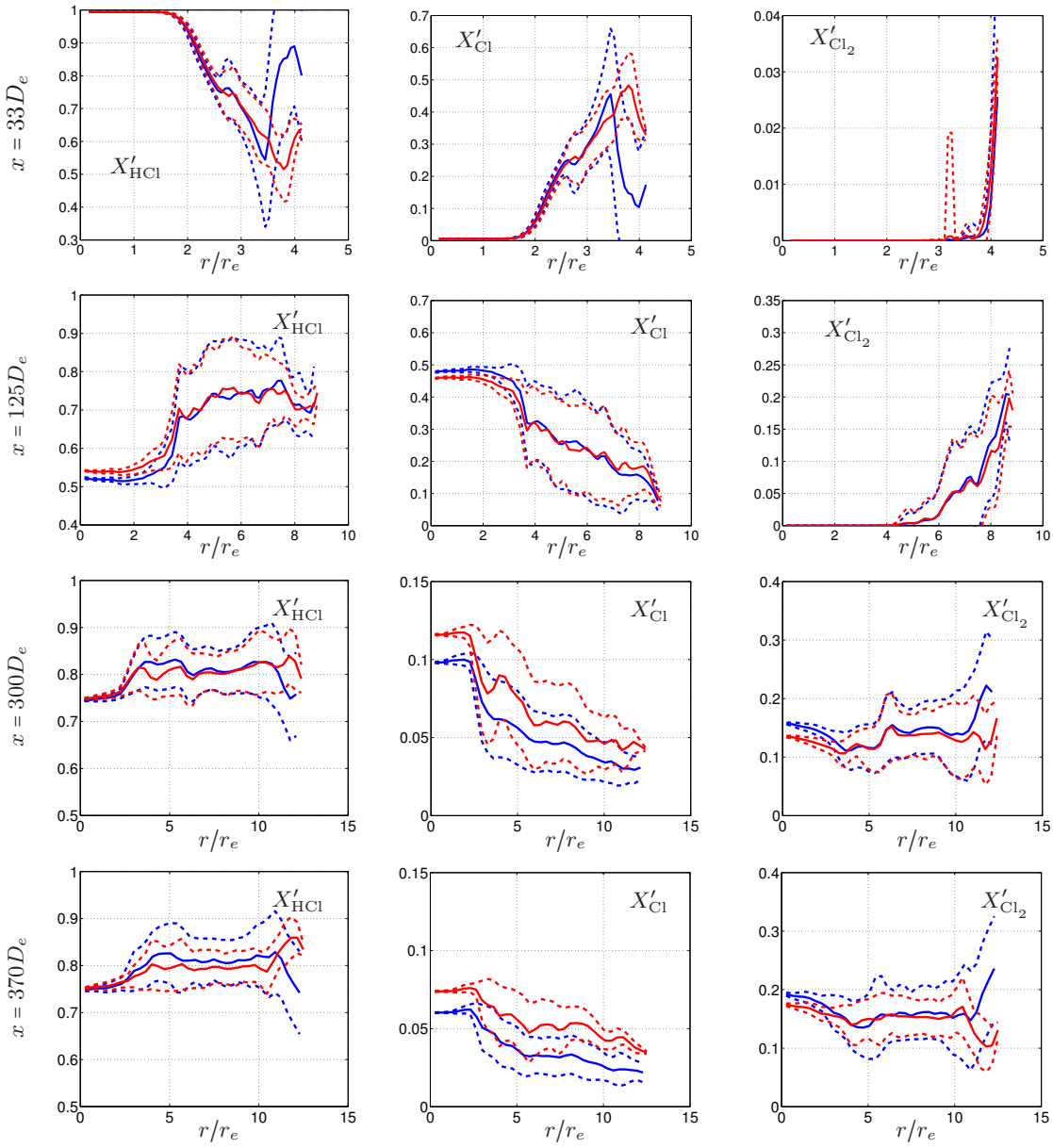

Figure 7.6 – Azimuthal averages (solid curves) and standard deviations (dashed curve) of mole fractions X'_{HCl}, X'_{Cl} and X'_{Cl_2} versus radial distance at $x = 33D_e$, $x = 125D_e$, $x = 300D_e$ and $x = 370D_e$, for reference scheme (red) and reduced scheme (blue).

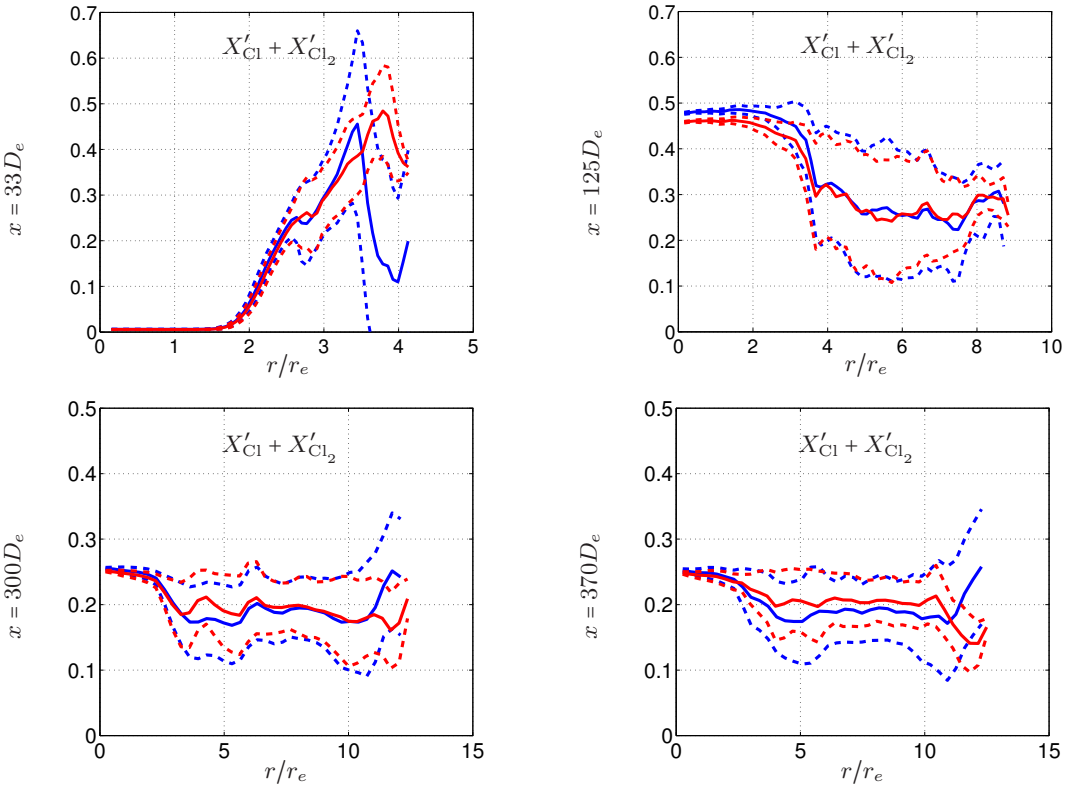

Figure 7.7 – Azimuthal averages (solid curves) and standard deviations (dashed curve) of mole fraction $X'_{Cl} + X'_{Cl_2}$ versus radial distance at $x = 33D_e$, $x = 125D_e$, $x = 300D_e$ and $x = 370D_e$, for reference scheme (red) and reduced scheme (blue).

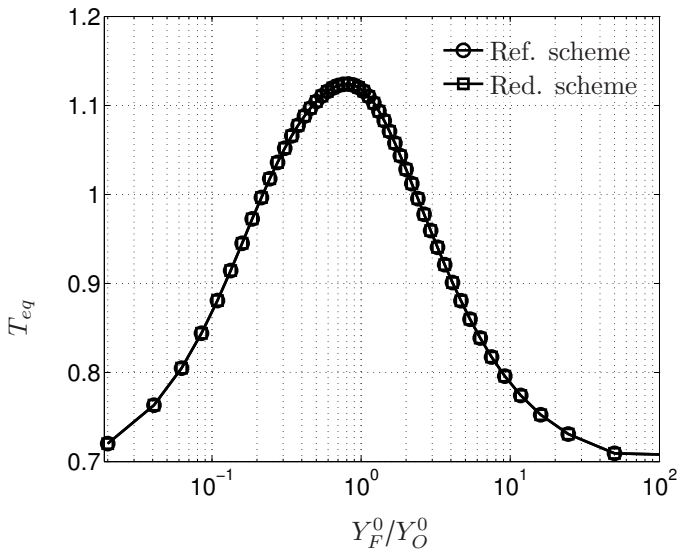

Figure 7.8 – Variation of equilibrium temperature with the mass fractions ratio Y_F^0/Y_O^0, for $P = 5600$ Pa and initial temperature $T^0 = T_{pc}$.

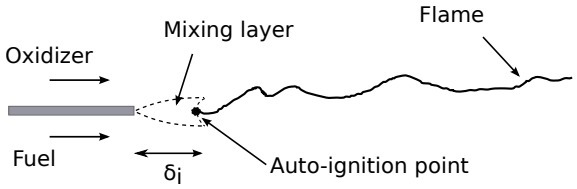

Figure 7.9 – Stabilization of a turbulent non-premixed flame by autoignition in the mixing layer, when one of the two stream is sufficiently preheated (adapted from Poinsot and Veynante (2005)).

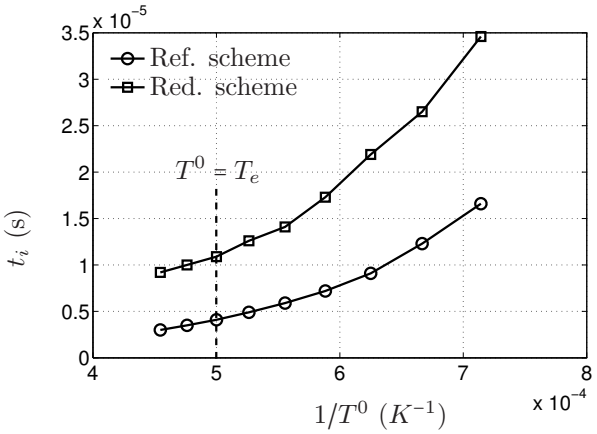

Figure 7.10 – Variation of ignition time with initial temperature of a mix of SRM exhaust gas/air at stoichiometric conditions and $P = P_e$.

mixture of SRM exhaust gas and air at stoichiometric conditions for the hydrogen atom, is studied. The ignition delay time (or induction time) t_i is obtained with the inflection-point criterion on temperature, i.e. the time for which the derivative of the temperature with respect to t is maximum. Both the reference and reduced scheme were tested, for different initial temperatures T^0 and for a value of pression equal to P_e, the pressure at the nozzle exit plan. Results are shown in Fig. 7.10. The ignition time decreases as the initial temperature increases, as expected. The reduced mechanism gives results within the same order of magnitude, but overpredicts the ignition time with a relatively important error. For $T^0 = T_e$, the values of t_i for the reference and reduced scheme give the following estimation for the ignition distance:

$$\delta_i^{ref} \approx 1.2 \text{ cm}$$
$$\delta_i^{red} \approx 3.3 \text{ cm}$$

These values are very small compared to the nozzle exit diameter ($< 0.01 D_e$). The delay in autoigntion induced by the reduced mechanism is therefore negligible, and will not affect significantly the stucture of the flame. [2]

7.3.2.3 Impact of strain rate

Counterflow flames implementing the reduced chemistry were simulated using the same configuration as in Sec.5.3, for various strain rates. The variations of maximum temperature and mole fraction of species with strain rate A are shown in Fig. 7.11, for both

2. More details about autoignition in mixing layers can be found in Sánchez et al. (1999).

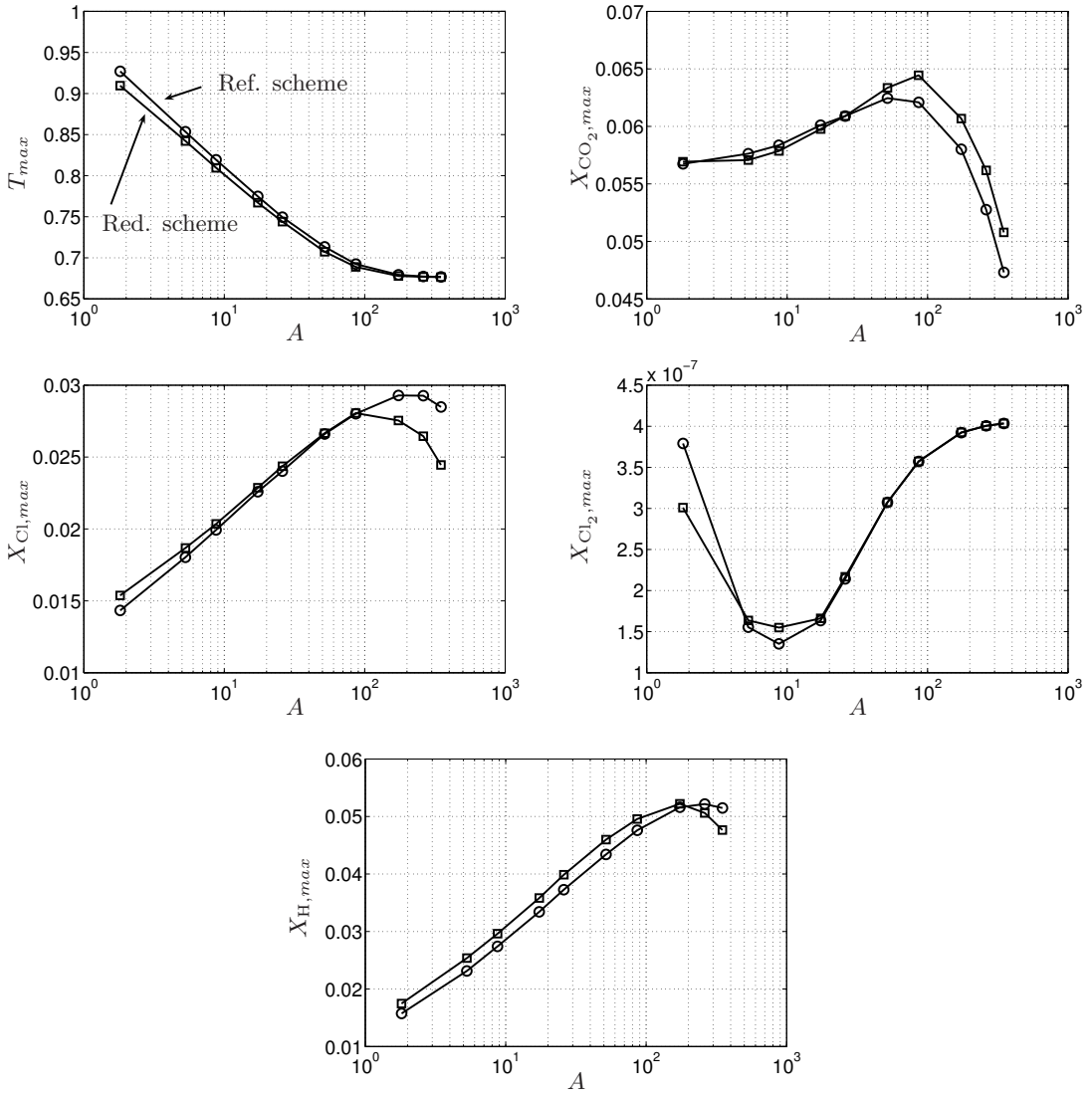

Figure 7.11 – Variations of the maximum temperature and mole fractions of CO_2, Cl, Cl_2 and H with strain rate A (1/s) for reference scheme (circles) and reduced scheme (squares).

mechanisms. The reduced chemistry reproduces with good accuracy the profiles predicted by the detailed chemistry. An error appears for Cl and CO_2 for sufficiently high values of A, and for species Cl_2 for the lowest values of A. This trend is also found for the variation of integrated reaction rate $\left|\dot{\Omega}_{H_2}\right|$ with $\chi_{st,H}$ (see Fig. 7.12). The value of $\chi_{st,H}$ for which $\left|\dot{\Omega}_{H_2}\right|$ starts decreasing is slightly smaller. Additionally, the profile of $\left|\dot{\Omega}_{H_2}\right|$ obtained with the reduced scheme varies like $\sqrt{\chi_{st,H}}$ even for low values of $\chi_{st,H}$, which is not the case for the profile obtained with the reference scheme. The variations of $\left|\dot{\Omega}_{CO}\right|$ with $\chi_{st,C}$ are similar for both schemes.

This study gives qualitative indications on the effect of the reduced scheme on the mixing layer of the jet. For strain rates too high or too low, larger errors can occur in the predictions of flame extinction or species mole fractions. This emphases the necessity to evaluate the strain rates (or the scalar dissipation rates) in the reactive regions of the SRM jet in order to determine potential areas with larger errors.

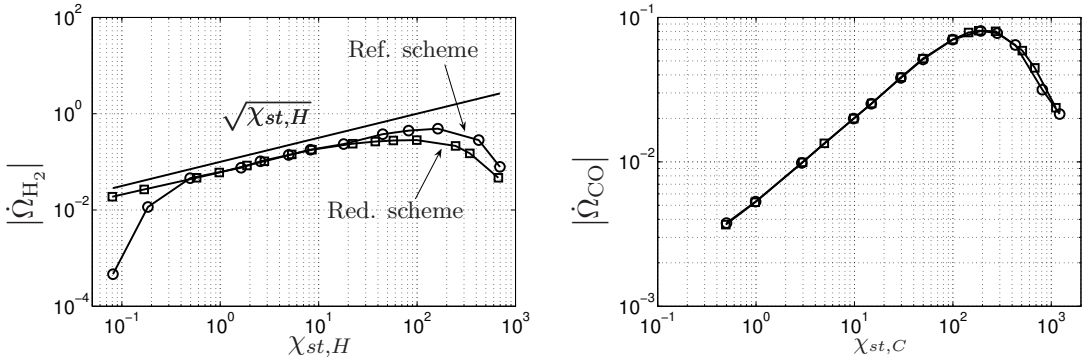

Figure 7.12 – Variations of integrated reaction rate $\left|\dot{\Omega}_{H_2}\right|$ with $\chi_{st,H}$ (1/s) and $\left|\dot{\Omega}_{CO}\right|$ with $\chi_{st,C}$ (1/s) for reference scheme (circles) and reduced chemistry (squares).

7.4 Conclusion

In this section, the set of reactions describing hot plume chemistry was reduced and adapted in order to run LES of a reactive SRM jet with an acceptable computational cost, while ensuring the accuracy of the results. A reduction "by hand" of the mechanism, with a estimation *a posteriori* of the induced error, was chosen. The resulting reduced scheme has 13 species and 13 reactions, and was validated by a series of test cases for laminar diffusion flames, with conditions met in the SRM jet (hot temperature of the jet, low pressure). First, the off-line chemical model was applied with the reduced scheme. Results were very close to those obtained with the reference scheme. In particular, a good accuracy was achieved at the extremity of the jet (an error less than 6% on the prediction of the fraction of active chlorine on the centerline). This location is crucial for future atmospheric simulations of the rocket plume, as the results in this region can be used to build an initial solution. Finally, tests were conducted using the chemical solver Cantera. They showed that the reduced scheme correctly predicts the adiabatic temperature, and that the delay on autoignition that it introduces should not impact the LES results. Counterflow flames simulations indicates that the reduced scheme responds correctly to variations of strain rate, except for a slight decrease in the extinction strain rate. As a results, it will be important to evaluate the scalar dissipation rates in the results of the LES of reactive SRM jet in order to determine if this error can have an impact on the flame (like holes).

CHAPTER 8

Large Eddy Simulations of a reactive SRM jet

The validation of the numerical setup in Chapter 4 and the reduction of the chemical mechanism in Chapter 7 allow to conduct LES of the multi-species, reactive SRM jet. Following a description of the simulation setup, an analysis of the flow-field, and in particular of the combustion region, is carried out. A comparison of the results to those obtained with the off-line model is performed. Then, the necessity of a combustion model is assessed. Finally, a coarse comparison of the production of active chlorine in the jet with previous studies is presented.

8.1 Simulation setup

The computational domain and the grid used for this simulation correspond to case B described in Sec. 4.1.2. The subgrid scale model follows the Dynamic Smagorinsky approach (see Sec. 2.1.7.5). The dynamic viscosity is determined by the power law (Eq. (2.16)), with the parameters given in Sec. 4.1.1.2. For each species k, the Schmidt number Sc_k corresponds to those of the burnt gas in a one-dimensional premixed flame computed with the solver CANTERA.

The chemical mechanism in Table 7.1 was implemented in the LES solver. To save CPU time, chemistry is only activated in the second domain AVBP 2. This approximation does not significantly alter the results, as shown in Sec. 8.2.1. No combustion model is applied at a subgrid scale level. This aspect is discussed in Sec. 8.5.

The introduction of chemistry in the simulations imposes time steps which are smaller than those for LES of a single-species SRM jet. The most adequate time steps for AVBP 1 and AVBP 2 were found to be respectively $\Delta t_1 = 0.5\mu s$ and $\Delta t_2 = 1\mu s$. The simulation was initialized using a converged solution of the LES of a single-species SRM jet. The equivalent SRM exhaust gas was replaced by a multi-species gas whose composition corresponds to those at the nozzle exit, and a mixing of N_2 and O_2 was introduced instead of the species representing air. The simulation was then run for 0.6s, which is enough to statistically converge the flow-field up to $x = 300D_e$, a location in the jet from which active chlorine should have reached its asymptotic level, according to simulations conducted with the off-line model (see the centerline evolution of $X'_{Cl_2} + X'_{Cl}$ in Fig. 7.1). The reactive flow-field was then time-averaged for 0.3s, which represents $0.5t_c$ (where t_c is determined for a domain limited to $x = 300D_e$ downstream of the nozzle). This time interval may not be long enough to get fully converged statistics for $x > 300D_e$, as discussed in Sec. 8.3. About 500,000 CPU hours were required for this simulation, using HPC resources of GENCI

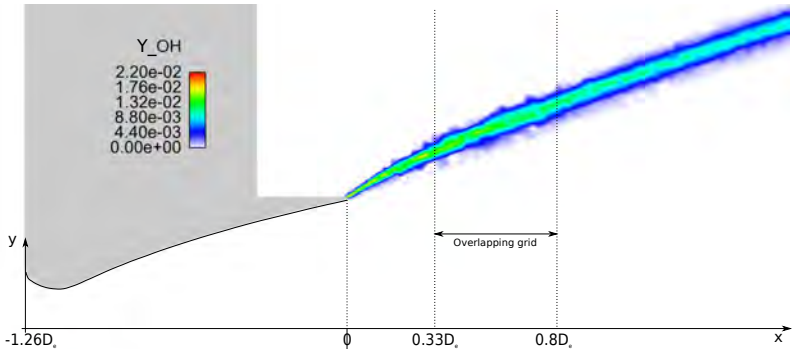

(a)

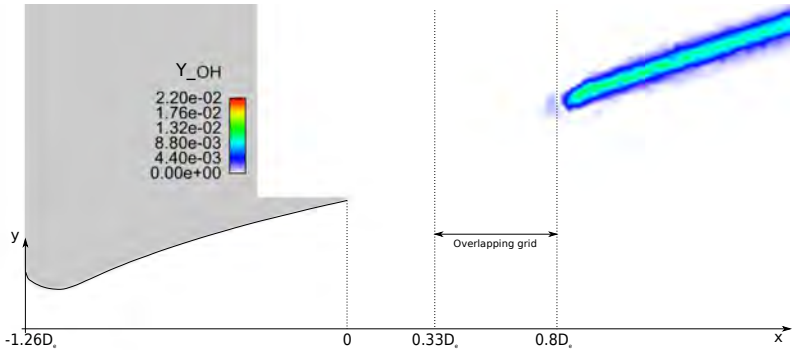

(b)

Figure 8.1 – Cut of the nozzle (dark curve) and near-field jet showing the mass fraction of radical OH for chemistry solved in both domains (a) and in the second domain only (b).

TGCC.

8.2 Flow visualization

8.2.1 Flame stabilization

To study flame stabilization, chemistry was computed in both domains for a few iterations. Figure 8.1a shows that the flame is attached to the nozzle lip, with an immediate production of radical OH, whereas a lifted flame could be expected (see Sec. 7.3.2.2). This result is to be addressed with caution: the mesh in the vicinity of the lip is too coarse for turbulence to develop, which could lead to an underestimation of the strain rate. A definitive conclusion regarding this zone of the flame would require extra computations using a finer mesh. Figure 8.1b depicts auto-ignition near the nozzle when chemistry is activated only in the second domain. Radical OH is produced immediately downstream of the overlapping grid. For $x > 0.8D_e$, the mixing layer is similar to those in Fig. 8.1a, suggesting that the deactivation of chemistry in the first domain (which represents a longitudinal distance of $0.8D_e$, since chemistry in the nozzle is not modelled) does not impact the rest of the simulation.

8.2.2 Global flame structure

Three stoichiometric iso-surfaces $z_{\mathrm{H}} = z_{st,\mathrm{H}}$, $z_{\mathrm{C}} = z_{st,\mathrm{C}}$ and $z_{\mathrm{Cl}} = z_{st,\mathrm{Cl}}$ (defined in Sec. 5.3.2) are represented by iso-contours in an instantaneous longitudinal cut in Fig. 8.2a and in instantaneous transverse cuts in Fig. 8.3. The same iso-contours are also plotted from

results of the off-line model presented in Sec. 6.3 (obtained with the reference scheme) in Fig. 8.2b. Figure 8.2 shows that the flame corresponding to combustion H_2-O_2 (black curve) is shorter than the two other flames (for the LES results, its extremity lies around $x = 100D_e$, compared to $x = 134D_e$ for the two other flames), and lies inside them, closer to the fuel side (also visible in Fig. 8.3). The two other iso-contours are closer to each other (particularly for the LES results), with the flame corresponding to combustion CO-O_2 lying inside the iso-contour $z_{Cl} = z_{st,Cl}$. The respective position of these stoichiometric mixture fractions corresponds to the results obtained for counterflow flames in Sec. 5.3.2. The comparison between Figs. 8.2a and 8.2b reveals that the turbulent flame modelled by LES is shorter than the flame modelled by the off-line model (even if a rigorous comparison cannot be performed between instantaneous LES and the averaged results of the off-line model). For instance, the tip of the H_2-O_2 flame is located around $x = 100D_e$ in the LES results, compared to $x = 118D_e$ for the off-line model. These differences are analysed in Sec. 8.3.

Figure 8.3 links the stoichiometric iso-contours to locations of maximum values of mass fractions of chemical products. The maximum values of Y_{H_2O} and Y_{CO_2} respectively lie around the iso-contours $z_H = z_{st,H}$ and $z_C = z_{st,C}$. However, the iso-contour $z_{Cl} = z_{st,Cl}$ is not located at the peak of Y_{Cl}, which confirms the lack of relevancy of this parameters, as mentioned in Sec. 5.3.2 (moreover, the value of $z_{st,Cl}$ does not take into account the production of Cl_2).

Figure 8.4a depicts iso-contours of negative values of instantaneous reaction rates $\dot{\omega}_{H_2}$ and $\dot{\omega}_{CO}$: they show the location where species H_2 and CO are respectively consumed. Similarly, positive values of instantaneous reaction rates $\dot{\omega}_{Cl}$ and $\dot{\omega}_{Cl_2}$ are plotted in Fig. 8.4b, indicating regions where Cl and Cl_2 are produced. These figures validate and complete the observations previously mentioned for Fig. 8.2: the combustion H_2-O_2 (dark curves) lies inside the combustion CO-O_2 (red curves). Species Cl (blue curves) is produced in these two combustion zones and Cl_2 exclusively outside (green curves), in the air side of the mixing layer. Finally, heat release, shown in Fig. 8.4c, is produced in the vicinity of the combustion zone, as expected.

The iso-contours in Figs. 8.2-8.4 reveal the evolution of the flames due to turbulence. In the near-field jet (from the expansion region up to $x = 33D_e$, approximately), they seem quasi-laminar, with very little wrinkling. This is particularly visible in Fig. 8.3, for the cuts at $x = 33D_e$. In this zone, the jet turbulence has just started its development under the influence of the velocity fluctuations imposed in the coflow. Further downstream, the flames become more and more wrinkled (also visible in Fig. 8.3 for the cuts at $x = 67D_e$). Localized pockets of species mass fractions start to appear for $x > 98D_e$ in Fig. 8.2 particularly for $z_C = z_{st,C}$. Furthermore, it can be seen in Fig. 8.3 that the larger levels of turbulence at $x = 67D_e$ exacerbate differences between flames locations. The flame corresponding to combustion H_2-O_2 lies closer to the jet centerline, therefore it is less perturbed by turbulence than the two other flames and appears less wrinkled.

Figure 8.5 illustrates the importance of turbulent combustion for chemical species distributions and temperature: large fluctuations around mean values are visible. As previously observed in the longitudinal cuts in Fig. 8.3, a rise in temperature and production of H_2O, CO_2, Cl and Cl_2 can be observed in the vicinity of the flames. In particular, Cl_2 is produced from $x = 180D_e$ (see Fig. 8.6), and in the external part of the boundary layer (see Fig. 8.3), a zone which was not entirely computed with the off-line model. The cut depicting X_{Cl_2} in Figure 8.5 shows that in the near-field of the jet ($x < 33D_e$), Cl_2 is not uniformly produced along the mixing layer. This could be due to strain rates too high in this region, causing quenching in the chemical mechanism of conversion from Cl to Cl_2.

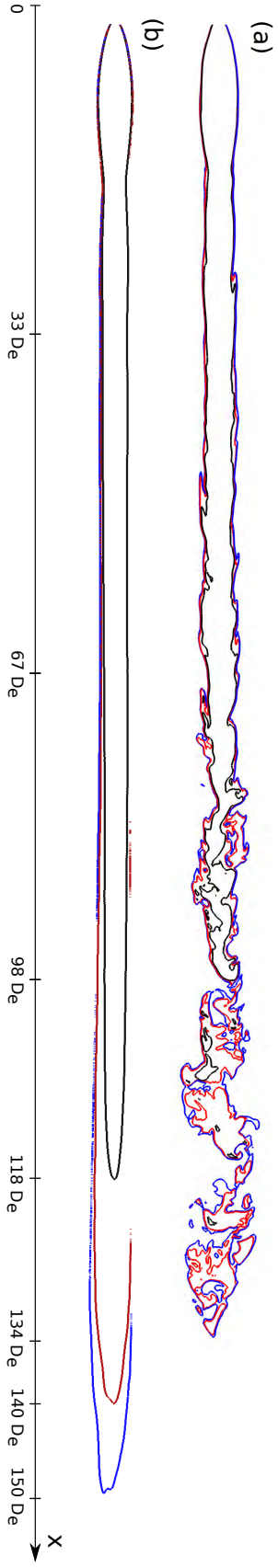

Figure 8.2 – Cuts of the jet showing three iso-contours $z_{\mathrm{H}} = z_{st,\mathrm{H}}$ (black curve), $z_{\mathrm{C}} = z_{st,\mathrm{C}}$ (red curve) and $z_{\mathrm{Cl}} = z_{st,\mathrm{Cl}}$ (blue curve) from (a) instantaneous LES and (b) the off-line model.

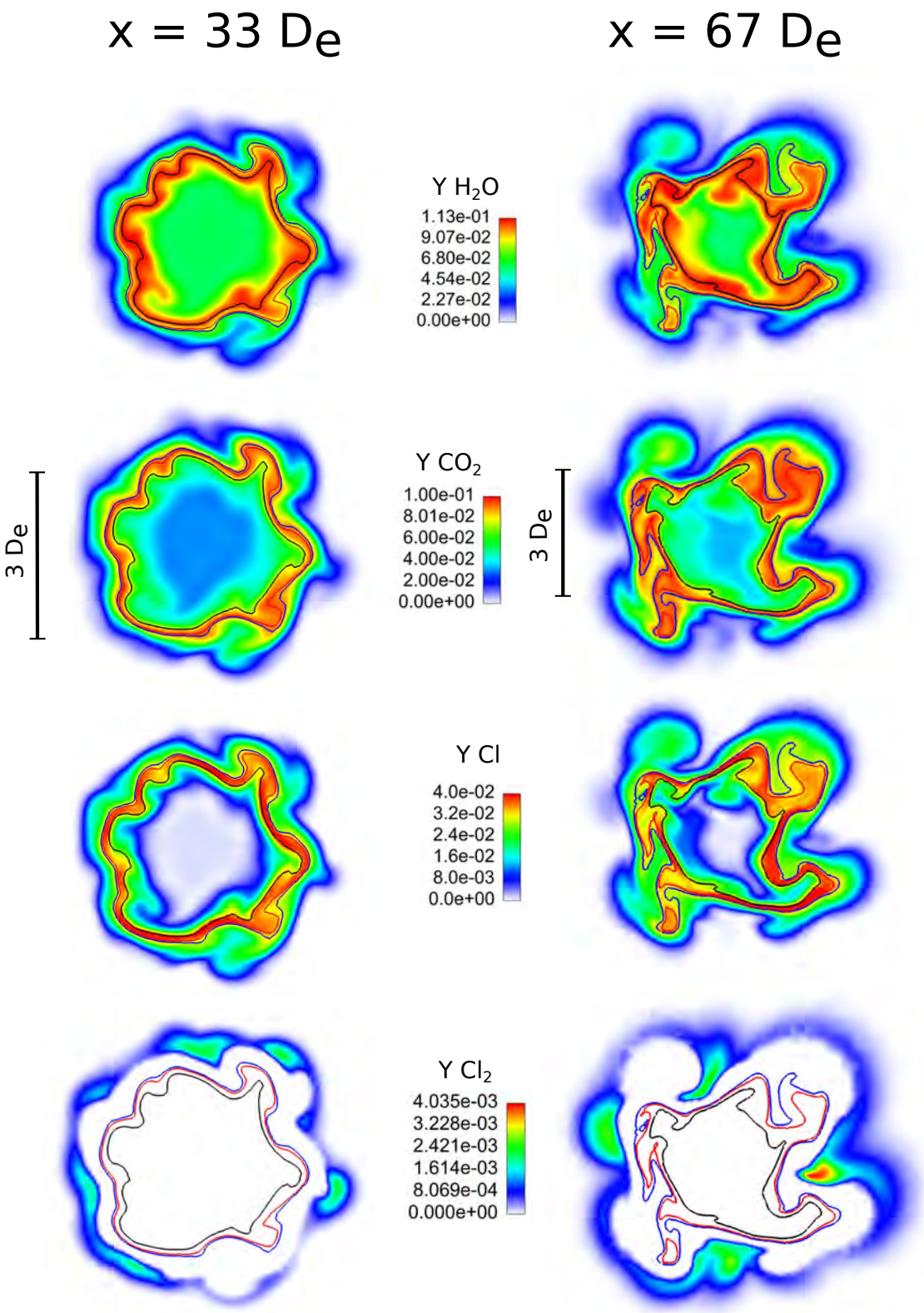

Figure 8.3 – Transverse cuts of the SRM jet at $x = 33D_e$ (left) and $x = 67D_e$ (right) showing instantaneous mass fraction of H_2O, CO_2, Cl and Cl_2. The iso-contours $z_H = z_{st,H}$ (black curve), $z_C = z_{st,C}$ (red curve) and $z_{Cl} = z_{st,Cl}$ (blue curve) are also plotted.

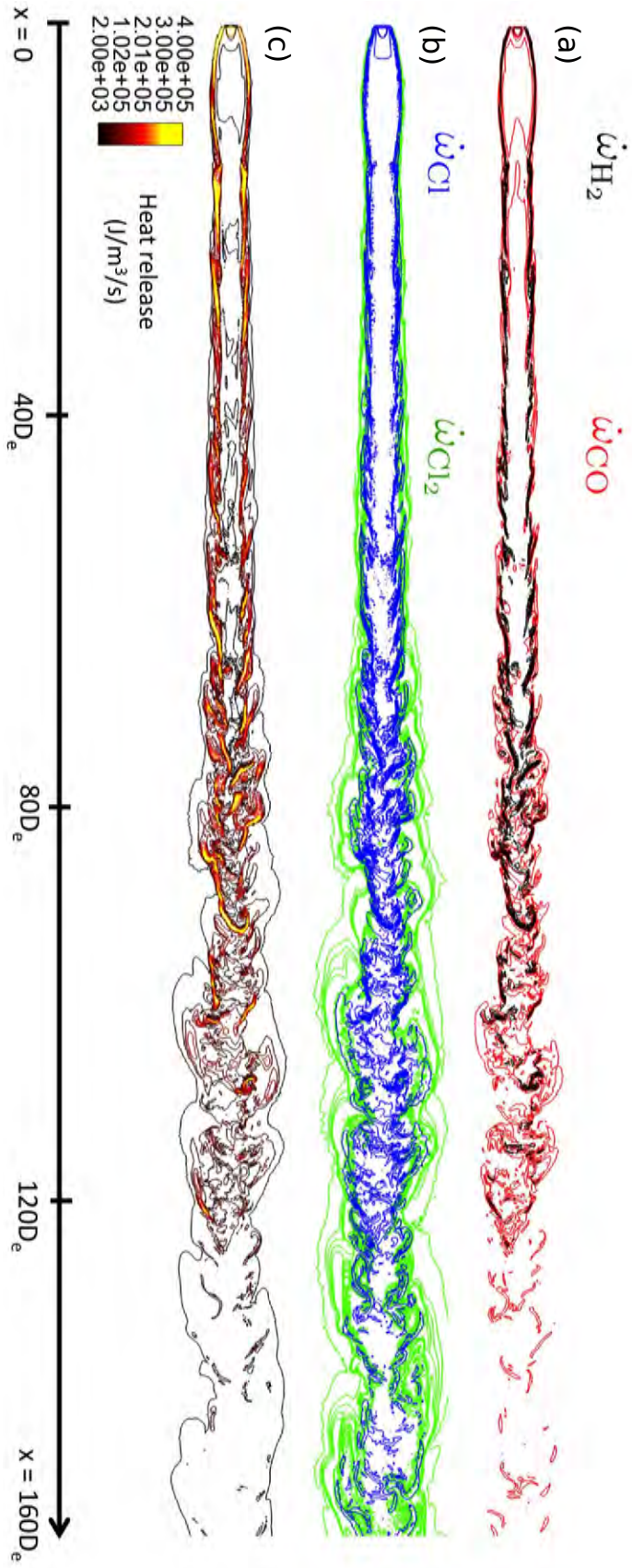

Figure 8.4 – Cuts of the jet showing (a) iso-contours of negative values of reaction rates $\dot{\omega}_{H_2}$ (black curves) and $\dot{\omega}_{CO}$ (red curves), (b) iso-contours of positive values of reaction rates $\dot{\omega}_{Cl}$ (blue curves) and $\dot{\omega}_{Cl_2}$ (green curves) and (c) iso-contours of instantaneous heat release.

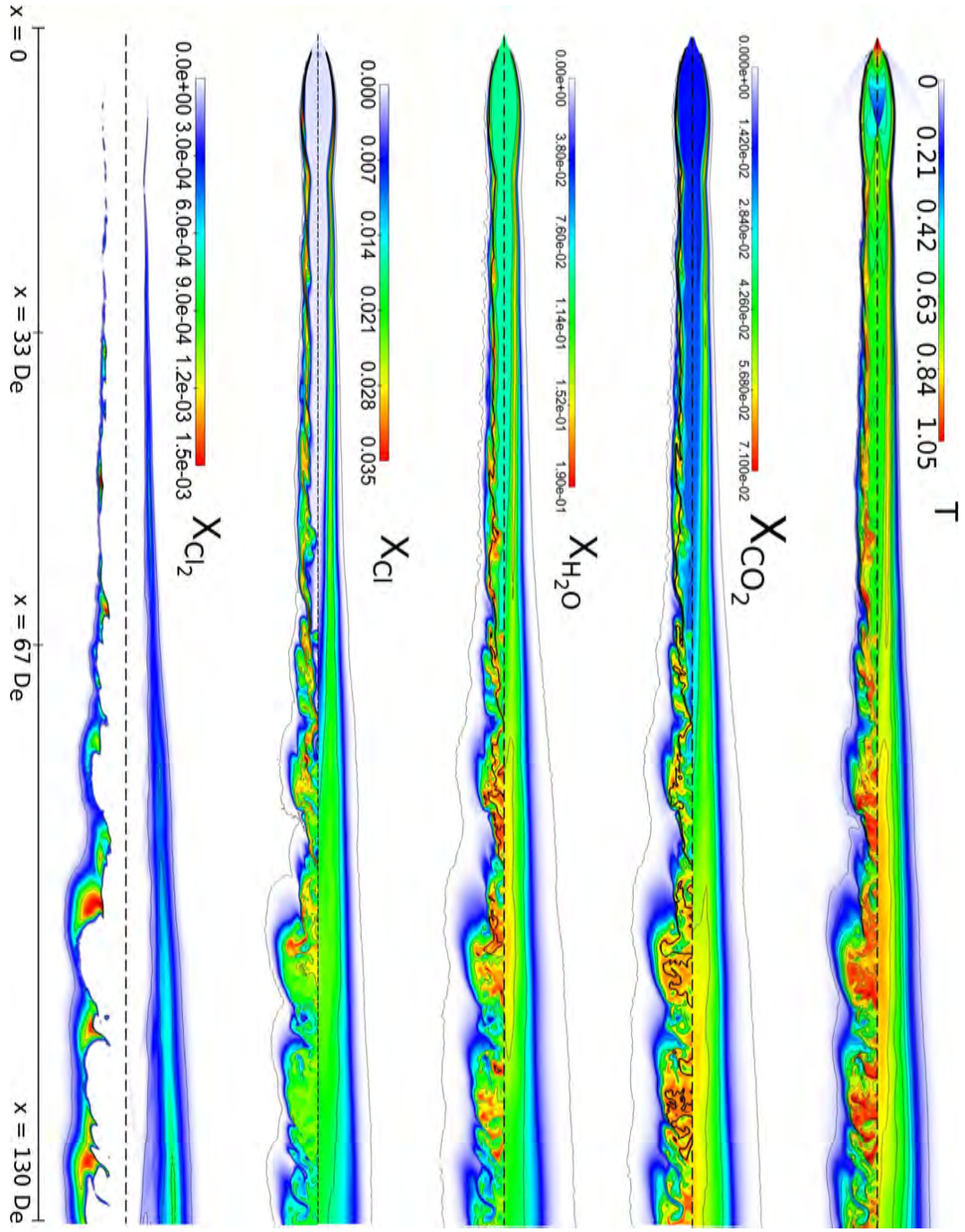

Figure 8.5 – Instantaneous (left half panels) and mean (right half panels) mole fractions of Cl, Cl_2, H_2O and CO_2 and temperature in the center plane of the jet. Five iso-contour lines are plotted for each species, equally spaced in the range $[10^{-4}, X_{max}]$. For the temperature, ten iso-contour lines are plotted equally space in the range $[T_{min}, T_{max}]$. Ths iso-contours $z_{\mathrm{H}} = z_{st,\mathrm{H}}$ and $z_{\mathrm{C}} = z_{st,\mathrm{C}}$ (bold curves) are respectively plotted on the instantaneous views of $X_{\mathrm{H_2O}}$ and $X_{\mathrm{CO_2}}$. The jet is represented from the nozzle inlet to $130D_e$ downstream of the nozzle exit.

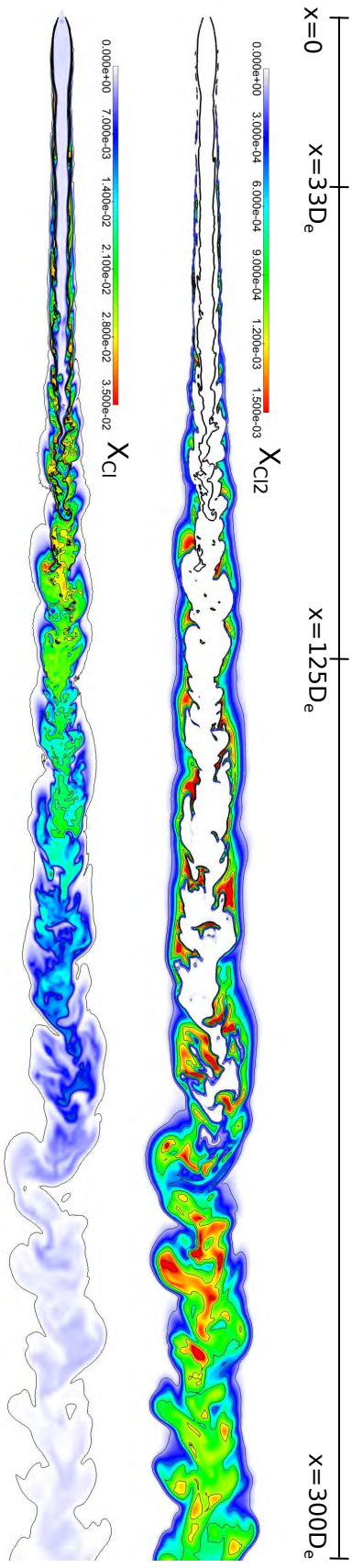

Figure 8.6 – Instantaneous mole fractions of Cl and Cl_2 in the center plane of the jet. Five iso-contour lines are plotted for each species, equally spaced in the range $[X_{min}, X_{max}]$. The jet is represented from the nozzle inlet to $300D_e$ downstream of the nozzle exit. The iso-contour $z_{st,H}$ is also represented (thick dark curve).

8.3 Species and temperature distribution

Figures 8.7 and 8.8 show the mean centerline profiles of mole fractions of CO_2, H_2O, chlorines species, temperature and heat release obtained from LES and the off-line model (using the reduced scheme). Figures 8.9-8.12 depict the mean radial profiles of these same parameters (except heat release), for three longitudinal locations: $x = 33D_e$, $x = 125D_e$ and $x = 300D_e$. For each mean variable, the interval of standard deviation is represented. It is important to note that the LES plots correspond to temporal and azimuthal averages, whereas the off-line model plots are purely spatial averages (with a spatial standard deviation). Therefore the standard deviations plotted from both models cannot be compared.

Despite a small averaging interval for the LES results (visible in the centerline profiles), both models give close profiles, particularly for the centerline profiles in Figs. 8.7 and 8.8 (except for the heat release, which presents a smaller peak value in LES). The outer part of the mixing layer, missing for the off-line simulations, is clearly modelled by the LES.

A few noticeable differences between the results given by both models can be pointed out. In the centerline profiles (Figs. 8.7 and 8.8), chemistry for reactive LES begins around $x = 60D_e$ (instead of $x = 80D_e$ for the off-line simulations), with a peak in temperature and products species H_2O, CO_2 and Cl at $x = 100D_e$ (instead of $x = 120D_e$). This means the potential core for the reactive LES is shorter, which results in shorter flames, as observed in Sec. 8.2.2. Furthermore, the mean radial profiles of temperature, X_{H_2O}, X_{CO_2} and X_{Cl} measured through the flame in the potential core region, at $x = 33D_e$ (Figs. 8.9 and 8.10), are wider for the reactive LES, and with a smaller peak value. The jet obtained with reactive LES is therefore larger. These differences can be attributed to two phenomena which are not take into account in the off-line model.

— molecular transport: in the reactive LES, molecular transport is modelled by a constant Schmidt number for each species. No transport is modelled in the off-line model itself, but its results include the transport modelled for the two species (equivalent exhaust gas and air) in the single-species LES. The transport model in the reactive LES is more accurate and takes into account the fact that radicals like O and H diffuse a lot more than other species, which enlarges the diffusion layer thickness.

— the effect of heat release on dynamics: the large heat release occurring in the mixing layer (see Fig. 8.2a) entails a dilatation of the gas, therefore a larger mixing layer. This phenomenon could also enhance entrainment of air into the jet, resulting in a faster development of turbulent structures and therefore a shorter potential core.

Concerning chlorine chemistry, in the near-field flame, Fig. 8.10 shows that at $x = 33D_e$, more Cl seems to be produced with the reactive LES (because of a wider reactive zone). As for Cl_2, the LES results depict a clear production from $r = 3r_e$. The entire profile of Cl_2 is modelled with LES, and corresponds well to the portion of radial profile obtained with the off-line model (even though with this selection of streamlines, it is difficult to judge the pertinence of the off-line model in this zone). Further downstream, the centerline profiles of X_{Cl} and X'_{Cl} (in Fig. 8.7) indicate a smaller production of Cl in the case of the reactive LES (the centerline profile of X_{Cl} reaches a maximum value of 0.0244 instead of 0.034). However, the radial profiles of X_{Cl} and X'_{Cl} (in Figs. 8.10 and 8.11) show that at $x = 125D_e$, the diffusion zone is larger for the LES results: the production of Cl seems less intense but occurs on larger radial distances. Beyond the combustion zone, in the far-field jet (for $x > 250D_e$), the centerline profile of variable X'_{HCl} obtained with LES (in Fig. 8.7) presents variations whereas no reaction involving HCl is supposed to

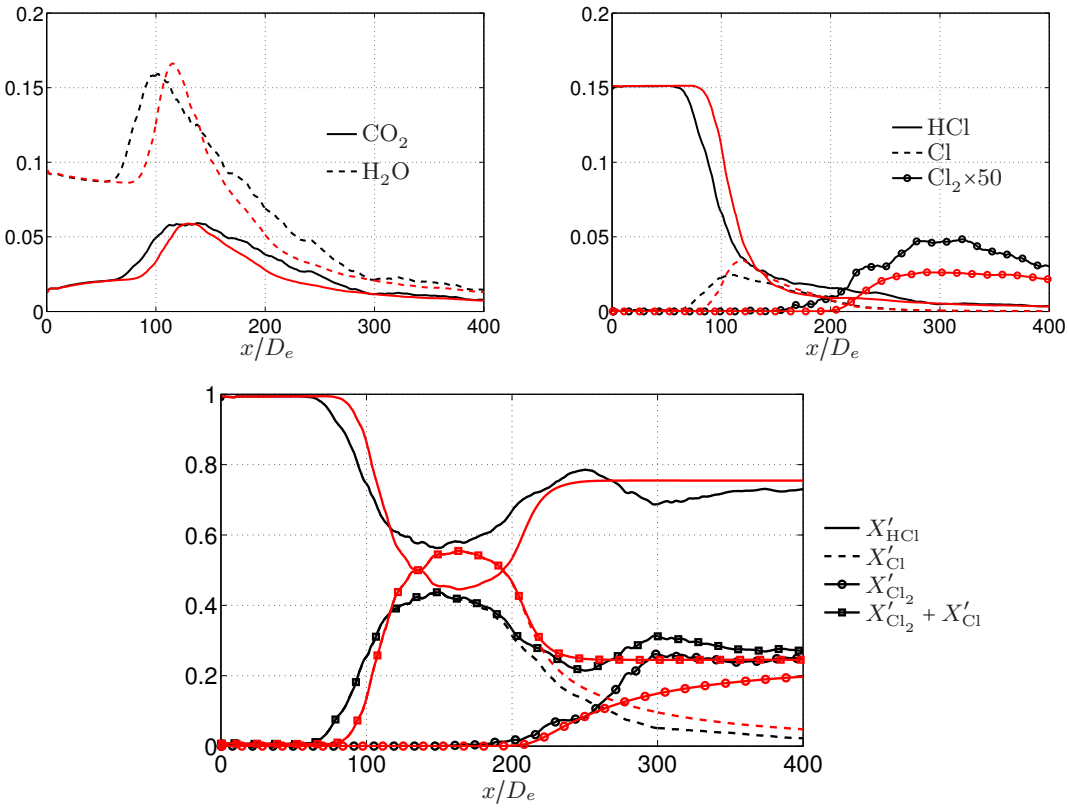

Figure 8.7 – Mole fractions of chemical species along the jet centerline obtained from averaged LES (dark lines) and the off-line model (red lines).

occur (due to the absence of radicals in this region). This is caused by the lack of time averaging of the results. Furthermore, the simulation has certainly not totally converged for $x > 300D_e$. The results in this region are therefore to be considered with caution, and more computations are required to draw definitive conclusions regarding differences between both models. However, the profile of fraction of active chlorine $X'_{Cl}+X'_{Cl_2}$ obtained with the reactive LES follows closely those of the off-line model, with slightly higher values (around 0.28 instead of 0.245).

Finally, the description of chlorine chemistry obtained with the reactive LES is more complete compared to those of the off-line model. This is due to the fact that the conversion from Cl to Cl_2 mainly occurs in the outer part of the mixing layer, a region not crossed by any of the streamlines used in the off-line model. More generally, Figs. 8.9-8.12 clearly point out that the radial representation of the jet offered by the off-line model decreases with the downstream distance. At $x = 33D_e$, the off-line model describes around 70% of the jet. At $x = 300D_e$, this percentage drops to 50%.

8.4 Heterogeneity of the chemistry for the near-field jet

The measurements of temperature and species concentrations in the flame over a long period of time reveal important information regarding mixing in the flame and reaction progress. Three probes were placed in the plan $x = 33D_e$ in the vicinity of the flame, at $z = 2.5r_e$, $z = 3.0r_e$ and $z = 3.6r_e$. Measurements of the flow parameters were taken every $1\mu s$ during $0.03s$. The results are plotted as a function of the mixture fractions z_H, z_C

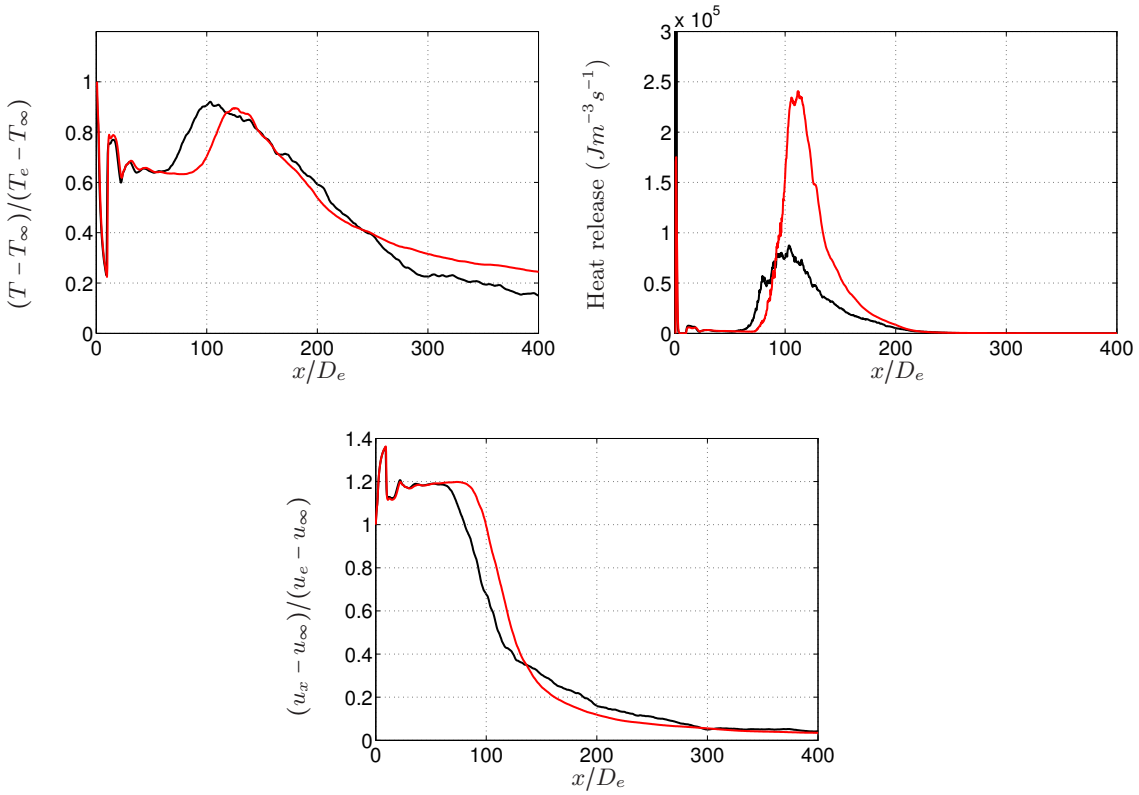

Figure 8.8 – Temperature, heat release and axial velocity along the jet centerline obtained from averaged LES (dark lines) and the off-line model (red lines).

and z_{Cl} in Figs. 8.13 and 8.14.

First, the measurements describe a very large range of mixture fractions. All chemical sub-mechanisms are represented (with the formation of H_2O, CO_2 and Cl), except the formation of Cl_2, which occurs for values of z_{Cl} smaller than 0.1. The temperature measured by the probes follows well the equilibrium curve. Species H_2O and CO_2 are also close to their respective equilibrium curves for high and low mixture ratios, but take lower values for mixture fractions close to stoichiometric values. As for radicals Cl and OH, their profiles are well above the equilibrium. These results correspond to a moderate non-equilibrium combustion (moderate because no flame extinction can be noticed), as already observed for instance by Bish and Dahm (1994) for simulations of H_2-air flames.

The measurements of the probes presented in Figs. 8.13 and 8.14 show very little fluctuations and rather follow large continuous curves whose shapes suggest an oscillation of the mixing layer. As previously mentioned, at this axial location, the mixing layer mainly undergoes the effect of velocity fluctuations imposed at the coflow inlet. This translates into slow, quasi-periodic movements represented by these curves. Further measurements downstream of this location (for instance at $x = 67D_e$, see Fig.8.3), where turbulence develops, and over longer periods of time, would be necessary to investigate the effect of turbulence on hot-plume chemistry.

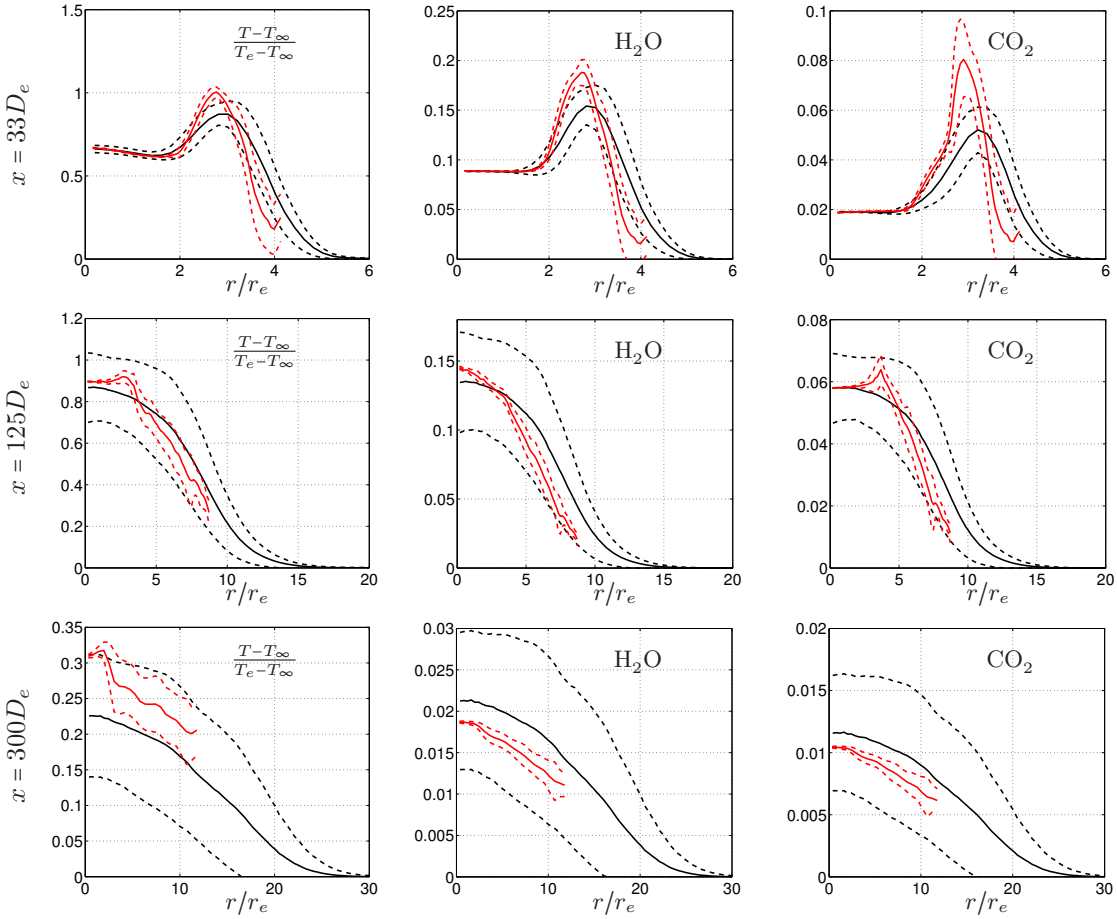

Figure 8.9 – Azimuthal averages (solid curves) and azimuthal averages plus/minus standard deviations (dashed curve) of temperature and mole fractions of species H_2O and CO_2 versus radial distance at $x = 33D_e$, $x = 125D_e$ and $x = 300D_e$ obtained from time-averaged LES (dark curves) and off-line model (red curves).

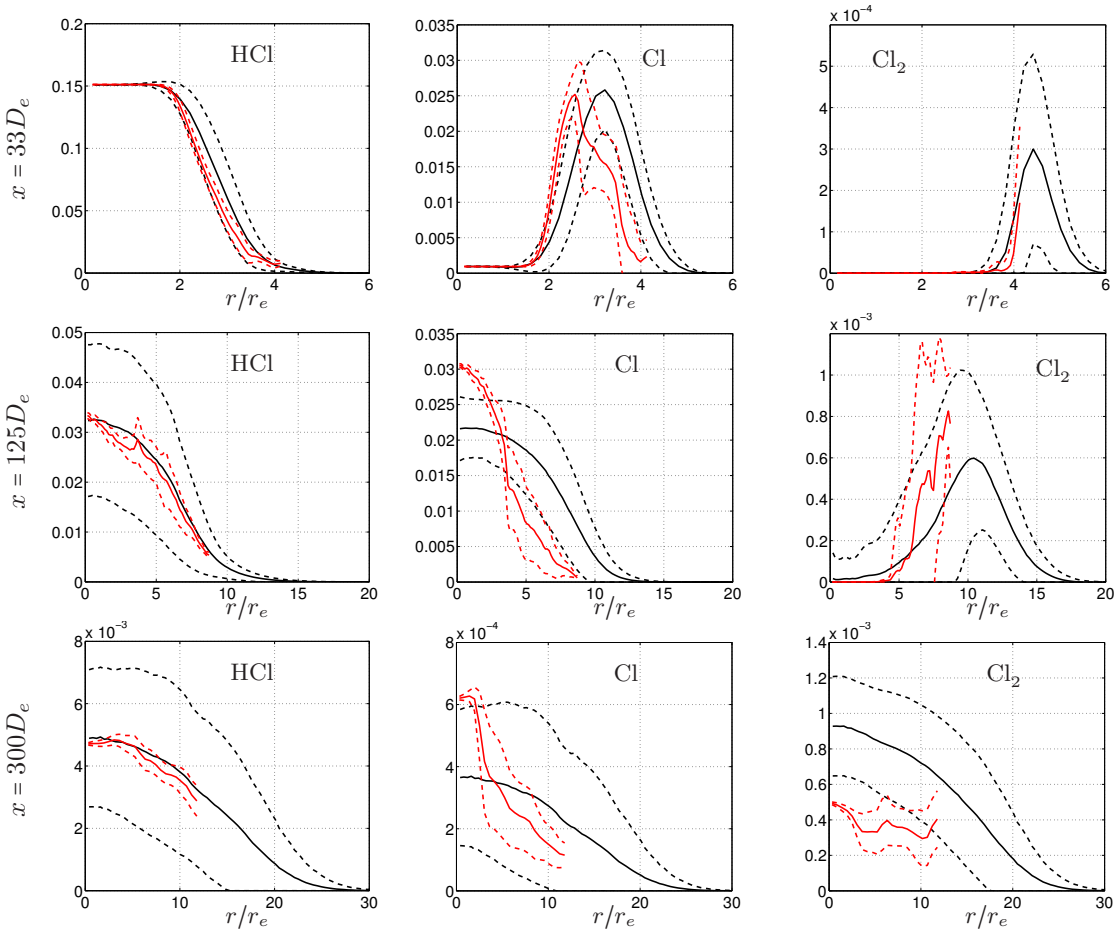

Figure 8.10 – Azimuthal averages (solid curves) and azimuthal averages plus/minus standard deviations (dashed curve) of mole fractions of species HCl, Cl and Cl_2 versus radial distance at $x = 33D_e$, $x = 125D_e$ and $x = 300D_e$ obtained from time-averaged LES (dark curves) and off-line model (red curves).

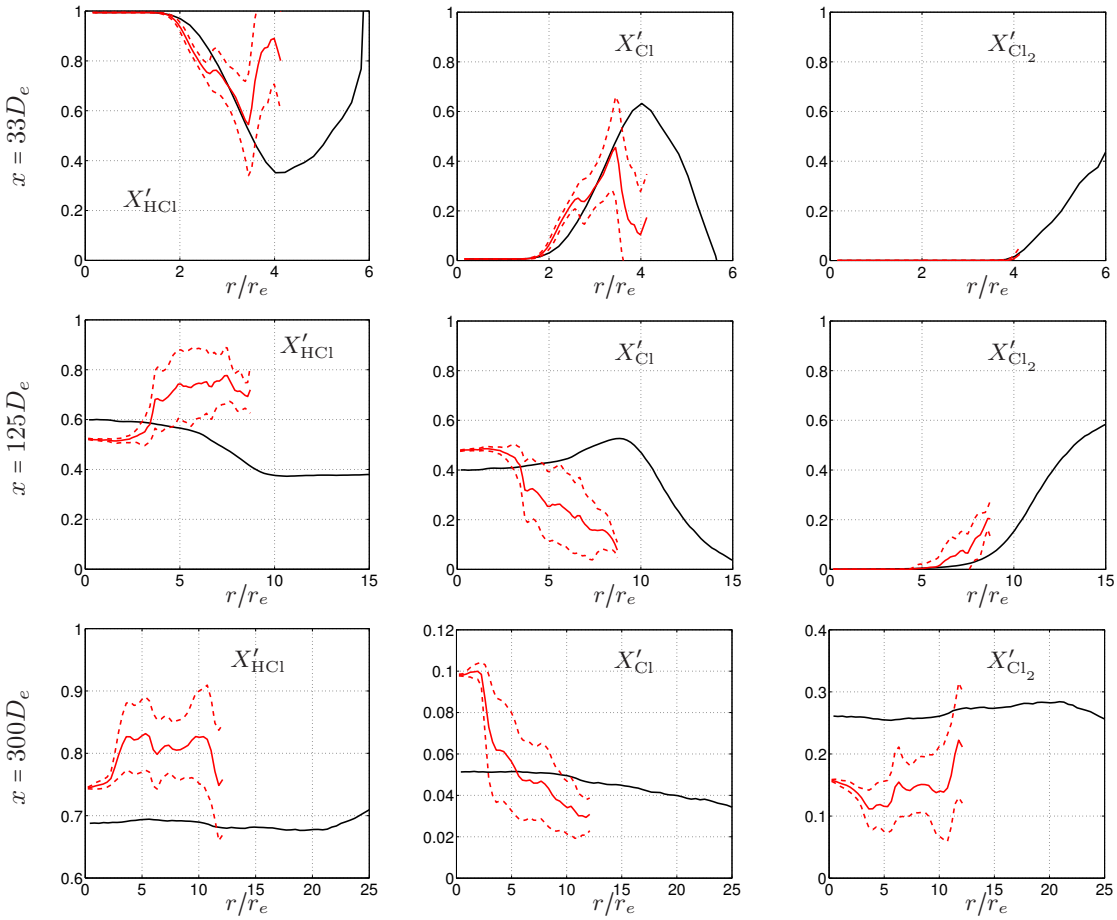

Figure 8.11 – Azimuthal averages (solid curves) and azimuthal averages plus/minus standard deviations (dashed curve) of mole fractions X'_{HCl}, X'_{Cl} and X'_{Cl_2} versus radial distance at $x = 33D_e$, $x = 125D_e$ and $x = 300D_e$ obtained from time-averaged LES (dark curves) and off-line model (red curves).

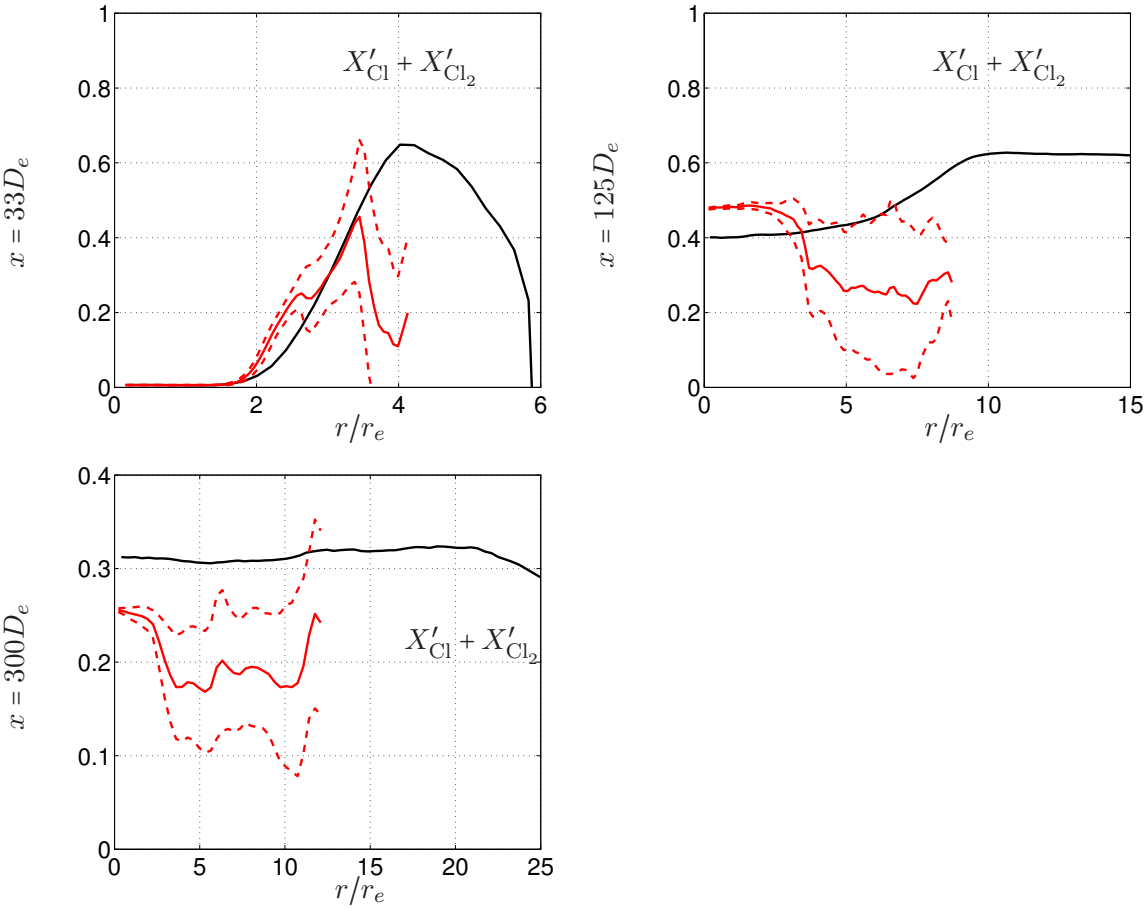

Figure 8.12 – Azimuthal averages (solid curves) and azimuthal averages plus/minus standard deviations (dashed curve) of mole fractions $X'_{Cl} + X'_{Cl_2}$ versus radial distance at $x = 33D_e$, $x = 125D_e$ and $x = 300D_e$ obtained from time-averaged LES (dark curves) and off-line model (red curves).

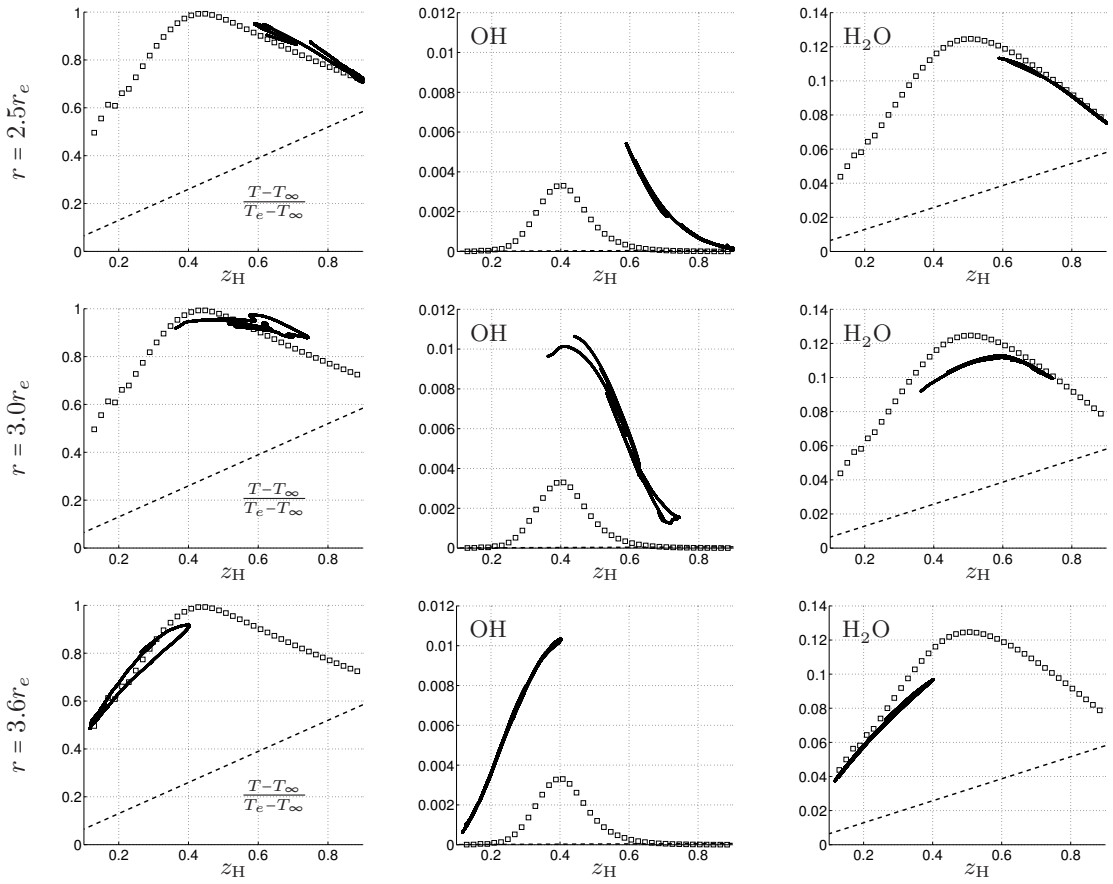

Figure 8.13 – Temperature and mass fractions of species OH and H_2O versus mixture fraction z_H measured by probes located at three radial positions $r = 2.5r_e$, $r = 3.0r_e$ and $r = 3.6r_e$ for the longitudinal position $x = 33D_e$ (solid curve). Equilibrium (squares) and mixing lines (dashed curve) are also included.

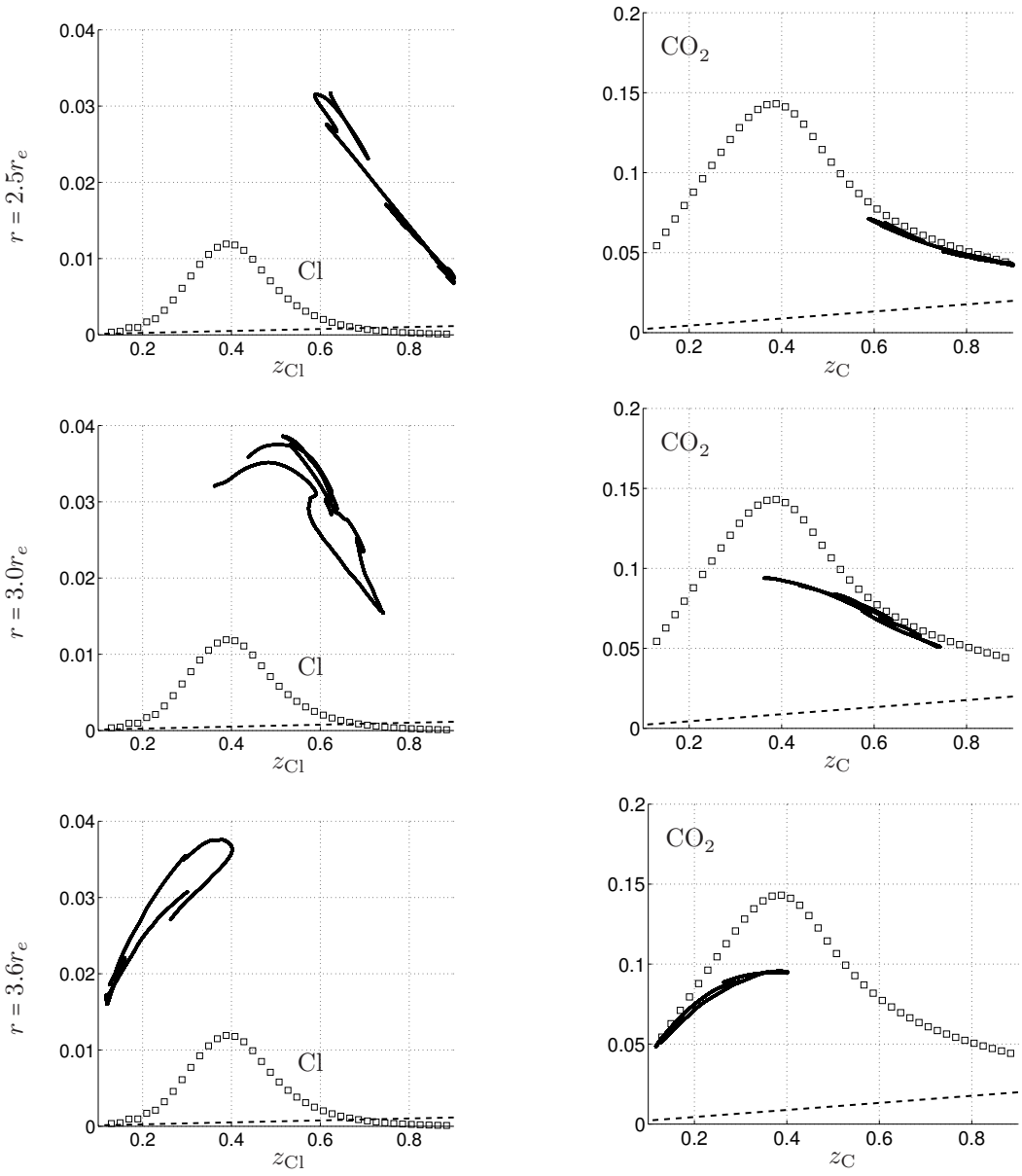

Figure 8.14 – Temperature and mass fractions of species Cl and CO_2 versus mixture fraction z_{Cl} and z_{C} measured by probes located at three radial positions $r = 2.5r_e$, $r = 3.0r_e$ and $r = 3.6r_e$ for the longitudinal position $x = 33D_e$ (solid curve). Equilibrium (squares) and mixing lines (dashed curve) are also included.

8.5 Need for a diffusion flame model

8.5.1 Inaccuracies of LES for diffusion flames

As defined in Sec. 5.1.5, non-premixed flames have no intrinsic length scales. For laminar flames, Eqs. 5.14 and 5.15 relate the diffusion and reaction thickness to flow conditions. For turbulent flows, the flame front is wrinkled by turbulent structures. Assuming homogeneous and isotropic turbulence, the smallest scale (associated to the shortest turbulent time) found in the flow is the Kolmogorov scale η_k, controlled by the viscosity ν and by the dissipation rate ϵ of the kinetic energy k (Kolmogorov, 1941):

$$\eta_k = \left(\frac{\nu^3}{\epsilon}\right)^{1/4} \tag{8.1}$$

The diffusion thickness l_d (and the corresponding flow time scale τ_f) is then assumed to be determined by the Kolmogorov scale:

$$l_d \approx \eta_k \tag{8.2a}$$

$$\tau_f \approx \tau_k \tag{8.2b}$$

where τ_k is the Kolmogorov time scale. For LES, the smallest resolved scale corresponds to the cutoff length scale l_{cut}, with $l_{cut} > \eta_k$. Equations (8.2a) and (8.2b) become (Rocchi, 2014)

$$l_d^{\mathrm{LES}} \approx l_{cut} \tag{8.3a}$$

$$\tau_f^{\mathrm{LES}} \approx \frac{1}{\widetilde{\chi}_{st}} \approx \tau_{cut} \tag{8.3b}$$

where $\widetilde{\chi}_{st}$ is the stoichiometric value of the resolved scalar dissipation rate. Equations (8.3a) and (5.15) give the following expression for the reaction thickness:

$$l_r^{\mathrm{LES}} \approx l_{cut} \left(D_a^{fl}\right)^{-1/\alpha} \tag{8.4}$$

This analysis leads to two main consequences (Rocchi, 2014). First, as the integrated reaction rates and heat release are proportional to $\sqrt{\chi_{st}} = \sqrt{D_{st}}/l_d$ (see Sec. 5.3.3), the over-estimation of the resolved flame thickness l_d^{LES} results in a smaller scalar dissipation rate χ_{st}^{LES}, therefore in a flame which does not burn at the right speed. This is illustrated in Fig. 8.15a. Secondly, the smaller values for χ_{st}^{LES} compared to the real flame entails a larger Damköhler number, which makes the flame less sensitive to turbulence, therefore less wrinkled (see Fig. 8.15b). The surface of the flame is smaller than for the real flame which, again, induces error on the burning rate. For the present simulation, this could lead to an under-estimation of the production of Cl in the combustion zone, and therefore of active chlorine in the cold plume.

8.5.2 Modelling non-premixed turbulent flames

A common approach to simulate premixed flame in LES is the thickened flame model. Initially proposed by Butler and O'Rourke (1977), this method consists in artificially thickening the flame front in order to propagate it on a coarse mesh. This operation causes the flame to be less wrinkled (Angelberger et al., 1998; Colin et al., 2000), therefore an efficiency function is derived to account for this effect. This model, called TFLES

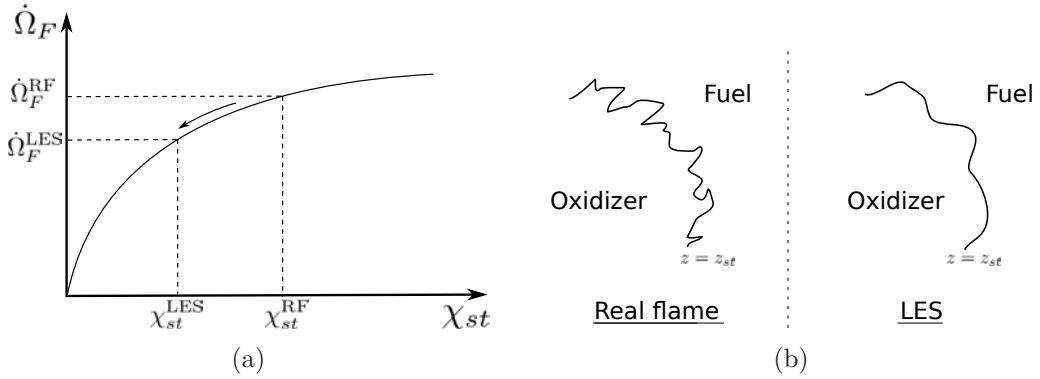

Figure 8.15 – Effect of LES filtering on a diffusion flame: under-estimation of the resolved scalar dissipation rate χ_{st}^{LES} compared to the real flame χ_{st}^{RF} (a) and under-estimation of the flame surface density (b).

(Thicken Flame for Large Eddy Simulation), has been extended to solve partially premixed flame (Légier, 2001; Kuenne et al., 2011), using a sensor ensuring that flame thickening occurs only in the reaction zone. This Dynamic Thickened Flame for LES (DTFLES) model is theoretically not correct for non-premixed flames, as pointed out by Poinsot and Veynante (2005). However, in many applications, turbulent diffusion flames exhibit local premixed flames behaviors. When the stoichiometric mixture fraction z_{st} is low (which is case for many industrial flames), a strong mixing between fuel and oxidizer can have the time to occur before combustion starts. The resulting flame does not lie exactly around the stoichiometric iso-surface as expected for a classic diffusion flame, but instead corresponds to a partially premixed regime. In these cases, the DTFLES model gives correct predictions. The present flame, however, seems to behave like a diffusion flame: the reaction zones lies around the stoichiometric iso-surfaces (see Fig. 8.3), and the values for stoichiometric mixture fractions are high ($z_{st,H} \approx 0.56$ and $z_{st,C} \approx 0.36$). *A priori*, the DTFLES model will not be able to handle correctly this flame. The approach proposed by Rocchi (2014) constitutes an interesting alternative. It aims to correct the integrated heat release and reaction rates by modelling the subgrid-scale scalar dissipation rate χ_{SGS} and the subgrid-scale wrinkling factor (in a similar fashion as for DTLES). The first tests conducted on a two-dimensional reactive mixing layer gave encouraging results (Rocchi, 2014), even if further investigations would be needed (for instance concerning the relevance of the wrinkling function) before an application to the present simulation.

8.6 Comparison of the results with previous studies

The results obtained with LES and the off-line model are qualitatively coherent with previous work on SRM exhaust plume modelling. First, all chemical processes of the hot plume identified in the literature (Zittel, 1994; Calhoon, 1998) were observed: production of water and carbon dioxide due to the H_2-CO combustion and large conversion of HCl to Cl and Cl_2, this latest phenomenon being the most important regarding ozone depletion in the cold plume.

To the best of our knowledge, there is no previous simulation corresponding to the configuration tested in the present study, therefore no precise validation of the levels of

active chlorine modelled by the reactive LES is possible. However, several studies focusing on the Titan IV hot plume give estimations of the fraction of converted HCl at 20 km of altitude. These values can be used for a coarse comparison, keeping in mind that the process of chlorine activation for a given altitude varies with the propellant composition, the thermodynamics properties in the combustion chamber, the nozzle shape, the launcher velocity and the level of turbulence induced by the launcher body. These parameters determine the SRM jet dynamics, which influence largely the hot-plume chemistry. Zittel (1994) conducted reactive simulations of the hot plume using the SPF (Standard Plume Flowfield) code and obtained a conversion of 37% of HCl to Cl_2. These results are corroborated by a laboratory study (Burke and Zittel, 1998), which produced H_2-CO-O_2 premixed flames and found a HCl loss of 38% in the conditions of a Titan IV plume at 20 km of altitude. If these two study show coherent results, they are to be considered with caution as direct measurements in the plume of a Titan IV revealed a lower conversion rate of HCl. Overall, these figures are of the same order of magnitude than the present results (between 24 to 30%) considering the margin of error due to the uncertainties on the chemical rate constants.

8.7 Conclusion

The present simulation of a reactive SRM jet is among the first simulations of an exhaust rocket wake on such a long domain combined with the accuracy of LES. However, the implementation of a model for diffusion flame appears a necessary step in order to account for the under-estimation of the burning rates and of the flame surface density due to LES filtering.

The analysis of the reactive LES jet allowed the identification of important inaccuracies in the results of the off-line model. First, the radial representation of the jet offered by the off-line model is not enough to describe properly the reactive flow-field. As previously mentioned, this issue can certainly be improved by an alternative selection of streamlines used as an input for the model. However, the molecular transport and the two-way coupling between heat release and jet dynamics, two phenomena proved to have an important impact, cannot be taken into account in the off-line model.

Finally, the lack of experimental results or previous simulations in similar conditions does not allow a precise comparison and validation of the species distributions. However, the results are found to be coherent, in terms of order of magnitudes of active chlorine concentrations, with previous studies on different launchers.

Conclusions and future prospects

Conclusions

It is known that chemical reactions occurring in the hot-plume of Solid Rocket Motors (SRMs) are responsible for a local destruction of stratospheric ozone. A second combustion takes place between the engine emissions and ambient air. This partially converts hydrogen chloride, present in the exhaust plume, into active chlorine species, which react with ozone in a catalytic cycle during minutes to hours after the passage of the rocket. Until now, the most accurate simulations of SRM hot plume were conducted using the RANS technique. The purpose of this study was to use Large Eddy Simulation to model the SRM jet dynamics and chemistry at 20 km altitude, over a long downstream distance, with the objective to provide a more reliable distribution of chlorine species.

The first challenge of this work was to conduct LES of the SRM nozzle flow and exhaust plume on a long domain while ensuring an affordable computational cost. As the LES solver is explicit, the computation of the nozzle flow entails a smaller time step which penalizes the entire simulation. To overcome this difficulty, the MISCOG method was applied to couple two computational subdomains, each one running with its own time step. LES of a single-species jet were performed to validate this technique. The flow dynamics of the resulting jet was thoroughly analyzed. The typical regions of a supersonic under-expanded jet were identified and their properties correspond well to current knowledge. In particular, this simulation was able to model a large portion of the self-similar region of a supersonic coflowing jet, which is usually only available through experiment. The analysis of the mean and turbulent flow conducted in this region can prove useful for future simulations of supersonic jets. The use of the MISCOG method reduced the computational cost by a factor of five, without introducing noticeable error in the simulation. This method can therefore be applied to LES of a reactive SRM jet but also, more generally, to a large range of multi-scale simulations.

The second step of this study was to implement an off-line chemical model, able to evaluate the hot-plume chemistry along streamlines extracted from a time-averaged flow-field from LES of a single-species SRM. This model does not completely represent the mixing layer and cannot model species segregation due to complex transport. However, despite these inaccuracies, it was still able to provide relevant results, featuring all chemical sub-mechanisms: the oxidation of the chemical species H_2 and CO by the ambient dioxygen, and the partial conversion of hydrogen chloride HCl into active chlorine Cl and Cl_2.

With the objective to run LES of the SRM jet including a full coupling with the hot-plume chemistry, the chemical mechanism previously applied with the off-line model was reduced to ensure a minimum impact on the computational cost. Classic tests on laminar diffusion flames were conducted to verify the accuracy of the reduced scheme in

the conditions of the SRM jet at 20 km of altitude. The off-line model was applied using the reduced scheme, providing results very close to those given by the reference chemical scheme.

Finally, the reduced chemical scheme was implemented to conduct LES of the multi-species reactive SRM jet. Including 13 species and reactions, this simulation probably represents the most accurate description of a SRM jet achieved so far. Modeling the molecular transport and the two-way coupling between turbulent combustion and jet dynamics made the species and temperature distributions more accurate compared to the off-line results. However, the results offered by both models are close enough to confirm the relevance of the off-line model. It can therefore be applied to future single-species jet simulations in order to evaluate rapidly one (or several) chemical mechanisms.

Future prospects

Improving modeling of the SRM jet

The LES of a reactive SRM jet presented in Chapter 8 modeled a diffusion flame. Constraints on CPU cost prevented the use of a grid fine enough to represent the flame with accuracy. The application of a combustion model relevant to diffusion flame seems necessary, as it may have an impact on the fraction of active chlorine produced due to afterburning. Such model is yet to be implemented in AVBP.

Concerning modeling of the hot-plume chemistry, further investigation should be pursued as for reactions involving chlorine-containing species. The choice of reactions varies between studies, and the important impact of inaccuracies on the reaction rate constants of several reactions for high temperatures was pointed out in this study. Secondly, further chemical scheme reduction should be considered, for instance by applying the Quasi-Steady State Approximation. This effort could lead to a smaller number of equations and species, resulting in a non-negligible reduction in computational cost.

The impact of particles on local and global ozone loss is still to be determined, and is the subject of ongoing research by CNES. Direct measurements in the plume of each launcher of interest are necessary to determine the size and surface density of alumina particles. Concerning LES of reactive SRM jet, particles should be included in the simulation using a Lagrangian or Eulerian approach to assess their effect on production of active chlorine.

The off-line model offered a relevant evaluation of the hot-plume chemistry, using only averaged results of LES of a single-species SRM jet. As such, this model could be improved for a better radial representation of the jet and used for future jet simulations. It can be particularly useful to apply rapidly different chemical schemes or, like in this study, to test reduced chemical schemes.

Simulation of the SRM cold plume: assessing the local impact of a SRM on ozone

The step following the present research naturally consists in conducting simulations of the SRM cold plume and its interactions with the atmosphere. Using an atmospheric (preferably LES) solver and the results of the LES of a reactive SRM jet as initial conditions, this work would lead to a precise evaluation of the profiles of ozone in the plume during minutes to hours after the passage of the rocket.

This chain of computations, from the small scales of the hot supersonic plume to the larger scales of the cold plume, should be applied to various altitudes, typically up to 40 km. The impact of different SRMs should also be assessed, as direct measurements in

rockets plumes showed that the impact of SRMs on ozone was not proportional to the SRM size (this is due to the non-linearity of chemistry). Large Eddy Simulations would also be particularly relevant to model the hot plume of rockets using multiple SRMs, and more precisely the turbulent interactions between the supersonic jets.

Towards a measurement campaign

Direct measurements in SRM plumes would bring essential information to complete and validate simulations. As previously mentioned, they are necessary to evaluate the size distribution (therefore obtain the surface density) of alumina particles, which varies with the type of SRM and the altitude. Then this data can be used to model heterogeneous chemistry on alumina surface in hot plume and cold plume simulations. Measurements of ozone and chlorine containing species Cl_2/ClO would validate the chemistry modeling, and measurements of CO_2, a species which is inert in the cold plume, would be used to evaluate the dilution of the plume. Measurements in rocket plumes at high altitudes require substantial resouces. Precedent campaigns used the NASA WB-57F aircraft [1] (see Fig. 8.16) which has the ability to fly at altitudes above 60,000 feet. An alternative could be to employ drones.

From the ground, it is also possible to conduct measurements of plume expansion at high altitudes. Such measurements were conducted in the past using electronic images of polarized, near-infrared solar radiation scattered from the exhaust particles (Beiting, 1999). They would be very useful to validate the plume expansion in simulations of cold plumes.

Figure 8.16 – The NASA WB-57F aircraft during the ACCENT campaign (photo taken by Paul A. Newman and Tom Kucsera of NASA/GSFC).

1. http://jsc-aircraft-ops.jsc.nasa.gov/wb57/

Conclusions et perspectives

Conclusions

Les réactions chimiques se produisant dans le panache chaud des moteurs à propergol solide sont connues pour être responsables d'un appauvrissement local de l'ozone stratosphérique. Une post-combustion se produit entre les émissions du moteur et l'air ambiant. Cela conduit à la conversion partielle de l'acide chlorhydrique, présent en grande quantité dans le panache, en chlore actif capable de réagir avec l'ozone dans un cycle catalytique durant plusieurs minutes à plusieurs heures après le passage de la fusée. Jusqu'à présent, les simulations de panache chaud les plus précises ont été réalisées à l'aide de la méthode RANS. L'objectif de la présente étude était d'utiliser la technique de Simulation aux Grandes Echelles (SGE) afin de modéliser avec le plus de précision possible la dynamique et la chimie d'un jet de moteur à propergol solide à une altitude de 20 km, sur des distances très longues.

La première étape de ce travail était de réaliser une SGE de l'écoulement de la tuyère et du jet sur un long domaine tout en assurant un coût de calcul abordable. Le solveur SGE étant explicite, le calcul de l'écoulement dans la tuyère impose un pas de temps plus petit, ce qui pénalise l'ensemble de la simulation. Afin de surmonter cette difficulté, la méthode MISCOG a été appliquée pour coupler deux sous-domaines de calcul, ayant chacun leur propre pas de temps. Une SGE d'un jet à deux espèces (une pour l'air, une pour les gaz d'émission) a été conduite pour valider cette technique. Les propriétés dynamiques du jet obtenu ont été soigneusement analysées. Les zones typiques d'un jet supersonique sous-détendu ont été identifiées et leur caractéristiques correspondent bien aux connaissances actuelles. En particulier, la simulation a été capable de modéliser une large portion de la région auto-similaire du jet supersonique à co-écoulement, ce qui n'est habituellement accessible qu'à travers l'expérimental. L'analyse de l'écoulement moyen et turbulent réalisé dans cette zone s'est révélée utile pour de futures simulations de jets supersoniques. L'utilisation de la méthode MISCOG a permis de réduire le coût de calcul d'un facteur 5, sans introduire d'erreur notable dans les calculs. Cette méthode peut donc être appliquée à une SGE d'un jet de moteur à propergol solide réactif mais aussi, plus généralement, à une large sélection de simulations multi-échelle.

La seconde étape de cette étude consistait à implémenter un modèle de chimie "hors-ligne", capable d'évaluer la chimie du panache chaud le long de ligne de courant extraites d'un écoulement moyenné dans le temps résultant de la SGE à deux espèces décrite précédemment. Ce modèle ne représente pas complètement la couche de mélange et ne peut modéliser la ségrégation des espèces due au transport complexe. Cependant, en dépit de ces inexactitudes, il s'est toutefois montré capable de produire des résultats pertinents en modélisant tous les sous-mécanismes chimiques : l'oxydation des espèces chimiques H_2 et CO par l'oxygène et la conversion partielle d'acide chlorhydrique en chlore actif Cl et Cl_2.

Avec l'objectif de réaliser une SGE du jet de moteur à propergol solide incluant la chimie du panache chaud, le mécanisme chimique précédemment appliqué avec le modèle de chimie hors-ligne a été réduit afin d'assurer un impact minimum sur le coût de calcul. Une série de tests classiques a été conduite pour vérifier la précision du schéma réduit dans les conditions du jet à 20 km d'altitude. Le modèle hors-ligne a également été appliqué en utilisant le schéma réduit, produisant des résultats très proches de ceux obtenus avec le schéma chimique de référence.

Enfin, le schéma réduit a été implémenté pour réaliser une SGE du jet réactif et multi-espèces. La modélisation du transport moléculaire et du couplage entre combustion turbulente et dynamique du jet ont permis d'obtenir des distributions de la température et des espèces chimiques plus précises que celles du modèle hors-ligne. Cependant, les résultats des deux modèles sont assez proches pour confirmer la pertinence du modèle de chimie hors-ligne. Il peut donc être appliqué sur de futures simulations non réactives afin d'évaluer rapidement l'effet d'un (ou de plusieurs) mécanisme chimique.

Perspectives

Amélioration de la modélisation du jet de moteur à propergol solide

La simulation aux grandes échelles d'un jet réactif de moteur à propergol solide présenté dans le chapitre 8 modélise une flamme de diffusion. Les limitations en temps de calcul ont empêché l'utilisation d'un maillage suffisamment fin pour représenter la flamme avec la précision requise. Il est donc nécessaire d'évaluer l'erreur induite par l'utilisation d'un tel maillage (et en particulier l'impact sur la distribution des espèces chlorées) et, le cas échéant, d'implémenter un modèle de combustion pertinent pour les flammes de diffusion.

Concernant la modélisation de la chimie du panache chaud, des études complémentaires doivent être menées concernant les réactions mettant en jeu les espèces chlorées. Le choix des réactions à considérer varie selon les études, et un impact important des incertitudes concernant les constantes de vitesse de certaines réactions sur la distribution des espèces chlorées a été relevé dans ces travaux. De nouvelles études en laboratoire sont donc nécessaires pour lever ces incertitudes. D'autre part, la réduction du schéma chimique pourrait être approfondie, notamment par l'application de l'approximation quasi-stationnaire. Cela pourrait permettre de réduire le nombre d'équations et d'espèces, et ainsi le coût CPU du calcul.

L'impact des particules sur l'appauvrissement local et global d'ozone reste très incertain. Des mesures directes dans le panache de chaque lanceur sont nécessaires pour déterminer la taille et la densité de surface des particules d'alumine. Ces paramètres déterminent l'intensité de la chimie hétérogène ayant lieu en surface de ces particules, la distribution des particules dans le jet et la quantité d'alumine qui restera dans la stratosphère pendant de longues durées. Concernant les simulations aux grandes échelles, les particules d'alumine doivent être incluses aux calculs en utilisant une approche lagrangienne ou eulérienne et la chimie hétérogène sur ces particules doit être modélisée afin de déterminer son effet sur la production de chlore actif.

Le modèle "hors-ligne" offre une évaluation pertinente de la chimie du panache chaud en utilisant seulement une solution moyenne de la simulation aux grandes échelles du panache non réactif. En conséquence, ce modèle pourrait être amélioré pour apporter une meilleure représentation radiale du jet et utilisé pour de futures simulations de jets. Il peut être particulièrement utile pour appliquer rapidement différents schémas chimiques ou, comme pour cette étude, afin tester des schémas réduits.

Simulation du panache froid d'un moteur à propergol solide : évaluation de son impact local sur l'ozone

L'étude et la modélisation du panache chaud doivent naturellement être suivies par des simulations du panache froid et de ses interactions avec l'atmosphère. En utilisant un solveur atmosphérique (de préférence implémentant la technique de simulation aux grandes échelles) ainsi que les résultats des simulations aux grandes échelles du jet supersonique réactif, ce travail devrait mener à une évaluation précise des profiles d'ozone dans le panache pendant les premières heures après le passage du lanceur.

Cette chaîne de calcul, qui couvre les plus petites échelles du panache supersonique aux larges échelles du panache froid, devrait être appliquée à différentes altitudes, typiquement jusqu'à 40 km, afin d'obtenir une évaluation de l'évolution de la concentration d'ozone sur toute une colonne. L'impact de différents types de lanceurs devrait aussi être calculé, car des mesures directes dans les panaches de lanceurs ont montré que l'impact des moteurs à propergol solide sur l'ozone n'est pas proportionnel à la taille du moteur (cela est dû à la non-linéarité de la chimie). La technique des simulations aux grandes échelles serait aussi tout à fait adaptée à la modélisation du panache chaud de lanceurs utilisant plusieurs moteurs, et plus particulièrement aux interactions turbulentes entre les jets supersoniques.

Vers une campagne de mesure

Des mesures directes dans le panache des lanceurs apporteraient des informations essentielles pour compléter et valider les simulations. Ainsi, concernant l'alumine, il est nécessaire d'évaluer la distribution des tailles de particules dans le panache (on obtiendra ainsi la densité de surface), qui varie avec le type de lanceur et l'altitude. Ces informations peuvent ensuite être utilisées pour modéliser la chimie hétérogène à la surface des particules. D'autre part, des mesures des concentrations d'ozone et des espèces chlorées Cl_2 ou ClO permettrait de valider la modélisation de la chimie, et des mesures de la concentration en dioxyde de carbone, une espèce inerte dans le panache à l'équilibre thermique, donnerait une évaluation de la dilution du panache.

De telles mesures, à haute altitude, nécessitent un équipement spécial. Des campagnes précédentes ont mobilisé un WB-57F, un avion de la NASA capable de voler à des altitudes dépassant 60,000 pieds [2] (see Fig. 8.16). Les drones pourraient également constituer une sérieuse alternative.

Il est aussi possible de mener des mesures de l'expansion du panache au sol. De précédentes études ont utilisé des images de radiations solaires polarisées et dispersées depuis les particules d'alumine (Beiting, 1999). Ces mesures pourraient permettre de corroborer l'expansion du panache dans les simulations atmosphériques.

2. `http://jsc-aircraft-ops.jsc.nasa.gov/wb57/`

APPENDIX A

Computation of stagnation conditions P_0 and T_0

The values of P_0 and T_0 can be deduced from the relations describing one-dimensional isentropic flow of a perfect gas in a duct. Let us first compute the Mach number at the nozzle exit M_e. Assuming that the ratio of specific heats γ for the mixture is constant, M_e can be deduced from

$$\frac{A_e}{A_{th}} = \frac{1}{M_e}\left(\frac{2}{\gamma+1} + \frac{\gamma-1}{\gamma+1}M_e^2\right)^{(\gamma+1)/(2(\gamma-1))} \tag{A.1}$$

where A_e and A_{th} are respectively the cross-sectional area at the nozzle exit and the throat. The temperature at the nozzle exit T_e being imposed by the nozzle flow code, T_0 can be directly computed from

$$T_0 = T_e\left(1 + \frac{\gamma-1}{2}M_e^2\right) \tag{A.2}$$

The evaluation of P_0 requires the knowledge of P_e, the pressure at the nozzle exit. The ideal-gas law gives

$$P_e = \rho_e \frac{R}{W} T_e \tag{A.3}$$

Introducing the mass flow rate $\dot{m}$ in Eq. A.3 yields

$$P_e = \frac{\dot{m} R T_e}{u_e W A_e} \tag{A.4}$$

with u_e the velocity at the nozzle exit. For a perfect gas, the speed of sound c is defined as

$$c = \sqrt{\gamma \frac{R}{W} T}, \tag{A.5}$$

where R is the perfect gas constant. Therefore, knowing M_e and T_e, it is possible to deduce u_e:

$$u_e = M_e \sqrt{\gamma \frac{R}{W} T_e} \tag{A.6}$$

Replacing Eq. A.6 in Eq. A.4 gives

$$P_e = \sqrt{\frac{R T_e}{\gamma W}} \frac{\dot{m}}{M_e A_e} \tag{A.7}$$

The value of P_e can be directly computed from Eq. A.7. Then P_0 can be deduced from the one-dimensional isentropic relation

$$P_0 = P_e \left(1 + \frac{\gamma - 1}{2} M^2\right)^{\gamma/(\gamma-1)} \tag{A.8}$$

APPENDIX B

Spreading and centerline property decay rates of compressible supersonic jets

For compressible coflowing jets, the momentum equations and conservation of mass give the following expression for the momentum flow rate:

$$\dot{M} = \int_0^\infty 2\pi\rho u_x(u_x - u_\infty)rdr \tag{B.1}$$

where u_x and ρ are respectively the mean axial velocity and mean density. If external volume forces are negligible, $\dot{M}$ is constant in the jet. Let us define ϵ such as

$$\epsilon = (u_x - u_\infty)/u_\infty. \tag{B.2}$$

Then we obtain

$$u_x(u_x - u_\infty) = u_\infty^2\epsilon(1+\epsilon). \tag{B.3}$$

In the strongly advected regime far from the nozzle exit, $\epsilon \to 0$ and one can consider

$$\epsilon(1+\epsilon) \approx \epsilon \quad \text{or} \quad u_x(u_x - u_\infty) \approx u_\infty(u - u_\infty). \tag{B.4}$$

In the far field, the momentum flow rate (Eq. B.1) can be rewritten

$$\dot{M} = 2\pi u_\infty \int_0^\infty \rho(u_x - u_\infty)rdr \tag{B.5}$$

Figure B.1 shows that $\rho(u_x - u_\infty)$ is self-similar. Following the approach presented in Pope (2000), by defining $f = \rho(u_x - u_\infty)$, it is therefore possible to write

$$f(x,r) = f_0(x)g(\zeta), \tag{B.6}$$

where

$$\zeta = r/r_{1/2,f}(x), \tag{B.7}$$

and g is the similarity profile. Then Eq. B.5 becomes

$$\dot{M} = 2\pi u_\infty f_0(x) r_{1/2,f}^2(x) \int_0^\infty g(\zeta)\zeta d\zeta \tag{B.8}$$

As the momentum flow rate does not vary with x, if f scales with $x^{-2/3}$, $r_{1/2,f}$ has to scale as $x^{1/3}$.

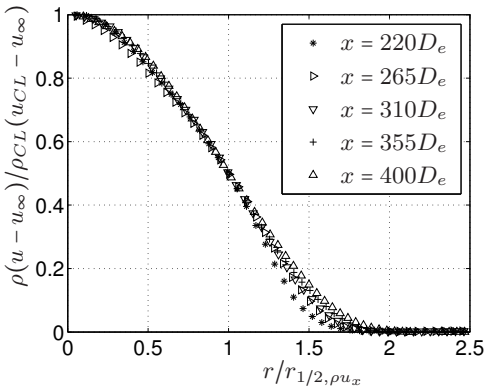

Figure B.1 – Mean normalized profiles of $\rho(u - u_\infty)$.

APPENDIX C

Equations for a fixed-mass, constant pressure reactor

We consider a constant pressure, fixed-mass, adiabatic reactor. For such a system, the first law of thermodynamic yields

$$dH = 0 \tag{C.1}$$

where H is the enthlapy of the system. H can be expressed in term of the system chemical composition as:

$$H = m\left(\sum_i Y_i h_i\right) \tag{C.2}$$

where Y_i and h_i are respectively the mass fraction and the mass enthalpy of species i, and m is the total mass of the system. Differentiation of Eq. (C.2) gives:

$$\frac{dH}{dt} = m\left(\sum_i Y_i \frac{dh_i}{dt} + \sum_i h_i \frac{dY_i}{dt}\right) \tag{C.3}$$

Assuming ideal-gas behavior, i.e. $h_i = h_i(T)$:

$$\frac{dh_i}{dt} = \frac{\partial h_i}{\partial T}\frac{dT}{dt} = c_{p,i}\frac{dT}{dt} \tag{C.4}$$

where $c_{p,i}$ is the mass heat capacity at constant pressure of species i. On the other hand, the equation of conservation of species i gives, when transport is neglected:

$$\boxed{m\frac{dY_i}{dt} = VW_i\dot{\omega}_i} \tag{C.5}$$

with V denotes the volume of the reactor and $\dot{\omega}_i$ the net production rate of species i. Replacing Eqs. (C.4) and (C.5) in Eq. (C.3) yields

$$\boxed{mc_p\frac{dT}{dt} = -V\sum_i h_i W_i \dot{\omega}_i} \tag{C.6}$$

where c_p is the mass heat capacity at constant pressure of the mixture, defined as $c_p = \sum_i Y_i c_{p,i}$. Using Eqs. (C.5) and (C.6) with $\rho = m/V$ and combining to the equation of state

for an ideal gas mixture yields the governing equations for a constant pressure, fixed-mass, adiabatic reactor:

$$\begin{cases} \rho \dfrac{dY_i}{dt} = W_i \dot{\omega}_i \\ \rho c_p \dfrac{dT}{dt} = -\sum_i h_i W_i \dot{\omega}_i \\ \rho = \dfrac{P}{RT} \dfrac{1}{\sum_k Y_k / W_k} \end{cases} \tag{C.7}$$

List of Figures

List of Tables

Bibliography

Altenkirch, R. A., Eichhorn, R., Hus, N. N., Brancic, A. B., and Cevallos, N. E. (1976). Characteristics of laminar gas jet diffusion flames under the influence of elevated gravity. Proc. Combust. Inst., 16:1165–1174.

Andersen, S. O., Sarma, K. M., and Taddonio, K. N. (2007). Technology Transfer for the Ozone Layer: Lessons for Climate Change. Routledge.

André, B., Castelain, T., and Bailly, C. (2013). Experimental study of flight effects on slightly underexpanded supersonic jets. In 19th AIAA/CEAS Aeriacoustics Conference, Berlin, Germany.

Angelberger, C., Veynante, D., Egolfopoulos, F., and Poinsot, T. (1998). Large eddy simulations of combustion instabilities in premixed flames. In Proc. of the Summer Program , pages 61–82. Center for Turbulence Research, NASA Ames/Stanford Univ.

Antonia, R. A. and Bilger, R. W. (1973). An experimental investigation of an axisymmetric jet in a co-flowing air stream. J. Fluid Mech, 61(4):805–822.

Balakrishnan, G., Smooke, M. D., and Williams, F. A. (1995). A numerical investigation of extinction and ignition limits in laminar nonpremixed counterflowing hydrogen-air streams for both elementary and reduced chemistry. Combust. Flame, 102(3):329–340.

Bauer, C. B., Koch, A., Minutolo, F., and Grenard, P. (2013). Engineering model for rocket exhaust plumes verified by CFD results. In 29th International Symposium on Space Technology and Science, Nagoya-Aichi, Japan.

Baulch, D. L., Duxbury, J., Grant, S. J., and Montague, D. C. (1981). Evaluated kinetic data for high temperature reactions, vol. 4: Homogeneous gas phase rections of halogen- and cyanide- containing species. J. Phys. Chem. Ref Data, 10, Suppl. No. 1:1–721.

Beiting, E. (1995). Characteristics of Alumina Particles From Solid Rocket Motor Exhaust in the Stratosphere. Technical Report 5231, The Aerospace Corporation.

Beiting, E. (1999). Stratospheric Plume Dispersion: Measurements from STS and Titan Solid Rocket Motor Exhaust. Technical Report TR-99(1306)-1, The Aerospace Corporation.

Beiting, E. J. (1997). Solid Rocket Motor Exhaust Model for Alumina Particles in the Stratosphere. J. Spacecr. Rockets, 34(3):303–310.

Bekki, S. (1997). On the possible role of aircraft-generated soot in the middle latitude ozone depletion. J. Geophys. Res., 102(D9):10751.

Bilger, R. W., Starner, S. H., and Kee, R. J. (1990). On Reduced Mechanisms for Methane-Air Combustion in Nonpremixed Flames. Combust. Flame, 80(2):135–149.

Bird, R., Stewart, W., and Lighfoot, E. (1960). Transport phenomena. John Wiley, New York.

Biringen, S. (1986). An experimental investigation of a turbulent round jet in a coflowing airstream. In Proc. ASME Winter Annual Meeting, Anaheim, California.

Bish, E. S. and Dahm, W. J. A. (1994). Nonequilibrium Structure of H_2-Air Combustion in Turbulent Jets. In 32nd Aerospace Sciences Meeting and Exhibit, pages 1–19, Reno, NV, USA.

Bogey, C. and Bailly, C. (2009). Turbulence and energy budget in a self-preserving round jet: direct evaluation using large eddy simulation. J. Fluid Mech., 627:129–160.

Boivin, P., Dauptain, A., Jiménez, C., and Cuenot, B. (2012). Simulation of a supersonic hydrogen-air autoignition-stabilized flame using reduced chemistry. Combust. Flame, 159(4):1779–1790.

Boivin, P., Jiménez, C., Sánchez, A., and Williams, F. (2011a). A four-step reduced mechanism for syngas combustion. Combust. Flame, 158(6):1059–1063.

Boivin, P., Jiménez, C., Sánchez, A., and Williams, F. (2011b). An explicit reduced mechanism for H2–air combustion. Proc. Combust. Inst., 33(1):517–523.

Brady, B. and Martin, L. (1997). Modeling the Multiphase Atmospheric Chemistry of Launch Clouds. J. Spacecr. Rockets, 34(6):780–784.

Brady, B. B. and Martin, L. R. (1995). Modeling solid rocket booster exhaust plumes in the stratosphere with SURFACE CHEMKIN. Technical Report TR-95(5231)-9, The Aerospace Corporation.

Brady, B. B., Martin, L. R., and Lang, V. I. (1997). Effects of launch vehicle emissions in the stratosphere. Journal of Spacecraft and Rockets, 34:774–779.

Branley, N. and Jones, W. (2001). Large Eddy simulation of a turbulent non-premixed flame. Combust. Flame, 127(1-2):1914–1934.

Brown, T. M., Tanoff, M. A., Osborne, R. J., Pitz, R. W., and Smooke, M. D. (1997). Experimental and Numerical Investigation of Laminar Hydrogen-c. Combust. Sci. Technol., 129(1):71–88.

Burke, M. L. and Zittel, P. F. (1998). Laboratory generation of free chlorine from HCl under stratospheric after burning conditions. Combust. Flame, 112(1-2):210–220.

Burke, S. P. and Schumann, T. E. W. (1928). Diffusion Flames. Ind. Eng. Chem., 20(10):998–1004.

Butler, T. D. and O'Rourke, P. J. (1977). A numerical method for two-dimensional unsteady reacting flows. Proc. Combust. Inst. , 16(1):1503 – 1515.

Calhoon, W. H., J. (1998). Evalution of Afterburning Cessation Mechanisms in Fuel Rich Rocket Exhaust Plume. In 34th AIAA/ASME/SAE/ASEE joint Propulsion Conference and Exhibit, Cleveland, OH, USA.

Chapman, S. (1930). A Theory of Upper Atmospheric Ozone. Q.J.R. Meteorol. Soc., (3):103–125.

Chung, S. H. and Williams, F. A. (1990). Asymptotic Structure and Extinction of CO-H2 Diffusion Flames with Reduced Kinetic Mechanisms. Combust. Flame, 82:389–410.

Cicerone, R. J. and Stedman, D. H. (1974). The Space Shuttle and other atmospheric chlorine sources. In Conf. Aerosp. Aeronaut. Meteorol., pages 9–11, El Paso, TX, USA.

Clark, K. and Loth, E. (2013). A multi-scale LES technique for coupling near-field and far-field domains for a jet flow. Computers & Fluids, 88:262–271.

Cofer, W. R., Purgold, G. C., Winstead, E. L., and Edahl, R. A. (1991). Space shuttle exhausted aluminum oxide: A measured particle size distribution. J. Geophys. Res., 96(D9):17371.

Colin, O., Ducros, F., Veynante, D., and Poinsot, T. (2000). A thickened flame model for large eddy simulations of turbulent premixed combustion. Phys. Fluids , 12(7):1843–1863.

Courant, R., Isaacson, E., and Rees, M. (1952). On the solution of nonlinear hyperbolic differential equations by finite differences. Commun. Pure Appl. Math., 5(3):243–255.

Cziczo, D. J. (2002). Composition of individual particles in the wakes of an Athena II rocket and the space shuttle. Geophys. Res. Lett., 29(21):2037.

Danilin, M. Y., Popp, P. J., Herman, R. L., Ko, M. K. W., Ross, M. N., Kolb, C. E., Fahey, D. W., Avallone, L. M., Toohey, D. W., Ridley, B. A., Schmid, O., Wilson, J. C., Baumgardner, D. G., Friedl, R. R., Thompson, T. L., and Reeves, J. M. (2003). Quantifying uptake of HNO_3 and H_2O by alumina particles in Athena-2 rocket plume. J. Geophys. Res., 108(D4):4141.

Danilin, M. Y., Shia, R. L., Ko, M. K. W., Weisenstein, D. K., Sze, N. D., Lamb, J. J., Smith, T. W., Lohn, P. D., and Prather, M. J. (2001). Global stratospheric effects of the alumina emissions by solid-fueled rocket motors. J. Geophys. Res., 106(D12):12727–12.

Dauptain, A., Gicquel, L. Y. M., and Moreau, S. (2012). Large Eddy Simulation of Supersonic Impinging Jets. AIAA Journal, 50(7):1560–1574.

de Cacqueray N., Bogey, C., and Bailly, C. (2011). Investigation of a High-Mach-Number Overexpanded Jet Using Large-Eddy Simulation. AIAA Journal, 49(10):2171–2182.

Denison, M. R., Lamb, J. L., Bjorndahl, W. D., Wong, E. Y., and Lohn, P. D. (1994). Solid rocket exhaust in the stratosphere: Plume diffusion and chemical reactions. Journal of Spacecraft and Rockets, 31:435–442.

Disselkamp, R. S., Carpenter, M. A., Cowin, J. P., Berkowitz, C. M., Chapman, E. G., Zaveri, R. A., and Laulainen, N. S. (2000). Ozone loss in soot aerosols. J. Geophys. Res. Atmos., 105(D8):9767–9771.

Domingo, P., Vervisch, L., and Veynante, D. (2008). Large-eddy simulation of a lifted methane jet flame in a vitiated coflow. Combust. Flame, 152(3):415–432.

Donea, J. (1984). Taylor-galerkin method for convective transport problems. Int. J. Numer. Meth. Fluids , 20(1):101–119.

Dubief, Y. and Delcayre, F. (2000). On coherent-vortex identification in turbulence. Journal of Turbulence, 1(11):1–11.

Duchaine, F., Jauré, S., Poitou, D., Quémerais, E., Staffelbach, G., Morel, T., and Gicquel, L. (2013). High performance conjugate heat transfer with the OpenPALM coupler. In V International Conference on Computational Methods for Coupled Problems in Science and Engineering - Coupled Problems 2013, Ibiza, Spain.

Esnault, O., Boileau, M., Vicquelin, R., Fiorina, B., and Gicquel, O. (2010). A Method To Accelerate LES Explicit Solvers Using Local Time-Stepping. In 48th AIAA Aerospace Sciences Meeting, Orlando, United States.

Fernández-Galisteo, D., Sánchez, A., Liñán, A., and Williams, F. (2009). One-step reduced kinetics for lean hydrogen–air deflagration. Combust. Flame, 156(5):985–996.

Freund, J. B., Lele, S. K., and Moin, P. (2000a). Compressibility effects in a turbulent annular mixing layer. J. Fluid Mech., 421:229–267.

Freund, J. B., Lele, S. K., and Moin, P. (2000b). Numerical Simulation of a Mach 1.92 Turbulent Jet and its Sound Field. AIAA Journal, 38(11):2023–2031.

Gates, A. M. (2002). In situ measurements of carbon dioxide, 0.37–4.0 μm particles, and water vapor in the stratospheric plumes of small rockets. J. Geophys. Res., 107(D22):4649.

Germano, M., Piomelli, U., Moin, P., and Cabot, W. H. (1991). A dynamic subgrid-scale eddy viscosity model. Physics of Fluids A, 3(7).

Gicquel, O., Darabiha, N., and Thévenin, D. (2000). Liminar premixed hydrogen/air counterflow flame simulations using flame prolongation of ILDM with differential diffusion. Proc. Combust. Inst., 28(2):1901–1908.

Gomberg, R. I. and Stewart, R. B. (1976). A computer simulation of the afterburning processes occurring within solid rocket motor plumes in the troposphere. Technical Report TN D-8303, NASA.

Goodwin, D., Malaya, N., Moffat, H., and Speth, R. (2013). Cantera: An object-oriented software toolkit for chemical kinetics, thermodynamics, and transport processes. Version 2.1.0, available at: https://code.google.com/p/cantera/.

Gordon, S. and McBride, B. (1971). Computer Program for Calculation of Complex Chemical Equilibrium Compositions, Rocket Performance, Incident and Reflected Shocks, and Chapman-Jouquet Detonations. NASA Report No. NASA-SP-273.

Grenard, P., Bauer, C., Koch, A., and Winkler, H. (2013). Evaluation of rocket launches' effect on climate. In ODAS 2013 - 13th ONERA-DLR Aerospace Symposium, Palaiseau, France.

Hirshfelder, J. O., Curtiss, C. F., and Bird, R. B. (1969). Molecular theory of gases and liquids. John Wiley and Sons, New York.

Hoshizaki, H., Anderson, L. B., Conti, R. J., Farlow, N., Meyer, J. W., Overcamp, T., Redler, K. O., and Watson, V. (1975). Aircraft wake microscale phenomena. The Stratosphere Perturbed by Propulsion Effluents, CIAP, DOT-TST-75-53.

Hottel, H. C. and Hawthorne, W. R. (1949). Diffusion in laminar flame jets. In 3rd Symposium on Combustion, Flame and Explosion Phenomena, pages 254 – 266. The Combustion Institute, Pittsburgh.

Jackman, C. H., Considine, D. B., and Fleming, E. L. (1998). A global modeling study of solid rocket aluminum oxide emission effects on stratospheric ozone. Geophysical research letters, 25(6):907–910.

Jameson, A., Schmidt, W., and Turkel, E. (1981). Numerical Solution of the Euler Equations by Finite Volume Methods Using Runge-Kutta Time Stepping Schemes. In 14th Fluid and Plasma Dynamics Conference, AIAA.

Jensen, D. E. and Jones, G. A. (1978). Reaction rate coefficients for flame calculations. Combust. Flame, 32:1–34.

Jones, A. E., Bekki, S., and Pyle, J. A. (1995). On the atmospheric impact of launching the Ariane 5 rocket. J. Geophys. Res., 100(D8):16,651–16,600.

Jones, W. and Rigopoulos, S. (2005). Rate-controlled constrained equilibrium: Formulation and application to nonpremixed laminar flames. Combust. Flame, 142(3):223–234.

Karypis, G. and Kumar, V. (1998). A Parallel Algorithm for Multilevel Graph Partitioning and Sparse Matrix Ordering. Journal of Parallel and Distributed Computing, 48(1):71–95.

Koch, A. D., Bauer, C., Dumont, E., Minutolo, F., Sippel, M., Grenard, P., Ordonneau, G., Winkler, H., Guénot, L., Linck, C., Wood, C. R., Vira, J., Sofiev, M., and Tarvainen, V. (2013). Multidisciplinary approach for assessing the atmospheric impact of launchers. In 4th CEAS Air Sp. Conf., Linköping.

Kolmogorov, A. N. (1941). The local structure of turbulence in incompressible viscous fluid for very large reynolds numbers. C. R. Acad. Sci. , USSR, 30:301.

Kraichnan, R. (1970). Diffusion by a random velocity field. Physics of Fluids, 13(22):22–31.

Kuenne, G., Ketelheun, A., and Janicka, J. (2011). LES modeling of premixed combustion using a thickened flame approach coupled with FGM tabulated chemistry. Combust. Flame , 158(9):1750 – 1767.

Lamarque, N. (2007). Schémas numériques et conditions limites pour la simulation aux grandes échelles de la combustion diphasique dans les foyers d'hélicoptère. Phd thesis, INP Toulouse.

Larson, R. S., McColgan, C. J., and Packman, A. B. (1978). Jet noise source modification due to forward flight. AIAA Journal, 16(3):225–232.

Lax, P. D. and Wendroff, B. (1964). Difference schemes for hyperbolic equations with high order of accuracy. Commun. Pure Appl. Math. , 17:381–398.

Légier, J.-P. (2001). Simulations numériques des instabilités de combustion dans les foyers aéronautiques. Phd thesis, INP Toulouse.

Leone, D. M. and Turns, S. R. (1994). Active chlorine and nitric oxide formation from chemical rocket plume afterburning. In 32nd Aerospace Sciences Meeting and Exhibit. Aerospace Sciences Meeting. AIAA., Reno, NV.

Lilly, D. K. (1992). A proposed modification of the germano subgrid-scale closure method. Physics of Fluids A, 4(3):633–635.

Lin, K.-C., Faeth, G. M., Sunderland, P. B., Urban, D. L., and Yuan, Z.-G. (1999). Shapes of Nonbuoyant Round Luminous hydrocarbon/air laminar jet diffusion flames. Combust. Flame, 116(3):415–431.

Linan, A. (1974). The asymptotic structure of counterflow diffusion flames for large activation energies. Acta Astronaut., 1:1007–1039.

Lions, P. (1988). On the Schwarz alternating method. I. In First international symposium on domain decomposition methods for partial differential equations., pages 1–42, AIAA.

Lohn, P. D., Wong, E. P., Smith, T. W., Edwards, J. R., and Pilson, D. (September 1999). Rocket exhaust impact on stratospheric ozone. Technical report, The Aerospace Corporation.

Lovaraju, P. and Rathakrishnan, E. (2011). Experimental studies on co-flowing subsonic and sonic jets. Flow Turbulence Combust., 87(1):115–132.

Lyons, K. M., Watson, K. A., Carter, C. D., and Donbar, J. M. (2005). On flame holes and local extinction in lifted-jet diffusion flames. Combust. Flame, 142(3):308–313.

Maas, U. and Pope, S. (1992). Simplifying chemical kinetics: Intrinsic low-dimensional manifolds in composition space. Combust. Flame, 88(3-4):239–264.

Maidi, M. and Lesieur, M. (2005). Large eddy simulations of spatially growing subsonic and supersonic turbulent round jets. Journal of Turbulence, 6(38):1–20.

Martin, L. R. (1994). Possible effect of the chlorine oxide dimer on transient ozone loss in rocket plumes. Technical report, DTIC Document.

Molina, M. J. (1991). Heterogeneous chemistry on polar stratospheric clouds. Atmos. Environ. Part A. Gen. Top., 25(11):2535–2537.

Molina, M. J., Molina, L. T., Zhang, R., Meads, R. F., and Spencer, D. D. (1997). The reaction of $ClONO_2$ with a HCl on aluminum oxide. Geophys. Res. Lett., 24:1619–1622.

Molina, M. J. and Rowland, F. S. (1974). Stratospheric sink for chlorofluoromethanes: chlorine atomc-atalysed destruction of ozone. Nature, 249:810–812.

Molina, M. J., Tso, T. L., Molina, L. T., and Wang, F. C. (1987). Antarctic stratospheric chemistry of chlorine nitrate, hydrogen chloride, and ice: release of active chlorine. Science (80-.)., 238(4831):1253–1257.

Morris, P. J. (1976). Turbulence measurements in subsonic and supersonic axisymmetric jets in parallel stream. AIAA Journal, 14(10):1468–1475.

Moureau, V., Domingo, P., and Vervisch, L. (2011). From Large-Eddy Simulation to Direct Numerical Simulation of a lean premixed swirl flame : Filtered laminar flame-PDF modeling. Combust. Flame, 158(7):1340–1357.

Munday, D., Gutmark, E., Liu, J., and Kailasanath, K. (2011). Flow structure and acoustics of supersonic jets from conical convergent-divergent nozzles. Physics of Fluids, 23(11):116102.

Murakami, E. and Papamoschou, D. (2002). Mean flow development in dual-stream compressible jets. AIAA Journal, 240(6):1131–1138.

Murray, N., Bekki, S., Toumi, R., and Soares, T. (2013). On the uncertainties in assessing the atmospheric effects of launchers. Prog. Propuls. Phys., 4:457–474.

Newman, P. A., Wilson, J. C., Ross, M. N., Brock, C. A., Sheridan, P. J., Schoeberl, M. R., Lait, L. R., Bui, T. P., Loewenstein, M., and Podolske, J. R. (2001). Chance encounter with a stratospheric kerosene rocket plume from Russia over California. Geophys. Res. Lett., 28(6):959–962.

Nickels, T. B. and Perry, A. E. (1996). An experimental and theoretical study of the turbulent coflowing jet. J. Fluid Mech., 309:157–182.

Oijen, J. V. and GOEY, L. D. (2000). Modelling of Premixed Laminar Flames using Flamelet-Generated Manifolds. Combust. Sci. Technol., 161(1):113–137.

Papadogiannis, D., Duchaine, F., Sicot, F., Gicquel, L., Wang, G., and Moreau, S. (2014). Large Eddy Simulation of a high pressure turbine stage: effects of sub-grid scale modeling and mesh resolution. In ASME Turbo Expo 2014 Turbine Tech. Conf. Expo., pages 1–13, Dusseldorf, Germany.

Papamoschou, D. and Roshko, A. (1988). The compressible turbulent shear layer: an experimental study. J. Fluid Mech., 197:453–477.

Pellett, G. L., Isaac, K. M., Humphreys JR., W. M., Gartrell, L. R., Roberts, W. L., Dancey, C. L., and Northam, G. B. (1998). Velocity and Thermal Structure, and Strain-Induced Extinction of 14 to 100% Hydrogen-Air Counterflow Diffusion Flames. Combust. Flame, 112(4):575–592.

Pergament, H. S. (1992). Standardized plume flowfield model SPF-III, vol. II, program user's manual. Propulsion Science and Technology Inc., Princeton, NJ., Report No. PST TR-11.

Piacentini, A., Morel, T., Thévenin, A., and Duchaine, F. (2011). An open source dynamic parallel coupler. In IV International Conference on Computational Methods for Coupled Problems in Science and Engineering - Coupled Problems 2011, Kos Island, Greece.

Poinsot, T. and Lele, S. (1992). Boundary conditions for direct simulations of compressible viscous flows. Journal of Computational Physics, 101(1):104–129.

Poinsot, T. and Veynante, D. (2005). Theoretical and Numerical Combustion. R.T Edwards.

Pons, L., Darabiha, N., and Candel, S. (2008). Pressure effects on nonpremixed strained flames. Combustion and Flame, 152(1-2):218–229.

Pope, S. B. (2000). Turbulent Flows. Cambridge University Press.

Popp, P. J., Ridley, B. A., Neuman, J. A., Avallone, L. M., Toohey, D. W., Zittel, P. F., Schmid, O., Herman, R. L., Gao, R. S., Northway, M. J., Holecek, J. C., Fahey, D. W., Thompson, T. L., Kelly, K. K., Walega, J. G., Grahek, F. E., Wilson, J. C., Ross, M. N., and Danilin, M. Y. (2002). The emission and chemistry of reactive nitrogen species in the plume of an Athena II solid-fuel rocket motor. Geophys. Res. Lett., 29(18):1–4.

Rana, Z. A., Thornber, B., and Drikakis, D. (2011). Transverse jet injection into a supersonic turbulent cross-flow. Physics of Fluids, 23(4):046103.

Rocchi, J. F. (2014). Large Eddy Simulations of the ignition phase in a cryogenic rocket engine. PhD thesis, Université de Toulouse - Ecole doctorale MEGeP Dynamique des Fluides.

Rosario, N. (2011). Simulation of the propulsive system of a rocket. Master Thesis. Instituto Superior Tecnico/ESA Internal Report.

Ross, M. (1996). Local Effects of Solid Rocket Motor Exhaust on Stratospheric Ozone. J. Spacecr. Rockets, 33(1):144–153.

Ross, M., Whitefield, P. D., Hagen, D. E., and Hopkins, A. R. (1999). In-situ measurement of the aerosol size distribution in stratospheric solid rocket motor exhaust plumes. Geophys. Res. Lett., 26(7):819–822.

Ross, M. N. (2004). Ozone depletion caused by NO and H2O emissions from hydrazine-fueled rockets. J. Geophys. Res., 109:1–7.

Ross, M. N., Ballenthin, J. O., Gosselin, R. B., Meads, R. F., Zittel, P., and Benbrook, J. R. (1997a). In-situ measurement of Cl_2 and O_3 in a stratospheric solid rocket motor exhaust plume. Geophys. Res. Lett., 24(14):1755–1758.

Ross, M. N., Benbrook, J. R., Sheldon, W. R., Zittel, P. F., and McKenzie, D. L. (1997b). Observation of stratospheric ozone depletion in rocket exhaust plumes. Nature, 390(6655):62–64.

Ross, M. N., Toohey, D., Peinemann, M., and Ross, P. (2009). Limits on the Space Launch Market Related to Stratospheric Ozone Depletion. Astropolitics, 7:50–82.

Ross, M. N., Toohey, D. W., Rawlins, W. T., Richard, E. C., Kelly, K. K., Tuck, A. F., Proffitt, M. H., Hagen, D. E., Hopkins, A. R., Whitefield, P. D., Benbrook, J. R., and Sheldon, W. R. (2000). Observation of stratospheric ozone depletion associated with Delta II rocket emissions. Geophys. Res. Lett., 27(15):2209–2212.

Rowland, F. S. and Molina, M. J. (1975). Chlorofluoromethanes in the environment. Reviews of Geophysics, 13:1–35.

Sánchez, A. L., Linan, A., and Williams, F. A. (1999). Chain-branching explosions in mixing layers. SIAM J. Appl. Math., 59(4):1335–1355.

Sánchez, A. L. and Williams, F. A. (2014). Recent advances in understanding of flammability characteristics of hydrogen. Prog. Energy Combust. Sci., 41:1–55.

Sander, S. P., Abbatt, J., Barker, J. R., Burkholder, J. B., Friedl, R. R., Golden, D. M., Huie, R. E., Kolb, C. E., Kurylo, M. J., Moortgat, G. K., Orkin, V. L., and Wine, P. H. (2011). Chemical kinetics and photochemical data for use in atmospheric studies. evaluation no. 17. Technical Report JPL Publication 10-6, Jet Propulsion Laboratory, Pasadena.

Sanderson, K. (2010). Science lines up for seat to space. Nature. Special Report, 463:716–717.

Sarohia, V. (1978). Some flight simulation experiments on jet noise from supersonic underexpanded flows. AIAA Journal, 16(7):710–716.

Saudreau, M., Borée, J., Bury, Y., and Charnay, G. (2004). Round Turbulent Air Jet Submitted to a Pulsed Coflow. AIAA Journal, 42(1):280–288.

Saxena, P. and Williams, F. A. (2006). Testing a small detailed chemical-kinetic mechanism for the combustion of hydrogen and carbon monoxide. Combust. Flame, 145(1-2):316–323.

Schmid, O. (2003). Size-resolved particle emission indices in the stratospheric plume of an Athena II rocket. J. Geophys. Res., 108(D8):4250.

Schönfeld, T. and Rudgyard, M. (1999). Steady and Unsteady Flow Simulations Using the Hybrid Flow Solver AVBP. AIAA Journal, 37(11):1378–1385.

Selmin, V. (1987). Third-order finite element schemes for the solution of hyperbolic problems. Technical Report 707, INRIA report.

Senoner, J.-M., García, M., Mendez, S., Staffelbach, G., Vermorel, O., and Poinsot, T. (2008). Growth of Rounding Errors and Repetitivity of Large-Eddy Simulations. AIAA Journal, 46(7):1773–1781.

Seshadri, K., Peters, N., and Williams, F. (1994). Asymptotic analyses of stoichiometric and lean hydrogen-air flames. Combust. Flame, 96(4):407–427.

Sheikhi, M., Drozda, T., Givi, P., Jaberi, F., and Pope, S. (2005). Large eddy simulation of a turbulent nonpremixed piloted methane jet flame (Sandia Flame D). Proc. Combust. Inst., 30(1):549–556.

Simmons, F. S. (2000). Rocket Exhaust Plume Phenomenology. Aerospace Press.

Smagorinsky, J. (1963). General circulation experiments with the primitive equations: 1. The basic experiment. Mon. Weather Rev., 91:99–164.

Smith, G. P., Golden, D. M., Frenklach, M., Moriarty, N. W., Eiteneer, B., Goldenberg, M., Thomas Bowman, C., Hanson, R. K., Song, S., Gardiner Jr., W. C., Lissianski, V. V., and Qin, Z. (1999). Gri-mech 3.0. `http://www.me.berkeley.edu/gri\_mech/`.

Spalding, D. B. (1979). Combustion and mass transfer: a textbook with multiple-choice exercises for engineering students. Pergamon Press Oxford.

Stewart, R. B. and Gomberg, R. I. (1976). The Production of Nitric Oxide in the Troposphere as a Result of Solid-Rocket-Motor Afterburning. Technical Report TN D-8137, NASA.

Sutton, G. P. and Biblarz, O. (2001). Rocket Propulsion Elements. Wiley, 7th edition.

Trees, D., Brown, T. M., Seshadri, K., Smooke, M. D., Balakrishnan, G., Pitz, R. W., Giovangigli, V., and Nandula, S. P. (1995). The Structure of Nonpremixed Hydrogen-Air Flames. Combust. Sci. Technol., 104(4-6):427–439.

Troutt, T. R. and McLaughlin, D. K. (1982). Experiments on the flow and acoustic properties of a moderate-reynolds-number supersonic jet. J. Fluid Mech., 116:123–156.

Troyes, J., Dubois, I., Borie, V., and Boischot, A. (2006). Multi-phase reactive numerical simulations of a model solid rocket motor exhaust jet. In 42nd AIAA/ASME/SAE/ASEE Jt. Propuls. Conf. Exhib., pages 1–13, Sacramento, CA.

Turns, S. R. (1996). An Introduction to Combustion. Concepts and Applications. McGraw-Hill, Inc.

Villermaux, E. and Durox, D. (1992). On the Physics of Jet Diffusion Flames. Combust. Sci. Technol., 84(1):279–294.

Vuorinen, V., Yu, J., Tirunagari, S., Kaario, O., Larmi, M., Duwig, C., and Boersma, B. J. (2013). Large-eddy simulation of highly underexpanded transient gas jets. Physics of Fluids, 25(1):016101.

Wang, G., Duchaine, F., Papadogiannis, D., Duran, I., Moreau, S., and Gicquel, L. (2014). An overset grid method for large eddy simulation of turbomachinery stages. Journal of Computational Physics, 274:333–355.

Wang, G., Papadogiannis, D., Duchaine, F., Gourdain, N., and Gicquel, L. Y. M. (2013). Towards massively parallel large eddy simulation of turbine stages. In ASME TURBO EXPO 2013 Gas Turbine Technical Congress & Exposition, San Antonio, USA.

Wehrleyer, J. A., Yeralan, S., and Tecu, K. S. (1996). Influence of Strain Rate and Fuel Dilution on Laminar Nonpremixed Hydrogen-Air Flame Structure : An Experimental Investigation. Combust. Flame, 107(1-2):125–140.

Williams, R. D. (1991). Performance of dynamic load balancing algorithms for unstructured mesh calculations. Concurrency: Practice, and Experience, 3(5):451–481.

World Meteorological Organization (1990, 1994, 1998, 2002 and 2006). Scientific Assessment of Ozone Depletion.

Wygnanski, I. and Fiedler, H. (1969). Some measurement in the self-preserving jet. J. Fluid Mech., 38(3):577–612.

Yu, H. (1999). Solving parabolic problems with different time steps in different regions in space based on domain decomposition methods. Applied Numerical Mathematics, 30(4):475–491.

Yüceil, K. B. and Ötügen, M. V. (2002). Scaling parameters for under expanded supersonic jets. Physics of Fluids, 14(12):4206–4215.

Zittel, P. F. (September 1994). Computer model predictions of the local effects of large, solid-fuel rocket motors on stratospheric ozone. Technical Report TR-94(4231)-9, The Aerospace Corporation.